Design Principles for Efficient Oxygen Reduction Electrocatalysts: Unveiling Structure-Activity Relationships in Non-Noble Metal Systems

Ph.D. Thesis

By

DIKESHWAR HALBA
(Roll Number: 2101151002)



DEPARTMENT OF PHYSICS
INDIAN INSTITUTE OF TECHNOLOGY INDORE

JUNE, 2026

Design Principles for Efficient Oxygen Reduction Electrocatalysts: Unveiling Structure-Activity Relationships in Non-Noble Metal Systems

A THESIS

Submitted in partial fulfillment of the requirements for the award of the degree

of

DOCTOR OF PHILOSOPHY

by

DIKESHWAR HALBA
(Roll Number: 2101151002)



DEPARTMENT OF PHYSICS
INDIAN INSTITUTE OF TECHNOLOGY INDORE

JUNE, 2026

INDIAN INSTITUTE OF TECHNOLOGY INDORE

I hereby certify that the work which is being presented in the thesis entitled **Design Principles for Efficient Oxygen Reduction Electrocatalysts: Unveiling Structure-Activity Relationships in Non-Noble Metal Systems** in the partial fulfillment of the requirements for the award of the degree of **DOCTOR OF PHILOSOPHY** and submitted in the **Department of Physics, Indian Institute of Technology Indore**, is an authentic record of my own work carried out during the time period from May 2021 to June 2026 under the supervision of **Dr. Srimanta Pakhira, Associate Professor, Indian Institute of Technology, Indore.**

The matter presented in this thesis has not been submitted by me for the award of any other degree of this or any other institute.

Dikeshwar Halba 26/10/2026

Signature of the student with date

(DIKESHWAR HALBA)

This is to certify that the above statement made by the candidate is correct to the best of my/our knowledge.

Signature of Thesis Supervisor with date

(DR. SRIMANTA PAKHIRA)

DIKESHWAR HALBA has successfully given his Ph.D. Oral Examination held on **26-10-2026**

Dr. Srimanta Pakhira, Ph.D.
Associate Professor
Department of Physics and
Centre for Advanced Electronics
Indian Institute of Technology Indore, M.P., India

Signature of Thesis Supervisor with date

Date: **26-10-2026**

ACKNOWLEDGEMENTS

I am deeply grateful to the supreme Lord for granting me this opportunity and blessing me with the abilities to succeed. Without divine guidance, this achievement would not have been possible. I thank him for answering my prayers and supporting me through my faith.

It is a great pleasure for me to acknowledge all the people who have helped and supported me to complete this Thesis. I would like to express my heartfelt thanks to my supervisor, ***Dr. Srimanta Pakhira****. I had the privilege of working with him throughout my doctoral studies. He consistently showed great care for my work, answered my questions promptly, and provided steady academic support, inspiration, and encouragement. His mentorship enriched me academically and nurtured my personal growth, changing my perspective and attitude. Through his guidance I developed and sharpened the skills and scientific methods essential for independent research. His vast knowledge, insightful feedback, and direction were crucial in shaping this research and advancing the investigation. For all this I will remain forever grateful and indebted to him.*

I would like to express my sincere gratitude to my PSPC members ***Prof. Rajesh Kumar****, Department of Physics,* ***Prof. Apurba K. Das****, Department of Chemistry, Indian Institute of Technology Indore for their invaluable suggestions, insights, and constructive comments that greatly improved this work. Furthermore, I am deeply grateful to the* ***Head, DPGC Convener****, all the faculty members, and staff of Department of Physics,* ***IIT Indore****, for fostering such an encouraging and supportive environment to carry out my research effectively.*

I would like to express my sincere gratitude to ***Prof. Suhas S. Joshi, Director IIT Indore,*** *for providing an exceptionally conducive research environment and giving me the opportunity to explore my scientific capabilities. I am equally thankful to* ***The Dean of Academic Affairs, The Dean of Research and Development and The Dean of student Affairs, IIT Indore*** *for their administrative support and encouragement throughout my doctoral journey.*

I extend my heartfelt thanks to my seniors, lab mates, and colleagues for their invaluable cooperation and for making my Ph.D. journey a memorable one. I am grateful to ***Dr. Nilima Sinha, Dr. Shrish Nath Upadhyay, Dr. Vikash Kumar, Dr. Ashok Singh, Dr. Himani Joshi, Mr. Lokesh, Ms.***

Kahkasha, Mr. Naveen, Mr. Anshuman, Mr. Deepesh, Mr. Hariom *and* ***Mr. Bhargab*** *with whom I shared not only great scientific discussions but also wonderful moments outside of research.*

I feel incredibly fortunate to be blessed with wonderful friends who have constantly encouraged, motivated, and cheered me on through every high and low. While it is impossible to name everyone individually, please know that your presence and support mean the world to me.

This acknowledgment would be incomplete without recognizing the profound patience and unwavering support of my family. I dedicate this thesis to my grandparents, parents, sister, and extended family members, who have always stood by me and given me the strength to pursue my goals. This milestone in my life would truly not have been possible without their endless love, cooperation, and sacrifices throughout this journey.

Lastly, I extend my heartfelt thanks to everyone who may not have been mentioned by name, but who contributed, directly or indirectly, to the successful completion of this Ph.D. research work.

-Dikeshwar Halba

Indian Institute of Technology Indore

Date: **26/10/2026**

Dedicated To

My Beloved Family

Mother, Father and Sister for their Love,

Care, and Blessings...

Design Principles for Efficient Oxygen Reduction Electrocatalysts: Unveiling Structure-Activity Relationships in Non-Noble Metal Systems

Synopsis of the Thesis

Submitted in partial fulfillment of the requirements for the award of the degree

of

DOCTOR OF PHILOSOPHY

by

DIKESHWAR HALBA
(Roll Number: 2101151002)

Under the supervision of
Dr. Srimanta Pakhira



DEPARTMENT OF PHYSICS
INDIAN INSTITUTE OF TECHNOLOGY INDORE

JUNE, 2026

SYNOPSIS

1. Introduction

The global energy demand continues to rise due to population growth, urbanization, industrial expansion, and the increasing use of electricity in daily life. The use of fossil fuels remains one of the main drivers of greenhouse gas emissions. Burning coal, oil, and natural gas releases large amounts of carbon dioxide, methane and other pollutants into the atmosphere, contributing to global warming and environmental degradation. Therefore, there is an urgent need to develop clean and efficient energy technologies that can reduce dependence on fossil fuels and support a more sustainable future. Fuel cells and metal–air batteries (MABs) have thus moved to the forefront of sustainable technology, offering a powerful combination of high energy efficiency and environment friendly characteristics.[1,2] In fuel cells, the oxygen reduction reaction (ORR: $O_2 + 4H^+ + 4e^- = 2H_2O$) is the most crucial reaction that takes place at the cathode. Oxygen molecules are reduced to water via addition of protons (H^+) and electrons (e^-) via multiple key reaction steps during the ORR process. However, the ORR kinetics which include cascade of reaction are slower compared to the anodic reaction (at anode: $H = H^+ + e^-$) in fuel cells.[3,4] Accelerating ORR kinetics requires efficient electrocatalysts that simultaneously deliver high activity, four-electron pathway selectivity, and long-term stability. Furthermore, such material should possess high electrical conductivity and abundant active sites, coupled with the economic viability necessary for large-scale applications. Till now various electrocatalyst have been explored by the researchers, among them Platinum (Pt) and Pt-based material were regarded as the best catalyst due to their superior catalytic activity and low overpotential.[5]

However, the high cost and scarcity of Pt and Pt-based electrocatalysts are the major factors which hamper their widespread commercialization in large-scale applications. Beyond economic concerns, Pt-based electrocatalysts face significant technical hurdles that impede their long-term viability. Specifically, they are highly susceptible to CO poisoning and fuel crossover effects, which diminish catalytic selectivity and overall power density. Consequently, there is an urgent need to develop cost-effective, Earth-abundant alternatives that can match the catalytic performance of noble metals without

compromising on durability.[2] Perovskite oxides, carbon-based materials such as graphene and carbon nanotubes (CNTs), and two-dimensional transition metal dichalcogenides (2D TMDs) can meet these requirements and are promising non-noble electrocatalysts for the ORR.

Perovskite oxides have emerged as promising electrocatalysts for the ORR because their crystal structure can be readily tuned by varying the A- and B-site cations and optimizing their electronic structure, oxygen-vacancy concentration, and surface reactivity. Current research focuses on improving their conductivity, stability, and catalytic activity through cation substitution, defect engineering, and nano structuring, while also developing a clearer understanding of the ORR mechanism. Perovskite oxides are attractive low-cost alternatives to noble-metal catalysts for fuel cells and other energy applications because they combine mixed ionic–electronic conductivity, adjustable metal-oxygen bonding, and the capacity to accommodate active transition-metal sites.[6] Similarly, CNTs have emerged as promising electrocatalyst supports and active materials for the ORR owing to their high electrical conductivity, large specific surface area, excellent chemical stability, and unique one-dimensional nanostructure. Their surface can be easily modified through heteroatom doping, defect engineering, and functionalization to create additional active sites and improve the adsorption of ORR intermediates. Encapsulated nanoparticles within CNTs/NCNTs have gained considerable attention as advanced ORR electrocatalysts because the CNT shell protects the nanoparticles from agglomeration, oxidation, and dissolution while still allowing efficient electron transport. The confinement effect of CNTs helps stabilize the active phase, control particle size, and improve catalytic durability under harsh electrochemical conditions. In addition, strong interactions between the encapsulated nanoparticles and the CNT framework can modulate the electronic structure and enhance catalytic performance, making these hybrid materials highly promising for fuel cells and next-generation energy systems.[7,8] On the other hand, the 2D materials, especially transition metal dichalcogenides (TMDs), have quickly become important candidates for the ORR and H_2 evolution reaction (HER). Their atomically thin structures produce unique electronic and surface properties that can significantly boost catalytic activity and selectivity. While large-scale commercial use remains limited, rapid advances in synthesis, characterization, and theory highlight strong potential for 2D TMDs to improve fuel-cell performance.[9]

Our present study includes theoretical and computational investigation of novel materials (perovskite oxides, CNTs, and 2D TMDs) to evaluate their potential as ORR electrocatalysts for fuel cell applications. Our work examines how the structural and electronic properties of these materials influence ORR activity, using first-principles calculations to predict and compare their electrocatalytic performance. These computational insights aim to guide the identification and design of promising, sustainable electrocatalysts for energy conversion technologies. The first chapter of the present thesis establishes the background of the study and evaluates the relevant literature in the field. The subsequent sections outline the motivation, central focus, and specific objectives of this work.

2. Motivation and Objective of the Work

The motivation of the present work is to design and investigate novel material such as perovskite oxide, CNTs and 2D TMDs which presents a viable pathway toward sustainable electrocatalysis. These materials exhibit exceptional properties that could transform electrocatalysis, providing enhanced efficiency and stability for essential energy conversion processes. Experimental evaluation is highly resource-intensive, we utilize first-principles calculations to accelerate material discovery. This theoretical approach aims to identify the key structural and electronic descriptors governing ORR activity, and drive the development of next-generation, sustainable energy technologies.

The main objectives of this work are as follows:

1. Elucidating the O_2 Reduction Mechanism on a 2D Monolayer $LaNiO_3$ Perovskite. (Published: D. Halba, S. Pakhira, ACS Omega 9 (2024) 35614–35626.)
2. Design and analysis of cobalt–platinum nanoparticle encapsulated within carbon nanotube for oxygen reduction reaction. (Published: D. Halba, A. Ojha, S. Pakhira, ACS Appl. Energy Mater. 8 (2025) 7948–7962.)
3. An Investigation of Electrocatalytic Activity of the FeCe Nanoparticle Encapsulated Carbon Nanotube towards Oxygen Reduction Reaction. (Published: D. Halba, L. Yadav, S. Pakhira, RSC Adv. 16 (2026) 9143-9154.)
4. A computational design of Mo Defective $MoTe_2$ for the highly efficient oxygen reduction reaction. (Published: S.N. Upadhyay, D. Halba, L. Yadav, S. Pakhira, Langmuir 39 (2023) 17700–17712.)

3. Methodology of the work

3.1: All the density functional theory (DFT) calculations have been performed using Vienna *Ab initio* simulation package (VASP) in the case of 2D Monolayer $LaNiO_3$ Perovskite.[10] The equilibrium structures, geometries, and electronic properties of 2D monolayer $LaNiO_3$ have been computed by using PBE-D3 method with the projector augmented wave (PAW) pseudopotentials. Exchange-correlation effects were described using the Perdew–Burke–Ernzerhof (PBE) generalized gradient approximation (GGA).[11] Grimme's semiempirical third-order dispersion correction was included in the DFT calculations to account for weak vdW interactions.[12] The pseudopotential basis sets used were PAW_PBE La_GW, PAW_PBE Ni_GW, and PAW_PBE O_GW for La, Ni, and O atoms, respectively.

3.2: The equilibrium structural, lattice, and electronic properties of the CoPt@CNT system were systematically computed utilizing a first principles-based hybrid periodic density functional theory method, incorporating D3 van der Waals corrections (DFT-D3).[8] The B3LYP-D3 method was implemented in the *ab initio*-based CRYSTAL17 suite code to execute all electronic structure calculations.[13] Gaussian-type orbitals (GTOs) basis sets were used in the electronic band structure calculations to provide a detailed representation of the atomic orbitals for C, Co, and Pt atoms.[14] Here, spin-polarized calculations using the periodic hybrid DFT-D3 method have been performed to optimize the equilibrium geometry and analyze the electronic properties of the studied system. In this study, triple-ζ valence with polarization (TZVP) quality basis sets specifically C_pob_TZVP_2012, Co_pob_TZVP_rev2, and Pt_pob_TZVP_rev2 were employed for the C, Co, and Pt atoms.[15] A TZVP basis set is important because it balances computational efficiency with high accuracy to precisely model electronic structures. The "ATOMSPIN" and "SPINLOCK" keywords are used to define the electron occupancy for either spin up or spin down.

3.3: All the DFT calculations were executed by using the CRYSTAL17 suite code.[13] The equilibrium crystal structure, electronic properties, band structure, and total density of states (TDOS) of FeCe@CNT system were evaluated using first principles based periodic hybrid DFT. The B3LYP-D3 method was employed to optimize the equilibrium structures and investigate the underlying ORR reaction mechanisms.[16] Semi-empirical Grimme's D3 corrections were incorporated in this study to capture

long-range vdW dispersion effects. Atomic orbitals were described using Gaussian-type basis sets implemented in the ab initio CRYSTAL17 code. We utilized triple-ζ valence polarization quality basis sets (Fe_pob_TZVP_2012 and C_pob_TZVP_2012) to describe the Fe and C atoms, respectively.[15] The effective core potential Ce_ECP_Meyer_2009 was used for the Ce atom. The equilibrium structures of the reaction intermediates were analyzed and visualized using the VESTA software.[17]

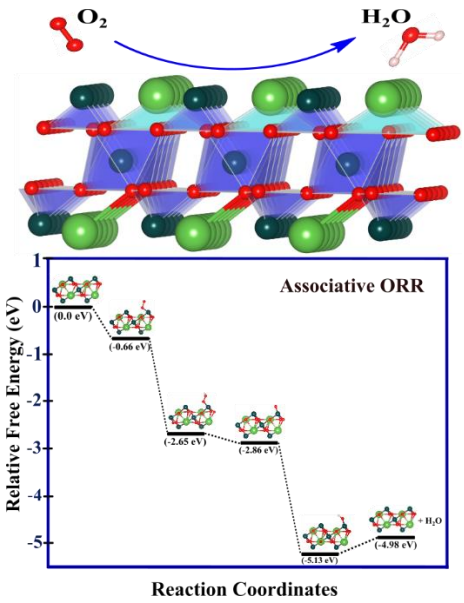
3.4: For the Mo defective 2D monolayer $MoTe_2$ TMD, the quantum mechanical periodic hybrid DFT approach was utilized to calculate the optimized geometries, single-point energies, and electronic properties. CRYSTAL 17 suite code was used to perform all the DFT calculations.[13] To establish the equilibrium structures and thoroughly evaluate the reaction mechanisms, calculations were performed at the B3LYP-D3 level of theory.[16] To account for exchange and correlation effects within DFT, Grimme's semiempirical dispersion correction (D3) was applied in this study to include long-range, weak vdW interactions.[18] Gaussian-type basis sets were utilized within the *ab initio*-based CRYSTAL17 suite code to describe the atomic orbitals.[14] In this work, molybdenum atoms were described using the Mo_SC_HAYWSC-311(d31)G_cora_1997 basis set, while Te, O, and H atoms were treated with triple-ζ valence basis sets including polarization (TZVP).[15] All geometric structures and orbitals were visualized by the VESTA software.

4. Summary of the Current Work

4.1 Elucidating the O_2 reduction mechanism on a 2D monolayer $LaNiO_3$ perovskite.

In this study, we computationally designed 2D monolayer $LaNiO_3$ from bulk 3D $LaNiO_3$ by cleaving (0 0 1) surface. We studied the structural and electronic properties of 3D $LaNiO_3$ and 2D monolayer $LaNiO_3$ using the first principle-based periodic hybrid DFT method. Electronic property calculations reveal that the bulk $LaNiO_3$ has metallic behavior, but its limited number of active sites led us to design 2D monolayer $LaNiO_3$. It was found that the 2D monolayer $LaNiO_3$ has small electronic density of states (DOS) around the Fermi level (E_F) showing semiconducting nature. The detailed reaction mechanisms of ORR have been explored on the surface of the 2D monolayer $LaNiO_3$ by employing the PBE-D3 method. The Gibbs free energy (ΔG) of each ORR reaction intermediate was computed to investigate the electrocatalytic activity of the 2D monolayer $LaNiO_3$. The ORR reaction mechanism involving both dissociative and

associative pathway have been explored on the surface of the 2D monolayer $LaNiO_3$. Our energy calculations demonstrated that the ORR followed $4e^-$ transfer mechanism on the surface of the 2D monolayer $LaNiO_3$.



All ORR steps are spontaneous and thermodynamically favorable, indicating that the 2D $LaNiO_3$ monolayer has promising catalytic properties for reducing O_2 molecules to water. We hope that our findings in this study will contribute to the development of new and more efficient non-noble metal electrocatalysts. The results discussed in this section correspond to the following article:

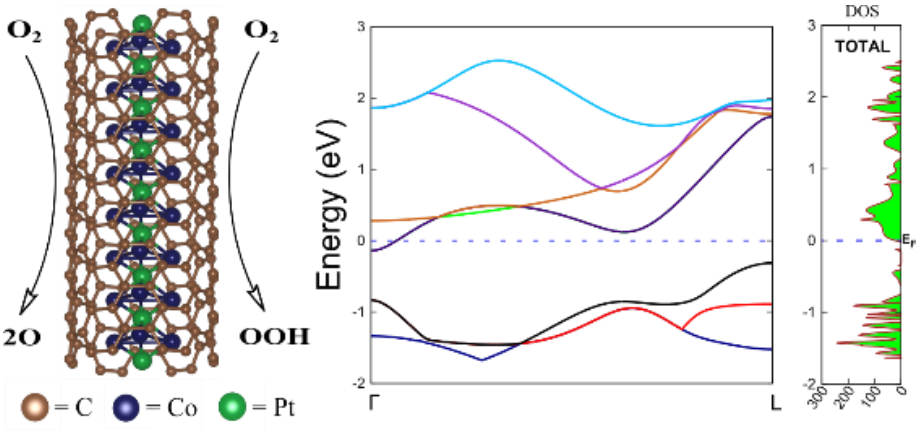
D. Halba, S. Pakhira, Unraveling the O_2 Reduction Reaction on 2D Monolayer $LaNiO_3$ Perovskite, ACS Omega 9 (2024) 35614–35626.

DOI: https://doi.org/10.1021/acsomega.4c03544

4.2 Design and analysis of cobalt–platinum nanoparticle encapsulated within carbon nanotube for oxygen reduction reaction.

We first constructed a (6,6) carbon nanotube model and examined its structural and electronic properties. The pristine CNT was found to be semiconducting with a zero-band gap (Eg = 0) and only a small electron density was present at the Fermi level (E_F). Then we strategically encapsulated CoPt nanoparticle within pristine CNT to get our studied material CoPt@CNT. Encapsulation produced a synergistic effect that enhanced the CNT's electrocatalytic performance. The electronic properties, band structure, total DOS of CoPt@CNT have been studied. Projected DOS (PDOS) analysis

shows a strong contribution from the Co and Pt *d*-orbitals, which gives CoPt@CNT conducting character.

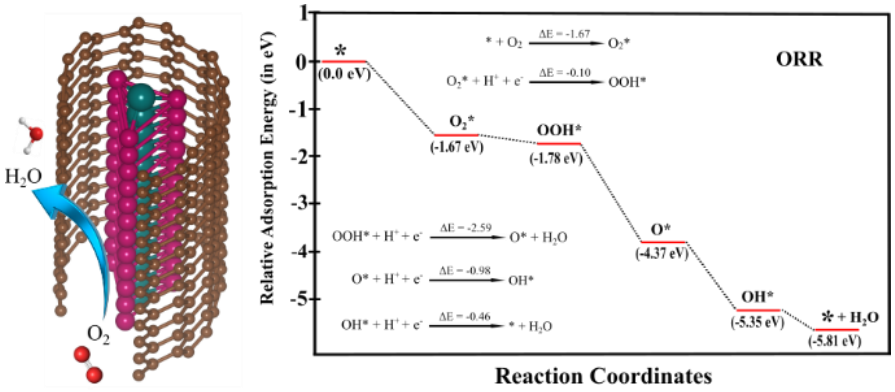


After establishing the material's conductive nature, we proceeded to investigate the ORR mechanism on the CoPt@CNT surface. This study analyzed both associative and dissociative reaction routes to understand the ORR activity of CoPt@CNT. We calculated the adsorption energy changes and Gibbs free energies for all reaction intermediates involved in the ORR mechanism. Our study demonstrated that the adsorption of O_2 on CoPt@CNT surface produces the O_2_CoPt@CNT intermediate, with computed ΔE and ΔG of approximately −0.79 eV and −0.71 eV, respectively. Negative adsorption and Gibbs free energy changes for the various intermediates of ORR show that the reaction steps are energetically favorable and do not require external energy. The active sites present on the surface of the CoPt@CNT material are thermodynamically and energetically favorable for the O_2 reduction reaction. Active sites on CoPt@CNT are energetically favorable and thermodynamically suited to catalyze ORR. The CoPt@CNT material demonstrates excellent activity as an ORR electrocatalyst for fuel cells. We anticipate that our findings will aid the discovery of new, efficient electrocatalysts for green energy conversion devices, including fuel cells and metal–air batteries. The results discussed in this section correspond to the following article:

D. Halba, A. Ojha, S. Pakhira, Cobalt–Platinum Nanoparticle Encapsulated within Carbon Nanotube for Superior O_2 Reduction Reaction, ACS Appl. Energy Mater. 8 (2025) 7948–7962. DOI: https://doi.org/10.1021/acsaem.5c00209

4.3 An investigation of electrocatalytic activity of the FeCe nanoparticle encapsulated carbon nanotube towards oxygen reduction reaction.

We computationally designed FeCe@CNT by encapsulating FeCe nanoparticle within pristine CNT. The pristine FeCe@CNT system was modeled as a van der Waals crystal, and its structural and electronic properties were studied. Our electronic structure calculations show that the FeCe@CNT system exhibits metallic behavior dominated by Fe and Ce *d*-orbital contributions near the Fermi level (E_F). We observe band crossings at E_F and a large total DOS near E_F, which together indicate metallic conductivity of FeCe@CNT material.

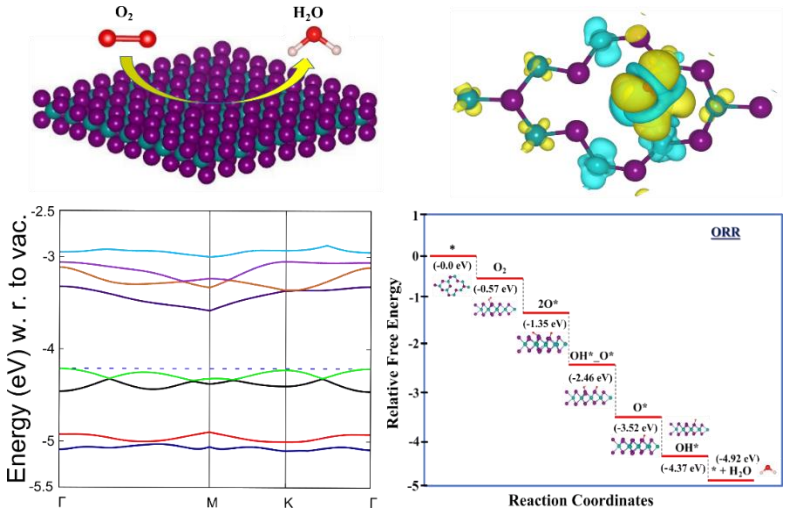


The ORR pathway on the FeCe@CNT surface was further explored by calculating the adsorption energies (ΔE) and relative adsorption energy of all the reaction intermediates. The present study finds that O_2 adsorption on the FeCe@CNT surface occurs with an energy cost of −1.67 eV, indicating spontaneous and energetically favorable O_2 activation. Our results indicate that the reaction predominantly follows the associative mechanism. We have explored all the reaction steps of the associative pathway on the FeCe@CNT surface. Our computed adsorption energies and the relative adsorption energies of each reaction intermediates demonstrate that the active sites on FeCe@CNT are energetically favorable for the ORR. The synergistic interaction of Fe and Ce with the CNT promotes efficient O_2 activation and stabilizes the reaction intermediates favorably. Our results show that FeCe@CNT is a very promising non-precious metal catalyst with exceptional activity for the oxygen reduction reaction. The results discussed in this section correspond to the following article:

D. Halba, L. Yadav, S. Pakhira, An investigation of electrocatalytic activity of the FeCe nanoparticle encapsulated carbon nanotube towards oxygen reduction reaction, RSC Adv. 16 (2026) 9143–9154. DOI: https://doi.org/10.1039/D6RA00601A

4.4 A computational design of Mo Defective $MoTe_2$ for the highly efficient oxygen reduction reaction.

We computationally modelled two-dimensional (2D) monolayer $MoTe_2$ and performed geometry optimization and electronic structure calculations. We found that the 2D monolayer $MoTe_2$ has a direct band gap of 1.64 eV and shows no electronic density of states at the Fermi level (E_F).



Then we designed a Mo-defective 2D monolayer $MoTe_2$ and studied its electronic properties. This study demonstrated that the Mo-defective 2D $MoTe_2$ exhibits a band gap of 0.53 eV. A low electronic band gap facilitates easier electron excitation from the valence band into the conduction band, promoting efficient charge transfer during the reaction. We then carried out a detailed investigation of the reaction pathways involved in the oxygen reduction reaction. To gain deeper insight into the reaction thermodynamics, we computed the relative Gibbs free energy of each reaction intermediate of the ORR process. Our study revealed that the Gibbs free energy (ΔG) changes for all intermediates of the ORR mechanism are negative, which indicates that ORR has an exothermic nature. The computed free energy change indicates that all reaction steps are not only feasible but also proceed spontaneously and are thermodynamically favorable. The calculation using the CHE model shows that the Mo-defective 2D monolayer $MoTe_2$ acts as a highly promising Pt-free electrocatalyst for the ORR in future fuel cell applications. The theoretical and computational results of our study are expected to inspire further experimental, computational, and theoretical

efforts toward the development of advanced two-dimensional Pt-free ORR catalysts. The results discussed in this section correspond to the following article:

S.N. Upadhyay, D. Halba, L. Yadav, S. Pakhira, Illuminating the Role of Mo Defective 2D Monolayer $MoTe_2$ toward Highly Efficient Electrocatalytic O_2 Reduction Reaction, Langmuir 39 (2023) 17700–17712.

DOI: https://doi.org/10.1021/acs.langmuir.3c02166

5. Conclusion

In conclusion, a 2D monolayer $LaNiO_3$ was computationally designed from the bulk 3D $LaNiO_3$. The structural and electronic properties of the 2D monolayer $LaNiO_3$ was investigated. The 2D monolayer $LaNiO_3$ shows a small electron density of states around the Fermi level (E_F), indicating semiconducting character. The ORR mechanism on the 2D monolayer $LaNiO_3$ surface was explored, considering both dissociative and associative pathways. The Gibbs free energies (ΔG) for all ORR intermediates were computed to explore the electrocatalytic activity of 2D monolayer $LaNiO_3$ material. Energy calculations confirm that ORR proceeds via a $4e^-$ transfer mechanism on the 2D monolayer $LaNiO_3$ surface, with all elementary steps being spontaneous and thermodynamically favorable. Our results identify the 2D monolayer $LaNiO_3$ as a promising non-noble metal electrocatalyst for the ORR.

A detailed investigation of the ORR mechanism has been performed on the surface of the CoPt@CNT material. Our study found that the CoPt@CNT system exhibits metallic behavior, primarily due to Co and Pt *d*-orbital contributions to the total DOS. The ORR mechanism involving both dissociative and associative pathways have been explored by analyzing key reaction intermediates. The adsorption energy (ΔE) and Gibbs free energies (ΔG) of various intermediates have been computed to study the electrocatalytic activity of CoPt@CNT towards ORR process. ORR investigations reveal that the O_2 adsorption on CoPt@CNT forms the O_2_CoPt@CNT intermediate with favorable adsorption and Gibbs free energy changes ($\Delta E \approx -0.79$ eV, $\Delta G \approx -0.71$ eV). All other subsequent reaction steps of ORR are spontaneous and thermodynamically favorable without requiring external energy. Our results demonstrate CoPt@CNT as an excellent electrocatalyst for fuel cells. Our findings are

expected to guide the development of advanced electrocatalysts for green energy devices such as fuel cells and metal–air batteries (MABs).

Computationally we designed FeCe@CNT system by encapsulating the FeCe nanoparticle within pristine CNT. Our study found that FeCe@CNT system exhibited metallic conductivity due to strong Fe and Ce *d*-orbital contributions near the Fermi level (E_F). The metallic conductivity of FeCe@CNT is confirmed from the total DOS where there is large electron density around the Fermi level (E_F). ORR mechanism has been explored on the surface of the FeCe@CNT by computing relative adsorption energy of key reaction intermediates. This study demonstrated that the ORR followed $4e^-$ transfer mechanisms on the surface of the FeCe@CNT material. The ORR proceeds mainly via the associative pathway because all the reaction steps are spontaneous and energetically favorable. The FeCe@CNT material is thus a highly promising non-precious metal electrocatalyst with exceptional ORR activity for fuel cells. We hope that our study will help in exploring new non-noble metal-based catalysts for the ORR.

We have computationally designed 2D monolayer $MoTe_2$ and studied its structural and electronic properties. Our results demonstrated that the pristine 2D monolayer $MoTe_2$ is a direct semiconductor with a 1.64 eV electronic band gap. This study found that introduction of Mo vacancies lowers the band gap to 0.53 eV, improving electronic conductivity of Mo defective 2D monolayer $MoTe_2$. Detailed ORR pathway analysis and change in Gibbs free energy (ΔG) calculations for each intermediate give negative ΔG values across all rection steps, indicating that the ORR process is exothermic and thermodynamically spontaneous on the surface of Mo defective $MoTe_2$ material. Our results position Mo defective 2D monolayer $MoTe_2$ as a potential candidate for a Pt-free ORR electrocatalyst for fuel cell applications. We hope this study will aid the exploration of new low cost, efficient electrocatalysts for ORR.

6. References

[1] J. Suntivich, H.A. Gasteiger, N. Yabuuchi, H. Nakanishi, J.B. Goodenough, Y. Shao-Horn, Design principles for oxygen-reduction activity on perovskite oxide catalysts for fuel cells and metal-air batteries, Nat. Chem. 3 (2011) 546–550.

[2] L. Yang, J. Shui, L. Du, Y. Shao, J. Liu, L. Dai, Z. Hu, Carbon-Based Metal-Free ORR Electrocatalysts for Fuel Cells: Past, Present, and Future, Adv. Mater.

31 (2019) 1804799.

[3] A. Kulkarni, S. Siahrostami, A. Patel, J.K. Nørskov, Understanding Catalytic Activity Trends in the Oxygen Reduction Reaction, Chem. Rev. 118 (2018) 2302–2312.

[4] J.K. Nørskov, J. Rossmeisl, A. Logadottir, L. Lindqvist, J.R. Kitchin, T. Bligaard, H. Jónsson, Origin of the Overpotential for Oxygen Reduction at a Fuel-Cell Cathode, J. Phys. Chem. B 108 (2004) 17886–17892.

[5] A.M. Patel, S. Ringe, S. Siahrostami, M. Bajdich, J.K. Nørskov, A.R. Kulkarni, Theoretical Approaches to Describing the Oxygen Reduction Reaction Activity of Single-Atom Catalysts, J. Phys. Chem. C 122 (2018) 29307–29318.

[6] Q. Ji, L. Bi, J. Zhang, H. Cao, X.S. Zhao, The role of oxygen vacancies of ABO_3 perovskite oxides in the oxygen reduction reaction, Energy Environ. Sci. 13 (2020) 1408–1428.

[7] D. Deng, L. Yu, X. Chen, G. Wang, L. Jin, X. Pan, J. Deng, G. Sun, X. Bao, Iron encapsulated within pod-like carbon nanotubes for oxygen reduction reaction., Angew. Chemie 125 (2013) 371–375.

[8] W. Niu, S. Pakhira, K. Marcus, Z. Li, J.L. Mendoza-Cortes, Y. Yang, Apically Dominant Mechanism for Improving Catalytic Activities of N-Doped Carbon Nanotube Arrays in Rechargeable Zinc–Air Battery, Adv. Energy Mater. 8 (2018) 1800480.

[9] K.N. Khattak, Y. Shao, J. Zhou, Recent development and challenges in TMD-based 2D materials towards OER/ORR electrocatalysis, React. Chem. Eng. 11 (2026) 11–41.

[10] G. Kresse, J. Furthmüller, Efficient iterative schemes for ab initio total-energy calculations using a plane-wave basis set, Phys. Rev. B 54 (1996) 11169–11186.

[11] J.P. Perdew, K. Burke, M. Ernzerhof, Generalized gradient approximation made simple, Phys. Rev. Lett. 77 (1996) 3865–3868.

[12] S. Grimme, J. Antony, S. Ehrlich, H. Krieg, A consistent and accurate ab initio parametrization of density functional dispersion correction (DFT-D) for the 94 elements H-Pu, J. Chem. Phys. 132 (2010) 154104.

[13] R. Dovesi, A. Erba, R. Orlando, C.M. Zicovich-Wilson, B. Civalleri, L. Maschio, M. Rérat, S. Casassa, J. Baima, S. Salustro, others, Quantum-mechanical condensed matter simulations with CRYSTAL, WIREs Comput. Mol. Sci. 8 (2018) e1360.

[14] J. Xiao, J. Wang, Z. Xue, T. Zhang, J. Wang, Q. Li, The study of oxygen reduction reaction on Ge-doped MoS_2 monolayer based on first principle, Int. J. Energy Res. 45 (2021) 13748–13759.

[15] M.F. Peintinger, D.V. Oliveira, T. Bredow, Consistent Gaussian basis sets of triple-zeta valence with polarization quality for solid-state calculations., J. Comput. Chem. 34 (2013) 451–459.

[16] A. Erba, J. Baima, I. Bush, R. Orlando, R. Dovesi, Large-scale condensed matter DFT simulations: performance and capabilities of the CRYSTAL code, J. Chem. Theory Comput. 13 (2017) 5019–5027.

[17] K. Momma, F. Izumi, VESTA 3 for three-dimensional visualization of crystal, volumetric and morphology data, J. Appl. Crystallogr. 44 (2011) 1272–1276.

[18] S. Pakhira, K.P. Lucht, J.L. Mendoza-Cortes, Iron intercalation in covalent-organic frameworks: A promising approach for semiconductors, J. Phys. Chem. C 121 (2017) 21160–21170.

LIST OF PUBLICATIONS

Related to Ph.D. Thesis:

1) ***D. Halba***, S. Pakhira*, Unraveling the O_2 Reduction Reaction on 2D Monolayer $LaNiO_3$ Perovskite, *ACS Omega* 9 (2024) 35614–35626.

2) ***D. Halba***, A. Ojha, S. Pakhira*, Cobalt–Platinum Nanoparticle Encapsulated within Carbon Nanotube for Superior O_2 Reduction Reaction, *ACS Appl. Energy Mater.* 8 (2025) 7948–7962.

3) ***D. Halba***, L. Yadav, S. Pakhira*, An investigation of electrocatalytic activity of the FeCe nanoparticle encapsulated carbon nanotube towards oxygen reduction reaction, *RSC Adv.* 16 (2026) 9143–9154.

4) S.N. Upadhyay, ***D. Halba***, L. Yadav, S. Pakhira*, Illuminating the Role of Mo Defective 2D Monolayer $MoTe_2$ toward Highly Efficient Electrocatalytic O_2 Reduction Reaction, *Langmuir* 39 (2023) 17700–17712.

Other than Ph.D. Thesis:

1) D. Pandey, C. Patel, S. Mishra, L. Yadav, ***D. Halba***, S. Pakhira**, S. Mukherjee**, A. Raghuvanshi**, Semiconducting Cu(I) Framework for Room Temperature NO_2 Sensing via Efficient Charge Transfer, *Small* 21 (2025) 2409553.

2) V. Kumar, ***D. Halba***, S.N. Upadhyay, S. Pakhira*, Electrocatalytic Performance of 2D Monolayer WSeTe Janus Transition Metal Dichalcogenide for Highly Efficient H_2 Evolution Reaction, Langmuir 40 (2024) 14872–14887.

* Corresponding Author

TABLE OF CONTENTS

SYNOPSIS ..... **i**

LIST OF PUBLICATIONS ..... **xv**

TABLE OF CONTENTS ..... **xvii**

LIST OF FIGURES ..... **xxi**

LIST OF TABLES ..... **xxv**

LIST OF ABBREVIATIONS ..... **xxvii**

ABSTRACT ..... **xxxi**

Chapter 1: Introduction and Literature Review **1**

1.1 Introduction 1

1.2 Fuel Cells as Sustainable Alternatives 3

1.3 Oxygen Reduction Reaction 4

1.4 The Need for Electrocatalysts 5

1.5 Perovskite 10

1.5.1 Structure of Perovskite 10

1.5.2 Perovskite Oxide and Its Electronic Properties 11

1.5.3 Key Applications of Perovskite Oxides 13

1.6 Carbon Nanotubes 13

1.6.1 Single-Walled Carbon Nanotubes (SWCNTs) 14

1.6.2 Double-Walled Carbon Nanotubes (DWCNTs) 14

1.6.3 Multi-Walled Carbon Nanotubes (MWCNTs) 14

1.6.4 Chirality 15

1.6.5 Electronic Properties of CNTs 16

1.6.6 Key Strengths of CNTs for ORR 16

1.6.7 Applications of CNTs 18

1.7 Transition Metal Dichalcogenides (TMDs) 19

1.7.1 Structure of TMDs 19

1.7.2 Advantages of TMDs for ORR 21

1.7.3 Applications of TMDs 22

1.8 Thesis Objectives 23
1.9 References 23
Chapter 2: Theory, Methodology and Computational Details 33
2.1 Schrödinger Equation 35
2.2 The Many-Body System 36
2.3 Born-Oppenheimer Approximation 36
2.4 The Hartree-Fock (HF) Approximation 37
2.5 Density Functional Theory (DFT) 39
2.5.1 The Hohenberg-Kohn theorems 39
2.5.2 The Kohn-Sham equations 41
2.5.3 Exchange-Correlation approximations 42
2.6 Softwares 49
2.6.1 CRYSTAL 17 49
2.6.2 Vienna *Ab initio* Simulation Package (VASP) 52
2.7 Basis Set 54
2.7.1 Slater-type orbitals (STO) 55
2.7.2 Gaussian-type orbitals (GTO) 56
2.7.3 Properties of basis functions 57
2.7.4 Classification of basis set 57
2.8 Instruments and Software Tools 59
2.9 References 60
Chapter 3: Unraveling the O_2 Reduction Reaction on 2D Monolayer $LaNiO_3$ Perovskite 63
3.1 Introduction 63
3.2 Methods and Computational Details 66
3.3 Theoretical Calculations and Equations 67
3.4 Results and Discussions 68
3.5 ORR Mechanisms 70
3.6 Summary 84
3.7 References 85
Chapter 4: Cobalt-Platinum Nanoparticle Encapsulated within Carbon Nanotube for Superior O_2 Reduction Reaction 93
4.1 Introduction 93
4.2 Computational Details 96

4.3 Theory 97
4.4 Results and Discussions 98
4.5 Dissociative Reaction Mechanism 103
4.6 Associative Reaction Mechanism 113
4.7 Summary 118
4.8 References 119
Chapter 5: An Investigation of Electrocatalytic Activity of the FeCe Nanoparticle Encapsulated Carbon Nanotube towards Oxygen Reduction Reaction 127
5.1 Introduction 128
5.2 Computational Details 130
5.3 Theoretical Calculation and Equation 131
5.4 Results and Discussions 131
5.5 Spin Density Calculation 142
5.6 Summary 143
5.7 References 144
Chapter 6: Illuminating the role of Mo Defective 2D Monolayer $MoTe_2$ toward Highly Efficient Electrocatalytic O_2 Reduction Reaction 151
6.1 Introduction 151
6.2 Methods and Computational Details 154
6.3 Material Preparation 155
6.4 Theoretical Calculations and Equations 156
6.5 Results and Discussion 157
6.6 Spin Density Calculations 171
6.7 Summary 173
6.8 References 174
Chapter 7: Conclusions and Future Perspectives 181
7.1 Major Conclusion 181
7.2 Future Perspective 183

LIST OF FIGURES

Figure 1.1: Schematic representation of a fuel cell and its components. 4

Figure 1.2: Schematic presentation of the $4e^-$ transfer mechanism for the ORR on a catalyst surface in fuel cell applications. 5

Figure 1.3: Three-dimensional crystal structure of a perovskite material. 11

Figure 1.4: Structure of (a) Graphene, (b) top and side view of SWCNT, and (c) top view of MWCNT. 15

Figure 1.5: Applications of carbon nanotubes (CNTs). 18

Figure 1.6: Schematic illustration of different phases in 2D layered transition metal dichalcogenides (TMDs): (a) 2H phase, (b) 1T phase, and (c) 1T' phase. 21

Figure 3.1: (a) Equilibrium geometry of the 3D bulk structure of $LaNiO_3$ and (b) top and side view of the equilibrium structure of 2D monolayer $LaNiO_3$. 66

Figure 3.2: (a) Equilibrium crystal structure, (b) electronic band structure, and (c) total DOS of the 3D $LaNiO_3$ perovskite. 69

Figure 3.3: (a) Top and side view, (b) electronic band structure, and (c) total DOS of the equilibrium 2D monolayer $LaNiO_3$ 69

Figure 3.4: Schematic representation of (a) dissociative and (b) associative reaction pathways of the ORR on the surface of the 2D monolayer $LaNiO_3$ with the $4e^-$ transfer mechanism. 71

Figure 3.5: Charge difference density of O_2 adsorbed on the Ni atom of the 2D monolayer $LaNiO_3$ perovskite, i.e., the O_2_$LaNiO_3$ reaction intermediate. The yellow region denotes charge depletion, and the cyan color denotes charge accumulation. 72

Figure 3.6: Equilibrium structures of all the reaction intermediates involved in the dissociative pathway of the ORR on the surface of the 2D monolayer $LaNiO_3$ perovskite. 73

Figure 3.7: Relative free energy profiles for the dissociative mechanism of the ORR on the surface of the 2D monolayer $LaNiO_3$ perovskite. 74

Figure 3.8: O_2 dissociation on the surface of 2D monolayer $LaNiO_3$ with a transition state (TS). 75

Figure 3.9: Electronic band structure and total DOS of (a) O_2_$LaNiO_3$, (b) 2O_$LaNiO_3$, (c) O_OH_$LaNiO_3$, (d) O_$LaNiO_3$, and (e) OH_$LaNiO_3$ reaction intermediates of the dissociative pathway, and (f) OOH_$LaNiO_3$ reaction intermediate of the associative ORR mechanism on the surface of the 2D monolayer $LaNiO_3$ perovskite. 78

Figure 3.10: Equilibrium structures of all the reaction intermediates involved in the associative reaction pathway of the ORR on the surface of the 2D monolayer $LaNiO_3$ perovskite. 81
Figure 3.11: Relative free energy profiles for the associative mechanism of the ORR on the surface of 2D monolayer $LaNiO_3$. 83
Figure 4.1: Top and side views of the equilibrium structure of (a) CNT and (b) CoPt@CNT system. 99
Figure 4.2: (a) Electronic band structure and total DOS of the equilibrium structure of pure CNT, (b) electronic band structure and total DOS of the CoPt@CNT, and (c) PDOS plot depicting the contribution of the d-orbital electron density of the Co and Pt atoms in the CoPt@CNT. 99
Figure 4.3: (a) Electron spin density plot of CoPt@CNT and (b) representation of possible adsorption sites on the surface of CNT. The sky-blue and yellow color shapes represent the positive (α-spin up) and negative (β-spin down) values. 105
Figure 4.4: Schematics of $4e^-$ transfer mechanism of ORR on the surface of the CoPt@CNT system. (The material enclosed within the dotted rectangle represents the CoPt@CNT where the ORR process occurs). 107
Figure 4.5: Top view and side view, electronic band structure, and total DOS of the equilibrium structure of (a) O_2_CoPt@CNT and (b) 2O_CoPt@CNT reaction intermediates. 107
Figure 4.6: Top view and side view, band structure, and total DOS of the equilibrium structure of (a) O_OH_CoPt@CNT, (b) O_CoPt@CNT, and (c) OH_CoPt@CNT. 109
Figure 4.7: Change in adsorption energy profile for various reaction intermediates involved during the dissociative mechanism of the ORR on the surface of the CoPt@CNT. 110
Figure 4.8: Gibbs free energy profile for the dissociative pathway of the ORR on the surface of the CoPt@CNT. 111
Figure 4.9: (a) Top and side views, (b) electronic band structures, and (c) total DOS of equilibrium OOH_CoPt@CNT reaction intermediate computed by the DFT-D3 method 113
Figure 4.10: Change in adsorption energy profiles for the reaction intermediates of the associative pathway of the ORR on the surface of the CoPt@CNT material 116
Figure 4.11: Gibbs free energy profile for the associative pathway of the ORR on the surface of the CoPt@CNT. 116

Figure 5.1: (a) Top and side views of the equilibrium structure of the FeCe@CNT, (b) electronic band structure and the total DOS of the FeCe@CNT material, and (C) PDOS depicting the contribution from the d subshell electron density of Fe and Ce atoms. 133
Figure 5.2: Schematic of the associative four-electron transfer pathway on the FeCe@CNT surface. 134
Figure 5.3: (a) Top and side views of the equilibrium structure of O_2_FeCe@CNT, and (b) the electronic band structure and the total DOS of the O_2_ FeCe@CNT reaction intermediate..... 136
Figure 5.4: (a) Equilibrium structure (top and side views) of OOH_FeCe@CNT, and (b) the electronic band structure and the total DOS of the OOH_FeCe@CNT reaction intermediate..... 138
Figure 5.5: (a) Top view and side view of the equilibrium structure of O_FeCe@CNT, and (b) the band structure and the total DOS of the O_FeCe@CNT intermediate.... 139
Figure 5.6: (a) Equilibrium structure depicting the top and side views of OH_FeCe@CNT, and (b) the electronic band structure and total DOS of the OH_FeCe@CNT intermediate. 140
Figure 5.7: Adsorption energy profile of various reaction intermediates of the associative mechanism of ORR on the surface of the FeCe@CNT material. 141
Figure 5.8: Spin density plot of all the reaction intermediates of the ORR mechanism: (a) pure FeCe@CNT, (b) O_2_FeCe@CNT, (c) OOH_FeCe@CNT, (d) O_FeCe@CNT and (e) OH_FeCe@CNT. The sky-blue color represents positive α spin-up electron density, and the yellow color represents negative β spin-down electron density..... 143
Figure 6.1: Representation of top view of 3 × 3 × 1 pure 2D single layer slab of the $MoTe_2$ (left side) and Mo-defective 2D monolayer slab of $MoTe_2$ (right side). The red dotted lines show the 3 × 3 supercell of both structures. 156
Figure 6.2: Graphical representation of top view and side view, (b) energy band structures, and (c) total DOS of the pristine 2D monolayer $MoTe_2$ TMD material. . 158
Figure 6.3: (a) Graphical representation of top view and side view, (b) energy band structure, and (c) total DOS of the Mo-defective 2D monolayer $MoTe_2$ TMD. 159
Figure 6.4: (a) Graphical representation of top view and side view, (b) energy band structures, and (c) total DOS of the O_2 adsorbed 2D monolayer Mo-defective $MoTe_2$ TMD material..... 163

Figure 6.5: (a) Graphical representation of equilibrium geometry, (b) energy band structures, and (c) total DOS of the 2O* adsorbed Mo-defective 2D monolayer $MoTe_2$ material. 165
Figure 6.6: (a) Graphical representation of equilibrium geometry, (b) electronic band structures, and (c) total DOS of the OH*_O* adsorbed Mo-defective 2D monolayer $MoTe_2$ material. 166
Figure 6.7: (a) Graphical representation of equilibrium geometry of top view and side view, (b) energy band structure, and (c) total DOS of the O* adsorbed Mo-defective 2D monolayer $MoTe_2$ material. 167
Figure 6.8: (a) Equilibrium geometry of top view and side view, (b) energy band structure, and (c) total DOS of OH* adsorbed Mo-defective 2D monolayer $MoTe_2$ material. 168
Figure 6.9: Calculated profiles of relative free energy for the $4e^-$ transfer mechanism of the ORR on the surface of Mo-defective 2D monolayer $MoTe_2$ material..... 169
Figure 6.10: Spin density calculations of (a) Mo-defective 2D monolayer of $MoTe_2$, (b) O_2* adsorbed on the Mo-defective 2D monolayer $MoTe_2$ material, (c) 2O* adsorbed Mo-defective 2D monolayer $MoTe_2$ material, (d) OH*_O* adsorbed Mo- defective 2D monolayer $MoTe_2$ material, (e) O* adsorbed Mo-defective 2D monolayer $MoTe_2$ material and (f) OH* adsorbed Mo-defective 2D monolayer $MoTe_2$ material……..…….173

LIST OF TABLES

Table 2.1: Comparison of the computational methods, software codes, exchange-correlation functionals, dispersion corrections, and basis sets used in the four studies. 60

Table 3.1: Equilibrium lattice parameters of 3D $LaNiO_3$ and 2D monolayer $LaNiO_3$. 70

Table 3.2: Equilibrium lattice parameters and space group symmetry of all the reaction intermediates of the dissociative mechanism in the ORR process. 76

Table 3.3: All the reaction intermediates of dissociative pathways of the ORR along with the change in their free energy (ΔG) occurring on the surface of the 2D monolayer $LaNiO_3$ perovskite. 77

Table 3.4: All the reaction intermediates in the associative mechanism of the ORR along with their Gibbs free energy (ΔG) and relative free energy..... 82

Table 4.1: Lattice constant and average bond distances of pristine CNT and CoPt@CNT. 103

Table 4.2: Lattice constant c and average bond distance of different reaction intermediates of the dissociative pathway. 112

Table 4.3: Change in adsorption energy (ΔE) and change in Gibbs free energy (ΔG) of various reaction intermediates of the dissociative mechanism of the ORR..... 112

Table 4.4: Values of change in adsorption energy (ΔE) and change in Gibbs free energy (ΔG) of various reaction intermediates involved in the associative pathway of the ORR on the surface of the CoPt@CNT material. 115

Table 5.1: The equilibrium lattice parameter and symmetry of all the reaction intermediates involved in the associative mechanism of ORR..... 136

Table 5.2: Relative adsorption energy of various intermediates during the associative pathway of ORR on the surface of the FeCe@CNT material..... 139

Table 6.1: Equilibrium lattice constants, average bond length, electronic band gaps, interfacial angles, and space group symmetry of 2D monolayer $MoTe_2$ and defective 2D monolayer $MoTe_2$. 160

Table 6.2: Equilibrium structural constraints, lattice parameters, and electronic band gap (E_g) of the different reaction intermediates of ORR occurring on the surface of Mo-Defective $MoTe_2$ TMD material. 164

Table 6.3: Free energy change (ΔG in eV) and the relative free energy (expressed in eV) for all the intermediates during the ORR carried out on the surface of Mo-Defective $MoTe_2$ TMD material are listed here. 169

LIST OF ABBREVIATIONS

ORR	:	Oxygen reduction reaction
TMDs	:	Transition metal dichalcogenides
CNT	:	Carbon nanotube
IEA	:	International energy agency
CO	:	Carbon monoxide
CO_2	:	Carbon dioxide
MABs	:	Metal-air batteries
PEM	:	Proton exchange membrane
O_2	:	Oxygen molecule
PEMFCs	:	Proton exchange membrane fuel cells
SOFCs	:	Solid oxide fuel cells
AFCs	:	Alkaline fuel cells
H_2O_2	:	Hydrogen peroxide
Pt	:	Platinum
OER	:	Oxygen evolution reaction
MWCNTs	:	Multi-walled carbon nanotubes
NCNTs	:	Nitrogen-doped carbon nanotubes
H_2O	:	Water molecules
DFT	:	Density functional theory
Co@NCNTs	:	Cobalt nanoparticle encapsulated in nitrogen-doped carbon nanotubes
Fe_4@SWCNT	:	Fe nanoparticles encapsulated in pea-pod-like CNTs
VA-NCNT	:	Vertically aligned nitrogen-doped carbon nanotube

NPs : Nanoparticles

Ni@NCNT : Nickel nanoparticles encapsulated in nitrogen-doped carbon nanotube

2D TMDS : Two-dimensional transition metal dichalcogenides

HER : Hydrogen evolution reaction

MoS_2 : Molybdenum disulfide

TDOS : Total density of states

$CaTiO_3$: Calcium titanate

t : Goldschmidt tolerance factor

E_g : Electronic band gap

E_F : Fermi energy level

CVD : Chemical vapor deposition

SWCNTs : Single-walled carbon nanotubes

DWCNTs : Double-walled carbon nanotubes

MWCNTs : Multi-walled carbon nanotubes

$\vec{C}_h$: Chiral vector

h-BN : Hexagonal boron nitride

vdW : Van der Waals

CoPt@CNT : Cobalt-platinum nanoparticle encapsulated carbon nanotube

FeCe@CNT : FeCe nanoparticle encapsulated carbon nanotube

QM : Quantum mechanics

MM : Molecular mechanics

DFT : Density functional theory

SE : Schrödinger equation

GS : Ground-state

PES	:	Potential energy surface
BO	:	Born-Oppenheimer
SCF	:	Self-consistent field
HF	:	Hartree–Fock
ML	:	Machine-learning
KS	:	Kohn–Sham
XC	:	Exchange-correlation
LDA	:	Local density approximation
LSDA	:	Local spin-density approximation
vdW	:	van der Waals
GGA	:	Generalized gradient approximation
PBE	:	Perdew–Burke–Ernzerhof
B3LYP	:	Becke, 3-parameter, Lee–Yang–Parr
DFT-D	:	Dispersion-corrected density functional theory
ATM	:	Axilrod-Teller-Muto
GTOs	:	Gaussian-type orbitals
BSE	:	Bethe-Salpeter equation
VASP	:	Vienna Ab initio simulation package
PAW	:	Projector augmented wave
MBD	:	Many-body dispersion
SOC	:	Spin-orbit coupling
AOs	:	Atomic orbitals
LCAO	:	Linear combination of atomic orbitals
CBS	:	Complete basis set

STO	:	Slater-type orbital
SVP	:	Split-valence polarized
TZVP	:	Triple-Zeta valence with polarization
ECP	:	Effective core potential
HPC	:	High performance computing
ΔE	:	Change in adsorption energy
ΔG	:	Change in Gibbs free energy
$4e^-$	:	Four electrons
$CoPt_3$@NC	:	$CoPt_3$ encapsulated N-doped carbon nanospheres
HORC	:	Harmonic Oscillator Rigid Rotator Models
E_{ads}	:	Adsorption energy
CHE	:	Computational hydrogen electrode
Å	:	Angstrom
PDOS	:	Partial density of states
Fe_4@SWCNT	:	Iron encapsulated within CNTs
H^+	:	Protons
NiCo@NCNT	:	NiCo metal cluster encapsulated by the N-doped CNTs
H_2O_2	:	Hydrogen peroxide
PDS	:	Potential determination step
Ce	:	Cerium
Fe	:	Iron
SHE	:	Standard hydrogen electrode

ABSTRACT

The first chapter of this thesis thoroughly surveys major topics in electrocatalysis, placing particular emphasis on the ORR mechanisms on novel materials including perovskite oxides, CNTs, and 2D TMDs. The present work analyzes the structural and electronic properties of perovskite oxides, CNTs, and 2D TMDs and assesses their activity as ORR electrocatalysts.

The second chapter of this thesis describes the methodology used in this study. It presents an overview of computational science and theoretical methods and discusses how computational materials science interface with chemistry.

The third chapter of this thesis encompasses the design of a 2D monolayer $LaNiO_3$. First, we investigated its electronic properties, focusing specifically on the energy band structure and total density of states (DOS). We then evaluated the electrocatalytic performance of 2D monolayer $LaNiO_3$ for the oxygen reduction reaction (ORR) by mapping its complete reaction pathways and mechanisms. To quantify these processes, DFT simulations were employed to calculate the relative Gibbs free energy (ΔG) of each reaction intermediates.

The fourth chapter of this thesis includes the computational designing of CoPt nanoparticle encapsulated in carbon nanotube (CoPt@CNT). The structural and electronic properties of the CoPt@CNT was explored employing DFT-D3 method to study its catalytic activity towards ORR. The ORR mechanism both associative and dissociative pathways have been explored on the surface of the CoPt@CNT by computing the relative adsorption energy (ΔE) and Gibbs free energy (ΔG) of key reaction intermediates.

In the fifth chapter of this thesis, we have computationally designed the FeCe nanoparticle encapsulated carbon nanotube (FeCe@CNT). The electronic structural properties, electronic band gap, total density of states (DOS) were investigated using DFT-D3 method. The whole ORR mechanism was explored on the FeCe@CNT surface by computing relative adsorption energy.

In the sixth chapter of this thesis, a Mo defective 2D monolayer $MoTe_2$ was studied. We investigated the electronic structural properties and electronic band

structure. The ORR mechanism was explored on Mo defective 2D monolayer $MoTe_2$ surface.

The seventh chapter summarizes the primary findings of this thesis, highlighting the conclusions drawn from our research on novel materials. Furthermore, it outlines potential future directions and proposes new conceptual frameworks for perovskite oxides, CNTs, and 2D TMDs.

Chapter 1

Introduction and Literature Review

The escalating global energy demand, driven by population growth and industrialization, has amplified fossil fuel reliance, worsening environmental degradation, and climate change. This chapter analyzes trends of energy consumption and the urgent need for sustainable alternatives like fuel cells, which efficiently convert chemical energy to electricity while producing minimal greenhouse gas emissions. It provides detailed insights into fuel cell technology and the O_2 reduction reaction (ORR), which sluggish kinetics demands the efficient electrocatalysts to overcome kinetic barriers. This chapter includes a comprehensive literature review of ongoing research on various electrocatalytic materials, such as perovskite oxides, two-dimensional transition metal dichalcogenides (2D TMDs), and carbon nanotube (CNT)-based materials for ORR applications. These key materials are reviewed in detail, including their structural and electronic properties along with their applications in the ORR catalysis. This chapter also reports the key advantages of perovskite oxides, CNTs, and TMDs as electrocatalysts for the ORR electrocatalysis in fuel cells. This chapter concludes with the thesis objectives, which establish the foundation for advanced electrocatalytic materials in subsequent ORR studies.

1.1 Introduction

Over the past few centuries, access to energy has fundamentally reshaped human civilization. Energy production and consumption have a significant role in influencing the global economy. Energy transformed societies from pre-industrial biomass reliance to modern abundance, enabling population growth and economic development since 1800. Global primary energy production has grown exponentially, stabilizing at 1-2% yearly in recent decades despite efficiency improvements, with coal and oil historically dominating (~50% combined today) while renewables like wind and solar have surged from negligible shares to 3-5%. Electricity makes up just ~20% of total primary energy, while fossil fuels dominate the rest for heat and transport.[1] The growing global

population and rapid industrialization have significantly increased the demands for global energy. The global energy demand will double by 2050, as projected by the International Energy Agency (IEA). Currently, fossil fuels supply ~82% of global energy demand, with the remainder met by renewables, nuclear, and other low-carbon sources, based on recent energy institute data.[2] In 2024, global energy demand surged by 2.2%, surpassing the decade's average. It was driven by energy needed for factories, electric cars, data centers, AI, and more. Renewable resources, mainly renewable energy sources (e.g., sunlight, wind, and water) are naturally replenished materials harnessed for sustainable power generation. They offer cleaner alternatives to fossil fuels but face challenges in scalability and reliability.[3,4] Solar and wind energy have covered almost the entire increase in electricity demand, with solar capacity hitting unprecedented growth.[5] Solar and wind energy production depend on environmental, geographical, and technological factors. These factors directly influence output variability and efficiency of solar and wind power. Both the solar and wind power have been suffering from weather-related intermittency. Solar output drops at night or during rain, while wind falters in calm conditions. This necessitates backup energy systems for smooth operation as per the requirements. Climate change could exacerbate this through shifting weather patterns.[6]

Currently, most of the energy is derived from conventional fossil fuels such as coal, oil, petroleum and natural gas, which are finite resources and major contributors to environmental pollution and greenhouse gas emissions. Greenhouse gases such as carbon monoxide (CO), methane (CH_4) and carbon dioxide (CO_2) are produced while extracting energy from fossil fuels. Greenhouse gases emitted during the exploitation of fossil fuels are harmful to the environment and contribute to global warming. It is necessary to use sustainable energy sources that can fulfil global energy demand without contributing to greenhouse gas emissions. Therefore, researchers are highly focused and motivated to gain deeper insight into clean and green energy-conversion devices such as fuel cells, metal-air batteries (MABs).[7] In this regard, fuel cells have gained wide attention owing to their high energy density, high efficiency, and low carbon emissions during operating conditions.

1.2 Fuel Cells as Sustainable Alternatives

Fuel cells emerge as one of the most promising clean energy technologies because they combine high efficiency, low environmental impact, and versatile applications. The fuel cell, an advanced electrochemical device, directly converts the chemical energy of fuels into electrical energy through electrochemical reactions. In fuel cells, hydrogen serves as fuel and oxygen as the oxidant, producing electrical energy without the combustion of hydrogen. It consists of three main components: an anode, a cathode, and electrolytes that enable ion transport between them. At the anode, hydrogen oxidation produces protons (H^+) and electrons (e^-). The protons migrate through the proton exchange membrane (PEM) to the cathode, while electrons travel via the external circuit to generate electricity. At the cathode, oxygen (O_2) molecules get reduced to water via the combination of protons, electrons, and oxygen atoms. The overall process inside the fuel cell is very clean and efficient, producing high energy without emitting greenhouse gases.[8] There are various types of fuel cells such as proton exchange membrane fuel cells (PEMFCs), solid oxide fuel cells (SOFCs), alkaline fuel cells (AFCs) etc. Fuel cells are classified primarily by the electrolyte used and their operating conditions. They have a wide range of applications due to their high-power density, good efficiency and low greenhouse emissions. Among all the fuel cells, PEMFCs are widely recognized and researched as they operate at low temperatures. In PEMFCs, a solid polymer electrolyte membrane conducts protons (H^+) from the anode to the cathode and restricts the flow of electrons (e^-) through it.[9] The fuel cell operates via two key half-cell reactions depicted in equations (1.1) and (1.2). At the anode, hydrogen molecules undergo oxidation to protons and electrons. Whereas at the cathode, O_2 molecules are reduced via the ORR process.

$$2H_2 \rightarrow 4H^+ + 4e^- \tag{1.1}$$

$$O_2 + 4H^+ + 4e^- \rightarrow 2H_2O \tag{1.2}$$

The above two half-cell reactions are important and determine the performance of the fuel cells. Typically, anode reactions are fast, whereas the O_2 reduction at the cathode is sluggish. The schematic representation of a fuel cell is depicted in Figure 1.1.

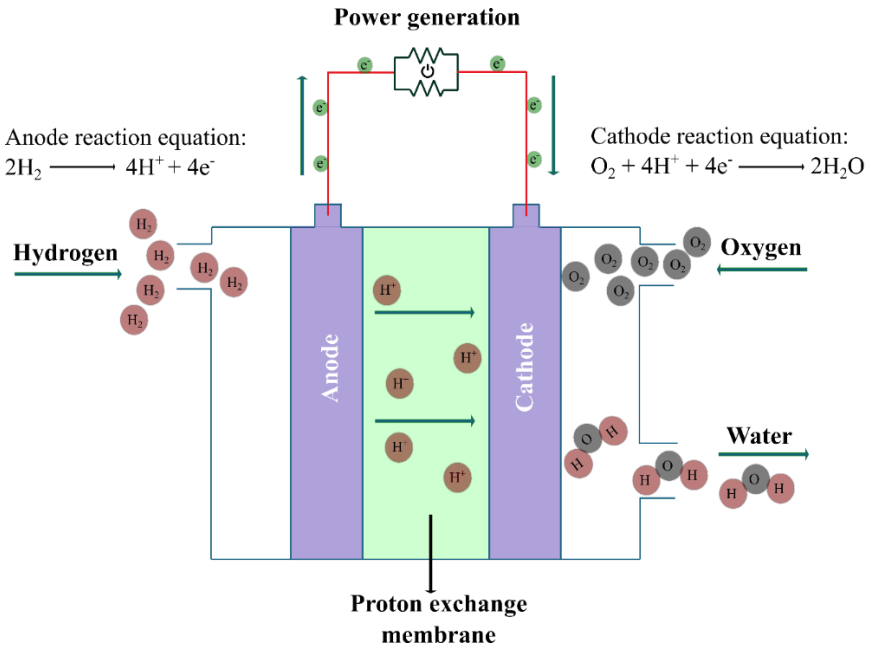


Figure 1.1: *Schematic representation of a fuel cell and its components.*

1.3 Oxygen Reduction Reaction

The O_2 reduction reaction (ORR) serves as a key cathodic half-cell reaction essential to fuel cell operation. In acidic conditions, the ORR can proceed through two reaction pathways, either a direct four-electron ($4e^-$) pathway or an indirect two-electron ($2e^-$) pathway.[8] However, the ORR reaction in alkaline conditions differs from acidic conditions, as it proceeds through multiple reaction steps. The $4e^-$ pathway of ORR involves the reduction of the oxygen (O_2) molecule to water (H_2O) via the combination of four electrons ($4e^-$) and four protons ($4H^+$). Generally, the $4e^-$ transfer mechanism is recognized as the most favorable pathway for the ORR mechanism because it provides high energy efficiency, and the products formed from this pathway are environmentally friendly. Whereas, the $2e^-$ pathway involves the formation of hydrogen peroxide (H_2O_2), which reduces the overall efficiency of fuel cells.[10] The $4e^-$ transfer mechanism of ORR can occur either via a dissociative or an associative pathway, as illustrated in Figure 1.2. The $4e^-$ and $2e^-$ routes are typically represented by the following equations (1.3) and (1.4).

$$O_2 + 4H^+ + 4e^- \rightarrow 2H_2O \qquad E^\circ_{cell} = 1.23\ V \tag{1.3}$$

$$O_2 + 2H^+ + 2e^- \rightarrow H_2O_2 \qquad E^\circ_{cell} = 0.695\ V \tag{1.4}$$

The associative and dissociative pathways of the ORR mechanism are depicted in equations (1.5) and (1.6) below. Here, * represents the favorable active sites of catalysts where the O_2 molecule adsorbs during the initial step of the ORR. Note that protons (H^+) and electrons (e^-) are omitted here for clarity.

$$O_2 \rightarrow O_2^* \rightarrow OOH^* \rightarrow O^* + H_2O\ (or\ H_2O_2) \rightarrow OH^* + H_2O \rightarrow 2H_2O \qquad (1.5)$$

$$O_2 \rightarrow O_2^* \rightarrow 2O^* \rightarrow O^* + OH^* \rightarrow O^* + H_2O\ (or\ H_2O_2) \rightarrow\ OH^* + H_2O \rightarrow 2H_2O \quad (1.6)$$

In fuel cells, the anodic reaction involves a single electron transfer, but the ORR is inherently sluggish, as it proceeds through a cascade of multi-step reactions. The high overpotential and sensitivity to catalyst poisoning require an efficient electrocatalyst to accelerate the ORR kinetics.[11] To tackle these challenges, researchers have proposed diverse strategies in theoretical studies, materials synthesis, and system design.

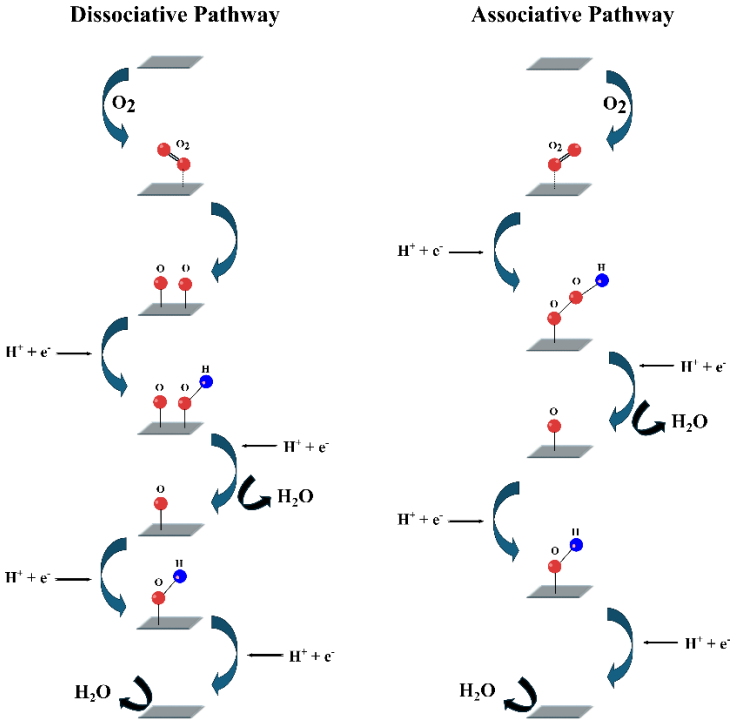


Figure 1.2: *Schematic presentation of the 4e⁻ transfer mechanism for the ORR on a catalyst surface in fuel cell applications.*

1.4 The Need for Electrocatalysts

In fuel cells, efficient electrocatalysts are crucial to overcome the kinetic limitations of the multi-step, sluggish ORR at the cathode. Platinum (Pt) and Pt-based electrocatalysts are widely regarded as highly efficient electrocatalysts for the ORR in fuel cells due to their low overpotential and superior catalytic activity. However, the high cost and

limited availability of Pt and Pt-based materials hinder their widespread commercialization for large-scale applications in fuel cells.[12–16] Replacing scarce precious metals with plentiful, affordable alternatives that deliver equal or better ORR activity resolves the economic challenges of ORR catalysis. Researchers are striving to replace Pt-based electrocatalysts with low-cost, non-noble, and reliable electrocatalysts for fuel-cell applications. Researchers have investigated and developed new electrocatalysts to replace Pt completely or to reduce Pt content, which can still deliver comparable activity towards ORR.[17–21] Researchers have found that the kinetics of ORR can be improved by alloying Pt with transition metals (e.g., Ni, Co, and Mn).[22] So, developing novel, high-performance, low-cost, stable, and efficient electrocatalysts is essential to meet the world's escalating energy demands through advanced fuel cell technologies. To address these needs, researchers have pursued diverse strategies including doping-engineered perovskites, single-atom catalysts on 2D supports, defect engineering, and hybrid nanostructures.[23,24] Despite significant progress, critical gaps remain in understanding the structure-activity relationships, long-term stability under operational conditions, and scalable synthesis of these materials. The following literature review examines key developments in perovskite oxides, carbon nanotubes, and 2D TMDs materials for ORR electrocatalysis, highlighting the foundation for this thesis.

In this regard, perovskite oxides have gained significant interest due to their unique electronic, catalytic, and eco-friendly properties, enabling application towards electrocatalytic fuel cells. Various studies have reported that the perovskite oxides (ABO_3: where A and B are metal ions), with their diverse A-site and B-site cations, exhibit a wide range of catalytic activities.[25–28] Recent studies on perovskite-based halide and oxide materials reveal that the perovskite oxides provide a superior alternative for ORR catalysis.[29–31] Researchers have explored that the La and Sr-based perovskite oxides represent highly promising, low-cost bifunctional catalysts for ORR and oxygen evolution reaction (OER).[32] Perovskite oxides exhibit superior intrinsic catalytic activity, excellent structural and chemical stability, and high compositional flexibility. Perovskite oxides, owing to their superior intrinsic catalytic activity, excellent structural and chemical stability, emerge as promising materials for ORR/OER in fuel cell applications.[33,34] Yang Shao-Horn and coworkers studied ORR performance in various perovskites. They discovered that the ORR activity links

to the occupancy of the σ*-orbital and the degree of covalent bonding between the B-site metal and oxygen atoms.[35] They established that the ORR activity of perovskite follows a volcano curve peaking at $e_g \approx 1$-1.2 electrons in the B-site σ antibonding orbitals, optimizing O_2 adsorption energetics via the Sabatier principle. Lower value of e_g over-binds the adsorbed O_2 leading to slow desorption, whereas the higher value of e_g under-binds the O_2 leading to slow adsorption during the ORR process.[35] Researchers have found that perovskite oxides with tailored oxygen vacancies offer high potential as noble-metal-free ORR electrocatalysts due to enhanced conductivity, charge transfer, and regulated oxygen adsorption via A-site substitutions.[36] Experimentally, it has been found that the $La_{0.8}Sr_{0.2}MnO_3$ (LSM) perovskite synthesized via urea-assisted co-precipitation with high surface area serves as an efficient bifunctional ORR/OER catalyst in 0.1 M KOH medium.[37] Similarly, in another study, the $La_{0.6}Ca_{0.4}CoO_3$ perovskite oxide have demonstrated promising performances as a bifunctional electrocatalyst for rechargeable Zinc-air battery in alkaline medium.[38] Among diverse metal oxide bi-functional electrocatalysts, $La_xCa_{1-X}MO_3$ (M = Co, Ni, Mn) perovskites have garnered sustained interest as promising bifunctional catalysts for metal-air batteries and fuel cells.[39–41] Experimentalists found that the thermal shock-engineered $LaNiO_3$ perovskites achieve superior ORR performance via synergistic defects while preserving bulk structure for scalable energy applications.[42]

Carbon nanotubes (CNTs) have gained considerable attention in recent years as promising candidates for ORR electrocatalysis, owing to their exceptional electronic conductivity, high surface area, and tunable chemical functionality. Multi-walled carbon nanotubes (MWCNTs) have emerged as promising candidates for ORR electrocatalysts in both acidic and alkaline media, driven by their high surface area and abundance of potential active sites.[43–46] Nowadays, nitrogen-doped carbon nanotubes (NCNTs) have attracted great interest as one of the best metal-free catalysts for the ORR.[47–52] Chen et al. experimentally synthesized NCNTs by varying pyridine/ethanol or nitrogen precursor ratios, and they revealed that higher nitrogen content directly boosts the ORR activity in alkaline media. The higher nitrogen concentrations substantially amplify limiting current density and H_2O selectivity, enhancing CNT-based ORR performance.[53] Density functional theory (DFT) calculations demonstrate that the Co@N_4-doped carbon nanotubes (Co@N_4CNTs)

serve as potential bifunctional catalysts for ORR and OER in metal-air batteries (MABs).[54] Deng et al. synthesized Fe nanoparticles encapsulated in pea-pod-like CNTs (Fe_4@SWCNT) via the one-step method and found that it delivered high ORR activity. Their DFT study revealed that the electron transfer from Fe to CNT lowers the carbon's local work function for O_2 activation during the ORR process.[55] Xiong et al. investigated vertically aligned nitrogen-doped carbon nanotube (VA-NCNT) arrays in polymer electrolyte membrane (PEM) fuel cell-like conditions, demonstrating exceptional ORR performance.[56] Researchers have found that encapsulating nanoparticles (NPs) like Fe, Co, or Ni in carbon nanotubes (CNTs) significantly boosts ORR performance due to greater stability, electronic tuning, synergistic effect, and mass transport. Wang et al. studied that the Co nanoparticles encapsulated at the tip of bamboo-like N-doped carbon nanotubes (NCNTs) grafted on N-doped polypyrrole-derived CNTs shown exceptional ORR activity. They confirmed that the ORR performance of NPCN@Co-NCNT arises from Co nanoparticles shielded by pyridinic-N-doped carbon, which minimizes the theoretical ORR overpotential.[57] Zhong et al. experimentally demonstrated that the Ni nanoparticles encapsulated in N-doped CNTs (Ni@NCNTS) synthesized via the pyrolysis method have exhibited excellent bifunctional ORR/OER activity and stability in alkaline media.[58] Wang and coworkers found that the Co@NCNT and Ni@NCNT catalysts, synthesized via one-step calcination with nanosized Co/Ni particles encapsulated in N-doped CNTs have exhibited excellent $4e^-$ ORR performance in alkaline media and better stability than commercial Pt/C.[59] Recently, Niu et al. identified an apically dominant mechanism that substantially boosts the ORR/OER electrocatalytic performance of NCNTs. Their approach involved targeted encapsulation of cobalt-nickel (CoNi) nanoparticles within the apical regions of NCNTs grown on Ni foam (CoNi@NCNT/NF).[60] The encapsulation of nanoparticles within CNTs has opened promising new avenues for discovering highly efficient ORR electrocatalysts.

Over the past decades, two-dimensional (2D) materials have emerged as transformative platforms in electrocatalysis, offering atomic-scale thickness and maximal active site exposure. Among the various 2D materials, two-dimensional transition metal dichalcogenides (2D TMDs) have emerged as a promising class of layered materials beyond graphene, offering tunable electronic properties and high surface-to-volume ratios that make them attractive for electrocatalytic applications.

Various 2D TMDs have been synthesized and investigated both experimentally and theoretically as electrocatalysts for key reactions like the hydrogen evolution reaction (HER) and ORR, owing to their exceptional electronic properties. The efficient electrocatalytic performance of 2D TMDs arises due to their atomic thickness, which exposes high active sites on basal planes and edges.[61,62] Molybdenum disulfide (MoS_2) stands out as an excellent 2D material for electrochemical reactions due to its unique layered structure, catalytic versatility, and rising interest in energy applications. Jaramillo et al. demonstrated that edge sites of the molybdenum disulfide (MoS_2) serve as highly catalytic sites for HER.[63] Recent studies demonstrate that the defect engineering, phase transitions (e.g., 2H to 1T′ phase), and formation of heterostructure significantly enhance the electrocatalytic performance of TMDs. Doping emerges as a highly effective approach to modify the structure and boost the electrocatalytic performance of TMD materials.[64] However, challenges in long-term stability and large-scale production underscore the importance of combined computational and experimental methods for next-generation catalyst development. TMDs emerge as promising noble-metal-free options for fuel cells. Defects in TMDs enhance the ORR performance by creating active sites that optimize O_2 adsorption, weaken O-O bonds, and facilitate intermediate desorption.[65] While the pristine TMDs (MoS_2, WS_2, $MoSe_2$) exhibit poor basal-plane activity, but defects such as vacancies and edges create undercoordinated sites that tune the d-band center which optimizes O_2/*OOH adsorption energies as per the Sabatier principle.[66,67] Introducing defects into TMDs effectively activates their basal planes, significantly enhancing electrocatalytic activity for the ORR.

In this thesis, we have computationally investigated promising and interesting materials which include perovskite oxides, carbon-based materials, and 2D TMDs, focusing on their structural and electronic properties with their possible applications towards electrochemical ORR catalysts. Employing a purely theoretical approach, we have evaluated their ORR activity using first-principles based DFT method. The ORR mechanisms are comprehensively explored through detailed energetics of each reaction intermediate, along with the key descriptors like total density of states (DOS), electronic band structures, Bader charge, and overpotential analysis.

1.5 Perovskite

Gustav Rose discovered the perovskite mineral in 1839 in Russia's Ural Mountains, naming it after the mineralogist Lev Perovski (1792–1856).[68] In 1926, Victor Goldschmidt described the crystal structure of perovskite while developing the tolerance factor.[69] In 1945, Helen D. Megaw studied the crystal structure of $BaTiO_3$ through X-ray diffraction, which defined the standard ABX_3 perovskite structure.[70] Perovskite structures exhibit versatile structural and electronic properties that enable their widespread use in energy technology. Perovskites have a wide range of applications in diverse technologies such as sensors, catalyst electrodes, fuel cells, solar cells, lasers, memory devices etc.

1.5.1 Structure of Perovskite

Compounds with the general ABX_3 formula that adopt the perovskite crystal structure are classified as perovskites. The crystal structure of the perovskite material is depicted in Figure 1.3. In the perovskite structure, A (e.g., La^{3+}, Ca^{2+}) and B (e.g., Ti^{4+}, Pb^{2+}) are cations having different sizes.[70] In this structure, B is coordinated by a cage of six X anions forming a corner-sharing $[BX_6]$ octahedron, while larger A cations occupy the 12-fold coordinated sites between octahedra. X is typically a monovalent or divalent anion such as oxygen or halides. The corner-sharing $[BX_6]$ octahedra form the structural backbone, linking at each vertex to create a rigid three-dimensional framework that accommodates the A cations without direct A–B bonding.[71] The stability of this ideal structure depends on appropriate ionic size ratios, which arise from the geometric requirement for anions to closely pack around cations.

$$r_A + r_X = \sqrt{2}(r_B + r_X) \tag{1.7}$$

In the above equation (1.7), r_A, r_B, and r_X represent the ionic radii of the A cation, B cation, and X anion, respectively. The Goldschmidt tolerance factor (t) provides a geometric criterion for the stability of the perovskite ABX_3 structure, quantifying the compatibility of the ionic radii of the constituent ions.[64] The tolerance factor is given by equation (1.8).

$$t = \frac{r_A + r_X}{\sqrt{2}(r_B + r_X)} \tag{1.8}$$

This parameter (t) allowed researchers to predict which compositions would adopt the distorted cubic perovskite lattice without extensive experiments. Goldschmidt's

pioneering work based on crystal chemistry principles enabled the rational design of oxide materials and profoundly shaped later research on synthetic perovskites.

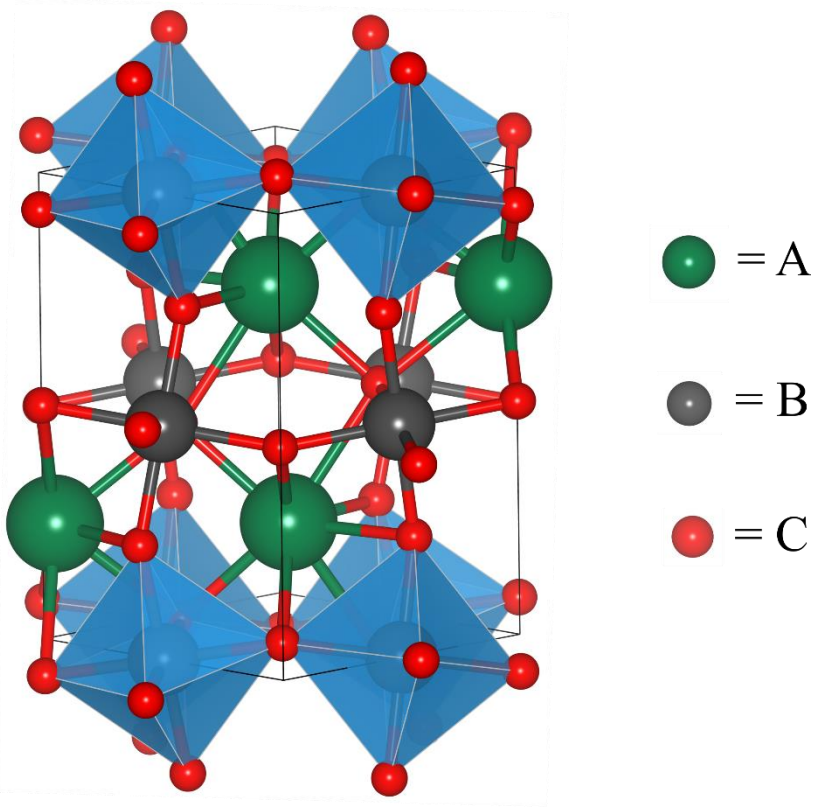


Figure 1.3: *Three-dimensional crystal structure of a perovskite material.*

1.5.2 Perovskite Oxide and Its Electronic Properties

The general chemical formula of perovskite oxide is ABO_3, where A and B are large electropositive cations, and O is an oxygen anion. The ideal cubic ABO_3 perovskite oxide features high symmetry and a flexible three-dimensional framework formed by corner-sharing $[BO_6]$ octahedra, with larger A cations occupying the 12-fold cub octahedral voids between eight such octahedra. This structure arises when the Goldschmidt tolerance factor (t) is near unity (0.9–1.0), ensuring minimal distortion. Deviations lead to lower-symmetry phases like orthorhombic or tetragonal.[71] Crystal structures are strongly linked to electrocatalytic performance through $[BO_6]$ octahedral distortions, thereby indirectly affecting ORR/OER activity. Perovskite oxide material exhibits diverse electronic properties ranging from insulation to metallic conduction that depend on the structure, composition, and doping etc. Their electronic properties can be tuned by doping or applying strain.[72] Doping in perovskite oxide alters the crystal structure, carrier concentration, orbital hybridization, etc, which in turn tunes

the electronic band gaps of the subject materials. The tuning of electronic band gap of perovskite oxide is applied in electrocatalytic applications. They have high electronic conductivity, which makes them a potential candidate in the field of electrocatalysis. High electronic conductivity is essential during ORR for rapid charge transfer that minimizes the overpotential. Various perovskite oxides function as semiconductors, particularly in transition metal variants such as $CaTiO_3$ and $CeTiO_3$. These materials can exhibit either direct or indirect band gaps depending on their composition and structure.[73] The perovskite material can have a direct or indirect band gap. In perovskite oxide material, the electronic behaviors are determined by the B-site transition metal and its interaction with oxygen.

(1) Splitting of orbitals: Orbital splitting in perovskite oxides significantly impacts ORR activity by tuning the e_g orbital occupancy of the B-site transition metal, which controls the binding energies of O_2 and reaction intermediates.[74] In the octahedral environment, the *d*-orbital of transition metal split into a low-energy t_{2g} and high-energy e_g states. An e_g filling of ~1 is considered optimal for ORR activity.

(2) Band gap variety: Perovskite oxides exhibit a massive range of band gaps (E_g). Perovskite oxides like $SrTiO_3$ and $BaTiO_3$ are wide-band gap semiconductors with E_g > 3.0 eV. Whereas other perovskites like $LaCoO_3$ have smaller band gaps (~0.89 eV). Band gap varieties in perovskite oxides significantly modulate ORR activity by controlling electronic conductivity, charge transfer kinetics, and *d*-band hybridization with ORR intermediates.[75] Metallic perovskites excel in ORR due to high conductivity, whereas wide gap insulators suffer sluggish ORR kinetics despite having stable surfaces.

(3) *d*-Band center: The *d*-band center in perovskite oxides serves as a key electronic descriptor for ORR catalysis, reflecting the energy position of the B-site transition metal's *d*-orbitals relative to the Fermi energy level (E_F).[76] This positioning governs the adsorption strength of ORR intermediates (e.g., O_2*, OH*) on active sites, optimizing activity as per the Sabatier principle when optimally tuned.

While perovskite oxides show strong potential for ORR electrocatalysis in fuel cells, their three-dimensional (3D) bulk forms often exhibit poor charge transfer due to metallic character. Recent experimental studies indicate that the reducing dimensionality to 2D monolayers may induce semiconducting behavior and boost

activity, though theoretical studies of ORR mechanisms, especially the $4e^-$ pathway energetics on basal planes remains limited. This work fills this gap by computationally exfoliating 3D perovskite oxides into 2D monolayers to reveal superior ORR performance, offering atomic-scale design principles for high-activity perovskite oxides in fuel cells.

1.5.3 Key Applications of Perovskite Oxides

Perovskite oxides exhibits exceptional applications due to their tunable electronic, optical, and magnetic properties. Perovskite oxides find applications across diverse fields, including solid oxide fuel cells (SOFCs), OER electrolyzers, thermal coatings, sensors, and superconductors. Perovskite oxides offer key advantages for ORR/HER electrocatalysis due to their robust design flexibility and tunable electronic structures. This broad utility highlights their role as multifunctional materials in advanced energy and sensing technologies.

1.6 Carbon Nanotubes

Carbon nanotubes (CNTs) are cylindrical structures composed of carbon (C) atoms. CNTs have diameters on the nanometer scale, making them a revolutionary class of materials. In 1950, Radushkevich and Lukyanovich first reported hollow graphitic fibers around 50 nm in diameter. Roger Bacon discovered ultra-thin, hair-like graphite filaments named “whiskers” in 1958–1960 during his experiment on graphite under extreme heat and pressure. Via electron microscopy, Bacon observed that whiskers looked like flat graphene sheets rolled up into tight tubes, anticipating modern carbon nanotubes. In 1976, Endo and colleagues produced nanometer-scale hollow carbon tubes using chemical vapor deposition (CVD) which was later recognized as multi-walled CNTs (MWCNTs). In 1991, Sumio Iijima revealed multi-walled carbon nanotube (MWCNTs) as tiny tube-like formations in arc-discharge soot byproducts. His discovery of MWCNTs sparked the modern nanotechnology revolution.[77,78] In 1993, Iijima and Bethune independently discovered single-walled CNTs (in short SWCNTs) using metal catalysts. CNT discoveries from the 1950s to 1990s quickly led to new uses, evolving from fundamental studies to widespread commercial technologies due to their unique physical and electronic properties. CNTs have excellent properties like high tensile strength, electrical and thermal conductivity due to their nanostructures and robust carbon atom bonds.[78] They have a wide range of applications in various

fields such as electronics, optics, nanotechnology and material science, etc. CNTs are classified into various types based on wall layers and chirality, which fundamentally define their properties.

1.6.1 Single-Walled Carbon Nanotubes (SWCNTs)

CNTs (diameter of 0.7–2 nm) consist of a single graphene layer rolled into a cylindrical tube. Figure 1.4a depicts the structure of a graphene sheet. SWCNTs have high tensile and mechanical strength due to the sp^2 hybridized carbon atoms within the cylindrical hexagonal lattice. They show metallic or semiconducting behavior due to their pure structure. The electronic properties of SWCNTs are determined by two factors, tube diameter and helicity, which further depend on the graphene layer that is rolled up. Top and side views of SWCNT are depicted in Figure 1.4b.

1.6.2 Double-Walled Carbon Nanotubes (DWCNTs)

They consist of two concentric circular graphene layers rolled into a cylindrical form, which provides enhanced stability in various applications. The inner tube typically measures 0.7–1.2 nm in diameter, while the outer tube spans approximately 1.3–3 nm. The inter-layer spacing between the two tubes is about 0.33-0.36 nm. The structure and properties of DWCNTs are like those of SWCNTs, but they have high resistance to chemical attacks. DWCNTs offer high mechanical and tensile strength with high electrical conductivity, which are based on wall chirality. They are used in energy storage devices like lithium-ion batteries for high capacity and rapid charge/discharge cycles.

1.6.3 Multi-Walled Carbon Nanotubes (MWCNTs)

CNTs have multiple concentric graphene circles (2 to more than 50 walls) nested together, which provide greater mechanical strength. The inter-layer spacing in MWCNTs is about 0.34 nm. MWCNTs exhibit high electrical conductivity via delocalized π-electrons and possess excellent mechanical strength. They find applications in energy storage, biomedicine, electronics, and more. The top view of MWCNT is shown in Figure 1.4c.

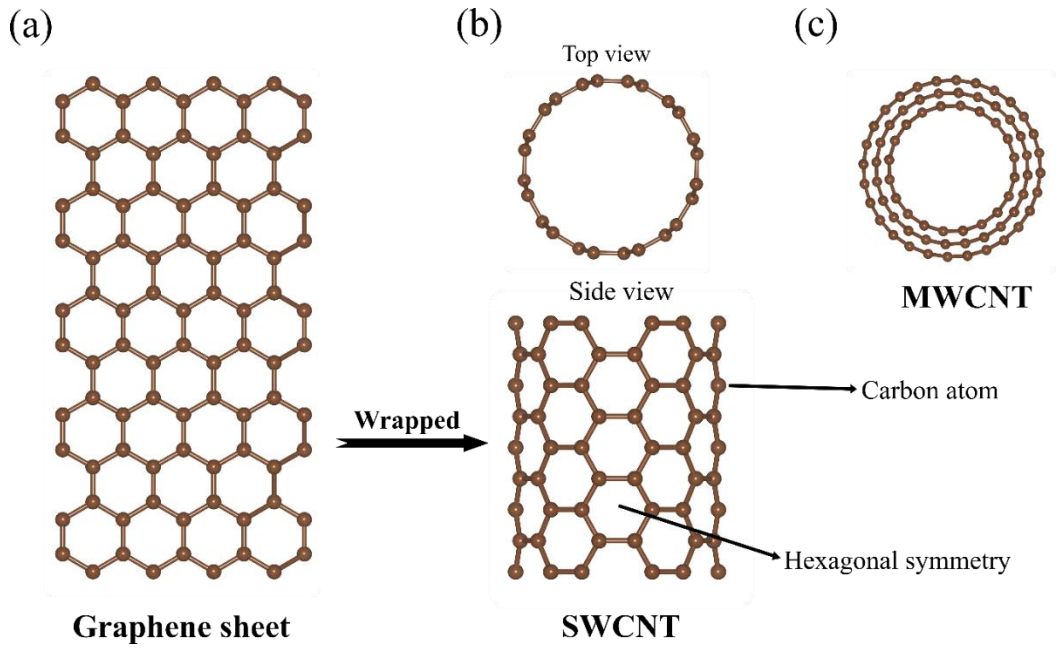


Figure 1.4: *Structure of (a) Graphene, (b) top and side view of SWCNT, and (c) top view of MWCNT.*

1.6.4 Chirality

Chirality refers to the twist or the angle at which the graphene layer is rolled into a cylinder. Chirality is an important factor that can determine whether a CNT can be metallic or a semiconductor. The structure of CNTs is defined by the chiral vector $\vec{C}_h$, given in equation (1.9) and specified by a pair of integers (*n, m*).[77] These integers (*n, m*) represent counts of unit vectors (a_1 and a_2) along the graphene honeycomb lattice directions.

$$\vec{C}_h = n\vec{a}_1 + m\vec{a}_2 \tag{1.9}$$

One more key parameter is the chiral angle, which is the angle between the chiral vector and the nearest zig-zag direction, ranging from 0˚ to 30˚. Chiral angle in CNTs influences the diameter and electronic properties, alongside chiral indices (*n, m*). CNTs are classified into three types based on the values of chiral indices (n, m):

(a) Armchair: When $n = m$, armchair nanotubes are formed when the chiral indices are equal, which results in a chiral angle $\theta \approx 30^{o}$. They are highly symmetric, which creates a uniform hexagonal lattice around the tube circumference. Here, the C-C bond aligns with the tube axis that enhances structural isotropy. They are always metallic in nature due to the band crossing at the Fermi level (E_F).

(b) Zigzag: When $m = 0$, Zigzag CNTs are defined by chiral indices (n, 0) that result in chiral angle $\theta \approx 0^{o}$. They have sharp, sawtooth-like edges when viewed end-on. They are less symmetric because the C-C bonds orient at angles to the tube axis, leading to distinct atomic packing and diameters. Zigzag CNTs can be metallic or semiconducting in nature, which depends on the n values.

(c) Chiral: When $n \neq m$, $m \neq 0$, Chiral CNTs have helical twist with chiral angle $0^{o} < \theta < 30^{o}$. It is formed when the graphene sheet is rolled at an intermediate angle. Most chiral CNTs are semiconducting, and they have a spiral lattice that lacks mirror symmetry, unlike armchair and zigzag CNTs.

1.6.5 Electronic Properties of CNTs

CNTs exhibit a unique electronic property derived from graphene that can show either metallic or semiconducting behavior which depends on chirality. Due to the high electrical conductivity and efficient electron transfer, CNTs enhances the ORR performance by facilitating easy charge transfer to active sites. Electrons propagate through the CNTs with minimal scattering over distances of several micrometers, allowing current transport at nearly zero resistance and with negligible heat dissipation. Encapsulating nanoparticles within CNTs promotes efficient charge transfer and transport, enhancing stability while minimizing ohmic losses.[57,60] CNTs have a wide range of electronic properties due to their unique structure, making them a potential candidate for application in energy devices. The chiral vector (n, m) determines how the graphene sheet is rolled, which in turn defines the electronic structure properties of CNTs.[77] The bandgap in semiconducting nanotubes varies inversely with tube diameter (d), providing control over their semiconducting behavior. When the tube diameter is high then the band gap is larger due to the quantum confinement and curvature effects on π-orbitals.

1.6.6 Key Strengths of CNTs for ORR

(a) Conductivity: CNTs (e.g., armchairs) have high electrical conductivity due to their graphitic structure, which provides efficient electron transfer during the multi-step ORR process. CNTs' 1D structure offers excellent axial conductivity and mass transfer efficiency for ORR. CNTs minimize junction resistance in networks, and the 1D pathway reduces ohmic losses during the multi-electron ORR, boosting current densities by 2-10 times in fuel cell cathodes.

(b) Mechanical and tensile strength: CNTs have exceptional mechanical strength due to their unique atomic structure. It is due to strong covalent sp^2 C–C bonds along the tube axis. They are one of the strongest known materials, exhibiting an ultra-high Young's modulus of nearly 1 TPa and being roughly five times stiffer than steel (~200 GPa). This property makes CNTs an excellent and durable electrocatalyst for ORR when operated in harsh conditions. Greater tensile strength of CNTs enhances their suitability as ORR catalysts in fuel cells by providing superior structural integrity under operational stresses.

(c) Large surface area: CNTs have a high surface area and high aspect ratio due to their nanoscale structure that maximizes active site exposure**.** They provide abundant active sites for the O_2 adsorption that improve ORR kinetics. The activity of the sites on the CNTs can be further improved by forming defects or by heteroatom doping.

(d) Stability: CNTs are highly resistant to corrosion in harsh acidic/alkaline media during the chemical reactions. The greater stability is due to the strong sp^2-hybridized carbon lattice that forms strong C-C bonds, which resist oxidation and degradation during electrochemical operation in fuel cells. Hence, CNTs are a potential candidate for long-term fuel cell operation.

(e) Cost effectiveness: CNTs are low-cost and can be abundantly produced and serve as alternatives to Pt or Pt-based catalysts for ORR applications. CNTs can be synthesized easily using various methods such as arc discharge, laser ablation, chemical vapor deposition (CVD), etc. Among these methods, CVD is widely recognized for producing CNTs with an optimal balance between quality and scalability.

(f) Catalyst support: CNTs are used as catalyst support due to their unique properties in the electrocatalysis process, like ORR. They are capable of anchoring metal nanoparticles (e.g., Pt, Pd) and different oxides (e.g., Fe_2O_3, CoO), which prevents their aggregation and improves uniform dispersion while promoting synergistic electrocatalytic activity.[79]

(g) Tunability: The electronic properties of CNTs can be tuned by doping different atoms. The Fermi energy level (E_F) can be shifted towards the valence or conduction bands. In a CNT-supported system, these shifts can improve electron donation to catalysts, which boosts ORR kinetics and durability.

While carbon nanotubes (CNTs) have been extensively explored for ORR electrocatalysis in fuel cells, their performance is limited by insufficient active sites and modest selectivity. Encapsulated nanoclusters within CNT remain theoretically underexplored despite experimental hints of enhanced stability and activity through synergistic metal-carbon interactions. We are motivated to model nanocluster encapsulation within CNT via theoretical approach, analyzing ΔE and ΔG for all intermediates to reveal superior $4e^-$ ORR performance, and providing atomic-scale insights for stable and efficient electrocatalysts for fuel cells.

1.6.7 Applications of CNTs

The diverse applications of CNTs arise from their unique physical and chemical properties, such as high electrical conductivity, and large surface area. CNTs serve as electrodes or additives in batteries, supercapacitors, and fuel cells, enhancing conductivity and capacity. CNTs serve as effective support materials for metal nanoparticles, oxides, or hybrid catalysts in heterogeneous catalysis, enhancing their dispersion and reducibility. CNTs strengthen the composites used in automotive parts, sporting goods, and boat hulls due to their remarkable mechanical strength. Figure 1.5 illustrates some of the innovative and promising applications of CNTs.

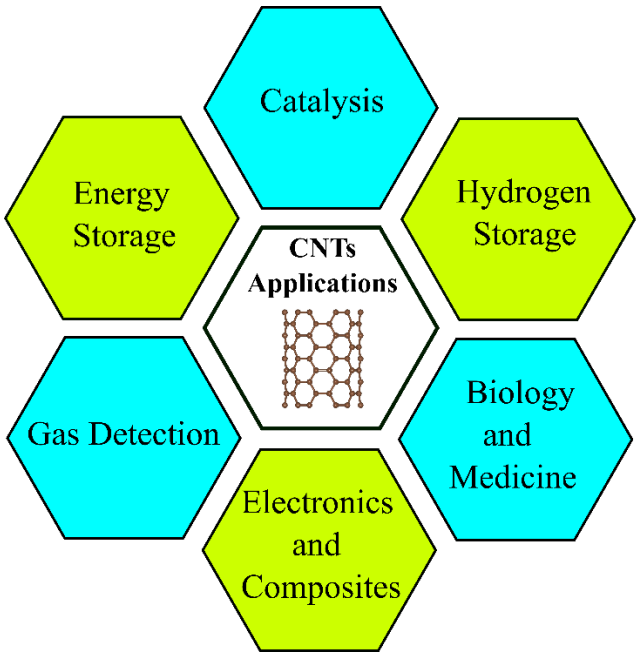


Figure 1.5: *Applications of carbon nanotubes (CNTs).*

1.7 Transition Metal Dichalcogenides (TMDs)

The two-dimensional transition metal dichalcogenides (2D TMDs) are a class of materials with the formula MX_2, where M is a transition metal (e.g., Mo, W, or Nb) and X is a chalcogen (e.g., S, Se, or Te). These materials consist of single atomic layers where the metal atoms are sandwiched between chalcogen layers. Bulk TMDs have been investigated since the 1920s, with early structural studies including Linus Pauling's work on molybdenum disulfide (MoS_2) in 1923.[80] Graphene has served as a cornerstone in the development of 2D material research by demonstrating that atomically thin, mechanically stable crystals can not only exist but also be systematically investigated. The isolation of graphene in 2004 sparked broad interest in other 2D materials such as TMDs, hexagonal boron nitride (h-BN), and MXenes, and created numerous new possibilities in electronics, optoelectronics, energy technologies, and quantum devices.[81] 2D TMDs gained wide attention in catalysis due to their post-graphene isolation, revealing high densities of active edge sites and tunable electronic properties ideal for replacing scarce Pt-based catalysts.[82] TMDs find wide-ranging uses in electronics, electrocatalysis, and biomedicine, driven by their adjustable bandgap, superior carrier mobility, and strong catalytic performance.

1.7.1 Structure of TMDs

TMDs are 2D layered materials composed of three atomic layers arranged in an X–M–X configuration, where M denotes a transition metal, and X represents a chalcogen, giving rise to monolayers with a honeycomb hexagonal lattice and threefold rotational symmetry.[83,84] Metal atoms reside in interstitial sites between the two chalcogen layers, forming strong in-plane covalent bonds while the layers are held together by weak van der Waals (vdW) interactions. TMDs are readily exfoliated into 2D layers because the individual X–M–X slabs are held together by weak vdW interactions, allowing them to be easily separated into thin or monolayer sheets.[85] A wide range of TMDs can be formed by pairing different transition metals with various chalcogens, and each combination can display unique electronic properties, including metallic, semi-metallic, or semiconducting behavior.[86] The behavior of graphene is dominated by carbon 2p-orbital π-bands with zero bandgap and Dirac-like dispersion, while TMDs derive their gap, anisotropy, and spin–valley features from the rich ***d***-orbital (in particular ***d***-subshell electrons) chemistry of the transition metal and its coupling to chalcogen ***p***-states.

TMDs exhibit distinct structural phases such as trigonal prismatic or octahedral, each defined by the coordination geometry of the transition metal atoms and their stacking arrangement. The primary phases (e.g., 2H, 1T, and 1T′) exhibit distinct electronic properties and stability, which directly impact their performance in electrocatalysis and electronics applications. In the 2H phase, transition metal atoms adopt a trigonal prismatic coordination, bonding to six chalcogen atoms in a hexagonal lattice. This semiconducting phase features ABA layer stacking, where A denotes chalcogen atoms and B denotes the transition metal atom, with the top and bottom chalcogen layers aligned directly above each other.[84] The 2H or trigonal prismatic phase of TMDs is depicted in Figure 1.6a, which has hexagonal symmetry. The 2H phase is commonly found in group 6 TMDs such as MoS_2 and WS_2 and features a direct monolayer electronic bandgap of approximately 1.8 eV, which is optimal for optoelectronic devices. The 1T phase of TMDs features octahedral coordination, where metal atoms are surrounded by six chalcogen atoms in an ABC stacking sequence, where A and C represent the same type of chalcogen atom.[61] The 1T metastable metallic phase is common in group 4 TMDs like TiS_2, which is stabilized via chemical exfoliation or intercalation. It offers superior electron mobility but reduced thermodynamic stability relative to the 1H phase. The 1T′ phase corresponds to a distorted octahedral structure, frequently observed in group 7 TMDs such as $MoTe_2$ and WTe_2, in which metal rows dimerize and undergo a lateral shift. 1T and 1T′ phases of the 2D layer structure of TMDs are depicted in Figure 1.6b and c, highlighting their distinct coordination geometries and stacking sequences. This structural distortion results in a monoclinic-like symmetry while preserving metallic conductivity. It acts as an intermediate state in phase transformations and exhibits potential for topological electronic properties.

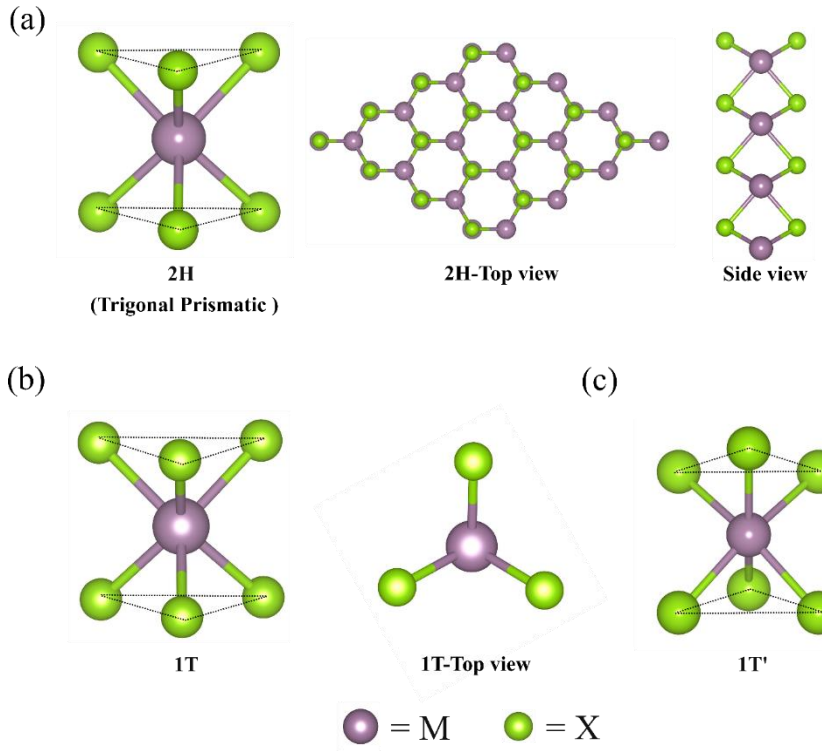


Figure 1.6: *Schematic illustration of different phases in 2D layered transition metal dichalcogenides (TMDs): (a) 2H phase, (b) 1T phase, and (c) 1T' phase.*

1.7.2 Advantages of TMDs for ORR

2D TMDs offer significant advantages for ORR electrocatalysis due to their high surface to volume ratio, tunable electronic structure, and abundant active sites at edges and defects that make them superior alternatives to Pt-based catalysts in fuel cell applications. Unlike platinum (Pt) and other noble metals, TMDs are made from more abundant elements, providing a lower-cost, non-precious metal alternative for ORR catalysts. Single- or few-layer TMDs expose more basal planes and edges compared to bulk materials, creating more undercoordinated metal and chalcogen sites that can adsorb and activate the O_2 molecule. 2D TMDs, particularly those in the 2H phase, show strong chemical stability in both acidic and alkaline environments, making them well-suited to withstand the harsh conditions of fuel cell cathodes. Many TMDs (e.g., 1T'-$MoTe_2$, $NbTe_2$) excel in both ORR and OER, ideal for rechargeable metal-air batteries and unitized regenerative fuel cells, with overpotentials under 0.5 V.[87] The electronic properties of 2D TMDs, including their bandgap and conductivity, can be finely tuned by varying the number of layers (e.g., monolayer, multilayer) and the coordination geometry of the metal atoms (such as trigonal prismatic 2H or octahedral 1T phases), enabling tailored optimization of intermediate adsorption energies during the ORR process. 2D TMDs can be combined with other 2D materials like graphene or

MXenes to form heterostructures that boost electron transport and active site density, compensating for their low intrinsic conductivity.[88,89] The electronic properties of TMDs can be precisely engineered via doping, strain, or phase conversion (e.g., semiconducting 2H to metallic 1T phase) to optimize the adsorption energy of reaction intermediates. The atomically thin 2D architecture of TMDs supports flexible, wearable fuel cell electrodes that exhibit robust mechanical durability under repeated cycling and can be seamlessly incorporated into textiles or membranes.[90]

TMDs exhibit promising ORR electrocatalytic activity in fuel cells due to their inherent semiconducting nature. Metal vacancies have emerged as an effective defect-engineering strategy to enhance electrical conductivity, create unsaturated coordination sites, and improve reaction selectivity. Despite experimental evidence of vacancy-induced performance improvements, comprehensive theoretical studies on ORR mechanisms remain limited. Our work designs metal-defective TMDs to demonstrate superior ORR performance and establish design principles for non-noble TMD electrocatalysts in fuel cells.

1.7.3 Applications of TMDs

2D TMDs excel in diverse fields like electronics, energy, and biomedicine due to their 2D layered structure, tunable phases, atomic-scale thickness, and unique electronic/optical properties arising from weak van der Waals bonds and MX_2 composition. Monolayer TMDs power transistors, photodetectors, and flexible displays with low power consumption and high switching speeds, surpassing silicon limits.[91] TMDs serve as catalysts for ORR, HER, and in batteries/supercapacitors due to tunable electronic properties and large surface areas. They enable efficient ion intercalation for rapid redox in energy storage and have numerous additional applications in sensing, optoelectronics, and related fields.

Although perovskite oxides, CNT-encapsulated nanoparticles, and 2D TMDs have each been studied as ORR electrocatalysts, they differ markedly in how their electronic structure controls oxygen intermediate (O*, OH*, OOH*) binding. In perovskites, adsorption is tuned mainly through e_g orbital occupancy and oxygen-vacancy formation, but the limited conductivity of many perovskite oxides can restrict charge transfer. In contrast, encapsulated nanoparticles overcome this limitation through the conductive CNT shell, which provides an efficient electron pathway, modifies the local

work function, and protects the metal core, although adsorption occurs indirectly through the shell. 2D TMDs differ from both, since their activity is governed by the d-band center and is largely confined to edge sites, with the basal plane relatively inert unless modified by defect engineering, phase engineering (2H to 1T), or doping. Thus, each material class offers a different balance of tunability, conductivity, and active-site accessibility, and none is optimal in all of these respects. These complementary trade-offs motivate the unified first-principles investigation of the ORR mechanism on all three classes presented in this thesis.

1.8 Thesis Objectives

This thesis employs a computational and theoretical approach to design novel electrocatalysts based on perovskite oxide, CNTs, and TMDs for the ORR. The primary objectives of this thesis are outlined below:

(1) To computationally investigate the structural, electronic properties, and four-electron ORR catalytic mechanism of 2D monolayer $LaNiO_3$ perovskite, demonstrating its potential as a non-Pt electrocatalyst for fuel cells.

(2) To investigate the electronic and structural properties of cobalt–platinum nanoparticle encapsulated carbon nanotube (CoPt@CNT) using first principle-based DFT method and evaluate its efficiency as an ORR electrocatalyst through band structure, adsorption energy (ΔE), and Gibbs free energy (ΔG) of key reaction intermediates.

(3) To investigate the FeCe nanoparticles encapsulated in carbon nanotubes (FeCe@CNT) as a non-noble-metal electrocatalyst for ORR, as a potential substitute for Pt-based catalysts.

(4) To investigate the ORR catalytic activity of Mo-defective $MoTe_2$ surface using first-principles DFT-D method, focusing on free energies (ΔG) of various intermediates of ORR to validate its potential as a Pt-free fuel cell electrocatalyst.

1.9 References

[1] H. Ritchie, P. Rosado, M. Roser, Energy Production and Consumption, Our World in Data (2020).

[2] Energy Institute, Statistical Review of World Energy 2025, (2025).

[3] M.Z. Jacobson, M.A. Delucchi, G. Bazouin, Z.A.F. Bauer, C.C. Heavey, E. Fisher, S.B. Morris, D.J.Y. Piekutowski, T.A. Vencill, T.W. Yeskoo, 100% clean and renewable wind, water, and sunlight (WWS) all-sector energy roadmaps for the 50 United States, Energy Environ. Sci. 8 (2015) 2093–2117.

[4] D. Tong, D.J. Farnham, L. Duan, Q. Zhang, N.S. Lewis, K. Caldeira, S.J. Davis, Geophysical constraints on the reliability of solar and wind power worldwide., Nat. Commun. 12 (2021) 6146.

[5] Euan Graham, Nicolas Fulghum, Katye Altieri, Chapter 3, Yearly electricity data, Global Electricity Review 2025, Ember (2025).

[6] F. Ueckerdt, R. Brecha, G. Luderer, Analyzing major challenges of wind and solar variability in power systems, Renew. Energy 81 (2015) 1–10.

[7] X. Wang, Z. Li, Y. Qu, T. Yuan, W. Wang, Y. Wu, Review of Metal Catalysts for Oxygen Reduction Reaction : From Nanoscale Engineering to Atomic Design, Chem 5 (2019) 1486–1511.

[8] S.M. Alfaifi, R. Balu, K. Chiang, N.R. Choudhury, N.K. Dutta, Electrocatalysts for the Oxygen Reduction Reaction in Proton Exchange Membrane Fuel Cells: Significant Advances, Major Challenges, and Future Directions, ACS Catal. 15 (2025) 9301–9345.

[9] S. Qamar, I. Irshad, R. Shahzad, E. Ali, Fuel Cells and their Role in Sustainable Energy Transition: A Review, Future Energy and Environ. Lett. 4 (2025) 1–18.

[10] E.I. Solomon, S.S. Stahl, Introduction: Oxygen Reduction and Activation in Catalysis, Chem. Rev. 118 (2018) 2299–2301.

[11] H. Wang, W. Xu, S. Richins, K. Liaw, L. Yan, M. Zhou, H. Luo, Polymer-assisted approach to $LaCo_{1-x}Ni_xO_3$ network nanostructures as bifunctional oxygen electrocatalysts, Electrochim. Acta 296 (2019) 945–953.

[12] Y. Nie, L. Li, Z. Wei, Recent advancements in Pt and Pt-free catalysts for oxygen reduction reaction, Chem. Soc. Rev. 44 (2015) 2168–2201.

[13] E. Antolini, Palladium in fuel cell catalysis, Energy Environ. Sci. 2 (2009) 915–931.

[14] N.M. Marković, T.J. Schmidt, V. Stamenković, P.N. Ross, Oxygen Reduction Reaction on Pt and Pt Bimetallic Surfaces: A Selective Review, Fuel Cells 1 (2001) 105–116.

[15] L. Huang, S. Zaman, X. Tian, Z. Wang, W. Fang, B.Y. Xia, Advanced Platinum-Based Oxygen Reduction Electrocatalysts for Fuel Cells, Acc. Chem. Res. 54 (2021) 311–322.

[16] J. Huang, M. Eikerling, Modeling the oxygen reduction reaction at platinum-based catalysts: A brief review of recent developments, Curr. Opin. Electrochem. 13 (2019) 157–165.

[17] W.-J. Niu, J.-Z. He, B.-N. Gu, M.-C. Liu, Y.-L. Chueh, Opportunities and challenges in precise synthesis of transition metal single-atom supported by 2D materials as catalysts toward oxygen reduction reaction, Adv. Funct. Mater. 31 (2021) 2103558.

[18] Z. Li, X. Li, Y. Gu, X. Hu, L. Wang, P. Li, Theoretical screening of transition metal atoms doped two-dimensional VSe_2 monolayers as single-atom catalysts for HER, OER and ORR, Appl. Surf. Sci. 646 (2024) 158959.

[19] Y. Hao, L.-C. Xu, J. Pu, L. Wang, L.-F. Huang, Stable zigzag edges of transition-metal dichalcogenides with high catalytic activity for oxygen reduction, Electrochim. Acta 338 (2020) 135865.

[20] L. Du, L. Xing, G. Zhang, M. Dubois, S. Sun, Strategies for engineering high-performance PGM-free catalysts toward oxygen reduction and evolution reactions, Small Methods 4 (2020) 2000016.

[21] E.F. Holby, Improving platinum group metal--free oxygen reduction reaction electrocatalyst activity: suggestions from density functional theory studies, Curr. Opin. Electrochem. 25 (2021) 100631.

[22] S. Mukerjee, S. Srinivasan, Enhanced electrocatalysis of oxygen reduction on platinum alloys in proton exchange membrane fuel cells, J. Electroanal. Chem. 357 (1993) 201–224.

[23] B. Lu, Q. Liu, S. Chen, Electrocatalysis of Single-Atom Sites: Impacts of Atomic Coordination, ACS Catal. 10 (2020) 7584–7618.

[24] M. Sajid, M.A. Qamar, A. Farhan, W. Qayyum, A. Khalid, A. Nawaz, S. Lee, H. Nawaz, Emerging paradigms in two-dimensional materials: Classification, synthesis, and the role of defects in electrocatalysis for water splitting and oxygen reduction reaction, J. Environ. Chem. Eng. 12 (2024) 113784.

[25] D. Chen, C. Chen, Z.M. Baiyee, Z. Shao, F. Ciucci, Nonstoichiometric Oxides as Low-Cost and Highly-Efficient Oxygen Reduction/Evolution Catalysts for Low-Temperature Electrochemical Devices, Chem. Rev. 115 (2015) 9869–9921.

[26] M. Shao, Q. Chang, J.-P. Dodelet, R. Chenitz, Recent advances in electrocatalysts for oxygen reduction reaction, Chem. Rev. 116 (2016) 3594–3657.

[27] Y. Jiao, Y. Zheng, M. Jaroniec, S.Z. Qiao, Design of electrocatalysts for oxygen- and hydrogen-involving energy conversion reactions, Chem. Soc. Rev. 44 (2015) 2060–2086.

[28] T. Poux, A. Bonnefont, G. Kéranguéven, G.A. Tsirlina, E.R. Savinova, Electrocatalytic oxygen reduction reaction on perovskite oxides: series versus direct pathway, ChemPhysChem 15 (2014) 2108–2120.

[29] Q. Ji, L. Bi, J. Zhang, H. Cao, X.S. Zhao, The role of oxygen vacancies of ABO_3 perovskite oxides in the oxygen reduction reaction, Energy & Environ. Sci. 13 (2020) 1408–1428.

[30] C.E. Beall, E. Fabbri, T.J. Schmidt, Perovskite oxide based electrodes for the oxygen reduction and evolution reactions: the underlying mechanism, ACS Catal. 11 (2021) 3094–3114.

[31] M. Humayun, Z. Li, M. Israr, A. Khan, W. Luo, C. Wang, Z. Shao, Perovskite Type ABO_3 Oxides in Photocatalysis, Electrocatalysis, and Solid Oxide Fuel Cells: State of the Art and Future Prospects, Chem. Rev. 125 (2025) 3165–3241.

[32] S. Ingavale, M. Gopalakrishnan, C.M. Enoch, C. Pornrungroj, M. Rittiruam, S. Praserthdam, A. Somwangthanaroj, K. Nootong, R. Pornprasertsuk, S. Kheawhom, Strategic Design and Insights into Lanthanum and Strontium Perovskite Oxides for Oxygen Reduction and Oxygen Evolution Reactions,

Small 20 (2024) 2308443.

[33] M. Bursell, M. Pirjamali, Y. Kiros, $La_{0.6}Ca_{0.4}CoO_3$, $La_{0.1}Ca_{0.9}MnO_3$ and $LaNiO_3$ as bifunctional oxygen electrodes, Electrochim. Acta 47 (2002) 1651–1660.

[34] X. Sun, Y. Yuan, S. Liu, H. Zhao, S. Yao, Y. Sun, M. Zhang, Y. Liu, Z. Lin, Recent advances in perovskite oxides for oxygen evolution reaction: structures, mechanisms, and strategies for performance enhancement, Adv. Funct. Mater. 35 (2025) 2416705.

[35] J. Suntivich, H.A. Gasteiger, N. Yabuuchi, H. Nakanishi, J.B. Goodenough, Y. Shao-Horn, Design principles for oxygen-reduction activity on perovskite oxide catalysts for fuel cells and metal-air batteries, Nat. Chem. 3 (2011) 546–550.

[36] Q. Ji, L. Bi, J. Zhang, H. Cao, X.S. Zhao, The role of oxygen vacancies of ABO_3 perovskite oxides in the oxygen reduction reaction, Energy Environ. Sci. 13 (2020) 1408–1428.

[37] C. Jin, X. Cao, L. Zhang, C. Zhang, R. Yang, Preparation and electrochemical properties of urchin-like $La_{0.8}Sr_{0.2}MnO_3$ perovskite oxide as a bifunctional catalyst for oxygen reduction and oxygen evolution reaction, J. Power Sources 241 (2013) 225–230.

[38] Y. Chen, Research on perovskite type catalyst for zinc-air battery air electrode, Wuhan Ligong Daxue Xuebao/Journal Wuhan Univ. Technol. 27 (2005) 34–37.

[39] S. Müller, K. Striebel, O. Haas, $La_{0.6}Ca_{0.4}CoO_3$: a stable and powerful catalyst for bifunctional air electrodes, Electrochim. Acta 39 (1994) 1661–1668.

[40] Y. Choi, M. emsp14C Lin, M. Liu, Computational study on the catalytic mechanism of oxygen reduction on $La_{0.5}Sr_{0.5}MnO_3$ in solid oxide fuel cells, Angew. Chemie Int. Ed. 46 (2007) 7214–7219.

[41] C.K. Lee, K.A. Striebel, F.R. McLarnon, E.J. Cairns, Thermal treatment of $La_{0.6}Ca_{0.4}CoO_3$ perovskites for bifunctional air electrodes, J. Electrochem. Soc. 144 (1997) 3801–3806.

[42] T. Ren, L.-K. Zhao, X. Zhang, X.-W. Gao, H. Chen, Z. Liu, D. Yang, W.-B. Luo, Optimizing $LaNiO_3$ surface structure for an efficient oxygen reduction reaction, J. Mater. Chem. A 13 (2025) 14737–14742.

[43] S. Shanmugam, A. Gedanken, Generation of Hydrophilic, Bamboo-Shaped Multiwalled Carbon Nanotubes by Solid-State Pyrolysis and Its Electrochemical Studies, J. Phys. Chem. B 110 (2006) 2037–2044.

[44] P.J. Britto, K.S.V. Santhanam, A. Rubio, J.A. Alonso, P.M. Ajayan, Improved charge transfer at carbon nanotube electrodes, Adv. Mater. 11 (1999) 154–157.

[45] B.H.R. Suryanto, S. Chen, J. Duan, C. Zhao, Hydrothermally Driven Transformation of Oxygen Functional Groups at Multiwall Carbon Nanotubes for Improved Electrocatalytic Applications, ACS Appl. Mater. Interfaces 8 (2016) 35513–35522.

[46] C. Hu, L. Dai, Carbon-Based Metal-Free Catalysts for Electrocatalysis beyond the ORR, Angew. Chemie Int. Ed. 55 (2016) 11736–11758.

[47] K. Gong, F. Du, Z. Xia, M. Durstock, L. Dai, Nitrogen-doped carbon nanotube arrays with high electrocatalytic activity for oxygen reduction, Science 323 (2009) 760–764.

[48] Z. Chen, D. Higgins, Z. Chen, Electrocatalytic activity of nitrogen doped carbon nanotubes with different morphologies for oxygen reduction reaction, Electrochim. Acta 55 (2010) 4799–4804.

[49] D. Yu, Q. Zhang, L. Dai, Highly efficient metal-free growth of nitrogen-doped single-walled carbon nanotubes on plasma-etched substrates for oxygen reduction, J. Am. Chem. Soc. 132 (2010) 15127–15129.

[50] Z. Wang, R. Jia, J. Zheng, J. Zhao, L. Li, J. Song, Z. Zhu, Nitrogen-promoted self-assembly of N-doped carbon nanotubes and their intrinsic catalysis for oxygen reduction in fuel cells, ACS Nano 5 (2011) 1677–1684.

[51] Y. Cheng, H. Zhang, C. V Varanasi, J. Liu, Highly efficient oxygen reduction electrocatalysts based on winged carbon nanotubes, Sci. Rep. 3 (2013) 3195.

[52] C.V. Rao, C.R. Cabrera, Y. Ishikawa, In search of the active site in nitrogen-doped carbon nanotube electrodes for the oxygen reduction reaction, J. Phys. Chem. Lett. 1 (2010) 2622–2627.

[53] Z. Chen, D. Higgins, Z. Chen, Nitrogen doped carbon nanotubes and their impact on the oxygen reduction reaction in fuel cells, Carbon 48 (2010) 3057–3065.

[54] N. Ma, Y. Zhang, Y. Wang, J. Zhao, B. Liang, Y. Xiong, S. Luo, C. Huang, J. Fan, Curvature effects regulate the catalytic activity of Co@N_4-doped carbon nanotubes as bifunctional ORR/OER catalysts, J. Colloid Interface Sci. 654 (2024) 1458–1468.

[55] D. Deng, L. Yu, X. Chen, G. Wang, L. Jin, X. Pan, J. Deng, G. Sun, X. Bao, Iron Encapsulated within Pod-like Carbon Nanotubes for Oxygen Reduction Reaction, Angew. Chemie Int. Ed. 52 (2013) 371–375.

[56] W. Xiong, F. Du, Y. Liu, A.J. Perez, M. Supp, T.S. Ramakrishnan, L. Dai, L. Jiang, 3-D Carbon Nanotube Structures Used as High Performance Catalyst for Oxygen Reduction Reaction, J. Am. Chem. Soc. 132 (2010) 15839–15841.

[57] C. Wang, Y. Ha, X. Mao, W. Xu, A. Du, R. Wu, S. Chou, H. Zhang, Co Nanoparticles Encapsulated in N-Doped Carbon Nanotubes Grafted CNTs as Electrocatalysts for Enhanced Oxygen Reduction Reaction, Adv. Mater. Interfaces 9 (2022) 2101877.

[58] G. Zhong, S. Li, S. Xu, W. Liao, X. Fu, F. Peng, Nickel Nanoparticles Encapsulated in Nitrogen-Doped Carbon Nanotubes as Excellent Bifunctional Oxygen Electrode for Fuel Cell and Metal–Air Battery, ACS Sustain. Chem. Eng. 6 (2018) 15108–15118.

[59] N. Wang, X. Zheng, Y. Buba, H. Wang, X. Wang, Y. Zhao, Electrocatalytic performance of cobalt/nickel nanoparticles encapsulated by N-doped carbon nanotubes toward the oxygen reduction reaction, Appl. Surf. Sci. 615 (2023) 156317.

[60] W. Niu, S. Pakhira, K. Marcus, Z. Li, J.L. Mendoza-Cortes, Y. Yang, Apically dominant mechanism for improving catalytic activities of N-doped carbon nanotube arrays in rechargeable zinc-air battery, Adv. Energy Mater. 8 (2018) 1800480.

[61] W. Choi, N. Choudhary, G.H. Han, J. Park, D. Akinwande, Y.H. Lee, Recent development of two-dimensional transition metal dichalcogenides and their applications, Mater. Today 20 (2017) 116–130.

[62] A. Mondal, A. Vomiero, 2D Transition Metal Dichalcogenides-Based

Electrocatalysts for Hydrogen Evolution Reaction, Adv. Funct. Mater. 32 (2022) 2208994.

[63] T.F. Jaramillo, K.P. Jørgensen, J. Bonde, J.H. Nielsen, S. Horch, I. Chorkendorff, Identification of Active Edge Sites for Electrochemical H_2 Evolution from MoS_2 Nanocatalysts, Science 317 (2007) 100–102.

[64] Q.-M. Liang, T. Ma, L. Lin, Recent advances and future perspectives on metal doping strategies for regulating the electrocatalytic performance of MoS_2, J. Mater. Chem. C 14 (2026) 1360–1376.

[65] K.N. Khattak, Y. Shao, J. Zhou, Recent development and challenges in TMD-based 2D materials towards OER/ORR electrocatalysis, React. Chem. Eng. 11 (2026) 11–41.

[66] Z.H. Tan, X.Y. Kong, B.-J. Ng, H. Sen Soo, A.R. Mohamed, S.-P. Chai, Recent Advances in Defect-Engineered Transition Metal Dichalcogenides for Enhanced Electrocatalytic Hydrogen Evolution: Perfecting Imperfections, ACS Omega 8 (2023) 1851–1863.

[67] X. Yang, H. Liu, Z. Qu, Y. Xie, Y. Ma, A theoretical roadmap for the best oxygen reduction activity in two-dimensional transition metal tellurides, Chem. Sci. 13 (2022) 11048–11057.

[68] S. Li, Y. Pan, W. Wang, Y. Li, $CsPbX_3$ (X = Cl, Br, I) perovskite quantum dots embedded in glasses: Recent advances and perspectives, Chem. Eng. J. 434 (2022) 134593.

[69] V. Goldschmidt, Die Gesetze der Krystallochemie, Naturwissenschaften 14 (1926) 477–485.

[70] Crystal Structure of Barium Titanate, Nature 155 (1945) 484–485.

[71] M.A. Peña, J.L.G. Fierro, Chemical Structures and Performance of Perovskite Oxides, Chem. Rev. 101 (2001) 1981–2018.

[72] S. Brittman, G.W.P. Adhyaksa, E.C. Garnett, The expanding world of hybrid perovskites: materials properties and emerging applications., MRS Commun. 5 (2015) 7–26.

[73] S.H. Saikot, A. Apon, A. El-rayyes, First-principles investigation of structural, electronic, optical, mechanical, and phonon properties of Pb- and Sn-based cubic oxide perovskites for optoelectronic applications, 15 (2025) 39071–39091.

[74] C.E. Beall, E. Fabbri, T.J. Schmidt, Perovskite Oxide Based Electrodes for the Oxygen Reduction and Evolution Reactions: The Underlying Mechanism, ACS Catal. 11 (2021) 3094–3114.

[75] J.-W. Zhao, Y. Li, D. Luan, X.W. (David) Lou, Structural evolution and catalytic mechanisms of perovskite oxides in electrocatalysis, Sci. Adv. 10 (2024) eadq4696.

[76] R. Jacobs, J. Hwang, Y. Shao-Horn, D. Morgan, Assessing Correlations of Perovskite Catalytic Performance with Electronic Structure Descriptors, Chem. Mater. 31 (2019) 785–797.

[77] J. Chen, S. Wei, H. Xie, A brief introduction of carbon nanotubes: history, synthesis, and properties, J. Phys. Conf. Ser.1948 (2021) 12184.

[78] N. Srikanth, A.C. Kumar, J. Abraham, S. Thomas, N. Kalarikkal, History of Carbon Nanotubes, Handb. Carbon Nanotub., Springer International Publishing, Cham, (2022) 3–24.

[79] H.-J. Zhang, Z. Zhou, L. Jia, Z.-F. Ma, Y. Xue, Collaborative Anchoring of Pt Nanoparticles and Metal Oxide Nanoparticles on N-Doped Carbon as Catalysts for Oxygen Reduction, ACS Appl. Nano Mater. 6 (2023) 13314–13319.

[80] R.G. Dickinson, L.C. Pauling, The Crystal Structure of Molybdenite, J. Am. Chem. Soc. 45 (1923) 1466–1471.

[81] M.M. Uddin, M.H. Kabir, M.A. Ali, M.M. Hossain, M.U. Khandaker, S. Mandal, A. Arifutzzaman, D. Jana, Graphene-like emerging 2D materials: recent progress, challenges and future outlook., RSC Adv. 13 (2023) 33336–33375.

[82] B. Saeloo, T. Saisopa, P. Chavalekvirat, P. Iamprasertkun, K. Jitapunkul, W. Sirisaksoontorn, T.R. Lee, W. Hirunpinyopas, Role of Transition Metal Dichalcogenides as a Catalyst Support for Decorating Gold Nanoparticles for Enhanced Hydrogen Evolution Reaction., Inorg. Chem. 63 (2024) 18750–18762.

[83] S.H. Sung, N. Schnitzer, L. Brown, J. Park, R. Hovden, Stacking, strain, and

twist in 2D materials quantified by 3D electron diffraction, Phys. Rev. Mater. 3 (2019) 064003.

[84] C. Ataca, H. Şahin, S. Ciraci, Stable, Single-Layer MX_2 Transition-Metal Oxides and Dichalcogenides in a Honeycomb-Like Structure, J. Phys. Chem. C 116 (2012) 8983–8999.

[85] K.S. Novoselov, A.K. Geim, S. V Morozov, D. Jiang, M.I. Katsnelson, I. V Grigorieva, S. V Dubonos, A.A. Firsov, Two-dimensional gas of massless Dirac fermions in graphene, Nature 438 (2005) 197–200.

[86] J.A. Wilson, A.D. Yoffe, The transition metal dichalcogenides discussion and interpretation of the observed optical, electrical and structural properties, Adv. Phys. 18 (1969) 193–335.

[87] N. Karmodak, L. Bursi, O. Andreussi, Oxygen Evolution and Reduction on Two-Dimensional Transition Metal Dichalcogenides, 13 (2022) 58–65.

[88] Z. Lu, E. Zhao, C. Zhang, C. Chen, Two-dimensional materials and their applications in fuel cells, IScience 27 (2024) 109841.

[89] X. Tong, X. Zhan, D. Rawach, Z. Chen, G. Zhang, S. Sun, Low-dimensional catalysts for oxygen reduction reaction, Prog. Nat. Sci. Mater. Int. 30 (2020) 787–795.

[90] M.P. Minadakis, N. Tagmatarchis, Exfoliated Transition Metal Dichalcogenide-Based Electrocatalysts for Oxygen Evolution Reaction, Adv. Sustain. Syst. 7 (2023) 2300193.

[91] J. Yu, S. Wu, X. Zhao, Z. Li, X. Yang, Q. Shen, M. Lu, X. Xie, D. Zhan, J. Yan, Progress on Two-Dimensional Transitional Metal Dichalcogenides Alloy Materials: Growth, Characterisation, and Optoelectronic Applications., Nanomater. 13 (2023) 2843.

Chapter 2

Theory, Methodology and Computational Details

The second chapter of this thesis presents a comprehensive overview of the computational framework and methodological choices employed in the study of electrocatalytic materials. It begins with foundational quantum physics/chemistry concepts, including the Schrödinger equation for many-body systems and the Born–Oppenheimer approximation. This leads to density functional theory (DFT) formalism, covering Hohenberg–Kohn theorems, Kohn–Sham equations, and exchange-correlation approximations. The chapter then describes the computational packages CRYSTAL17 and VASP, along with basis sets. The chapter also covers key instruments and software tools employed for quantum computations.

Quantum physics serves as the core branch of physics, offering the theoretical foundation for matter and energy behavior at atomic and subatomic levels, with key emphasis on wave-particle duality, quantization, and probabilistic particle interactions. Quantum physics provides the essential theoretical principles that quantum chemistry applies to understand molecular structure, bonding, and reactivity at the electronic level. Quantum chemistry emerged in the early twentieth century, when physicists and chemists began confronting the limitations of classical mechanics in explaining phenomena such as atomic spectra and black-body radiation. Max Planck's 1900 quantum hypothesis introduced the concept of discrete energy quanta ($E = h\nu$), which was then reinforced by Einstein's 1905 explanation of the photoelectric effect, together laying the foundations of quantum theory. These early developments marked the emergence of quantum chemistry, a discipline that has since advanced into a powerful framework of computational methods for investigating electronic structure, chemical bonding, and reactivity at the atomic and molecular scale. In the foundational period of the 1920s, Niels Bohr's 1913 atomic model introduced quantized electron orbits, but the field was fundamentally reshaped by Erwin Schrödinger's 1926 wave equation,

which exactly solved the hydrogen atom. In 1927, Heitler and London's study of the H_2^+ ion provided the first quantum-mechanical explanation of the chemical bond via exchange symmetry, widely regarded as marking quantum chemistry's birth. While Werner Heisenberg's matrix mechanics offered a complementary formulation to classical physics, Schrödinger's wave mechanics gained favor among chemists for its greater intuitiveness and accessibility. During the 1930s–1950s, Linus Pauling's valence bond theory elegantly united quantum mechanics with practical chemistry, seamlessly blending Lewis' electron-pair bonds and Heitler–London resonance principles.

Hartree–Fock (HF) theory (1930) enabled practical multi-electron computations via self-consistent fields (SCF), complemented by Slater-type orbitals that simplified basis-set design. John Pople's Gaussian-type orbitals in the 1950s laid the foundation for computational progress, ultimately enabling today's density functional theory (DFT) approaches. From the 1960s onward, computational advances revolutionized quantum chemistry. The Hohenberg–Kohn theorems (1964) and Kohn–Sham formulation (1965) established DFT method, shifting the focus from many-electron wavefunctions to electron density. In the 1970s, early quantum chemistry codes laid the groundwork for today's software like CRYSTAL, GAUSSIAN and VASP. Today, quantum chemistry drives electrocatalysis research through refined DFT methodologies. Quantum chemistry has evolved from initial analyses of atomic spectra into a refined, method-centric field that forms the backbone of contemporary computational materials science. Anchored in the Schrödinger equation and wavefunction-based ab initio methods, DFT provides a range of techniques from Hartree–Fock and post-Hartree–Fock methods to sophisticated DFT functionals that balance precision with computational demands for molecular and solid-state systems. Higher-fidelity methods like coupled-cluster theory and quantum Monte Carlo (QMC) capture electron correlation more effectively but remain too resource-intensive for extended materials systems. Modern quantum chemistry incorporates multiscale approaches such as quantum mechanics (QM) and molecular mechanics (MM) and machine-learned (ML) force fields to bridge different length and time scales in complex systems. At the same time, cutting-edge developments including machine-learned exchange-correlation functionals and quantum-computing strategies are aimed at tackling strongly correlated systems and advancing the rational design of functional materials.

Building on these foundations, DFT has emerged as a central quantum-mechanical method for computing the electronic structure of atoms, molecules, and solids. Within the broader framework of quantum chemistry, DFT provides an efficient yet powerful approach to investigate electronic structure, chemical bonding, and reactivity from first principles, making it particularly well-suited for the study of catalytic materials and complex systems.

2.1 Schrödinger Equation

The Schrödinger equation (SE) forms the cornerstone of quantum mechanics, governing the time evolution of a system's quantum state through its wave function (Ψ). Erwin Schrödinger formulated the equation in 1925–1926, building on de Broglie's wave-particle duality and Heisenberg's matrix mechanics. The time-independent SE is expressed as:

$$\hat{H}\Psi = E\Psi \tag{2.1}$$

Where, $\hat{\boldsymbol{H}}$ and $\boldsymbol{\Psi}$ are the Hamiltonian operator and wave function, respectively, and $\boldsymbol{E}$ is the corresponding energy eigenvalue. The Hamiltonian operator $\hat{\boldsymbol{H}}$ represents the total energy of the quantum system, comprising kinetic energy and potential energy:

$$\hat{H} = -\frac{\hbar^2}{2m}\nabla^2 + V \tag{2.2}$$

Where:

- $\hbar$ is the reduced Planck's constant.
- m is the particle mass.
- ∇^2 is the Laplacian operator $\left(\nabla^2 = \frac{\partial^2}{\partial x^2} + \frac{\partial^2}{\partial y^2} + \frac{\partial^2}{\partial z^2}\right)$.
- V represents potential energy.

Although the SE admits exact analytical solutions for hydrogen-like atoms (single-electron systems), multi-electron systems demand sophisticated numerical approximations. These computational methods are now fundamental for elucidating the electronic structure of complex molecules, crystalline solids, and nanoscale materials across chemistry and materials science.[1]

2.2 The Many-Body System

The many-body Schrödinger equation describes the quantum evolution of a system with multiple interacting particles, such as electrons in atoms or molecules. It governs the collective quantum behavior of electrons, nuclei, and other particles, determining all ground-state (GS) properties like energy, density, and bonding in molecules and materials. A general many-body SE can be described as follows:

$$\hat{H}\Psi\,(r,R) = E\Psi\,(r,R) \tag{2.3}$$

Where $\boldsymbol{r}$ and $\boldsymbol{R}$ represents the position of the electrons and nuclei, respectively. $\hat{\boldsymbol{H}}$ is the Hamiltonian operator, and $\boldsymbol{E}$ is the total energy of the system.

The Hamiltonian for a many-body system can be written as:

$$\hat{H} = \hat{T}_e + \hat{T}_N + \hat{V}_{eN} + \hat{V}_{ee} + \hat{V}_{NN} \tag{2.4}$$

$$\hat{H} = -\sum_i \frac{\hbar^2}{2m_e}\nabla_i^2 - \sum_A \frac{\hbar^2}{2M_A}\nabla_A^2 - \sum_{\{i,A\}} \frac{Z_A e^2}{|r_i - R_A|} + \sum_{\{i<j\}} \frac{e^2}{|r_i - r_j|} + \sum_{\{A<B\}} \frac{Z_A Z_B}{|R_A - R_B|} \tag{2.5}$$

In the above equation (2.4) and (2.5):

- 1st term represents the kinetic energy of the electrons ($\hat{T}_e$).
- 2nd term is the kinetic energy of the nuclei ($\hat{T}_N$).
- 3rd term accounts for the Coulomb attraction between electrons and nuclei ($\hat{V}_{eN}$).
- 4th term describes electron-electron repulsion ($\hat{V}_{ee}$).
- 5th term corresponds to nucleus-nucleus repulsion ($\hat{V}_{NN}$).

Nuclei move much more slowly than electrons because they are far heavier, so the Born-Oppenheimer approximation separates these motions to simplify the many-body SE. Electrons are assumed to instantaneously follow fixed nuclear positions, generating electronic energies that define potential energy surfaces (PESs) for nuclear motion. In practice, it anchors DFT simulations by fixing nuclei positions throughout electronic structure calculations.

2.3 Born-Oppenheimer Approximation

The Born-Oppenheimer (BO) approximation, introduced by Max Born and J. Robert Oppenheimer in 1927, forms the cornerstone of quantum chemistry by separating nuclear and electronic motions on account of their large difference in mass. This enables

practical calculations for complex molecular systems that would otherwise be computationally intractable. The approach solves the electronic structure for fixed nuclear positions to generate potential energy surfaces (PES), then treats nuclear dynamics on these surfaces, drastically reducing complexity while enabling accurate predictions of molecular geometries, reaction pathways, spectroscopic properties, and thermodynamic quantities. The standard BO equation is written as:

$$\Psi(r, R) = \Psi_{elec}(r; R)\Psi_{nuc}(R) \tag{2.6}$$

Here, $\boldsymbol{r}$ and $\boldsymbol{R}$ denote electronic and nuclear coordinates. $\Psi_{elec}(r; R)$ represents the electronic wavefunction with the nuclei held fixed at a particular geometry, and $\Psi_n(R)$ describes the motion of the nuclei. This approach first involves solving the electronic SE for a given nuclear configuration to generate potential energy surfaces, followed by treating the nuclear dynamics on these surfaces.

The electronic SE under the BO approximation is given by,

$$\widehat{H}_{elec}\Psi_{elec}(r;\ R) = \mathrm{E}_{elec}(R)\Psi_{elec}(r; R) \tag{2.7}$$

Where:

- $\widehat{H}_{elec}$ is the electronic Hamiltonian operator.
- $\mathrm{E}_{elec}(R)$ represents electronic energy.

This approximation greatly reduces the computational complexity of solving the many-body SE, making it feasible to treat realistic systems with many electrons and nuclei. As a result, it is widely employed in quantum chemistry calculations and molecular dynamics simulations, where accurate yet tractable descriptions of electronic and nuclear motion are essential.

2.4 The Hartree-Fock (HF) Approximation

The BO approximation exploits the mass disparity between nuclei and electrons, treating nuclear positions **R** as fixed parameters. This decouples the full molecular Hamiltonian into separate electronic and nuclear problems, yielding electronic energies $E_e(\boldsymbol{R})$ as PES for nuclear motion. Douglas Hartree introduced the self-consistent field (SCF) method in 1927 for atoms, using a mean-field approach inspired by semi-empirical Bohr model techniques from researchers like E. Fues and R. B. Lindsay. The

Hartree method treated electrons as independent particles in an average potential but ignored wavefunction antisymmetric.

$$\Psi(r) = \Psi_1(r_1) \cdot \Psi_2(r_2) \cdot \Psi_3(r_3) \cdot \ldots \cdot \Psi_n(r_n). \tag{2.8}$$

Slater and Fock (1930) demonstrated that Hartree's product wavefunction failed to satisfy the antisymmetric requirement for fermions, since swapping any two electrons produced no sign change as mandated by the Pauli principle. They introduced the Slater determinant as a replacement, which inherently ensures antisymmetric and generates a quantum exchange interaction in the effective one-electron potential. This advancement properly implemented the Pauli exclusion principle while capturing the Fermi hole phenomenon, where electrons of parallel spin naturally repel each other through quantum statistics. Thus, establishing the first rigorous mean-field description of multi-electron systems.

$$\Psi_{HF} = \frac{1}{\sqrt{N!}} \begin{bmatrix} \psi_{1\alpha}(1) & \psi_{1\beta}(1) & \ldots & \psi_{N\alpha}(1) \\ \psi_{1\alpha}(2) & \psi_{1\beta}(2) & \ldots & \psi_{N\alpha}(2) \\ \vdots & \vdots & \ddots & \vdots \\ \psi_{1\alpha}(N) & \psi_{1\beta}(N) & \ldots & \psi_{N\alpha}(N) \end{bmatrix} \tag{2.9}$$

In the above equation (2.9), the columns represent individual spin-orbitals evaluated at each electron coordinate, while the rows correspond to the coordinates of successive electrons. The determinant vanishes if any two spin-orbitals are identical, enforcing the Pauli's exclusion principle by preventing two electrons from occupying the same spin-orbital. Swapping the coordinates of two electrons is equivalent to exchanging two rows in the determinant's matrix, which reverses the sign of the determinant and thus guarantees that the wave function is antisymmetric in nature. The main limitation of the Hartree–Fock (HF) approximation is that it treats each electron as moving in an average field produced by the others and neglects instantaneous electron correlation. Correlation energy is usually defined as the difference between the exact (non-relativistic) energy of the system and the HF energy:

$$E_{correlation} = E_{exact} - E_{HF} \tag{2.10}$$

Sometimes, density functional theory (DFT) replaces the HF method. DFT includes both exchange and correlation effects through an approximate functional, giving a more balanced and accurate picture of electrons. Moreover, because DFT scales more efficiently with system size than correlated post-HF methods, it has become the method

of choice for studying large molecules, solids, and surfaces, while still providing a reasonable description of exchange and correlation effects.[2]

2.5 Density Functional Theory (DFT)

The DFT is a quantum mechanical computational method applied in physics, chemistry, and materials science to analyze the electronic structure, mainly the ground state (GS) of many-body systems like atoms, molecules, and condensed phases. DFT originated from early 20th-century attempts to streamline many-electron quantum mechanical computations, evolving from models like Thomas-Fermi. The theory gained its rigorous basis in 1964–1965 through Hohenberg-Kohn-Sham formulations, revolutionizing computational quantum chemistry. DFT is grounded in the Hohenberg-Kohn theorems (HK), establishing that the ground-state properties of a many-electron system are uniquely defined by its electron density alone, bypassing the need for the full many-body wavefunction.[3] This principle is operationalized through the Kohn-Sham (KS) equations, which map the interacting system onto a fictitious non-interacting reference via an effective potential comprising external, Hartree, and exchange-correlation terms. The BO approximation underpins these calculations by decoupling nuclear and electronic motion, justifying fixed nuclear positions during electronic structure determination. Established by the Hohenberg-Kohn theorems and Kohn-Sham framework, DFT has evolved from local density approximations to sophisticated hybrid functionals.[4–6]

The DFT methods are widely used across, physics, chemistry and materials science to predict the electronic structure and related properties of atoms, molecules, and solids. It is applied to study molecular geometries, reaction mechanisms, and reaction energies in chemistry, as well as to analyze adsorption, active sites, and reaction pathways in surface science and catalysis. Extensions such as time-dependent DFT are employed to model optical and spectroscopic properties. Owing to its favorable balance between accuracy and computational cost, DFT serves as a cornerstone for the development of machine-learning (ML) potentials and data-driven models, making it a key tool in the rational design of functional materials and devices.[7,8]

2.5.1 The Hohenberg-Kohn theorems

The Hohenberg–Kohn (HK) theorems, proposed by Hohenberg and Kohn in 1964, constitute the theoretical foundation of DFT. They showed that the electron density

$\rho(\boldsymbol{r})$ alone uniquely determined all ground-state properties of any interacting many-electron system, rather than requiring explicit knowledge of the full many-body wavefunction. The HK theorems consist of two fundamental statements that together justify using the electron density $\rho(\boldsymbol{r})$ as the basic variable in DFT.

(1) First HK Theorem

The first theorem states that, for a given pair interaction (electron–electron Coulomb term), the external potential $V_{ext}(\boldsymbol{r})$ is uniquely determined by the ground-state electron density $\rho(\boldsymbol{r})$, up to an additive constant. This means the density carries all the information needed to reconstruct the system's Hamiltonian. Since the Hamiltonian governs all ground-state properties, the electron density alone determines every ground state observable, such as energy, atomic forces, bond lengths, and magnetic moments. Thus, these properties can be derived directly from the electron density without solving the full many-electron wavefunction.

(2) Second HK Theorem

The second theorem introduces a variational principle in terms of the electron density. The second HK theorem introduces a universal energy functional $E[\rho]$ such that,

$$E[\rho] = T[\rho] + V_{ee}[\rho] + \int V_{ext}(r)\,\rho(r)dr \tag{2.11}$$

Where, $T[\rho]$ represents the kinetic energy of the electrons and $V_{ee}[\rho]$ is the electron-electron interaction energy, respectively. The theorem states that the true ground-state density $\rho(\boldsymbol{r})$, corresponding to the physical external potential $V_{ext}(\boldsymbol{r})$, minimizes this functional,

$$E[\rho'] \geq E[\rho_{GS}] \tag{2.12}$$

Where, $E[\rho']$ and $E[\rho_{GS}]$ represent the energy functional evaluated with a trial density ρ' and actual ground state energy, respectively. This variational principle is what renders DFT computationally tractable and forms the basis of all practical implementations of the method, ranging from Kohn–Sham DFT to modern ML schemes for approximating the exchange–correlation functional.

2.5.2 The Kohn-Sham equations

The Kohn–Sham (KS) equations were introduced in 1965 by Walter Kohn and Lu Jeu Sham in the University of California, San Diego, USA as a practical realization of the earlier HK framework for DFT. Kohn and Sham introduced a single-particle approximation in which they constructed a fictitious system of non-interacting electrons that move in an effective potential, chosen so that the resulting electron density matches that of the real, interacting system. This approach led to the now-famous Kohn–Sham equations, which take the form of a set of modified Schrödinger-like equations whose effective potential combines the external potential, the Hartree (classical Coulomb) term, and an exchange-correlation contribution.

In the KS approach, the total energy functional is expressed as a sum of several terms that are all written in terms of the electron density (and the KS orbitals used to compute it). The energy functional is expressed as:

$$E[\rho] = T_s[\rho] + E_{ext}[\rho] + E_H(\rho) + E_{XC}[\rho] \tag{2.13}$$

In the above equation (2.13),

- $T_s[\rho]$ represents the kinetic energy of the non-interacting reference system, computed exactly from the KS orbitals.
- $E_{ext}[\rho] = \int V_{ext}(r)\rho(r)dr$ is the electron–nuclear (external-potential) energy.
- $E_H(\rho) = \frac{1}{2}\iint \frac{\rho(r)\rho(r\prime)}{|r-r\prime|} drdr'$ is the classical Coulomb (Hartree) energy.
- $E_{XC}[\rho]$ represents the exchange-correlation energy, written as an approximate functional of the density.

The KS equations take the form of a set of single-particle Schrödinger-like equations given below,

$$\left[-\frac{\hbar^2}{2m}\nabla^2 + V_{\text{eff}}(r)\right]\varphi_i(r) = \varepsilon_i\varphi_i(r) \tag{2.14}$$

Where:

- $V_{eff}(r) = V_{ext}(r) + V_H(r) + V_{XC}(r)$ represent the effective potential.
- $V_H(r) = \int \frac{\rho(r\prime)}{|r-r\prime|} dr'$ is the Hartree potential.
- $V_{XC}(r) = \frac{\delta E_{XC}[\rho]}{\delta\rho(r)}$ is the exchange correlation potential.

- $\varphi_i(r)$ represents KS orbitals.

The total electron density is built from the KS orbitals as

$$\rho(r) = \sum_{i=1}^{N} |\varphi_i(r)|^2 \tag{2.15}$$

Here, N is the number of electrons. The KS equations are significant because they convert the abstract HK energy functional into a practical, orbital-based framework in which the interacting many-electron problem is replaced by a set of single-particle equations for non-interacting electrons that yield the same density. This enables efficient, widely applicable DFT calculations across physics, chemistry, and materials science.[9]

2.5.3 Exchange-Correlation approximations

Exchange-correlation (XC) approximations provide the specific formulas used in Kohn-Sham DFT method to estimate the elusive exchange-correlation energy functional $E_{XC}[\rho]$. Since no exact analytical expression for $E_{XC}[\rho]$ exists, every practical DFT calculation relies on one of these approximations to generate the XC potential and carry out self-consistent Kohn-Sham iterations. The choice of XC approximation directly controls accuracy, robustness, and, in some cases, even the qualitative predictions of a DFT calculation. Different XC functionals describe electron exchange and correlation in distinct ways, which influences how well the method reproduces bond lengths, reaction barriers, band gaps, magnetic ordering, and other important physical properties.[10] The XC approximations in Kohn–Sham DFT are usually classified into several broad families, arranged in order of increasing complexity and, typically, higher accuracy. These families are provided below.

(a) Local density approximation (LDA)

The Local density approximation (LDA) is the simplest and most used approximation for the exchange-correlation (XC) energy functional in Kohn-Sham DFT. It assumes that the XC energy at each point in space depends solely on the local electron density at that point, neglecting density gradients, higher derivatives, and the Kohn-Sham (KS) orbitals themselves. LDA models the complex, inhomogeneous electron system as being locally similar to a homogeneous electron gas (HEG) at every point in space. The

XC energy density at a point with density $\rho(r)$ is taken to be equal to the XC energy per particle of a HEG at the same density. The LDA XC energy is written as,

$$E_{XC}^{LDA}[\rho] = \int \rho(r)\varepsilon_{XC}^{HEG}(\rho(r))\, dr \tag{2.16}$$

Here, $\varepsilon_{XC}^{HEG}(\rho(r))$ is the XC energy per particle of the uniform electron gas at density ρ. Whereas $\rho(r)$ represents the local density at position at r. LDA offers a computationally efficient starting point for XC functionals, allowing rapid calculations for large systems such as bulk solids and simple metals. It accurately describes the uniform electron gas, delivering reasonable total energies and structural trends due to error cancellation, typically overestimating the exchange part while underestimating the correlation part. LDA also forms the basis for more advanced functionals like GGAs and hybrids and can be easily extended to magnetic systems through the local spin-density approximation (LSDA). The LDA in DFT relies on the XC energy depending solely on the local electron density, mimicking a uniform electron gas. This ignores density gradients and non-local effects, leading to key shortcomings. LDA overbinds atoms and molecules, producing overly short bond lengths, excessive binding energies, and slightly underestimated solid volumes. It drastically underestimates band gaps in both the semiconductors and insulators, and it mishandles Rydberg levels and ionization potentials, and fails to account for long-range van der Waals (vdW) interactions, making it unsuitable for layered materials or physisorbed adsorbates. Self-interaction errors worsen its performance on anions and electron-rich systems. For strongly correlated materials with localized ***d*** or ***f*** electrons (like transition-metal oxides), LDA often predicts incorrect magnetism or insulating states. Overall, it excels less for molecules and surfaces than bulk solids, so GGA or hybrid functionals are typically needed for reliable chemical and electronic structure predictions. While LDA offers computational efficiency ideal for initial DFT studies of bulk solids, its limitations in band gaps, dispersion, and strong correlations demand advanced functionals like GGAs or hybrids for accurate predictions.

(b) Generalized gradient approximation (GGA)

Generalized gradient approximation (GGA) functionals go beyond the LDA by incorporating the gradient of the electron density into the XC functional, enabling a

more accurate description of density inhomogeneities in realistic systems such as molecules and solids that cannot be captured by the purely local assumption of LDA.

The XC energy in GGA is written as,

$$\mathrm{E_{XC}^{GGA}}[\rho] = \int \rho(\mathrm{r})\, \varepsilon_{\mathrm{XC}}^{\mathrm{GGA}}[\rho(r), \nabla\rho(r)]\, \mathrm{d}r \qquad (2.17)$$

Here, ε_{XC}^{GGA} represents the exchange-correlation energy density, which depends on both the local electron density $\rho(r)$ and the magnitude of its gradient $|\nabla\rho(r)|$. GGA addresses electron density non-uniformity more effectively than LDA by incorporating the density gradient $|\nabla\rho(r)|$ into the exchange-correlation functional, explicitly modeling spatial density variations that LDA overlooks. Widely used non-empirical GGAs include Perdew–Burke–Ernzerhof (PBE) functional, which enhances the accuracy to estimate the lattice constants and cohesive energies in solids. PBEsol is optimized for accurate equilibrium geometries in solids, while revPBE and RPBE serve as more repulsive forms suited for surface chemistry and catalysis. WC and AM05 are constructed to improve the description of solid-state properties by incorporating gradient-expansion constraints, while HTBS is specifically designed to yield more accurate predictions of semiconductor band gaps. Empirical or semi-empirical GGAs comprise BLYP, favored in molecular quantum chemistry for reliable thermochemistry, B88 exchange frequently incorporated into hybrids like B3LYP, and the HCTH family (e.g., HCTH120, HCTH147) parameterized against atomization energies and small-molecule data. GGAs provide semi-local efficiency and a significant step up from the LDA, but their limitations in strong correlation, dispersion forces, and non-local exchange are effectively addressed by advancing to meta-GGAs and hybrid functionals.

(c) Hybrid functionals

Hybrid functionals in the DFT represent sophisticated approximations that boost electronic structure predictions by incorporating a portion of exact HF exchange into GGA-based XC terms. This approach reduces self-interaction errors and corrects the band gap underestimation typical of LDA/GGA functionals, resulting in superior structural, electronic, and optical properties despite greater computational expense.

The general form of hybrid functional in DFT for the exchange-correlation energy E_{XC} is typically,

$$E_{\mathrm{XC}}^{\mathrm{Hybrid}} = aE_X^{HF} + (1-a)E_X^{DFT} + E_C^{DFT} \quad (2.18)$$

Here,

- E_X^{HF} is the exact Hartree-Fock exchange.
- E_X^{DFT} is the semi-local approximation (e.g., GGA like PBE).
- E_C^{DFT} represents the DFT correlation part.
- $\boldsymbol{a}$ is a mixing parameter.

Hybrid functionals mitigate self-interaction errors, providing more accurate electronic band gaps (E_g), ionization potentials, and reaction barriers essential for molecular spectroscopy, catalysis, and materials design. They incorporate exact HF exchange to better capture charge transfer, dispersion interactions, and open-shell systems. Although the non-local exchange increases computational expense, their optimal balance of precision and practicality renders them essential for simulations in solid-state physics, chemistry, and biology. Hybrid functionals in the DFT include global hybrid functionals such as B3LYP (combining Becke's GGA exchange with LYP correlation), PBE0 (built on the PBE functional), and BHandHLYP. They also comprise range-separated hybrids like HSE06 (which uses short-range Hartree–Fock exchange), CAM-B3LYP, and ωB97X-D, in which the fraction of HF exchange varies with electron distance to better describe charge-transfer processes and solid-state systems. In addition, meta-hybrid GGAs such as the M06 family (M06, M06-2X, and M06-HF) incorporate the kinetic energy density, leading to improved accuracy for main-group chemistry and transition-metal compounds.[3,5,10]

B3LYP functional

B3LYP (Becke, 3-parameter, Lee–Yang–Parr) is a widely used hybrid XC functional (~20% exact HF exchange) in Kohn-Sham DFT, combining it with GGA-type semi-local exchange (Becke 88) and correlation (LYP) terms. This hybrid approach enhances accuracy for numerous molecular properties over purely local or GGA functionals. The general form of the B3LYP functional is given below,

$$E_{XC}^{B3LYP} = E_{XC}^{LSDA} + a_0(E_X^{HF} - E_X^{LSDA}) + a_X\Delta E_X^{B88} + a_C\Delta E_C^{LYP} \quad (2.19)$$

Where:

- E_{XC}^{LSDA} is the XC energy from the LSDA.

- E_X^{HF} is the exact HF exchange energy.
- ΔE_X^{B88} represents the gradient correction to exchange energy by Becke (1988).
- ΔE_C^{LYP} is the gradient correction to correlation energy by Lee–Yang–Parr.
- $a_0 = 0.20$, $a_X = 0.72$, and $a_C = 0.81$ are empirical fitting parameters optimized against experimental data.

B3LYP remains one of the most popular DFT functionals in quantum physics, materials science and chemistry, offering strong performance for molecular geometries, vibrational frequencies, electronic properties of crystals, and bandgap predictions at a reasonable computational cost. It is widely available in standard software packages like Gaussian, CRYSTAL, VASP, ORCA, and Q-Chem, frequently serving as a benchmark for new methods or validation studies. It has some weaknesses, such as inadequate handling of non-covalent interactions and long-range charge-transfer excitations, prompting the use of corrected variants like B3LYP-D3 (with dispersion) or CAM-B3LYP (range-separated hybrid).[11]

In the present thesis, the B3LYP exchange–correlation functional has been used within the Kohn–Sham DFT framework to investigate the electronic structure and energetics of the systems under study. In the context of ORR research, B3LYP provides reliable geometries and electronic structures for catalytically active sites, while also offering reasonable descriptions of reaction intermediates and their relative energies. It further facilitates a detailed analysis of charge transfer and orbital interactions along the ORR pathway. Furthermore, B3LYP is extensively benchmarked and well documented in the literature, which enables direct comparison with earlier computational studies on ORR catalysts and supports the validation of the present findings.

(d) van der Walls (vdW) correction

van der Waals (vdW) forces, named after Dutch physicist Johannes Diderik van der Waals (1837–1923) are much more important during the computations to account the weak interactions. The vdW forces represent weak intermolecular attractions between neutral atoms or molecules. They arise from transient fluctuations in the electron distribution that generate temporary dipoles. vdW corrections, empirical or semi-empirical additions to the standard DFT functionals such as LDA, GGA, or hybrids like B3LYP, are used to capture the long-range London dispersion forces that result from correlated electron fluctuations between non-bonded atoms. Nevertheless,

conventional DFT functionals, including the LDA and GGA, inadequately describe these long-range vdW interactions. Being local or semi-local approximations to the XC energy, they overlook the nonlocal, long-range electron correlation components essential to the vdW forces.

DFT-D method

DFT-D (dispersion-corrected density functional theory) method enhances standard DFT functionals by adding an empirical dispersion term, effectively addressing their limitations in capturing long-range van der Waals (vdW) interactions. In the DFT-D approach, the total energy is given by:

$$E_{total} = E_{KS-DFT} + E_{disp} \tag{2.20}$$

Where:

- E_{KS-DFT} is the standard DFT energy obtained from the Kohn-Sham calculation.
- E_{disp} is the empirical dispersion correction term.

The dispersion term is given by,

$$E_{disp} = -\frac{1}{2}\sum_{A\neq B}^{atoms}\sum_{n=6,8} S_n \frac{C_n^{AB}}{R_{AB}^n} f_{damp,6}(R_{AB}) \tag{2.21}$$

Here,

- C_n^{AB} is the dispersion coefficient specific to atoms pair $\boldsymbol{A}$ and $\boldsymbol{B}$.
- S_n is the global scaling factor.
- R_{AB}^n is the distance between atoms $\boldsymbol{A}$ and $\boldsymbol{B}$.
- $f_{damp,6}(R_{AB})$ is the damping function to correct for short-range forces.

DFT-D3 method

DFT-D3 is an empirical dispersion correction DFT method developed by Stefan Grimme to address the deficiency of standard DFT functionals in capturing weak long-range London dispersion (vdW) interactions, which are crucial for accurately modelling non-covalent interactions like those in molecular crystals and adsorption processes. In DFT-D3, the two-body term provides the main dispersion correction by describing pairwise London interactions between atoms, which decrease with the inverse sixth

power of distance. The interaction strength is adjusted using environment-dependent C_6 coefficients, while damping functions prevent overcorrection at short distances. The optional three-body term accounts for Axilrod–Teller–Muto (ATM) interactions among three atoms, which can contribute about 10–20% of the total dispersion energy in dense systems such as clusters and solids. The total dispersion correction is the sum of two- and three-body terms:

$$E_{disp}^{D3} = E^{(2)} + E^{(3)} \tag{2.22}$$

The two-body dispersion term includes both C_6 and C_8 coefficients, which account for dipole-dipole and dipole-quadrupole interactions, respectively.

$$E^{(2)} = -\frac{1}{2}\sum_{A}^{atoms}\sum_{B<A}^{atoms}\left[\left(\frac{C_6^{AB}}{R_{AB}^6}\right)f_{dmp,6}(R_{AB}) + \left(\frac{C_8^{AB}}{R_{AB}^8}\right)f_{dmp,8}(R_{AB})\right] \tag{2.23}$$

The three-body term accounts for non-additive Axilrod-Teller-Muto (ATM) effects through triplet interactions.[12–14]

$$E^{(3)} = -\sum_{A}^{atoms}\sum_{B<A}^{atoms}\sum_{C<B}^{atoms} 16\,.\,C_9^{ABC}\,.\,R_{ABC}^{-9}\,.\,f_9^d(R_{ABC},\theta_{ABC}) \tag{2.24}$$

Where:

- R_{AB} is the interatomic distance between atoms A and B.
- C_6^{AB} and C_8^{AB} are the dispersion coefficient.
- $C_9^{ABC} = -\sqrt{C_6^{AB}C_6^{AC}C_6^{BC}}$,
- R_{ABC} represents the geometric mean of the triangle sides R_{AB}, R_{BC} and R_{CA}.
- θ_A , θ_B, θ_C are the internal angles of the triangle formed by atoms A, B, and C.

The damping functions prevent overestimation of dispersion effects at short distances and are defined in equations (2.25) and (2.26). They ensure a smooth transition to zero correction as atoms approach equilibrium bonding distances, thereby preventing double-counting of short-range electron correlation already captured by the underlying DFT exchange-correlation functional.

$$f_{dmp,n}\,(R_{AB}) = \frac{S_n}{1 + 6\left(\frac{R_{AB}}{S_{r,n}R_{0,AB}}\right)^{-\alpha_n}} \tag{2.25}$$

$$f_9^d(R_{ABC}, \theta_{ABC}) = \frac{3\ cos\ \theta_A\ cos\ \theta_B\ cos\ \theta_C + 1}{1 + 6\left(\frac{R_{ABC}}{S_{r,n}R_{0,AB}}\right)^{-\alpha_n}} \quad (2.26)$$

DFT-D3 excels in DFT calculations by systematically accounting for absent long-range dispersion interactions across nearly all standard functionals. This markedly enhances accuracy for non-covalent systems such as molecular crystals and adsorption processes while maintaining high computational efficiency. In this thesis, we have employed DFT-D3 dispersion corrections to accurately model ORR on carbon nanotubes (CNTs) and transition metal dichalcogenides (TMDs), along with associated adsorption processes.

2.6 Softwares

This thesis employs several key software programs and packages essential to achieve its objectives. Each category includes specialized applications tailored for tasks such as electronic structure calculations and data analysis, ensuring robust and reproducible results throughout the study. These tools are categorized as follows:

2.6.1 CRYSTAL 17

CRYSTAL began in 1976 within the theoretical chemistry group at the University of Torino, Italy. Later it advanced through sustained collaboration with V. R. Saunders at the UK's SERC Daresbury Laboratory as an *ab initio* quantum chemistry code for periodic systems towards condensed matter physics. The first public release, CRYSTAL88, came in 1988.[15] The code evolved through major versions (e.g., CRYSTAL92, CRYSTAL95, and CRYSTAL98) with pivotal advancements by Professor Roberto Dovesi and his group, expanding its capabilities to crystals, slabs, polymers, and molecules using Gaussian-type orbital (GTO) basis sets to explore the modern physics problems. CRYSTAL supports a broad array of periodic DFT approximations, encompassing semi-local functionals such as local, gradient-corrected, and meta-GGA types like SCAN/r^{2}SCAN, along with hybrid HF-DFT functionals (e.g., B3LYP, PBE0, HSE06), user-defined hybrids, collinear/non-collinear spin DFT, and dispersion corrections (DFT-D2/D3). The code also facilitates calculations of elastic tensors under applied pressure, phonon frequencies, piezoelectric properties, and thermo-elastic behavior through quasi-harmonic approximations to investigate various properties of solids, liquids and gaseous systems. The program utilizes GTO basis sets

with all electron or pseudopotential methods, with internal libraries such as POB-TZVP covering most elements and dedicated sets for lanthanides/actinides that include f/g orbitals. It fully exploits crystal symmetry, which includes all 230 space groups, rod groups, and helical symmetry up to order 48 along with point groups for molecules, enabling efficient calculations for periodic structures ranging from 3D crystals to 0D clusters.[12,15,16] CRYSTAL includes automated geometry generation tools for slabs from (hkl) faces, single-wall and multi-wall nanotubes, nanoparticles, defects, and supercells. The code efficiently computes essential properties including electron density maps, electrostatic potentials, electronic band structures, dynamic structure factors, density of states (DOS), and Bader charge analysis, critical for modeling ORR intermediates.

In this thesis, the CRYSTAL17 software was employed for investigating the ORR and performing geometry optimizations of the associated materials under study. It enables the DFT calculations with hybrid functionals (e.g., B3LYP) and Gaussian-type orbital (GTO) basis sets to model ORR intermediates, determine adsorption energies, and examine electronic properties, including electronic band structure and total density of states (DOS).

CRYSTAL17 Input File: This section presents an example input file structure for pure CNT.

Pure CNT	# Title Line
CRYSTAL	# Dimensionality of the system
0 0 0	# Crystallographic information (3D only)
176	# Symmetry group number
24.7510 2.4595	# Lattice Parameters
6	# Number of atoms in the asymmetric unit
6 0.28467 0.14436 0.25000	
6 0.25334 0.23912 0.25000	
6 0.21656 0.26830 0.25000	# Atomic numbers and coordinates
6 0.28247 0.17186 0.75000	
6 0.26670 0.21957 0.75000	

```
6    0.19365   0.27753   0.75000
```

```
OPTGEOM
FULLOPTG                                # Keywords for geometry optimization
MAXCYCLE
800
ENDOPT
END
```

```
6 8
0 0 6 2.0 1.0
13575.349682 0.00022245814352
2035.2333680 0.00172327382520
463.22562359 0.00892557153140
131.20019598 0.03572798450200
42.853015891 0.11076259931000
15.584185766 0.24295627626000
0 0 2 2.0 1.0
6.2067138508 0.41440263448000
2.5764896527 0.23744968655000           # Basis sets for non-equivalent atoms
0 0 1 0.0 1.0
0.4941102000 1.00000000000000
0 0 1 0.0 1.0
0.1644071000 1.00000000000000
0 2 4 2.0 1.0
34.697232244 0.00533336578050
7.9582622826 0.03586410909200
2.3780826883 0.14215873329000
0.8143320818 0.34270471845000
0 2 1 0.0 1.0
0.5662417100 1.00000000000000
0 2 1 0.0 1.0
0.2673545000 1.00000000000000
0 3 1 0.0 1.0
0.8791584200 1.00000000000000
```

99 0	
# Optional keywords	
END	# End of basis set input section
SHRINK 0 16 4 4 8	# Reciprocal space integration parameters
# Optional keywords	
END	# End of SCF input section

2.6.2 Vienna *Ab initio* Simulation Package (VASP)

Vienna *Ab Initio* simulation package (VASP) stands as a leading commercial package for first-principles atomic-scale materials modeling towards condensed matter physics. Developed from the early 1990s in the University of Vienna (initially as VAMP) primarily by Prof. Georg Kresse and collaborators [17], its major releases (VASP.5, VASP.6) introduced GPU acceleration, advanced RPA/GW methods, and machine-learning force fields.[18] These advancements have established VASP as the standard tool across more than 1400 global research groups in the materials science and solid-state physics. VASP is a plane-wave DFT code that solves the Kohn-Sham equations self-consistently using a basis set of plane waves and periodic boundary conditions. VASP implements DFT and hybrid-DFT (e.g., HSE06), as well as many-body perturbation theory via GW and the Bethe-Salpeter equation (BSE). The XC functional is selected via the GGA, METAGGA, or LHFCALC tags in the INCAR file. LDA, PBE, PBEsol, SCAN, and r^2SCAN are among the most used functionals towards solid-state physics. All wave functions are expanded in a plane-wave basis up to a kinetic energy cutoff ENCUT (in eV). The convergence of results with respect to ENCUT must always be checked. The rule of thumb is to use 1.3x the largest ENMAX in the POTCAR files. Core electrons are treated via the Projector Augmented Wave (PAW) method, which reconstructs all-electron-like wave functions near the nucleus. PAW potentials are stored in the POTCAR file.

In VASP, the Brillouin zone is sampled using a Monkhorst-Pack grid defined in the KPOINTS file. For metals, smearing methods (Methfessel-Paxton, Fermi) are used (ISMEAR $\geq$ 0); for insulators/semiconductors, tetrahedron methods or Gaussian smearing (ISMEAR = 0) are appropriate. Convergence of total energy with k-mesh

density must be tested. VASP iterates the charge density and wave functions to self-consistency. The electronic minimization algorithm is selected with ALGO (Normal = RMM-DIIS, Fast = blocked Davidson, All = conjugate gradient). Convergence threshold is set by EDIFF (typically 10-5 to 10-6 eV). Charge density mixing is controlled by AMIX, BMIX, and related tags. Atomic positions are relaxed using forces derived from the Hellmann-Feynman theorem. The relaxation algorithm is set by IBRION (2 = conjugate gradient, 1 = quasi-Newton RMM). Convergence is controlled by EDIFFG: if negative, it refers to the maximum force (e.g., −0.01 eV/Å); if positive, it refers to the total energy change. Weak vdW interactions absent from the standard DFT can be added via DFT-D2, DFT-D3 (Grimme), DFT-D3 (BJ), or the many-body dispersion (MBD) method using IVDW in INCAR. Collinear spin is enabled with ISPIN = 2; non-collinear magnetism and spin-orbit coupling (SOC) require LSORBIT = .TRUE. and the appropriate PAW potentials with SOC included. VASP parallelizes over k-points (KPAR), bands (NCORE/NPAR), and plane-wave coefficients. Efficient scaling on HPC clusters requires tuning both KPAR and NCORE for the specific system size.

VASP excels in the DFT calculations due to its superior efficiency and scalability. It routinely handles total-energy optimizations and molecular dynamics for systems containing thousands of atoms, making it perfect for simulating complex materials in electrocatalysis research. VASP delivers superior parallel performance on HPC clusters, lower memory usage, and robust handling of periodic boundary conditions for slabs and supercells, making it the preferred choice for reproducible, high-quality results in materials science research. In this thesis, the VASP software was used to design the catalysts and investigate the ORR mechanisms with the geometry optimizations of the associated studied materials. It enables the GGA calculations with plane-wave basis sets and periodic boundary conditions (PBE or similar functionals) to model the ORR intermediates, determine adsorption energies, and examine electronic properties, including total density of states (DOS).

VASP Input File (INCAR) : Example settings for 2D monolayer $LaNiO_3$ structural relaxation

SYSTEM	# 2D monolayer $LaNiO_3$
ISTART = 0	# 0 = new wavefunctions, 1 = restart
ICHARG = 2	# 2 = atomic charge (no CHGCAR restart)
ISMEAR = 0	# 0 = Gaussian smearing
SIGMA = 0.05	# 0.05 eV for smearing width
ENCUT = 500	# Plane-wave cutoff in eV
EDIFF = 1E-6	# Ionic energy convergence
EDIFFG = -0.01	# Force convergence (eV/A)
IBRION = 2	# Ionic relaxation (conjugate gradient)
NSW = 200	# Max ionic steps
ISIF = 2	# Relax ions only, keep in plane cell fixed (typically for 2D)
LWAVE = .TRUE.	# Write WAVECAR
LCHARG = .TRUE.	# Write CHGCAR
# Optional keywords	# Additional keywords (parameters that can be included or omitted)

2.7 Basis Set

In the computations, a basis set is a predefined collection of mathematical functions (basis functions) used to expand and approximate the electronic wavefunction or KS orbitals, transforming the intractable many-electron problem into a tractable set of algebraic equations. They discretize the continuous space of electron wavefunctions into a finite, solvable form for the quantum software like VASP or CRYSTAL. Without basis sets, calculations would be impossible on computers due to the infinite-dimensional problem. A basis function approximates the shape and characteristics of atomic orbitals (AOs). The molecular orbital (Φ_i) is generally expressed as a linear combination of M atomic basis functions $\chi_a(r)$:

$$\Phi_i(r) = \sum_{\alpha}^{M} C_{\alpha i}\chi_\alpha(r) \tag{2.27}$$

Where $\Phi_i(r)$, $\chi_\alpha(r)$ and $C_{\alpha i}$ represent the molecular orbital, basis function, and expansion coefficient, respectively. If M is infinite, the molecular orbital is expressed in terms of a complete (infinite) basis set. In this limit, the linear combination of atomic orbitals (LCAO) expansion exactly describes single-particle states using orthonormal functions like plane waves or infinite GTOs.

Unfortunately, complete basis sets involve an infinite number of basis functions and are thus impractical for real computational work. In practice, a finite basis set is employed to represent molecular orbitals in electronic structure calculations. Smaller basis sets struggle to accurately represent the shape, energy, and nodal structure of molecular orbitals. This limitation introduces significant errors in computed properties, including total and orbital energies, as well as derived values like reaction barriers and binding energies. Minimal or small basis sets may qualitatively capture bonding features but often fail to converge observables to the complete-basis-set (CBS) limit, whereas larger, systematically constructed basis sets (e.g., correlation-consistent families) progressively improve the representation of molecular orbitals at the cost of increased computational effort.[19,20] Slater-type orbitals (STO) and Gaussian-type orbitals (GTO) are the two main functional forms used for atomic-orbital-like basis functions in quantum mechanical calculations.

2.7.1 Slater-type orbitals (STO)

Slater-type orbitals (STOs) are physically accurate basis functions that mimic real atomic orbitals through exponential decay, excelling at describing electron behavior both near and far from the nucleus. However, because they are computationally difficult to process, most modern software approximates them by combining several Gaussian-type orbitals (GTOs) to balance accuracy with speed. The functional form of STOs is expressed as:

$$S_{\xi nlm}(r,\theta,\phi) = N\, Y_{l,m}(\theta,\phi) r^{n-1} e^{-\xi r} \tag{2.28}$$

Where, N is the normalization constant, $Y_{l,m}(\theta,\phi)$ represents the spherical harmonic functions, and n represents the principal quantum number. Nevertheless, multi-center integrals over STOs lack closed analytical forms, making them computationally

expensive and impractical for large systems. For this reason, modern quantum-chemistry and DFT programs avoid STOs as primitives and instead approximate them with linear combinations of GTOs, retaining much of their physical accuracy while gaining analytical and computational efficiency.

2.7.2 Gaussian-type orbitals (GTO)

Gaussian-type orbitals (GTOs) can be expressed in either cartesian or spherical polar coordinates. The mathematical definition of GTOs is given by:

$$G_{\xi,l_x,l_y,l_z} = N\, X^{l_x} Y^{l_y} Z^{l_z} e^{-\xi r^2} \tag{2.29}$$

$$G_{\xi,n,l,m}(r,\theta,\phi) = N\, Y_{l,m}(\theta,\phi) r^{2n-2-1} e^{-\xi r^2} \tag{2.30}$$

Where:

- G_{ξ,l_x,l_y,l_z} represents the Gaussian primitive orbital labelled by an exponent ξ, and angular-momentum indices l_x, l_y, l_z.
- N is the normalization constant that ensures $\int |G|^2$ dV = 1.
- ξ is the Gaussian exponent, larger ξ means a more tightly localized orbital.
- $r^2 = X^2 + Y^2 + Z^2$ is the squared distance from the center of the Gaussian.
- $G_{\xi,n,l,m}(r,\theta,\phi)$ is a Gaussian basis function.
- $Y_{l,m}(\theta,\phi)$ is the spherical harmonic giving the angular part of the orbital where l is the orbital angular-momentum and m is its projection along the z-axis.
- $e^{-\xi r^2}$ is the Gaussian radial decay that makes the orbital vanish quickly at large r.

GTOs form a widely used family of basis sets in quantum chemistry and electronic structure theory. Each GTO consists of a Gaussian function centered at an atomic position. In contrast to the STOs, GTOs exhibit slower decay near the nucleus and faster drop-off at long range, deviating somewhat from the precise asymptotic form of actual atomic orbitals. Nevertheless, their computational efficiency stands out, as the product of two GTOs on separate centers reduces to a single Gaussian at a shifted position, streamlining multi-center overlap and repulsion integral computations. This key advantage drives the widespread adoption of GTO basis sets in contemporary quantum chemistry and DFT programs, despite needing more functions than STOs for equivalent precision. GTOs are organized into basis set families such as split valence, polarized,

and diffuse variants that progressively improve descriptions of bonding, dispersion forces, and electronic excitations, making them the foundation of standard electronic structure calculations.

2.7.3 Properties of basis functions

Gaussian basis functions excel due to their nuclear localization, which accurately captures atomic electron densities, and their angular momentum properties (*s*-, *p*-, *d*-, etc.), enabling precise modeling of bonding, antibonding, lone pairs, and polarization effects. They provide variational flexibility through adjustable primitives, contraction schemes, and polarization/multi-zeta expansions, allowing systematic improvement in wavefunction quality and energies. GTOs exhibit rapid exponential decay at long range superior to polynomials for bound states, though diffuse functions are crucial for anions, Rydberg states, and dispersion interactions. Their computational efficiency stems from the Gaussian product theorem, where the product of two Gaussians yields a Gaussian sum, accelerating two-electron repulsion integral evaluation in modern quantum chemistry codes. Normalization and near-orthogonality yield an overlap matrix close to the identity, promoting SCF stability and obviating explicit orthogonalization.

2.7.4 Classification of basis set

(a) Minimal basis set: A minimal basis set in quantum chemistry provides the smallest complete description of an atomic electron configuration by assigning exactly one basis function per occupied atomic orbital in the neutral atom's ground state (e.g., a single *1s* function for hydrogen, *1s* and *2s* for lithium, or *1s*/*2s*/*2p* for carbon) ensuring the correct number of molecular orbitals for electron occupancy. Common examples include STO-3G and STO-6G, where STOs are approximated by 3 or 6 Gaussians, respectively, offering extremely fast computations ideal for large systems or initial geometry optimizations.[12] While advantageous for computational speed, minimal basis sets lack radial flexibility needed for accurate bonding, polarization, and correlation effects, often yielding energies 1-10 eV too high compared to larger double-zeta or triple-zeta sets.

(b) Split valence basis Set: A split-valence basis set in quantum chemistry employs a minimal basis for core orbitals (one function each) but splits valence orbitals into two or more basis functions. This allows valence orbitals to flexibly contract or expand during bonding, enhancing accuracy for geometries, energies, and reaction barriers at a

reasonable computational expense relative to larger basis sets. Pople-style notations (developed by Prof. John Pople's group) like 6-31G and 3-21G exemplify this approach, with a double-zeta description for valence regions and minimal core treatment.[12]

(c) Diffuse basis Set: A diffuse basis set in quantum physics and chemistry is a basis that includes additional, loosely localized (low-exponent) Gaussian functions, known as diffuse functions. They are specifically designed to describe the long-range, low-density tails of atomic orbitals that extend far from the nucleus. These functions are especially important for accurately modeling anions, excited and Rydberg states, and weakly bound (non-covalent) complexes, where the electron density is much more diffuse than in a typical neutral ground-state molecule. Such diffuse basis sets are commonly indicated by a plus sign in Pople-type notations (e.g., 6-31+G or 6-31++G).

(d) Double-zeta basis set: Double-zeta basis sets improve upon minimal basis sets by representing each atomic orbital with two basis functions. This leads to more accurate electron distributions, molecular geometries, and relative energies than minimal sets, while remaining computationally affordable for routine geometry optimizations and exploratory calculations. Typical examples include split-valence double-zeta bases such as 6-31G and 6-31G*, as well as the widely used DFT-oriented basis set, def2-SVP (Split-Valence Polarized), which combines double-zeta quality for valence orbitals with polarization functions to systematically improve the description of bonding and related polarization effects.

(e) Triple-zeta basis Set: A triple-zeta (TZ) basis set in quantum chemistry is characterized using three basis functions (usually contracted GTOs) for each atomic orbital, in contrast to the single function of minimal basis sets or the two functions in double-zeta descriptions. This increased flexibility enables atomic orbitals to adjust their shape, size, and spatial distribution more effectively under bonding, polarization, or charge-transfer conditions, thereby delivering improved accuracy for molecular geometries, electronic energies, and reaction energetics relative to smaller basis sets, while demanding higher computational resources. Triple-zeta basis sets are widely adopted in high-precision quantum-chemical studies, with common examples including split-valence TZ bases such as 6-311G, correlation-consistent families like cc-pVTZ, and polarized triple-zeta sets such as TZVP (Triple-Zeta Valence with Polarization).

These basis sets systematically enlarge the one-particle basis to better capture electron correlation and polarization effects in molecular systems.[12]

(f) Effective core potential (ECP) basis set: An effective core potential (ECP) basis set approximates the inner-core electrons of a heavier atom with a parametrized potential while explicitly representing only the valence electrons with a basis set. This reduces the computational cost for heavy elements such as transition metals and lanthanides, mitigates basis-set collapse, and often includes built-in relativistic corrections. ECPs are typically used in mixed-basis setups, in which heavy atoms are described with ECP-valence basis sets like LANL2DZ or SDD and lighter atoms with conventional all-electron basis sets such as 6-31G or def2-SVP, thereby maintaining a favorable trade-off between accuracy and efficiency in quantum-chemical simulations.

2.8 Instruments and Software Tools

In our research, we employed the following instruments and software tools.

- High performance computing (HPC) system
- Software packages (CRYSTAL 17 and VASP)
- Computer workstation
- Visualization and analysis software such as VESTA and Materials Studio, high-quality graphics software (Inkscape), and software for visualizing data trends (Gnuplot) were employed.
- Resources include access to library databases and printing facilities.

Table 2.1 presents a comparison of the computational methods, software codes, exchange-correlation functionals, dispersion corrections, and basis sets employed in the four studies. It provides a consolidated overview of the theoretical framework used throughout this thesis.

Table 2.1: *Comparison of the computational methods, software codes, exchange-correlation functionals, dispersion corrections, and basis sets used in the four studies.*

Chapter	System	Code/Software	Functional & Dispersion	Basis Set/Pseudopotentials
Chapter 1	2D Monolayer $LaNiO_3$	VASP	PBE-D3 (Grimme's D3)	• PAW_PBE pseudopotentials (La_GW, Ni_GW, O_GW)
Chapter 2	CoPt@CNT	CRYSTAL17	B3LYP-D3 (Grimme's D3)	• TZVP Gaussian-type basis set (C_pob_TZVP_2012, Co_pob_TZVP_rev2, Pt_pob_TZVP_rev2 for C, Co and Pt atoms respectively.)
Chapter 3	FeCe@CNT	CRYSTAL17	B3LYP-D3 (Grimme's D3)	• TZVP Gaussian-type basis set (Fe_pob_TZVP_2012 and C_pob_TZVP_2012 for Fe and C atoms respectively.) • Effective Core Potential (Ce_ECP_Meyer_2009 for Ce atom)
Chapter 4	Mo Defective 2D Monolayer $MoTe_2$	CRYSTAL17	B3LYP-D3 (Grimme's D3)	• Mo_SC_HAYWSC-311(d31)G_cora_1997 for Mo atom • TZVP Gaussian-type basis sets for Te, O and H atoms

2.9 References

[1] P. Echenique, J.L. Alonso, A mathematical and computational review of Hartree–Fock SCF methods in quantum chemistry, Mol. Phys. 105 (2007) 3057–3098.

[2] N. Argaman, G. Makov, Density functional theory: An introduction, Am. J. Phys. 68 (2000) 69–79.

[3] P. Geerlings, F. De Proft, W. Langenaeker, Conceptual Density Functional Theory, Chem. Rev. 103 (2003) 1793–1874.

[4] C.J. Cramer, Essentials of Computational Chemistry : Theories and Models, John and Sons, Chichester (2002).

[5] R.O. Jones, Density functional theory: Its origins, rise to prominence, and future, Rev. Mod. Phys. 87 (2015) 897–923.

[6] E. Engel, R.M. Dreizler, Density functional theory. An advanced course, Springer, 2025.

[7] M.A.L. Marques, E.K.U. Gross, Time-Dependent Density Functional Theory, Annu. Rev. Phys. Chem. 55 (2004) 427–455.

[8] F.M. Bickelhaupt, E.J. Baerends, Kohn-Sham Density Functional Theory: Predicting and Understanding Chemistry, in: Rev. Comput. Chem., John Wiley & Sons (2000) 1–86.

[9] J.P. Perdew, K. Burke, Y. Wang, Generalized gradient approximation for the exchange-correlation hole of a many-electron system, Phys. Rev. B 54 (1996) 16533–16539.

[10] N. Mardirossian, M. Head-Gordon, Thirty years of density functional theory in computational chemistry: an overview and extensive assessment of 200 density functionals, Mol. Phys. 115 (2017) 2315–2372.

[11] J. Tirado-Rives, W.L. Jorgensen, Performance of B3LYP Density Functional Methods for a Large Set of Organic Molecules, J. Chem. Theory Comput. 4 (2008) 297–306.

[12] A. Erba, J.K. Desmarais, S. Casassa, B. Civalleri, L. Donà, I.J. Bush, B. Searle, L. Maschio, L. Edith-Daga, A. Cossard, C. Ribaldone, E. Ascrizzi, N.L. Marana, J.-P. Flament, B. Kirtman, CRYSTAL23: A Program for Computational Solid State Physics and Chemistry, J. Chem. Theory Comput. 19 (2023) 6891–6932.

[13] S. Grimme, S. Ehrlich, L. Goerigk, Effect of the damping function in dispersion corrected density functional theory., J. Comput. Chem. 32 (2011) 1456–1465.

[14] S. Grimme, J. Antony, S. Ehrlich, H. Krieg, A consistent and accurate ab initio parametrization of density functional dispersion correction (DFT-D) for the 94 elements H-Pu, J. Chem. Phys. 132 (2010) 154104.

[15] R. Dovesi, A. Erba, R. Orlando, C. Zicovich-Wilson, B. Civalleri, L. Maschio, M. Rérat, S. Casassa, J. Baima, S. Salustro, B. Kirtman, Quantum-mechanical condensed matter simulations with CRYSTAL, Wiley Interdiscip. Rev. Comput. Mol. Sci. 8 (2018) e1360.

[16] www.crystal.unito.it/index.html

[17] G. Kresse, J. Furthmüller, Efficient iterative schemes for ab initio total-energy calculations using a plane-wave basis set, Phys. Rev. B 54 (1996) 11169–11186.

[18] G. Kresse, D. Joubert, From ultrasoft pseudopotentials to the projector augmented-wave method, Phys. Rev. B 59 (1999) 1758–1775.

[19] E.R. Davidson, D. Feller, Basis Set Selection for Molecular Calculations, Chem. Rev. 86 (1986) 681–696.

[20] F. Jensen, Atomic orbital basis sets, WIREs Comput. Mol. Sci. 3 (2013) 273–295.

Chapter 3

Unraveling the O_2 Reduction Reaction on 2D Monolayer $LaNiO_3$ Perovskite

In this chapter, we theoretically studied the structural and electronic properties of 3D bulk $LaNiO_3$ perovskite. We have cleaved the (0 0 1) surface from 3D $LaNiO_3$, which has a zero electronic band gap (E_g), to create 2D monolayer $LaNiO_3$ computationally and studied its electronic properties. Our study demonstrates that the 2D monolayer $LaNiO_3$ is a suitable candidate for catalyzing the ORR because of its high catalytic activity with a tiny electronic band gap of 0.25 eV. We explored the ORR mechanism on the 2D monolayer $LaNiO_3$ perovskite by inspecting each intermediate. Our present findings show that the 2D monolayer $LaNiO_3$ can efficiently catalyze the ORR through a four-electron ($4e^-$) reduction reaction due to the excellent catalytic activity of its basal plane, which accords with the experimental findings. The change in Gibbs free energy (ΔG) calculations of various intermediate steps of the ORR demonstrates that all reaction steps are spontaneous and thermodynamically favorable. The 2D monolayer $LaNiO_3$ perovskite can be a potential candidate for catalyzing the ORR efficiently. This study helps to enable the development of high-activity, stable 2D perovskites for use in future solid oxide fuel cells and related applications in green energy technologies.

3.1 Introduction

In a variety of energy conversion and storage application devices such as fuel cells and metal–air batteries (MABs), the oxygen reduction reaction (ORR) occurring at the cathode is an essential reaction that plays a critical role. The multistep ORR kinetics at the cathode are usually slow in comparison to anodic reactions, which significantly affects the performance and commercialization of electrochemical energy conversion devices in short applications.[14] An electrocatalyst plays a significant role in enhancing the efficiency and performance of fuel cells by making the ORR process faster. The volcano-type relationship is present between the surface's electronic

structure of a catalyst and its catalytic activity for the ORR.[15,16] The replacement of precious metal-based catalysts with alternatives having comparable or even better electrocatalytic activity is necessary for practical applications by reducing the cost. In fuel cells, oxides have demonstrated excellent catalytic activity for the ORR.[23,24] To date, various non-noble metal-based catalysts have been studied and have shown good performance for the ORR but still have some limitations within them.[24–27] The search for efficient and long-lasting catalysts for the ORR has been a major challenge, and perovskite oxides have emerged as a promising class of materials in this regard. The segregation of alkaline earth elements such as Ba, Sr, and Ca on perovskite surfaces under an oxygen-enriched atmosphere has been widely reported.

In an alkaline medium, perovskite-based oxides are an alternative solution for efficiently catalyzing the ORR because they are highly resistive to alkaline solutions. Recently, it has been explored that the 2D monolayer $CsPbBr_3$ has shown excellent catalytic activity for the ORR that followed both associative and dissociative pathways.[6] Expanding on the promising catalytic activity of 2D monolayer $CsPbBr_3$ for the ORR, it is noteworthy to explore lanthanum nickelate ($LaNiO_3$) as another intriguing candidate in the realm of electrocatalysis. $LaNiO_3$ has gained considerable attention due to its unique electronic and magnetic properties. $LaNiO_3$ is a promising candidate for a range of applications such as catalysis due to its good conductivity and magnetic behavior. It has been reported that tuning its properties is possible via the substitution of anions and cations, e.g., adding Fe and Mg to the B-site of Ni makes $LaNiO_3$ more catalytically active.[15,33] A few studies showed that perovskite oxide with diverse compositions having better catalytic activity can be prepared by replacing the A-site and B-site with other metal ions.[34,35] Recently, it has been demonstrated that the substitution of Fe in a Co-based perovskite has shown excellent catalytic performance in an alkaline electrolyte toward the ORR.[27,36] The bifunctional catalytic activity of the most promising candidate, perovskite-based $LaNiO_3$, is efficient and comparable to those of other best-performing precious metals. Very recently, Shao-Horn et al. experimentally proved that the e_g electron number of transition metal cations is an important parameter that influences the performance of ORR activity.[27,37] The $LaNiO_3$ perovskite with Ni centers having a valency state of 3^+ and moderate e_g electron occupation ($e_g \approx 1$) promotes the efficient ORR with a $4e^-$ transfer pathway. Additionally, the splitting of e_g orbitals is effective in tuning the catalytic performance

of $LaNiO_3$ under the action of epitaxial strain due to changes in the electronic structure. Those compounds have exhibited higher activity whose 3d transition metal cations had only one electron in their e_g orbital.[16] Unfortunately, there is no theoretical and computational study to explain the experimental observations.

In this study, we have introduced a highly efficient ORR catalyst using a Pt-free 2D material computationally. Using the first principles-based quantum mechanical density functional theory (DFT) method, we have proposed a 2D monolayer $LaNiO_3$ perovskite material as a potential cathodic material for the ORR. At first, the equilibrium structure and electronic properties of the 3D bulk structure of $LaNiO_3$ have been studied by generating crystal structures using theoretical methods. The 3D $LaNiO_3$ material lacks the necessary high surface area for an efficient ORR. To address this issue, we cleaved a (0 0 1) surface from the 3D bulk structure of the $LaNiO_3$ perovskite material as shown in Figure 3.1a and computationally designed a 2D monolayer LaNiO3 slab structure as depicted in Figure 3.1b. We have selected the (0 0 1) surface because in the perovskite structure such surfaces are generally the most stable, and the atoms which drive the ORR catalytic activity are the redox-active transition metals.[15,27] We performed structural optimization and electronic property calculations of the 2D monolayer $LaNiO_3$ system. Our electronic property calculation reveals that the 3D $LaNiO_3$ is a metallic conductor with a zero band gap. But in comparison to 3D $LaNiO_3$, 2D monolayer $LaNiO_3$ has an excellent catalytic property due to its highly active exposed surface area, indicating its promising potential as an effective ORR catalyst. Furthermore, our study investigates various reaction intermediates involved on the surface of 2D monolayer $LaNiO_3$ to study the ORR process. We utilized a 2D monolayer slab configuration of the $LaNiO_3$ perovskite to thoroughly investigate each reaction step involved in the ORR mechanism, considering the standard hydrogen electrode (SHE) or computational hydrogen electrode (CHE) model. We explored the ORR mechanism on the surfaces of the 2D monolayer $LaNiO_3$ perovskite to determine its catalytic activity and to explain the experimental observations.

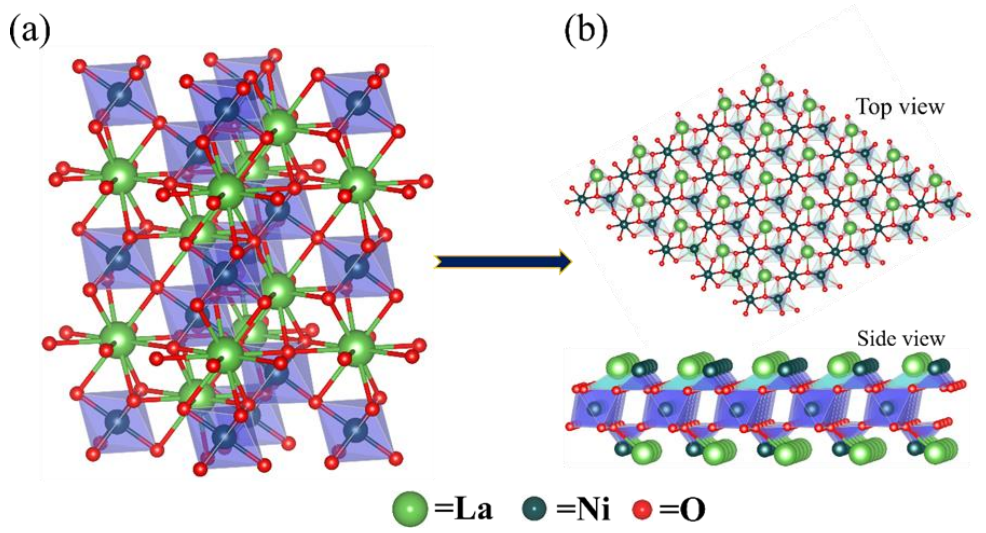


Figure 3.1: *(a) Equilibrium geometry of the 3D bulk structure of $LaNiO_3$ and (b) top and side view of the equilibrium structure of 2D monolayer $LaNiO_3$.*

3.2 Methods and Computational Details

All the calculations were performed by using the Vienna Ab initio Simulation package (VASP).[38,39] The equilibrium structure, geometry, and electronic properties of both the 3D crystal structure of $LaNiO_3$ and 2D monolayer of $LaNiO_3$ perovskite materials were computed by utilizing the projector augmented wave (PAW) approach with pseudopotentials.[40,41] The calculations involved the application of the Perdew–Burke–Ernzerhof (PBE) form of generalized gradient approximation (GGA) to describe the exchange and correlation effects.[42] A simple formulation of a GGA method for both the exchange and correlation energies of electrons was developed by Perdew, Burke, and Ernzerhof (PBE), i.e., this method includes both PBE exchange and PBE correlation parameters during computations.[42,43] To account for weak van der Waals (vdW) interactions in the systems, Grimme's semiempirical third-order dispersion correction parameters (Grimme's D3) were included in the DFT computation.[43] We employed spin-polarized calculations using periodic hybrid DFT-D (i.e., PBE-D3) method to determine the equilibrium structures and investigate the electronic properties of the studied system. In our study, the pseudopotential basis sets employed for La, Ni, and O atoms were PAW_PBE La_GW, PAW_PBE Ni_GW, and PAW_PBE O_GW, respectively, and a plane-wave cutoff energy of 450 eV was provided. A 1 × 1 × 1 Monkhorst–Pack[44] k-point grid with a Gaussian smearing of 0.05 eV was used for the PBE-D3 calculations of the $LaNiO_3$ slab, and the convergence energy was set to 1 × 10^{-5} eV. To calculate and plot the total density of states (DOS), the atomic orbitals of

La, Ni, and O atoms were employed. A 2D vacuum slab was utilized to consider the electrostatic potential of the 2D $LaNiO_3$ material. In our calculation, we have created a vacuum slab of 2D monolayer $LaNiO_3$ for studying the structural and electronic properties of the studied systems. The vacuum region was employed to avoid periodicity along the z-direction. A 15 Å vacuum region was created perpendicular to the 2D monolayer $LaNiO_3$ slab to avoid spurious interactions between the repeated layers. We employed the visualization code VESTA to generate visual representations and conduct the crystal structure analysis of the $LaNiO_3$ perovskite 2D slab.[45,46]

3.3 Theoretical Calculations and Equations

In our current investigation, the reaction steps of the ORR have been explored on the surface of 2D monolayer $LaNiO_3$ with respect to the standard hydrogen electrode (SHE) or computational hydrogen electrode (CHE) model, which has been mentioned earlier. Therefore, the thermodynamical equations can be written as below to compute the relative free energy during the ORR.

$$G = E_{DFT} + E_{ZPE} + \int C_P \, dT - TS \tag{3.1}$$

The above equation (3.1) was used to calculate the free energy of various intermediate species, where E_{DFT}, E_{ZPE}, and S are the ground-state electronic energy, zero-point vibrational energy, and entropy, respectively. T denotes the temperature which is 298.15 K in the present investigation.

$$\Delta G_{ads} = \Delta E_{ads} + \Delta E_{ZPE} - T\Delta S \tag{3.2}$$

The above equation (3.2) was used to calculate the change in the free energy of reaction intermediates (adsorbates) at pH = 0, where ΔG_{ads} represents the adsorption free energy of adsorbates. ΔE_{ads}, ΔE_{ZPE}, and ΔS are the differences of electronic energy (E_{DFT}), zero-point vibrational energy (E_{ZPE}), and entropy (S), respectively. The contribution of specific heat capacity at constant pressure (C_P) was carried out in the free energy (G) calculation as expressed in equation (3.1). The value of the lattice specific heat capacity C_P was maintained constant at a temperature (T) equal to 298.15 K. The temperature (T) was taken to be constant while calculating the change of free energy during the H-adsorption. Thus, during the calculation of the change of free energy of the ORR steps, the integral part of $\int C_P \, dT$ was zero. The following equation (3.3) was used to calculate

the free energy of O_2 as the DFT method could not describe the high-spin ground state of the oxygen molecule satisfactorily.

$$G_{O_2} = 2G_{H_2O} - 2G_{H_2} - 4.92 \quad (3.3)$$

3.4 Results and Discussions

The equilibrium structure of the 3D bulk crystal of $LaNiO_3$ was obtained by the PBE-D3 method as shown in Figure 3.2a. The optimized lattice constants and equilibrium bond angles of 3D $LaNiO_3$ were found to be a = b = 5.48 Å, c = 13.04 Å, $\alpha = \beta = 90^o$, and $\gamma = 120^o$. The bulk crystal structure of $LaNiO_3$ has a rhombohedral $R\bar{3}c$ space group symmetry. The equilibrium La–O and Ni–O bond lengths were 2.76 Å and 1.94 Å, respectively, obtained by the same method. The obtained lattice parameters are well consistent with the previous reported values.[50] The electronic property calculations, i.e., the electronic band structure and total density of states (DOS) of the bulk 3D $LaNiO_3$, were obtained by the same PBE-D3 method. A highly symmetric ***Γ−T−H−L−Γ−S−F−Γ*** direction was used to plot the electronic band structure and total DOS of 3D $LaNiO_3$ in the first Brillouin zone represented in Figure 3.2b,c. The electronic band structure and total DOS were calculated with respect to the Fermi energy level (E_F) while using the atomic orbital of La, Ni, and O atoms in DOS calculations.

We found that the 3D crystal structure of the $LaNiO_3$ perovskite has a zero electronic band gap ($E_g = 0$) from the property calculations, and the total DOS shows the presence of a high electron density around the $\mathbf{E_F}$. Therefore, from both the band and DOS calculations, we can say that the 3D crystal structure of the $LaNiO_3$ perovskite is a good conductive material in nature. However, it could not be directly used as an electrocatalyst for the ORR because of the smaller exposed surface area. To address this, we computationally created a 2D monolayer $LaNiO_3$ from 3D $LaNiO_3$ by cleaving the (0 0 1) surface with a perpendicular 15 Å vacuum region along the z-direction to avoid symmetry in that direction. The height of the unit cell was maintained at 15 Å to fit the vacuum space to avoid periodicity. We cleaved the (0 0 1) surface from 3D $LaNiO_3$ because, according to previous studies, it enhances the catalytic activity of perovskite materials by decreasing the overpotential.[15]

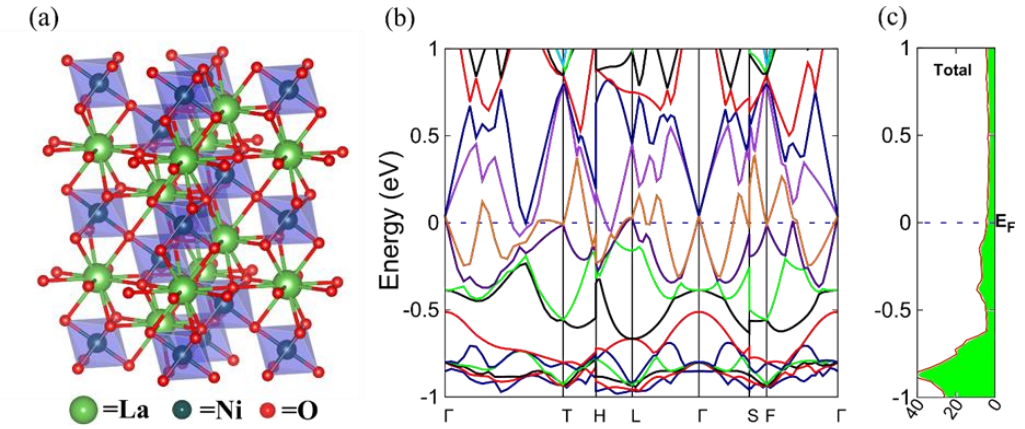


Figure 3.2: *(a) Equilibrium crystal structure, (b) electronic band structure, and (c) total DOS of the 3D $LaNiO_3$ perovskite.*

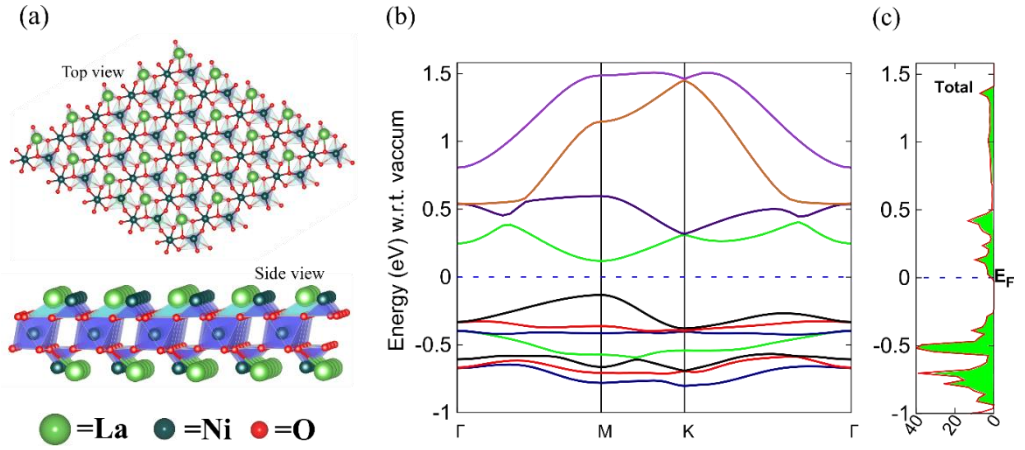


Figure 3.3: *(a) Top and side view, (b) electronic band structure, and (c) total DOS of the equilibrium 2D monolayer $LaNiO_3$.*

Then, we utilized the PBE-D3 method to obtain the equilibrium geometry and electronic properties of the 2D monolayer $LaNiO_3$. Figure 3.3a represents the equilibrium structure of the 2D monolayer $LaNiO_3$. In this study, we have utilized a 1 × 1 unit cell of the 2D monolayer $LaNiO_3$ system defined by the lattice parameters a = b = 5.58 Å, α = β = 90º, and γ = 120º, respectively. We observed that the equilibrium structure of the 2D monolayer $LaNiO_3$ perovskite has a trigonal $P\bar{3}$ layer group symmetry. Additionally, the optimized La–O bond length was 2.56 Å, and the Ni–O bond distance was 1.94 Å. The electronic band structure and total DOS of 2D monolayer $LaNiO_3$ were calculated w.r.t. vacuum using a highly symmetric ***Γ−M−K−Γ*** path. In our study, we have selected a highly symmetric k-vector path to compute the electronic properties, i.e., the electronic band structure and total DOS of the 2D monolayer $LaNiO_3$ and various reaction intermediates of the ORR. The k-paths are the

high-symmetry paths in the reciprocal space that are frequently used to compute the electronic band structures in the periodic solids, and they are essential for studying the physical characteristics. Due to processing limitations, energy bands are usually calculated along high-symmetry line segments in the irreducible Brillouin zone followed by the original symmetry of the system. The stationary points in a band structure can be found along the high-symmetry points and line segments within the Brillouin zone to avoid the crossings in the energy spectrum. In the present work, the highly symmetric k-path is well consistent with the symmetry of our studied material. The selection of a high symmetric k-vector path reduces the computational time and resources compared to computing energies across the entire boundary, making it feasible to explore the dispersion landscape efficiently. The energy band structure and total density of states of the 2D monolayer $LaNiO_3$ are illustrated in 3.3b,c. Table 3.1 summarizes the equilibrium lattice constants, band gap, bond lengths, and space group symmetry of 2D monolayer $LaNiO_3$ and 3D $LaNiO_3$ with the earlier reported results. From our DFT calculations of the 2D monolayer $LaNiO_3$, we found that it has an indirect band gap of 0.25 eV, and there is a low electron density of states around the $\mathbf{E_F}$ in the total density of states, confirming that it is a very low band gap semiconducting material.

Table 3.1: *Equilibrium lattice parameters of 3D $LaNiO_3$ and 2D monolayer $LaNiO_3$.*

System	Lattice constant (Å)	Angles (In degree)	Space group	Bond distance (In Å)	Band gap (E_g)	Reference
3D bulk $LaNiO_3$	a=b=5.48 c=13.04	α=β=90, γ=120	$R\bar{3}c$	La-O=2.76 Ni-O=1.94	0.00	This work
2D monolayer $LaNiO_3$	a=5.58 b=5.58	α=89.93, β=90.05, γ=120.07	$P\bar{3}$	La-O=2.56 Ni-O=1.94	0.25	This work
3D $LaNiO_3$ (Previous work)	a=b=5.45 c=13.14	α=β=90, γ=120	$R\bar{3}c$	Ni-O=1.93	0.00	[15]

3.5 ORR Mechanisms

From the electronic property calculations of the 2D monolayer $LaNiO_3$, we confirmed that it is a very low band gap semiconductor in nature, and it may have good catalytic activity because of less band gap and the presence of small electron density around the $\mathbf{E_F}$. Therefore, the electrons can easily transfer from the valence bands to the conduction

bands, and the charge transfer is easy during the chemical reactions (especially electrochemical reactions) on its surface. To know whether this 2D monolayer $LaNiO_3$ perovskite is a suitable candidate for catalyzing the ORR, we started exploring the ORR mechanisms on the surface of the 2D monolayer $LaNiO_3$ by creating various reaction intermediates computationally. Figure 3.4a,b represents the schematic diagram of the proposed four-electron ($4e^-$) transfer mechanisms of the ORR performed on the surfaces of 2D monolayer $LaNiO_3$ that can follow either dissociative or associative pathways. The consecutive reaction steps with the addition of electrons (e^-), protons (H^+), and removal of water (H_2O) molecules are represented by various arrows.

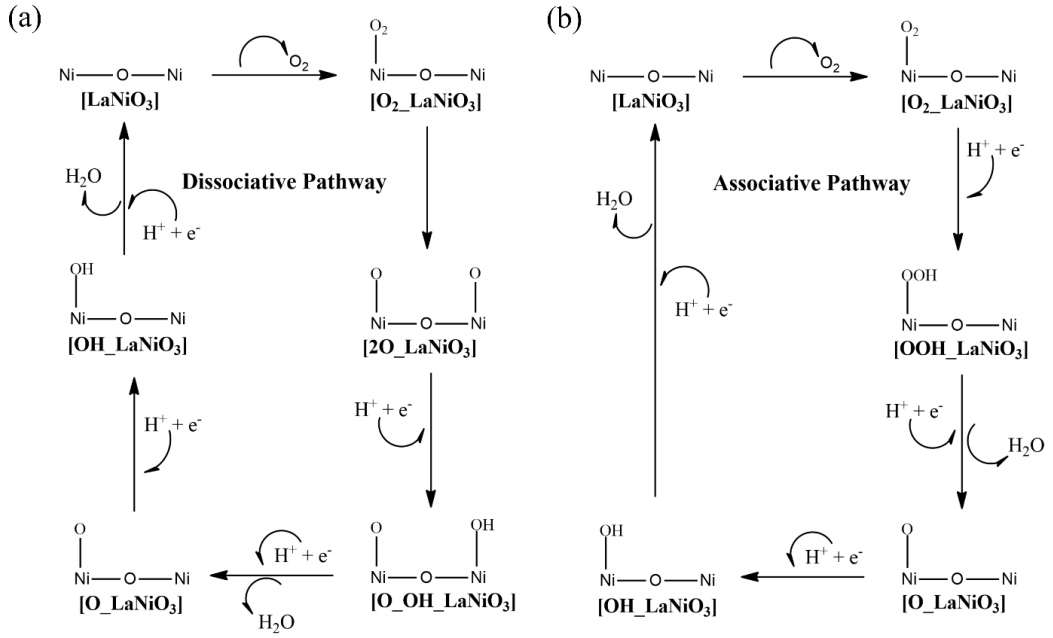


Figure 3.4: *Schematic representation of (a) dissociative and (b) associative reaction pathways of the ORR on the surface of the 2D monolayer $LaNiO_3$ with the $4e^-$ transfer mechanism.*

During the adsorption of the O_2 molecule on the Ni site of the 2D monolayer $LaNiO_3$, charge transfer occurs between the oxygen (O) and the nickel (Ni) atoms. The charge transfer from the Ni atom to the O atom is necessary for the initiation of the O_2 reduction reaction. The electronic charge variation on the Ni and O centers during the reaction was verified through charge difference density and Bader charge analysis.[51] We found that the charge on the Ni atom before the O_2 adsorption was 0.692e. After the O_2 adsorption, the charge on the Ni atom was 1.043e; where e is the charge of an electron. Similarly, the charge on the oxygen atom (which is bonded to the Ni atom) before and after the O_2 adsorption was −0.011e and −0.470e, respectively. So, 0.351e unit of charge was transferred from the Ni atom to the O atom during the O_2 adsorption step.

Figure 3.5 shows the charge difference density of the O_2_$LaNiO_3$ reaction intermediate, where the yellow and cyan regions represent charge depletion and accumulation, respectively.

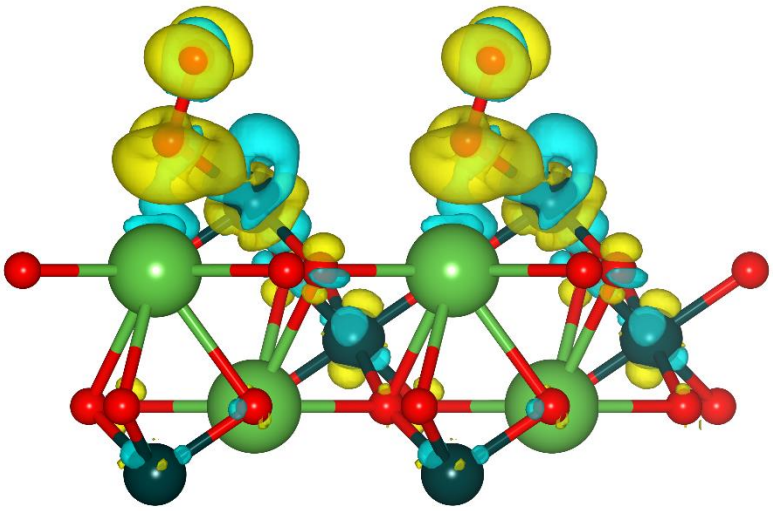


Figure 3.5: *Charge difference density of O_2 adsorbed on the Ni atom of the 2D monolayer $LaNiO_3$ perovskite, i.e., the O_2_$LaNiO_3$ reaction intermediate. The yellow region denotes charge depletion, and the cyan color denotes charge accumulation.*

Dissociative reaction pathway

The most important issue during the ORR process is the number of exposed active sites for the adsorption of the O_2 adsorbate, which determines the ORR activity. All of the reaction intermediates that occur during the ORR mechanisms followed by the dissociative pathway on the surface of the 2D monolayer $LaNiO_3$ are shown in Figure 3.6. A solvent can influence a chemical reaction in various ways, such as by changing the reaction rate, modifying the geometry of the reactants, altering the energy landscape of the reaction, and affecting the stability of the intermediates. This issue can be resolved by using gas phase modeling, which involves modeling individual molecules or small clusters of molecule's behavior in a gaseous environment under controlled conditions. Under these conditions, DFT computations are easier and more accurate even in a gas–solid interface. We initialized the modeling of the O_2 reduction reaction steps on the active exposed surface of the 2D monolayer $LaNiO_3$ computationally for further calculations under computational hydrogen electrode conditions (CHE) i.e., H_2 pressure is 1 bar with zero pH.

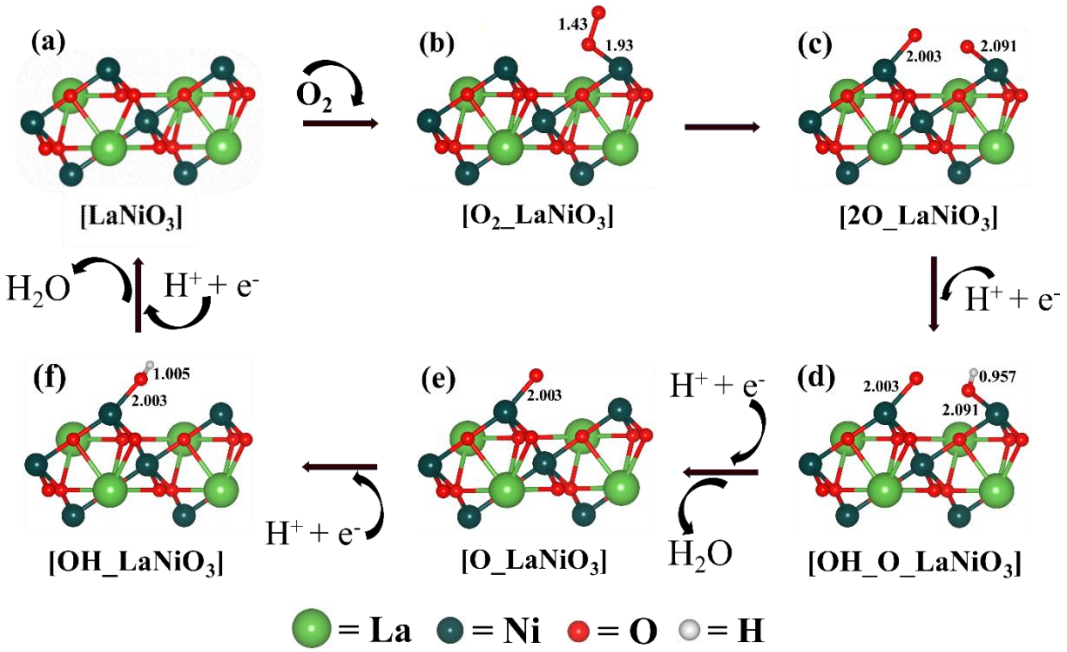


Figure 3.6: *Equilibrium structures of all the reaction intermediates involved in the dissociative pathway of the ORR on the surface of the 2D monolayer $LaNiO_3$ perovskite.*

The initial step of the ORR involves the adsorption of the O_2 molecule on the surface of 2D monolayer $LaNiO_3$ at the nickel site, which leads to the formation of a reaction intermediate represented by O_2_$LaNiO_3$ with the change in free energy (ΔG) equal to −0.66 eV as shown in Figure 3.6b. The free energy calculation indicates that the adsorption of O_2 on the surface of 2D monolayer $LaNiO_3$ at the nickel site is thermodynamically feasible as the relative free energy (ΔG) is negative, depicted in Figure 3.7. The calculated equilibrium bond lengths La–O and Ni–O of the O_2_$LaNiO_3$ reaction intermediate were found to be 2.61 Å and 1.93 Å, respectively. The optimized O–O bond length was 1.43 Å. In the next step, the extended bond between oxygen atoms in the adsorbed O_2 of reaction intermediate O_2_$LaNiO_3$ is broken, leading to the adsorption of one oxygen atom onto a distinct Ni site, resulting in the formation of new reaction intermediate 2O_$LaNiO_3$. In the 2O_$LaNiO_3$ reaction intermediate, the two activated oxygen atoms attach to two distinct Ni sites of the 2D monolayer $LaNiO_3$ perovskite. The equilibrium lattice parameters of all the reaction intermediates of the ORR involved during the dissociative mechanism are reported in Table 3.2.

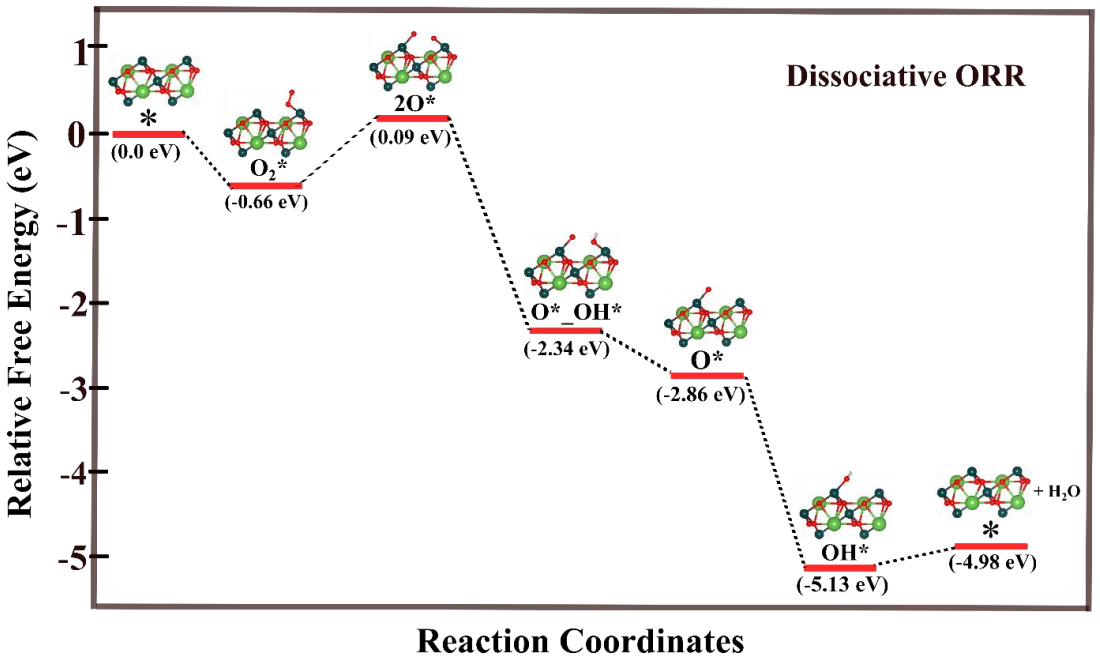


Figure 3.7: *Relative free energy profiles for the dissociative mechanism of the ORR on the surface of the 2D monolayer $LaNiO_3$ perovskite.*

In this study, the transition state (TS) during the O_2 dissociation step was obtained by using the climbing-image nudged elastic band (CI-NEB) method.[52,53] The approximate path of O_2 dissociation was generated, and one intermediate image was relaxed. We found that the cleavage of the O–O bond occurs with a transition state (TS) during the O_2 dissociation step. Figure 3.8 represents the free energy profile for the dissociation of O_2 on the surface of 2D monolayer $LaNiO_3$ with the transition state (TS). We found that the O_2 dissociation barrier was +1.42 eV during the cleavage of the O–O bond. There is a complex interaction between the O_2 molecule and the Ni atoms on the surface of the 2D monolayer $LaNiO_3$ perovskite during the ORR mechanism. In the $LaNiO_3$ perovskite, Ni has a +3 oxidation state. The O–O cleavage process occurs after the adsorption of the O_2 molecule on the Ni atom of the 2D monolayer $LaNiO_3$. The O_2 molecule dissociates into two activated oxygen atoms, and they get attached to two different Ni atoms on the surface of the 2D monolayer $LaNiO_3$. The oxygen atom having a −2 oxidation state forms a bond with the Ni atom. This involves charge transfer from the oxygen atom to the Ni atom, due to which Ni reduces from the +3 to +2 oxidation state. Hence, to accommodate the additional negative charge from the oxygen atom during the O–O cleavage process, the oxidation state of Ni changes from Ni^{3+} to Ni^{2+}.

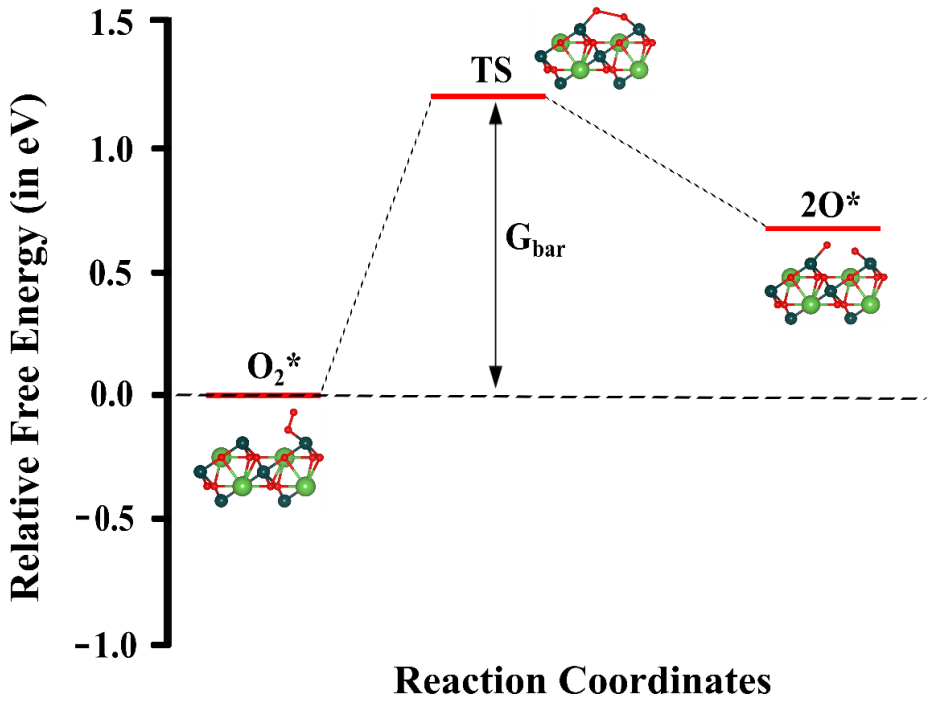


Figure 3.8: *O_2 dissociation on the surface of 2D monolayer $LaNiO_3$ with a transition state (TS).*

The equilibrium structure of the 2O_$LaNiO_3$ reaction intermediate is depicted in Figure 3.6c and the relative free energy profile for the dissociative mechanism of the ORR is represented in Figure 3.7. The completion of this reaction step ($O_2 \rightarrow 2O$) has occurred with a change of relative free energy (ΔG) of 0.09 eV which indicates that this step is endothermic in nature. We found that in equilibrium 2O_$LaNiO_3$ intermediate, the La–O and Ni–O bond distances are 2.56 Å and 2.01 Å, respectively. The reaction intermediate 2O_$LaNiO_3$ is unstable, as the relative free energy required for its formation is positive. In the next step, one adsorbed oxygen atom at the nickel site gets reduced to form a hydride ion (OH^-) on the perovskite surface, giving the O_OH_$LaNiO_3$ reaction intermediate as depicted in Figure 3.6d. Our study demonstrates that the O–H bond length is 0.95 Å, and both the equilibrium La–O and Ni–O bond lengths remain unchanged i.e., 2.56 Å and 2.01 Å, respectively. The relative free energy change in this reaction step is about −2.34 eV as depicted in Table 3.3.

The formation of the O_OH_$LaNiO_3$ intermediate from 2O_$LaNiO_3$ involves the transfer of an electron from the electrode to one adsorbed oxygen atom on the surface of the perovskite, which reduces it to a hydride ion via the addition of one proton. Now, the hydride ion reacts with a proton (H^+) and electron (e^-) to form a water (H_2O) molecule with a free energy change of −0.51 eV and the relative free energy change of about −2.86 eV, giving the reaction intermediate O_$LaNiO_3$ as shown in Figure 3.4a.

Here, the equilibrium La–O bond length is 2.56 Å, and the Ni–O bond length decreases to 1.97 Å. The equilibrium structure of O_$LaNiO_3$ reaction intermediate is shown in Figure 3.6e. The addition of one electron and proton to the O_$LaNiO_3$ reaction intermediate results in the formation of the OH_$LaNiO_3$ intermediate with an energy cost of −2.27 eV. In the last step of the dissociative mechanism, the addition of one more electron and proton with reaction intermediate OH_$LaNiO_3$ results in the removal of the second water molecule as depicted in Figure 3.4a with the change of free energy of about 0.15 eV. Equilibrium lattice parameters of all the reaction intermediates of the ORR involved in the dissociative mechanism are listed in Table 3.2. The change in the free energy of each reaction step and the relative free energy of different reaction intermediates of ORR are listed in Table 3.3.

Table 3.2: *Equilibrium lattice parameters and space group symmetry of all the reaction intermediates of the dissociative mechanism in the ORR process.*

System	Lattice constants (Å)	Angles (In degree)	Space group symmetry	The band gap (eV)	Average bond distances (Å)			
					La-O	Ni-O	O-O	O-H
O_2_$LaNiO_3$	a=5.58 b=5.15	α=79.46 β=97.06 γ=116.36	*P1*	0.10	2.61	1.93	1.43	-
2O_$LaNiO_3$	a=5.48 b=5.40	α=87.12 β=96.74 γ=126.45	*P1*	0.00	2.56	2.01	-	-
O_OH_$LaNiO_3$	a=5.52 b=5.46	α=84.27 β=94.74 γ=120.22	*P1*	0.01	2.56	2.01	-	0.95
O_$LaNiO_3$	a=5.54 b=5.43	α=89.92 β=89.96 γ=119.82	*P1*	0.13	2.56	1.97	-	-
OH_$LaNiO_3$	a=5.62 b=5.48	α=91.14 β= 92.41 γ=121.26	*P1*	0.76	2.56	1.97	-	1.00
OOH_$LaNiO_3$	a=5.62 b=5.90	α=95.76 β= 80.47 γ=125.26	*P1*	0.00	2.52	1.88	1.30	0.96

Table 3.3: *All the reaction intermediates of dissociative pathways of the ORR along with the change in their free energy (ΔG) occurring on the surface of the 2D monolayer $LaNiO_3$ perovskite.*

O_2 reduction reaction steps	ΔG (in eV)	Reaction intermediates	Relative free energies (in eV)
$[LaNiO_3] \rightarrow [O_2_LaNiO_3]$	-0.66	$O_2_LaNiO_3$	-0.66
$[O_2_LaNiO_3] \rightarrow [2O_LaNiO_3]$	0.76	$2O_LaNiO_3$	0.09
$[2O_LaNiO_3] \rightarrow [O_OH_LaNiO_3]$	-2.44	$O_OH_LaNiO_3$	-2.34
$[O_OH_LaNiO_3] \rightarrow [O_LaNiO_3]$	-0.51	$O_LaNiO_3 + H_2O$	-2.86
$[O_LaNiO_3] \rightarrow [OH_LaNiO_3]$	-2.27	OH_LaNiO_3	-5.13
$[OH_LaNiO_3] \rightarrow [LaNiO_3]$	0.15	$LaNiO_3 + H_2O$	-4.98

A Review of the Different Stages of the ORR Mechanism

Step 1. The VASP suit code with the PBE-D3 method was used to obtain the equilibrium geometry of the $O_2_LaNiO_3$ reaction intermediate, which is represented in Figure 3.6b. The oxygen molecule is adsorbed on the surface of the 2D monolayer $LaNiO_3$ perovskite at the Ni site because nickel has a higher density of electrons which is favorable for O_2 adsorption. Computationally, the reaction intermediate $O_2_LaNiO_3$ was examined, and we found that the La–O, Ni–O, and O–O bond distances were 2.61 Å, 1.93 Å, and 1.43 Å, respectively. We found that the equilibrium structure of the $O_2_LaNiO_3$ reaction intermediate has a P1 layer group symmetry with lattice parameters a = 5.58 Å, b = 5.15 Å, α = 79.46º, β = 97.06º, and γ = 116.36º, respectively, as given in Table 3.2. The electronic band structure and total DOS of the $O_2_LaNiO_3$ reaction intermediate is illustrated in Figure 3.9a, which is plotted using a high-symmetry $\boldsymbol{\Gamma-M-K-\Gamma}$ direction. The electronic band structure and total DOS are normalized, i.e., computed with respect to the E_F. The eigenvalues of the valence band maximum (VBM) and conduction band maximum (CBM) were −0.95 eV and −0.85 eV. The calculated energy band gap was found to be 0.10 eV (indirect band gap), and in the total DOS, there is a small electron density present near the E_F showing the conducting properties of the $O_2_LaNiO_3$ reaction intermediate.

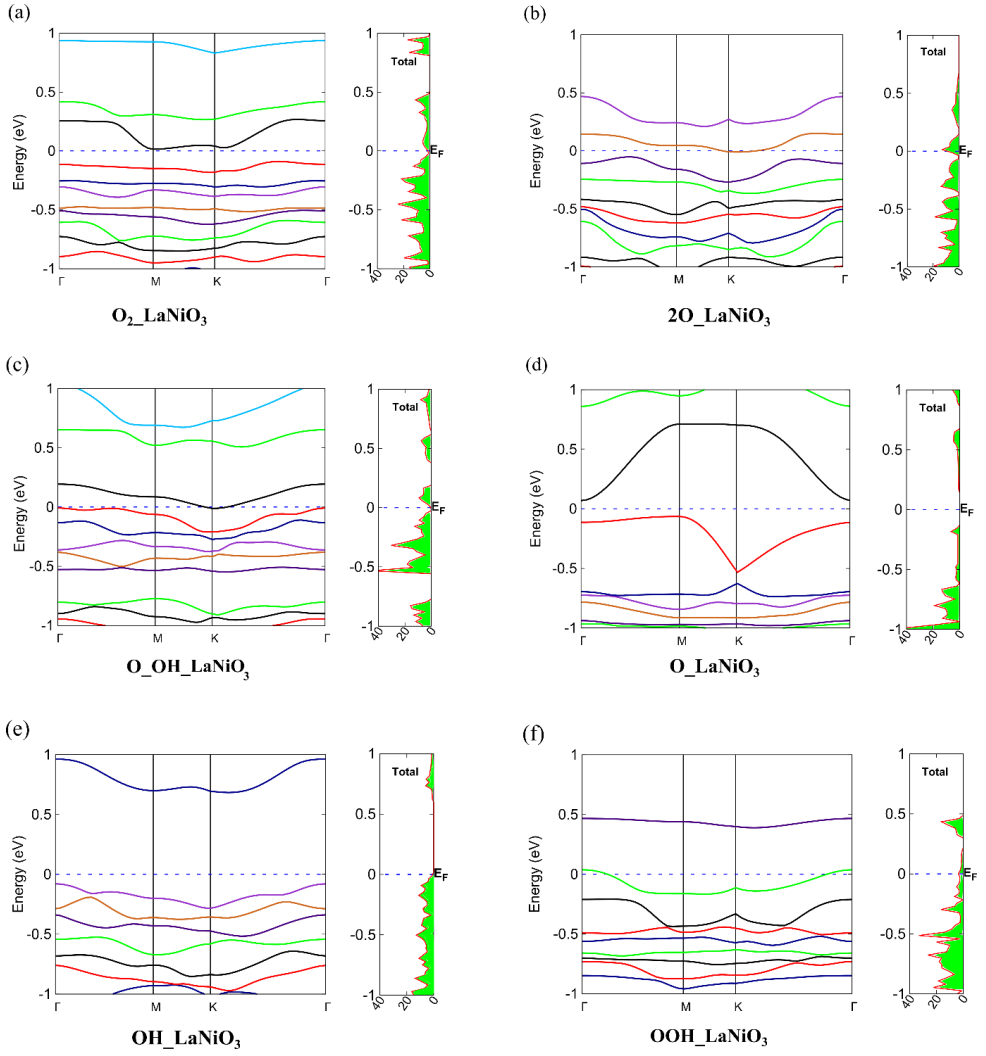


Figure 3.9: *Electronic band structure and total DOS of (a) O_2_$LaNiO_3$, (b) 2O_$LaNiO_3$, (c) O_OH_$LaNiO_3$, (d) O_$LaNiO_3$, and (e) OH_$LaNiO_3$ reaction intermediates of the dissociative pathway, and (f) OOH_$LaNiO_3$ reaction intermediate of the associative ORR mechanism on the surface of the 2D monolayer $LaNiO_3$ perovskite.*

Step 2. In this step, the equilibrium structure of the 2O_$LaNiO_3$ reaction intermediate was achieved through the dissociation of the O–O bond in the O_2_$LaNiO_3$ reaction intermediate. This process was followed by the migration of a single oxygen atom to an adjacent Ni site within the 2D $LaNiO_3$ perovskite structure. The equilibrium structure of the 2O_$LaNiO_3$ reaction intermediate is shown in Figure 3.6c. The equilibrium lattice parameters of 2O_$LaNiO_3$ are a = 5.48 Å, b = 5.40 Å, α = 87.12°, β = 96.74º, and γ = 126.45º, and it has a P1 layer group symmetry. Here, the equilibrium La–O bond distance is decreased by 0.05 Å and the Ni–O bond distance is elongated by 0.08 Å, respectively. The electronic band structure and total DOS of 2O_$LaNiO_3$ were plotted w.r.t. vacuum using the high-symmetry ***Γ−M−K−Γ*** path. The eigenvalues

of the VBM and CBM were −0.65 eV. The calculated energy band gap is zero, meaning that this intermediate completely behaves like a conductor. The total DOS of the 2O_$LaNiO_3$ reaction intermediate has small electron DOS around the E_F, as depicted in Figure 3.9b.

Step 3. The equilibrium structure of the O_OH_$LaNiO_3$ reaction intermediate is shown in Figure 3.6d. The formation of O_OH_$LaNiO_3$ takes place when an electron and proton react with the 2O_$LaNiO_3$ intermediate. The present calculation reveals that equilibrium O_OH_$LaNiO_3$ has P1 symmetry. The equilibrium La–O, Ni–O, and O–H bond lengths are 2.56 Å, 2.01 Å, and 0.95 Å, respectively. Here, the lattice parameters, i.e., lattice constants and bond angles, were found to be a = 5.52 Å, b = 5.46 Å, α = 84.27º, β = 94.74º, and γ = 120.22º, respectively. A highly symmetric k-vector ***Γ−M−K−Γ*** path was used to compute the electronic band structure and total DOS of the O_OH_$LaNiO_3$ reaction intermediate by using the PBE-D3 method. Here, the eigenvalues obtained for the VBM and CBM were −0.95 eV and −0.94 eV. The band gap was found to be about 0.01 eV. Figure 3.9c represents the electronic band structure and total DOS of the O_OH_$LaNiO_3$ reaction intermediate.

Step 4. In the next step, the addition of one proton and one electron to the O_OH_$LaNiO_3$ reaction intermediate results in the removal of one water molecule from the surface of 2D $LaNiO_3$ with the formation of the O_$LaNiO_3$ reaction intermediate. Figure 3.6e shows the equilibrium structure of the O_$LaNiO_3$ reaction intermediate which has P1 symmetry. The equilibrium lattice parameters of the O_$LaNiO_3$ intermediate were a = 5.54 Å, b = 5.43 Å, α = 89.92º, β = 89.96º, and γ = 119.82º, respectively. The equilibrium Ni–O and La–O bond distances were found to be 1.97 and 2.56 Å. The electronic properties, i.e., the band structure and total DOS of the O_$LaNiO_3$ reaction intermediate were calculated w.r.t vacuum using a high-symmetry ***Γ−M−K−Γ*** direction. In Figure 3.9d, the electronic band structure and total DOS of the O_$LaNiO_3$ reaction intermediate are normalized. The eigenvalues of the VBM and CBM were −0.97 eV and −0.84 eV. Our study found that the O_$LaNiO_3$ reaction intermediate has a band gap of about 0.13 eV. A small band gap of O_$LaNiO_3$ shows good conductivity for mass electron and charge transfer during the chemical reaction.

Step 5. The formation of the last reaction intermediate OH_$LaNiO_3$ in the dissociative mechanism of the ORR results via the addition of one proton and electron to the

O_$LaNiO_3$ intermediate, where the activated oxygen atom attached to the Ni site forms a bond with the hydrogen atom. The equilibrium structure of the OH_$LaNiO_3$ reaction intermediate is shown in Figure 3.6f, and it acquired P1 layer group symmetry. The equilibrium lattice parameters were found to be a = 5.62 Å, b = 5.48 Å, α = 91.14º, β = 92.41º, and γ = 121.26º, respectively. The equilibrium O–H bond distance between was found to be 1.0 Å. The normalized electronic band structure and total DOS of the OH_$LaNiO_3$ reaction intermediate are represented in Figure 3.9e, which has a band gap of about 0.76 eV. In this case, the eigenvalues of the VBM and CBM were −0.53 eV and 0.23 eV. We can see a small electron density around the E_F. Furthermore, the addition of one more electron and proton to the OH_$LaNiO_3$ reaction intermediate results in the formation of the second H_2O molecule, and 2D monolayer $LaNiO_3$ is ready for further O_2 adsorption at the Ni site, and the reaction steps continue. Hence, a total of four electrons and four protons are used to reduce the O_2 molecule into two H_2O molecules in the ORR mechanism.

Associative reaction pathway

Additionally, we studied the associative O_2 reduction reaction mechanism computationally on the surface of the 2D monolayer $LaNiO_3$ perovskite. The initial step of the ORR involves the adsorption of the O_2 molecule at the Ni site, giving the O_2_$LaNiO_3$ reaction intermediate. The initial O_2 adsorption step in the associative path is similar to the first step of the dissociative mechanism. A schematic representation of the ORR associative mechanism is illustrated in Figure 3.4b. In contrast to the dissociative mechanism where O_2 dissociates into 2O (two activated oxygen atoms), here in the associative mechanism, one hydrogen gets attached to the O_2 molecule giving the OOH_$LaNiO_3$ reaction intermediate due to the reaction of the adsorbed O_2 molecule with one electron and one proton. The equilibrium structure of the OOH_$LaNiO_3$ reaction intermediate is shown in Figure 3.10c.

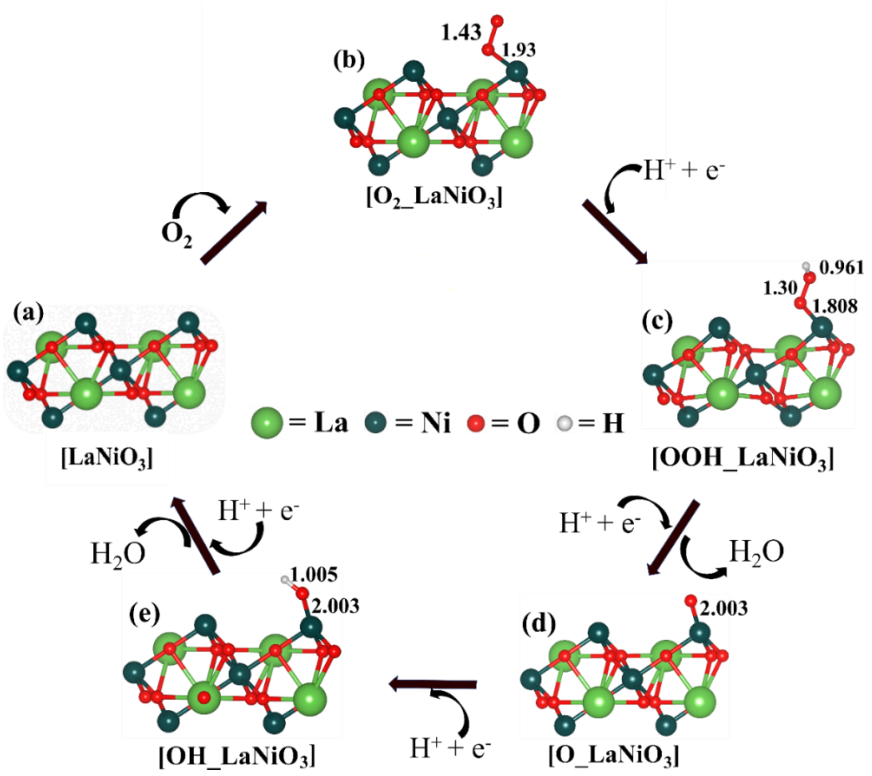


Figure 3.10: *Equilibrium structures of all the reaction intermediates involved in the associative reaction pathway of the ORR on the surface of the 2D monolayer $LaNiO_3$ perovskite.*

The formation of the OOH_$LaNiO_3$ reaction intermediate from the O_2_$LaNiO_3$ intermediate takes place with a free energy change of −1.99 eV, whose value is negative, which implies that this step does not require any additional energy input. It means the occurrence of this reaction step is spontaneous and thermodynamically favorable. Figure 3.10 illustrates all of the equilibrium structures of reaction intermediates involved in the associative mechanism of the ORR on the surface of the 2D monolayer $LaNiO_3$. Computationally, after the structure relaxation of the OOH_$LaNiO_3$ reaction intermediate, we found that it has P1 symmetry. The lattice parameters, i.e., lattice constant and bond angles, were a = 5.62 Å, b = 5.90 Å, α = 95.76º, β = 80.47º, and γ = 125.26º, respectively. The equilibrium La–O, Ni–O, and O–O bond lengths were 2.52 Å, 1.88 Å, and 1.30 Å, respectively. The equilibrium O−H bond distance was 0.96 Å. The electronic band structure and total DOS of the OOH_$LaNiO_3$ reaction intermediate are shown in Figure 3.9f, which are computed using a high symmetric ***Γ−M−K−Γ*** direction. We found that the equilibrium structure of the OOH_$LaNiO_3$ reaction intermediate has a zero band gap and there is a small electron density of states present near the E_F. In the further step, the addition of one electron (e^-) and one proton (H^+) to the OOH_$LaNiO_3$ reaction intermediate gives the

O_LaNiO_3 reaction intermediate with the removal of one H_2O molecule with a free energy change of −0.21 eV as represented in Figure 3.4b. The equilibrium structure of the O_LaNiO_3 reaction intermediate is depicted in Figure 3.10d. The negative value of the Gibb's free energy change clarifies that the occurrence of this reaction step is spontaneous, i.e., does not require any additional energy inputs, and is thermodynamically favorable.

In a further step, the OH_LaNiO_3 reaction intermediate is formed by the protonation of the O_LaNiO_3 intermediate, where the activated oxygen atom reacts with one electron and proton. The amount of energy required for this step to occur is −2.28 eV. The equilibrium structure of the OH_LaNiO_3 reaction intermediate is shown in Figure 3.10e. In the last step of the associative ORR, one more electron and proton reacts with the OH_LaNiO_3 intermediate which results in the removal of the second H_2O molecule at a free energy cost of 0.15 eV as depicted in Figure 3.4b. The relative free energy profile for the reaction intermediates of the associative mechanism of the ORR is shown in Figure 3.11. Here, four electrons and four protons are utilized to complete the whole ORR mechanism by reducing the O_2 molecule on the surface of the 2D monolayer $LaNiO_3$ perovskite, producing two H_2O molecules. The relative free energy and Gibb's free energy (ΔG) of various reaction intermediate steps during the associative pathway of the ORR are listed in Table 3.4.

Table 3.4: *All the reaction intermediates in the associative mechanism of the ORR along with their Gibbs free energy (ΔG) and relative free energy.*

O_2 reduction reaction steps	**ΔG (in eV)**	**Reaction intermediates**	**Relative free energies (in eV)**
$[LaNiO_3] \rightarrow [O_2_LaNiO_3]$	-0.66	$O_2_LaNiO_3$	-0.66
$[O_2_LaNiO_3] \rightarrow [OOH_LaNiO_3]$	-1.99	OOH_LaNiO_3	-2.65
$[OOH_LaNiO_3] \rightarrow [O_LaNiO_3]$	-0.21	$O_LaNiO_3 + H_2O$	-2.86
$[O_LaNiO_3] \rightarrow [OH_LaNiO_3]$	-2.28	OH_LaNiO_3	-5.13
$[OH_LaNiO_3] \rightarrow [LaNiO_3]$	0.15	$LaNiO_3 + H_2O$	-4.98

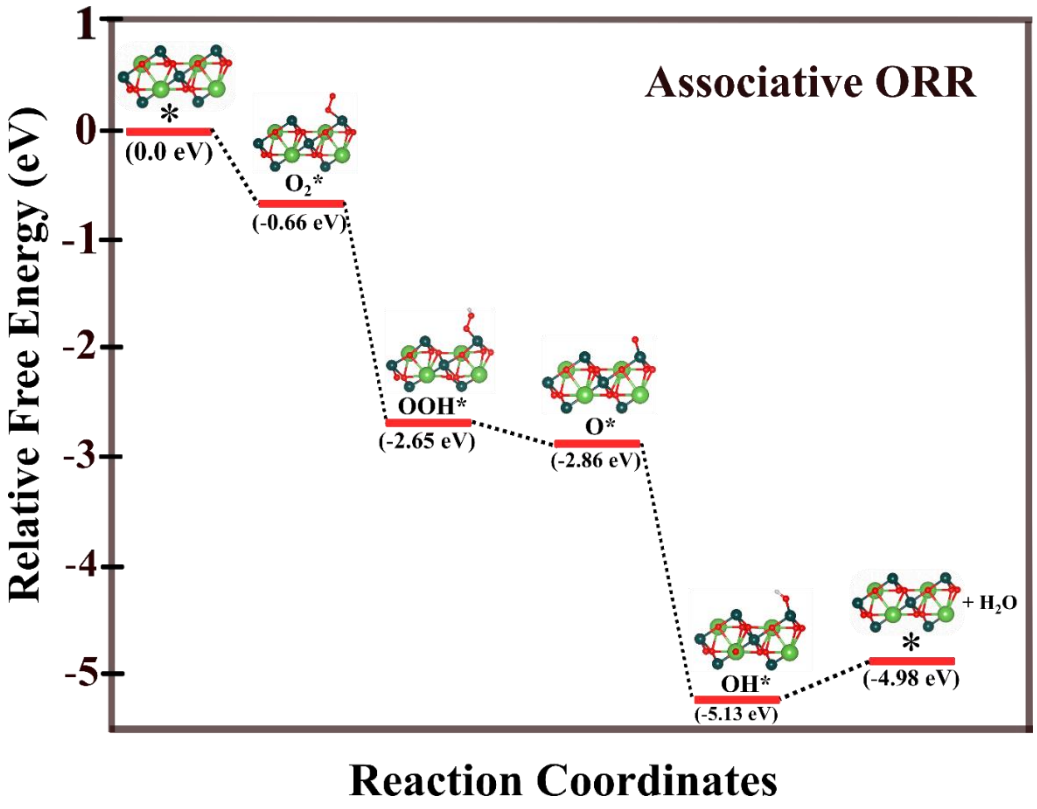


Figure 3.11: *Relative free energy profiles for the associative mechanism of the ORR on the surface of 2D monolayer $LaNiO_3$.*

To get a better understanding of thermodynamics related to a chemical reaction, we have computed and examined the relative Gibbs free energy (ΔG) of each reaction step of the ORR. We found that the change of Gibbs free energy (ΔG) during the reaction step involving O_2 dissociation ($O_2 \rightarrow 2O$) after O_2 adsorption was 0.76 eV. The positive value of ΔG signifies that the O_2 dissociation reaction step is endothermic which means an additional energy input is required for this step to proceed the ORR, whereas the associative pathway involves the formation of an OOH reaction intermediate after the O_2 adsorption. We found that reaction intermediate OOH_$LaNiO_3$ formed from the O_2_$LaNiO_3$ intermediate with a value of ΔG of about −1.99 eV, which is negative. The negative value of ΔG signifies that this reaction step is exothermic which means this step is spontaneous and no external energy input is needed in this ORR step. Comparing the values of ΔG in both cases, we can conclude that the most thermodynamic favorable pathway will be the one whose reaction step is spontaneous and energetically favorable. Hence, the associative reaction pathway of the ORR on the surface of 2D monolayer $LaNiO_3$ is thermodynamically more favorable than the dissociative pathway.

If a particular step in the ORR process has a positive Gibbs free energy ($\Delta G > 0$), it indicates that the step is endergonic in nature under the standard conditions. Oxidation–reduction reactions, commonly known as redox reactions, are reactions that involve the transfer of electrons from one species to another. The species that loses electrons is said to be oxidized, while the species that gains electrons is said to be reduced. The driving force for redox reaction is the difference in the electric potential of the two substances that are involved in electron transfer. In the subject reaction, the last step of the ORR in both dissociative and associative reaction pathways is [OH_$LaNiO_3$] → [$LaNiO_3$] + H_2O with an energy cost (ΔG) of about 0.15 eV obtained by the PBE-D3 method as reported in Tables 3.3 and 3.4. Therefore, the driving force of this step is simple, the difference in the electric potential of these two consecutive reaction steps which is $|\Delta G/e| = 0.15$ V. The positive value of ΔG of the last reaction step ([OH_$LaNiO_3$] → [$LaNiO_3$] + H_2O) of both the ORR pathways is favorable for the easy desorption of the H_2O molecule from the surface of the 2D monolayer $LaNiO_3$ perovskite; where the relative value of free energy of this step is about −4.98 eV as reported in Tables 3.3 and 3.4.

Theoretical Overpotential

Overpotential is the minimum additional potential required for the ORR to occur and effectively signifies the likelihood of an ORR taking place.[54,55] Overpotential can be calculated using the following equation (3.4),

$$\eta^{ORR} = 1.23 - \frac{min\ (\Delta G\ of\ ORR\ steps)}{e} \tag{3.4}$$

Here, the rate-determining step is the OH desorption step which produces the second H_2O molecule that again makes the catalyst's surface ready for further O_2 adsorption. The overpotential was found to be 1.08 V.

3.6 Summary

In our present study, we used DFT-D3 calculations to investigate the electronic structure and properties of the 3D bulk $LaNiO_3$ perovskite. From the electronic property calculations of the 3D $LaNiO_3$ system, we found that it has conducting properties with a zero band gap and a large electron density is present around the Fermi level (E_F) in the total density of states. However, this property alone is not sufficient for it to be used as an electrocatalyst for the ORR as it has a less active surface area. To address this, we

computationally designed a 2D monolayer $LaNiO_3$ from the 3D $LaNiO_3$ by cleaving the (0 0 1) surface to increase the active surface area. Additionally, we made a vacuum space perpendicular to the 2D single-layer $LaNiO_3$ slab to avoid spurious interactions between different layers, i.e., two consecutive layers. Using the PBE-D3 method, we studied the structural and electronic properties of 2D monolayer $LaNiO_3$ to determine its catalytic activity. Then, we computationally explored the mechanism of the ORR on the surface of the 2D monolayer $LaNiO_3$ by realizing different reaction intermediates at each step. Theoretically, we calculated Gibbs free energy and relative free energies of various reaction intermediates occurring in the ORR mechanisms. As per our study, the ORR mechanism follows both the associative and the dissociative reaction pathways on the surface of the 2D monolayer $LaNiO_3$ slab. In the dissociative pathway of the ORR, all of the reaction steps in the potential energy surface (PES) are downhill except during the O_2 dissociation step, whereas in the case of the associative pathway, we obtained negative free energies with downhill in the PES for each reaction step. All the ORR steps are spontaneous and thermodynamically favorable, which shows the suitable catalytic properties of the 2D monolayer $LaNiO_3$ for reducing O_2 molecules to water. Our energy calculations demonstrate that 2D monolayer $LaNiO_3$ has excellent catalytic properties for catalyzing oxygen reduction reaction through the $4e^-$ transfer mechanism. To sum up, our findings indicate that the 2D monolayer $LaNiO_3$ exhibits high electrocatalytic activity, making it a highly promising candidate for fuel cells and other energy conversion devices that require efficient ORR catalysts. The theoretical calculations performed in this study provide insight into the fundamental mechanisms and thermodynamics of the ORR on the surface of 2D monolayer $LaNiO_3$. It should be noted here that the active basal plane of 2D monolayer $LaNiO_3$ perovskite exhibits excellent catalytic activity toward the ORR with a high four-electron reduction pathway selectivity. These results suggest that it breaks the catalytic performance of the Pt-free electrodes with a high surface area and makes it a favorable contestant for fuel cell elements in renewable technology. We hope that our findings in this study are useful for developing new and more efficient non-noble metal-based electrocatalysts that can help meet the growing energy demand for clean and renewable energy sources.

3.7 References

[1] K.A. Khan, M. Hasan, M.A. Islam, M.A. Alim, U. Asma, L. Hassan, M.H. Ali, A Study on Conventional Energy Sources for Power Production, Ijariie-Issn(O)

4 (2018) 214–228.

[2] H.B. Gray, Powering the planet with solar fuel, Nat. Chem. 1 (2009) 7.

[3] V. Kumar, S. Pakhira, Mechanistic Understanding of Efficient Electrocatalytic Hydrogen Evolution Reaction on a 2D Monolayer WSSe Janus Transition Metal Dichalcogenide, Mol. Syst. Des. Eng. 8 (2023) 1060–1074.

[4] A. Tyagi, K.M. Tripathi, R.K. Gupta, Recent progress in micro-scale energy storage devices and future aspects, J. Mater. Chem. A 3 (2015) 22507–22541.

[5] F. Papiya, A. Nandy, S. Mondal, P.P. Kundu, Co/Al_2O_3-rGO nanocomposite as cathode electrocatalyst for superior oxygen reduction in microbial fuel cell applications: The effect of nanocomposite composition, Electrochim. Acta 254 (2017) 1–13.

[6] S.N. Upadhyay, V.B. Sardar, A. Singh, V. Kumar, S. Pakhira, Elucidating the oxygen reduction reaction mechanism on the surfaces of 2D monolayer $CsPbBr_3$ perovskite, Phys. Chem. Chem. Phys. 24 (2022) 28283–28294.

[7] S.N. Upadhyay, S. Pakhira, Nanostructured Pt-doped 2D $MoSe_2$: an efficient bifunctional electrocatalyst for both hydrogen evolution and oxygen reduction reactions, Phys. Chem. Chem. Phys. 24 (2022) 22823–22844.

[8] S. Pakhira, V. Kumar, S. Ghosh, Revealing the Superior Electrocatalytic Performance of 2D Monolayer WSe_2 Transition Metal Dichalcogenide for Efficient H_2 Evolution Reaction, Adv. Mater. Interfaces 10 (2023) 2202075.

[9] Y. Zhu, Q. Lin, Y. Zhong, H.A. Tahini, Z. Shao, H. Wang, Metal oxide-based materials as an emerging family of hydrogen evolution electrocatalysts, Energy Environ. Sci. 13 (2020) 3361–3392.

[10] M.A. Abdelkareem, E.T. Sayed, N. Nakagawa, Significance of diffusion layers on the performance of liquid and vapor feed passive direct methanol fuel cells, Energy 209 (2020) 118492.

[11] W.H.S.Y.-C.-P. Razumney, G. Electroreduction of Oxygen: A New Mechanistic Criterion, J. Electroanal. Chem. Interfacial Electrochem 69 (1976) 195–201.

[12] A.A. Gewirth, M.S. Thorum, Electroreduction of dioxygen for fuel-cell

applications: Materials and challenges, Inorg. Chem. 49 (2010) 3557–3566.

[13] L. Khotseng, Oxygen reduction reaction, Electrocatal. Fuel Cells Hydrog. Evol. Theo. to Des. (2018) 27–44.

[14] L. Jörissen, Bifunctional oxygen/air electrodes, J. Power Sources 155 (2006) 23–32.

[15] S.F. Yuk, V.R. Cooper, Tuning oxygen electrocatalysis: Via strain on $LaNiO_3$(001), Phys. Chem. Chem. Phys. 21 (2019) 4738–4745.

[16] Y. Abe, I. Satoh, T. Saito, D. Kan, Y. Shimakawa, Oxygen Reduction Reaction Catalytic Activities of Pure Ni-Based Perovskite-Related Structure Oxides, Chem. Mater. 32 (2020) 8694–8699.

[17] Y. Zhu, D. Liu, H. Jing, F. Zhang, X. Zhang, S. Hu, L. Zhang, J. Wang, L. Zhang, W. Zhang, B. Pang, P. Zhang, F. Fan, J. Xiao, W. Liu, X. Zhu, W. Yang, Oxygen activation on Ba-containing perovskite materials, Sci. Adv. 8 (2022) eabn4072.

[18] J. Liu, J. Ma, Z. Zhang, Y. Qin, Y.-J. Wang, Y. Wang, R. Tan, X. Duan, T.Z. Tian, C.H. Zhang, others, 2021 Roadmap: electrocatalysts for green catalytic processes, J. Phys. Mater. 4 (2021) 22004.

[19] S.N. Upadhyay, D. Halba, L. Yadav, S. Pakhira, Illuminating the Role of Mo Defective 2D Monolayer $MoTe_2$ toward Highly Efficient Electrocatalytic O_2 Reduction Reaction, Langmuir 39 (2023) 17700–17712.

[20] Y. Gorlin, T.F. Jaramillo, A bifunctional nonprecious metal catalyst for oxygen reduction and water oxidation, J. Am. Chem. Soc. 132 (2010) 13612–13614.

[21] Y.C. Lu, Z. Xu, H.A. Gasteiger, S. Chen, K. Hamad-Schifferli, Y. Shao-Horn, Platinum-gold nanoparticles: A highly active bifunctional electrocatalyst for rechargeable lithium-air batteries, J. Am. Chem. Soc. 132 (2010) 12170–12171.

[22] Y. Wang, Y. Li, T. Heine, PtTe Monolayer: Two-Dimensional Electrocatalyst with High Basal Plane Activity toward Oxygen Reduction Reaction, J. Am. Chem. Soc. 140 (2018) 12732–12735.

[23] D.B. Meadowcroft, Low-cost oxygen electrode material, Nature 226 (1970) 847–848.

[24] J. Suntivich, H.A. Gasteiger, N. Yabuuchi, Y. Shao-Horn, Electrocatalytic measurement methodology of oxide catalysts using a thin-film rotating disk electrode, J. Electrochem. Soc. 157 (2010) B1263.

[25] I. Roche, E. Chainet, M. Chatenet, J. Vondrák, Carbon-supported manganese oxide nanoparticles as electrocatalysts for the oxygen reduction reaction (ORR) in alkaline medium: physical characterizations and ORR mechanism, J. Phys. Chem. C 111 (2007) 1434–1443.

[26] M.-H. Shao, K. Sasaki, R.R. Adzic, Pd- Fe nanoparticles as electrocatalysts for oxygen reduction, J. Am. Chem. Soc. 128 (2006) 3526–3527.

[27] J. Suntivich, H.A. Gasteiger, N. Yabuuchi, H. Nakanishi, J.B. Goodenough, Y. Shao-Horn, Design principles for oxygen-reduction activity on perovskite oxide catalysts for fuel cells and metal-air batteries, Nat. Chem. 3 (2011) 546–550.

[28] P. Gao, M. Grätzel, M.K. Nazeeruddin, Organohalide lead perovskites for photovoltaic applications, Energy Environ. Sci. 7 (2014) 2448–2463.

[29] P. Tan, M. Liu, Z. Shao, M. Ni, Recent Advances in Perovskite Oxides as Electrode Materials for Nonaqueous Lithium–Oxygen Batteries, Adv. Energy Mater. 7 (2017) 1602674.

[30] C.E. Beall, E. Fabbri, T.J. Schmidt, Perovskite Oxide Based Electrodes for the Oxygen Reduction and Evolution Reactions: The Underlying Mechanism, ACS Catal. 11 (2021) 3094–3114.

[31] M. Bursell, M. Pirjamali, Y. Kiros, $La_{0.6}Ca_{0.4}CoO_3$, $La_{0.1}Ca_{0.9}MnO_3$ and $LaNiO_3$ as bifunctional oxygen electrodes, Electrochim. Acta 47 (2002) 1651–1660.

[32] D. Chen, C. Chen, Z.M. Baiyee, Z. Shao, F. Ciucci, Nonstoichiometric Oxides as Low-Cost and Highly-Efficient Oxygen Reduction/Evolution Catalysts for Low-Temperature Electrochemical Devices, Chem. Rev. 115 (2015) 9869–9921.

[33] D. Zhang, Y. Song, Z. Du, L. Wang, Y. Li, J.B. Goodenough, Active $LaNi_{1-x}Fe_xO_3$ bifunctional catalysts for air cathodes in alkaline media, J. Mater. Chem. A 3 (2015) 9421–9426.

[34] H. Liang, Y. Hong, C. Zhu, S. Li, Y. Chen, Z. Liu, D. Ye, Influence of partial

Mn-substitution on surface oxygen species of $LaCoO_3$ catalysts, Catal. Today 201 (2013) 98–102.

[35] Y. Da, L. Zeng, C. Wang, C. Gong, L. Cui, A simple approach to tailor OER activity of Sr_x $Co_{0.8}Fe_{0.2}O_3$ perovskite catalysts, Electrochim. Acta 300 (2019) 85–92.

[36] M. Cheriti, A. Kahoul, Double perovskite oxides Sr_2MMoO_6 (M = Fe and Co) as cathode materials for oxygen reduction in alkaline medium, Mater. Res. Bull. 47 (2012) 135–141.

[37] W.T. Hong, M. Risch, K.A. Stoerzinger, A. Grimaud, J. Suntivich, Y. Shao-Horn, Toward the rational design of non-precious transition metal oxides for oxygen electrocatalysis, Energy Environ. Sci. 8 (2015) 1404–1427.

[38] G. Kresse, J. Furthmüller, J. Hafner, Theory of the crystal structures of selenium and tellurium: The effect of generalized-gradient corrections to the local-density approximation, Phys. Rev. B 50 (1994) 13181–13185.

[39] G. Kresse, J. Furthmüller, Efficiency of ab-initio total energy calculations for metals and semiconductors using a plane-wave basis set, Comput. Mater. Sci. 6 (1996) 15–50.

[40] J.P. Perdew, Y. Wang, Erratum: Accurate and simple analytic representation of the electron-gas correlation energy, Phys. Rev. B 45 (1992) 13244.

[41] J. Hafner, Ab-initio simulations of materials using VASP: Density-functional theory and beyond, J. Comput. Chem. 29 (2008) 2044–2078.

[42] J.P. Perdew, K. Burke, M. Ernzerhof, Generalized gradient approximation made simple, Phys. Rev. Lett. 77 (1996) 3865–3868.

[43] S. Grimme, J. Antony, S. Ehrlich, H. Krieg, A consistent and accurate ab initio parametrization of density functional dispersion correction (DFT-D) for the 94 elements H-Pu, J. Chem. Phys. 132 (2010) 154104.

[44] K. Hu, M. Wu, S. Hinokuma, T. Ohto, M. Wakisaka, J.I. Fujita, Y. Ito, Boosting electrochemical water splitting via ternary NiMoCo hybrid nanowire arrays, J. Mater. Chem. A 7 (2019) 2156–2164.

[45] K. Momma, F. Izumi, VESTA 3 for three-dimensional visualization of crystal, volumetric and morphology data, J. Appl. Crystallogr. 44 (2011) 1272–1276.

[46] C. Patel, R. Singh, M. Dubey, S.K. Pandey, S.N. Upadhyay, V. Kumar, S. Sriram, M. Than Htay, S. Pakhira, V. V Atuchin, others, Large and uniform single crystals of MoS_2 monolayers for ppb-level NO_2 sensing, ACS Appl. Nano Mater. 5 (2022) 9415–9426.

[47] A. Singh, S. Pakhira, Unraveling the Electrocatalytic Activity of Platinum Doped Zirconium Disulfide toward the Oxygen Reduction Reaction, Energy and Fuels 37 (2023) 567–579.

[48] A. Kulkarni, S. Siahrostami, A. Patel, J.K. Nørskov, Understanding Catalytic Activity Trends in the Oxygen Reduction Reaction, Chem. Rev. 118 (2018) 2302–2312.

[49] L. Yadav, S. Pakhira, Platinum-adsorbed defective 2D monolayer boron nitride: a promising electrocatalyst for O_2 reduction reaction, J. Mater. Chem. C 11 (2023) 15215–15232.

[50] L. Guan, B. Liu, L. Jin, J. Guo, Q. Zhao, Y. Wang, G. Fu, Electronic structure and optical properties of $LaNiO_3$: First-principles calculations, Solid State Commun. 150 (2010) 2011–2014.

[51] W. Tang, E. Sanville, G. Henkelman, A grid-based Bader analysis algorithm without lattice bias, J. Phys. Condens. Matter 21 (2009) 084204.

[52] G. Henkelman, H. Jónsson, Improved tangent estimate in the nudged elastic band method for finding minimum energy paths and saddle points, J. Chem. Phys. 113 (2000) 9978–9985.

[53] D. Sheppard, P. Xiao, W. Chemelewski, D.D. Johnson, G. Henkelman, A generalized solid-state nudged elastic band method, J. Chem. Phys. 136 (2012) 074103.

[54] S. Das, S. Bhattacharjee, S. Mondal, S. Dutta, N. Bothra, S. Pati, S. Bhattacharyya, Bimetallic Zero-Valent Alloy with Measured High-Valent Surface States to Reinforce the Bifunctional Activity in Rechargeable Zinc-Air Batteries, ACS Sustain. Chem. Eng. 9 (2021) 14868–14880.

[55] Y. Hao, P.-L. Gong, L.-C. Xu, J. Pu, L. Wang, L.-F. Huang, Contrasting Oxygen Reduction Reactions on Zero- and One-Dimensional Defects of MoS_2 for Versatile Applications, ACS Appl. Mater. Interfaces 11 (2019) 46327–46336.

Chapter 4

Cobalt-Platinum Nanoparticle Encapsulated within Carbon Nanotube for Superior O_2 Reduction Reaction

In this chapter, we have studied the cobalt-platinum (CoPt) nanoparticle encapsulated by a carbon nanotube (CNT), e.g., CoPt@CNT material as an efficient electrocatalyst for O_2 Reduction Reaction (ORR) by employing the first-principles based density functional theory (DFT) method. We have studied the structural and electronic properties of the CoPt@CNT system. We found that the equilibrium structure of the CoPt@CNT system has zero electronic band gap (E_g = 0). The presence of a large electron density of states (DOS) around the Fermi energy level ($\boldsymbol{E_F}$) in the total DOS confirms its conducting nature. The ORR mechanisms have been investigated on the surface of the CoPt@CNT by calculating the change in adsorption energy (ΔE) and Gibbs free energy (ΔG) of each reaction intermediate. Our energy calculations demonstrate that the active sites on the CoPt@CNT material are thermodynamically and energetically favorable for ORR. The four electron ($4e^-$) transfer mechanism of ORR including both dissociative and associative paths has been explored on the surface of the CoPt@CNT system. It should be mentioned here that the active basal plane of the subject material exhibits excellent catalytic activity toward the ORR with a high four-electron reduction pathway selectivity. This work indicates that the CoPt@CNT holds great promise as an efficient electrocatalyst for the ORR in fuel cells, offering a viable alternative to traditional Pt electrodes.

4.1 Introduction

The growing population and industrialization have increased the demand for advanced energy conversion devices.[12] The exploitation of fossil fuels and global energy demand has encouraged scientists to explore new clean energy sources such as fuel cells

and metal-air batteries (MABs) that can meet future energy demands.[50] In this regards, Fuel cells have gained wide attention due to their high efficiency and low greenhouse gas emissions.[17,44] An effective electrocatalyst is required to speed up the sluggish ORR process to that of hydrogen oxidation ($H \rightarrow H^+ + e^-$) at the anode for enhanced performance of the fuel cell.[45,48] Till now, platinum (Pt) and Pt-based catalysts are known to be the best electrocatalysts for ORR. [38] Exploring low-cost and efficient electrocatalysts for ORR is of utmost importance for replacing the high-cost Pt and Pt-based catalysts.[15] Low-cost transition metals Co, Fe, and Ni excel in ORR via bimetallic alloys, but their stability under harsh conditions improves when supported on CNTs.[32] Researchers have studied numerous electrocatalysts based on the CNTs by tuning with metal nanoparticles that have shown exceptional performance.[57] These attributes make CNTs a highly promising candidate for applications in fuel cells and energy conversion devices.

The abundant carbon material present on the Earth can be a potential candidate for catalyzing ORR than the precious metal-based catalyst through an in-depth study of its structure and electronic properties. Gong et al. found that the nitrogen-doped CNT (i.e., NCNT) in an alkaline medium has shown excellent electrocatalytic properties compared to the platinum supported on carbon (Pt/C).[8] The electrocatalytic activity of carbon material has been increased by N-doping which alters the spin density and charge density of the carbon atoms. Li et al. found that the Ni_3Fe nanoparticles encapsulated in N-doped carbon nanotube (i.e., Ni_3Fe@NCNT)-grafted carbon fibers in KOH medium showed excellent catalytic activity for H_2 evolution reaction (HER) with low overpotential.[18] Experimentally, it has been found that the Fe_4 encapsulation in single-walled CNT (i.e., SWCNT) showed better performance for ORR.[28] The transfer of electrons from Fe nanoparticles to the CNT reduces the local work function on the carbon surface during the reaction and dramatically boosts its catalytic activity.[5] Recently, Zhong et al. prepared a bifunctional catalyst by encapsulating Ni nanoparticles in the N-doped CNT (e.g., Ni@NCNTs) through the pyrolysis method and they found that it showed excellent performance and stability for both the ORR and OER in alkaline medium.[58] Similarly, Co-Ni nanoparticles encapsulated in N-doped graphite CNT (e.g., CoNi@NCNT) have demonstrated good ORR activity with higher durability due to the synergic effect between the NCNT layers and the nanoparticles.[28]

Very recently, Singh and Pakhira explored the ORR mechanism on the surface of the Co@SWCNT material in their study.[43] Recently, Liao et al. found that the CoPt nanoparticles exhibited remarkable ORR activity. They revealed that the Pt stabilized the structure of the CoPt nanoparticles, and it modifies the electronic property that improves ORR performance and durability.[20] Bi et al. proposed that the synergistic effect of Co and Pt enhances the electrocatalytic activity of $CoPt_3$ encapsulated N-doped carbon nanospheres (e.g., $CoPt_3$@NC) for both HER and OER.[1] Cai et al. experimentally synthesized $PtCo_3$ nanoparticle encapsulated carbon nanotube (e.g., $PtCo_3$@CNT) and they revealed that the $PtCo_3$@CNT exhibited high stability and performance for methanol oxidation reaction (MOR).[2] These experimental results demonstrate that the encapsulation of a combined Co and Pt nanoparticle inside CNT exhibits remarkable structural and electronic properties which significantly increases electrocatalytic activity. Following these experimental findings, we substituted Pt in the Co nanocluster of Co@SWCNT to form our studied material CoPt@CNT. Pt substitution in Co nanocluster introduces unique structural and electronic modifications for efficient electrocatalytic performance. The electronic property study of CoPt@CNT material reveals a significantly large electron DOS around the $\mathbf{E_F}$ compared to the Co@SWCNT, which is crucial for mass electron and charge transfer during chemical reactions. A high electron DOS near the $\mathbf{E_F}$ demonstrates excellent electrocatalytic nature of the CoPt@CNT. Also, the O_2 adsorption energy on the surface of CoPt@CNT and Co@SWCNT was -0.79 eV and +0.15 eV, respectively. Comparing the value of O_2 adsorption energy in both cases, we can conclude that the adsorption of O_2 molecule is energetically more favorable on the surface of CoPt@CNT. The electronegativity of Pt (the value of 2.28 in the Pauling scale) polarizes electron density at the CoPt-CNT interface, which creates localized electron rich regions that stabilize O_2 adsorption. This suggests that the CoPt nanoparticle has enhanced the activity of the CNT surface for adsorption of ORR intermediate species. This study introduces CoPt@CNT material as a novel electrocatalyst for ORR while utilizing minimal platinum content.

In this work, we have computationally designed a novel approach for exploring an efficient electrocatalyst for ORR. Here, we have aimed that a Co-Pt nanoparticle encapsulated within a carbon nanotube (e.g., CoPt@CNT) can be an efficient electrocatalyst towards ORR based on DFT-D3 calculations. At first, we

computationally studied the equilibrium structure and electronic properties of pure CNT (6,6) by employing the dispersion-corrected DFT method.[11,34–36,53] Then, we have encapsulated the Co-Pt nanoparticles inside the equilibrium structure of CNT and performed structural optimization to get the equilibrium geometry of CoPt@CNT material. Next, we have extended our study to determine the electronic properties (i.e., electronic band structures, total DOS, electronic band gap, etc.) of the CoPt@CNT material by applying the DFT-D3 method. We found that it is a conducting system with zero electronic band gap ($E_g = 0$), which was later confirmed from the total DOS where there is a presence of large electron DOS around the $\mathbf{E_F}$. After investigating the electronic and structural properties of the subject material, we have further continued our studies to explore the various reaction intermediates of the ORR by examining both the dissociative and associative reaction mechanisms on the surface of the CoPt@CNT material. It is found that the subject material is experimentally feasible, with high mechanical, thermodynamic, and chemical stability. We have calculated the change in adsorption energy (ΔE) and Gibbs free energy (ΔG) of various reaction intermediates involved in the subject reaction to investigate the energy profile during the subject reaction. Our study demonstrates that all the active sites present on the surface of the CoPt@CNT material have strong thermodynamic favorability for ORR which makes it a promising candidate for catalyzing O_2 reduction reaction efficiently. Quantum mechanical calculations using hybrid density functional theory reveal that the improved performance is due to the synergistic contributions from CoPt nanoparticles and the apical active sites on the CNT surface. Our current study can be used to explore new electrocatalysts that can show better catalytic performance which can further drive the research towards more clean and green energy conversion devices. The CoPt@CNT exhibits superior catalytic activity and high four-electron ($4e^-$) selectivity toward electrochemical ORR, making it promising for applications in fuel cells.

4.2 Computational Details

The first principles-based hybrid periodic density functional theory (DFT-D3) method was utilized to compute the equilibrium structure, lattice constants, and electronic properties of the CoPt@CNT system.[30,33,35] The calculations involved the application of the B3LYP-D3 method and were carried out using the *ab initio* CRYSTAL17 suite code.[6,7,47] To account for weak van der Walls (vdW) interactions, Grimme's semi-empirical third-order dispersion correction parameters

(Grimme's D3) were included in the DFT computation.[9–11] In the electronic band structure calculations, Gaussian-type orbitals (GTOs) were applied to obtain a detailed representation of the atomic orbitals of C, Co, and Pt atoms.[42,52] We employed non-spin polarized calculations using periodic hybrid DFT-D3 method to determine the equilibrium structure and investigate the electronic properties of our studied system. The *ab initio* CRYSTAL17 program computed a spin-polarized solution by defining electron occupancy as either up spin (α) or down spin (β) with the "ATOMSPIN" and "SPINLOCK" keywords.[6] In our present study, the basis sets employed for C, Co, and Pt atoms were of triple-ζ valence with polarization quality C_pob_TZVP_2012, Co_pob_TZVP_rev2, and Pt_pob_TZVP_rev2.[37] A 4x4x8 Monkhorst-Pack k-point grid was used for the geometry optimization, which was integrated inside the first Brillouin zone.[26] To compute the total DOS of the CoPt@CNT system, the atomic orbitals of C, Co, and Pt atoms were used. The energy, force, and electron density convergence were evaluated by setting the convergence threshold at 10^{-7} atomic units during all the calculations. We employed the VESTA software to generate visual representations and conduct structure analysis of our studied systems.[25]

4.3 Theory

In this study, we have computed the change in adsorption energy (ΔE) and Gibbs free energy (ΔG) of all the reaction intermediates of ORR, including basic thermodynamic corrections such as zero-point vibrational energy (ZPE) corrections and entropy contributions. All thermodynamic calculations were performed at room temperature (T = 298.15 K). The electrocatalytic activity of the CoPt@CNT material has been studied by realizing different reaction intermediates involved in the subject reaction. The thermodynamic stability of the reaction intermediates has been studied by calculating the adsorption energy (E_{ads}) given by,

$$E_{ads} = E_{adsorbate/CoPt@CNT} - E_{adsorbate} - E_{CoPt@CNT} \quad (4.1)$$

Where $E_{adsorbate/CoPt@CNT}$ is the total energy of the CoPt@CNT material with the adsorbate entities. $E_{adsorbate}$ and $E_{CoPt@CNT}$ are the energies of adsorbate entities (i.e., O_2, 2O, OOH, OH, etc.) and CoPt@CNT system, respectively. A negative value of adsorption energy indicates thermodynamic favorability due to exothermic chemisorption during the chemical reaction. The change in Gibbs free energy (ΔG) of reaction intermediates is calculated using the following equation at pH = 0,

$$\Delta G = \Delta E + \Delta E_{ZPE} - T\Delta S \quad (4.2)$$

Where ΔE, ΔE_{ZPE}, and ΔS are the differences in electronic energy, zero-point vibrational energy (ZPE), and entropy between the reactants and products. T is the temperature and the value of T is 298.15 K used here, i.e., all the thermodynamic calculations were performed at room temperature. The change in Gibbs free energy (ΔG) determines the thermodynamic favorability of the ORR mechanism. A reaction is thermodynamically favorable when ΔG < 0. Similarly, when adsorption energy is less than zero (ΔE < 0), the reaction is said to be energetically favorable.[3,23] When both the values of ΔG and ΔE of the ORR reaction steps are less than zero, the reaction steps are thermodynamically and energetically favorable, as no external energy is needed for ORR steps to proceed. In our calculations, entropic effects have been considered for the ORR mechanism. The Gibbs free energy (ΔG) for each ORR step has been calculated, which includes entropic contributions as per equation (4.2). The key difference between thermodynamically and energetically favorable lies in considering entropy. Energetically favorable reactions only consider the energy of the system, while thermodynamically favorable reactions consider both energy and entropy.[4] The total standard free energy of the subject reaction $O_2 + 2H_2 \rightarrow 2H_2O$ would be equal to or close to -4.92 eV. According to the computational hydrogen electrode (CHE) model proposed by Nørskov et al. at standard conditions, the free energy of $(H^+ + e^-)$ in solution is expressed as the energy of $1/2H_2$.[31]

$$G_{H^+ + e^-} = G_{\frac{1}{2}H_2} \quad (4.3)$$

4.4 Results and Discussions

In the present study, we have utilized 1D structure of pristine CNT to model our subject material CoPt@CNT for ORR. The equilibrium structure and electronic properties i.e., electronic band structure and total DOS of the pure CNT (6,6) have been computed after creating its initial geometry computationally. The equilibrium structure of pure CNT is shown in Figure 4.1a, and the value of the lattice constant was c = 2.44 Å. The equilibrium C–C bond length was found to be 1.42 Å, which is consistent with previously reported results.[39] The electronic band structure and total DOS of the pristine CNT are shown in Figure 4.2a, which has been computed by using ***Γ-L*** *k*-vector pathway. We found that the optimized structure of the pure CNT has zero band gap and

there is a small electron DOS around the E_F in the total DOS showing its semiconducting nature which accord with previous reported results.[30,43]

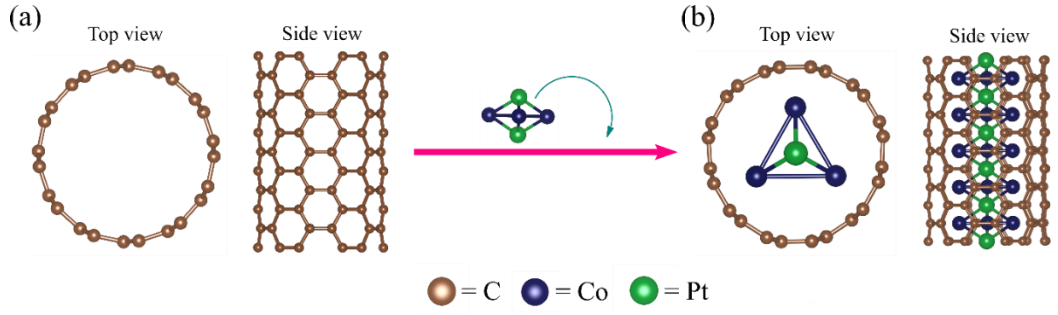


Figure 4.1: *Top and side views of the equilibrium structure of (a) CNT and (b) CoPt@CNT system.*

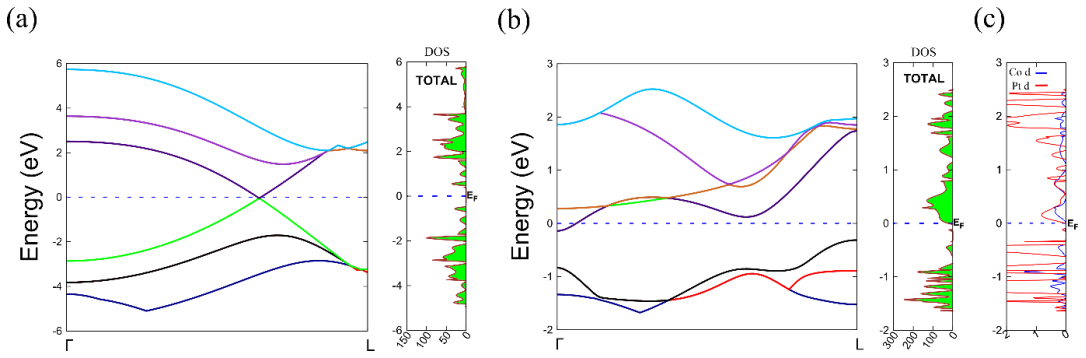


Figure 4.2: *(a) Electronic band structure and total DOS of the equilibrium structure of pure CNT, (b) electronic band structure and total DOS of the CoPt@CNT, and (c) PDOS plot depicting the contribution of the d-orbital electron density of the Co and Pt atoms in the CoPt@CNT.*

The CoPt nanoparticle was strategically encapsulated within the pristine CNT to study ORR. The DFT-D3 method was used to analyze the electronic structure and properties. The interaction between CoPt nanoparticle and CNT is crucial for understanding how encapsulation enhances ORR activity. The encapsulation of CoPt nanoparticles inside the CNT was modeled to examine the effects on the total DOS and adsorption energy of oxygen intermediate on the CNT surface during the ORR mechanism. Bi et al. experimentally studied water electrolysis using $CoPt_3$ nanoparticles encapsulated in nitrogen-doped carbon nanospheres, and they found that it showed excellent HER and OER activity.[1] Similarly, experimental studies have proposed that the cobalt-encapsulated nitrogen-doped carbon nanotubes show excellent ORR and OER performance.[19,22] Niu et al. proposed CoNi@NCNT material as a potential electrocatalyst for ORR.[30] These experimental findings suggested that the encapsulating nanoparticles within CNTs enhances electrocatalytic activity due to a synergistic effect. Following this theoretical and experimental evidence, the geometry

of CoPt nanoparticle was chosen to encapsulate inside the CNT to illuminate the ORR process. The electron DOS around the $\mathbf{E_F}$ was significantly improved by encapsulating the CoPt nanoparticle inside the pristine CNT, which is essential during the electrochemical reaction.

Zhang et al. demonstrated that the Co nanoparticles encapsulated by N-doped carbon nanotubes (Co@NCNTs) exhibited superior ORR activity compared to surface-decorated counterparts.[54] Similarly, Leng et al. found that the encapsulation of Co nanoparticles by nitrogen-doped carbon nanotube (Co@NCNT) demonstrated excellent ORR performance. The encapsulation results in high activity and stability during the ORR process.[16] The experimental study conducted by Bi et al. reveals that the synergistic effect of Co and Pt enhances the HER and OER performance of $CoPt_3$ encapsulated N-doped carbon nanospheres (e.g., $CoPt_3$@NC).[1] Some experimental studies revealed that the decorated nanoclusters on the surface of CNT have poor long-term durability because they are exposed to harsh electrochemical environments.[56] Recently, Singh and Pakhira reported excellent ORR electrocatalytic activity of Co nanocluster encapsulated inside SWCNT.[43] A theoretical and experimental study conducted by Niu et al. found that the CoNi cluster encapsulated within NCNT (CoNi@NCNT) exhibits promising electrocatalytic performance for both ORR and OER. Their research revealed that the encapsulation of CoNi nanoparticles significantly enhances the catalytic activity of the outer nitrogen-doped carbon layer.[30] Considering all the previously reported results, we have strategically encapsulated the CoPt nanoparticle within the pristine CNT to study the ORR mechanism. We have considered the equilibrium geometry of pristine CNT to model CoPt@CNT and optimized the resulting geometry of the CoPt@CNT to get the real minimum energy structure.

The equilibrium structure and electronic properties of the CoPt@CNT material were studied using DFT-D3 method. The equilibrium structure of the CoPt@CNT system is depicted in Figure 4.1b. The equilibrium lattice constant was found to be c = 2.48 Å. In the CoPt@CNT material, the equilibrium C–C bond distance was 1.43 Å while the equilibrium Co–Co and Co–Pt bond lengths were 3.68 Å and 2.46 Å, respectively, computed by the DFT-D3 method in the present study. A k-vector ***Γ-L*** path has been implemented to compute the electronic band structures and total DOS of the CoPt@CNT material as shown in Figure 4.2b. The equilibrium lattice constant c and

various bond distances of both the pristine CNT and CoPt@CNT materials are listed in Table 4.1. The present study finds that the equilibrium structure of CoPt@CNT shows conducting in nature, which means the electronic bands (both the valence bands and conduction bands) overlap with each other around the $\mathbf{E_F}$ as depicted in the electronic band structures calculations in Figure 4.2b. In the total DOS, there is a presence of large electron density in the vicinity of the $\mathbf{E_F}$ due to the overlapping of electronic bands that confirms the conducting property of the CoPt@CNT material.

We have theoretically designed CNT in such a way that it should have a high symmetry which is computationally feasible during all the calculations using CRYSTAL17 suite code. It is very hard to consider a long nanotube in the CRYSTAL17 program. Therefore, we have followed one joint experimental and theoretical work published by Niu et. al., and they designed their CNT and NCNT with the metal nanocluster.[30] In a similar way, Singh and Pakhira computationally designed a unit cell for the Co@CNT followed by the experimental work, and the nanotube is basically formed by the expansion of the unit cell (~Å). For the theoretical study of the ORR process, we have considered 1D nanostructure of the CoPt nanoparticle encapsulated within the pristine CNT with a high symmetry which reduces the computational costs. CoPt@CNT is not a zero-dimensional system because the electrons are not confined in all three spatial dimensions. Previous studies have demonstrated that the encapsulated Pt nanoparticles with 0D confinement cannot alter the 1D structure of the host CNT.[14] The electrons can propagate freely along the 1D axis of CNT, which is crucial during the reaction process. Here we have considered 1D CNT and CoPt@CNT nanotube structures, and in the Supporting Information, we have reported the simulated a van der Waals crystal with a 3D unit cell system consisting CoPt nanoparticle (0D) inside the CNT (quasi 1D) followed by previous joint experimental and theoretical work published by Niu et. al. It has been revealed that the encapsulated Sb_4Se_6 chains in carbon nanotubes (CNTs) exhibit 1D periodicity along the tube axis, which justifies the use of k-path analysis for band structure computation.[24] Encapsulation of nanoparticles within CNT creates a hybrid system where nanoparticles are physically isolated from direct environmental exposure but remain electronically and chemically interactive through the CNT walls. Similarly, in the CoPt@CNT system, electron mobility is anisotropic, with preferential conduction along the CNT axis. The computation of electronic band structure is essential for

studying the electronic properties and catalytic activity of the subject material. Herein, the ***Γ-L*** *k*-vector direction has been used to compute the electronic band structure of theoretically modeled CoPt@CNT material followed by previous joint experimental and theoretical work published by Niu et. al.

Comparing the total DOS of the pure CNT and CoPt@CNT as represented in Figures 4.2a and b, we have concluded that the encapsulation of CoPt nanoparticle has significantly increased the electron DOS near the $\mathbf{E_F}$ of CoPt@CNT material. We have plotted partial density of states (PDOS) of Co and Pt atoms to highlight the contribution of their ***d***-orbital electron density of states to the total DOS of CoPt@CNT material. The PDOS plot of Co and Pt atoms is shown in Figure 4.2c, where the blue and red lines represent the contributions of ***d***-orbital electrons of the Co and Pt atoms to the DOS. In Figure 4.2c, the blue line shows peaks near and below the $\mathbf{E_F}$, indicating significant contributions from the ***d***-orbital electrons of Co to the electronic structure of the system. Whereas the red line in PDOS represents the ***d***-orbital electrons of Pt, which shows broader peaks compared to the Co, indicating delocalized electronic states. In the PDOS plot, there is an overlap between the blue and red lines around the E_F, suggesting hybridization between the ***d***-orbital electrons of both Co and Pt atoms. The hybridization due to electronic coupling enhances the properties such as charge transfer and catalytic activity of the CoPt@CNT material. The synergic effect between encapsulated Co-Pt nanoparticle and CNT modifies the electronic properties of CoPt@CNT, making it an efficient candidate for mass electron and charge transfer.

There is a structural and electronic interaction between the pristine CNT and CoPt nanoparticle. In our present study, spin density analysis revealed localized electron density at the CoPt-CNT interfaces, as shown in Figure 4.3a, indicating interactions between the CoPt nanoparticle and the pristine CNT. Covalent bonds exist between the Co and C atoms in the CoPt@CNT material, as depicted in Figure 4.3b, resulting in efficient charge transfer during the ORR reaction. We have computed the change in adsorption energy (ΔE) and Gibbs free energy (ΔG) of each intermediate species involved in the ORR mechanism which are essential to understand the electrocatalytic performance of the CoPt@CNT material. This study shed light on the most favorable pathway followed by the ORR mechanism via analyzing electronic properties and free energies of each reaction intermediate. Zhang et al. found that the Co@NCNT have exhibited superior ORR and HER activity.[55] Recently, Singh and Pakhira proposed

that the Co nanocluster encapsulated within SWCNT has potential electrocatalytic activity for ORR.[43] Our results demonstrate that the CoPt encapsulation in CNT significantly improves catalytic activity, due to increased electron DOS near the $\mathbf{E_F}$, which is consistent with the finding of the recent investigation performed by Singh and Pakhira. Similarly, Deng et al. in their joint theoretical and experimental study explored that the iron encapsulated within CNTs (Fe_4@SWCNT) has shown excellent ORR activity. They found that the electron transfer takes place to the CNTs from the encapsulated Fe nanoparticle, which in turn enhances the catalytic activity of the SWCNT surface.[5] Our proposed material CoPt@CNT is a potential candidate for use in fuel cell applications for ORR catalysis, and it is comparable to other carbon-based materials that were reported earlier.

Now, we are quite curious whether this novel material CoPt@CNT is a promising candidate for fuel cell applications, as other Pt-based nanomaterials have displayed outstanding performance for launching the sluggish ORR. After confirming the conducting nature of the CoPt@CNT material, we have investigated the O_2 reduction reaction mechanisms on its surface by exploring various reaction intermediates w.r.t computational hydrogen electrode (CHE) model, and to this end, the ORR electrocatalytic activity with the reaction pathways of the subject material has been explored in detail.

Table 4.1: *Lattice constant and average bond distances of pristine CNT and CoPt@CNT.*

System	Lattice constant (c) (Å)	Average bond distance (Å)		
		C–C	Co–Co	Co–Pt
CNT	c = 2.44	1.42	-	-
CoPt@CNT	c = 2.48	1.43	3.68	2.46

4.5 Dissociative Reaction Mechanism

The dissociative mechanism of ORR involves O–O bond dissociation after the adsorption of O_2 molecules on the surface of CoPt@CNT. Successive reactions take place to form water via the combination of electrons and protons with oxygen atoms simultaneously.[40] The ORR mechanism steps have been explored by creating various reaction intermediates on the surface of the CoPt@CNT w.r.t computational hydrogen

electrode (CHE) model. The schematic representation of the $4e^-$ transfer mechanism of ORR is shown in Figure 4.4, where both the dissociative and associative reaction pathways have been represented with their incoming reaction intermediates formed during the ORR process. The addition of protons (H^+), electrons (e^-), and the removal of water (H_2O) molecules are shown with arrows. We have calculated the values of ΔG to plot the free energy diagram of the ORR mechanism. The change of Gibbs free energy values are cumulative sums of ΔG values after each reaction step, referenced to the pure surface (CoPt@CNT). This calculation was performed to track the total energy changes in the multistep ORR process.

CoPt@CNT material is obtained by encapsulating CoPt nanoparticles within the equilibrium CNT. The O_2 molecule gets adsorbed on the surface of the CNT rather than on the encapsulated CoPt nanocluster. Here, the carbon atom is the active site where the O_2 molecule gets adsorbed. Niu et al. proposed that the active site present on the surface of NCNT in CoNi@NCNT material, where O_2 can be adsorbed efficiently.[30] Nie et al. studied NiCo metal cluster encapsulated by the N-doped CNTs (NiCo@NCNT) for ORR and found that the encapsulation improved the charge transfer between the alloy and the NCNTs.[27] Recently, an ORR study by Singh and Pakhira on Co@SWCNT demonstrated that the encapsulation of Co nanoparticles altered the electronic properties of SWCNT. They also found that the encapsulated Co nanoparticles activated the surface of the SWCNT for efficient ORR.[43] Deng et al. found that the electron transfer from the Fe atoms to the CNT improved the electrocatalytic activity of iron encapsulated carbon nanotubes (e.g, Fe@SWCNT).[5] We have computed spin density calculations to explore the interaction between the CNT and encapsulated CoPt nanoparticle. From the spin density plot of the CoPt@CNT system as depicted in Figure 4.3a, it is clear that the *d* orbitals of Co and Pt atoms hybridize with the π-orbitals of the CNT which alter the electronic properties of the CoPt@CNT material. The adsorption of the O_2 molecule and subsequent ORR activity depend on the electronic interactions between the encapsulated nanocluster and the CNT surface. Charge polarization is induced by the encapsulated CoPt nanocluster, which modifies the electronic properties of the CNT surface. The synergic effect between the CoPt nanoparticle and CNT makes the surface active on which an O_2 molecule can easily get adsorbed for efficient ORR process.

The spin density plot of equilibrium CoPt@CNT is depicted in Figure 4.3a and the region with high positive spin density is rich in unpaired electrons that strongly interact with the adsorbed O_2 molecule. So, the O_2 molecule will favor attaching to the C atom having high positive spin density. In contrast, the other C atoms with low positive spin density are less favorable for O_2 adsorption on the surface of CoPt@CNT. To locate the most favorable active site, we calculated the O_2 adsorption energy of various possible adsorption sites on the surface of the CoPt@CNT. Our study examined four distinct carbon sites (C1, C2, C3, and C4) on the CNT surface for O_2 adsorption, as depicted in Figure 4.3b. We found that the O_2 adsorption energy on C1, C2, C3, and C4 adsorption sites was -0.79 eV, 3.98 eV, 3.80 eV, and 4.03 eV, respectively. The O_2 adsorption energy with high positive values is energetically unfavorable because extra energy input is required for O_2 adsorption. We can conclude that the most favorable adsorption site for the O_2 molecule will be the C1 atom (with O_2 adsorption energy of ΔE = -0.79 eV). ORR mechanisms have been explored on the most favorable C1 site on the CNT surface. In this study, we refer to the carbon atom at position 1 (C1) simply as the 'C atom' throughout.

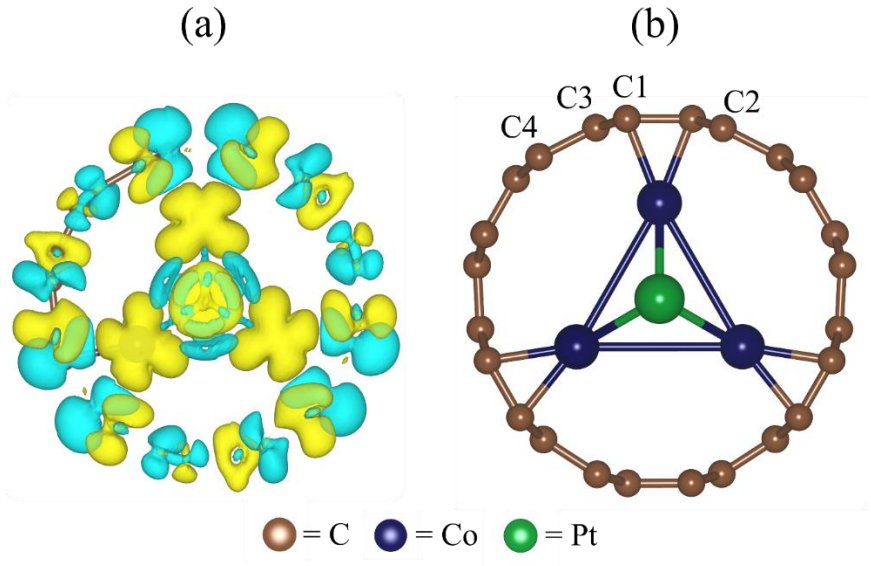


Figure 4.3: *(a) Electron spin density plot of CoPt@CNT and (b) representation of possible adsorption sites on the surface of CNT. The sky-blue and yellow color shapes represent the positive (α-spin up) and negative (β-spin down) values.*

Researchers have shown that the Co-encapsulated nanoparticle enhances and exposes active sites on the surface of NCNTs.[49] Similarly, the encapsulated CoPt nanoparticle modifies the electronic structure properties of CNT through charge redistribution, which enhances the reactivity of active sites for efficient O_2 adsorption. The interaction

of CoPt nanoparticle and CNT is represented through the spin density plot in Figure 4.3a. The *d*-orbital of CoPt and π-electrons of CNT induce spin polarization, which enhances the carbon site's reactivity for O_2 activation. Efficient O_2 activation on the CoPt@CNT surface is a critical step for initiating and facilitating the ORR mechanism.

***Step 1*:** In the first step, the O_2 molecule gets attached to the carbon atom close to Co of the CoPt@CNT, which results in the formation of the O_2_CoPt@CNT reaction intermediate. The equilibrium structure of the O_2_CoPt@CNT reaction intermediate is obtained by employing the DFT-D3 method. The equilibrium structure of the O_2_CoPt@CNT reaction intermediate is depicted in Figure 4.5a. The adsorption of the O_2 molecule on the CoPt@CNT material takes place with an energy release of about -0.79 eV. The formation of the O_2_CoPt@CNT reaction intermediate from CoPt@CNT is associated with a Gibbs free energy (ΔG) change of -0.71 eV. The negative value of change in adsorption energy (ΔE) and Gibbs free energy (ΔG) indicates that this reaction step is exothermic in nature. The formation of the O_2_CoPt@CNT reaction intermediate is spontaneous and thermodynamically favorable.

Deng et al. theoretically studied a Fe encapsulated single-walled carbon nanotube (Fe@SWCNT) for ORR and found that the O_2 adsorption energy on the pristine SWCNT and Fe@SWCNT was 1.43 eV and 0.03 eV.[5] Experimentally it has been found that the adsorption energy of the O_2 molecule on SWCNT and graphite was 0.80 eV and 0.52 eV.[46] Recently, Singh and Pakhira in their ORR study found that the O_2 adsorption energy on the surface of Co@SWCNT was +0.15 eV.[43] In the present study, the O_2 adsorption energy (ΔE) on the surface of the CoPt@CNT was found to be -0.79 eV (and the change in Gibbs free energy ΔG = -0.71 eV). The significantly lower (more negative) adsorption energy for CoPt@CNT (-0.79 eV) compared to the pristine CNTs indicates a much stronger interaction between O_2 and the CoPt@CNT surface. The negative value of adsorption energy signifies that the adsorption of the O_2 molecule on the surface of CoPt@CNT is exothermic and energetically favorable to initiate the ORR process. Unfortunately, there is no direct experimental value of the O_2 adsorption energy on the CoPt@CNT surface for direct comparison. The optimized lattice constant of O_2_CoPt@CNT was found to be c = 2.46 Å. The equilibrium C–O and O–O bond distances were 1.59 Å and 1.52 Å, respectively, obtained by the DFT-D3 method. The electronic band structures and total DOS of the O_2_CoPt@CNT reaction intermediate have been computed using ***Γ-L*** k-path which is

represented in Figure 4.5a. We observed that the equilibrium O_2_CoPt@CNT reaction intermediate has zero-band gap (E_g = 0). In the total DOS of the O_2_CoPt@CNT intermediate, there exists a large electron DOS around the $\mathbf{E_F}$ confirming its conducting property with higher mass electron and charge transfer during the chemical reaction.

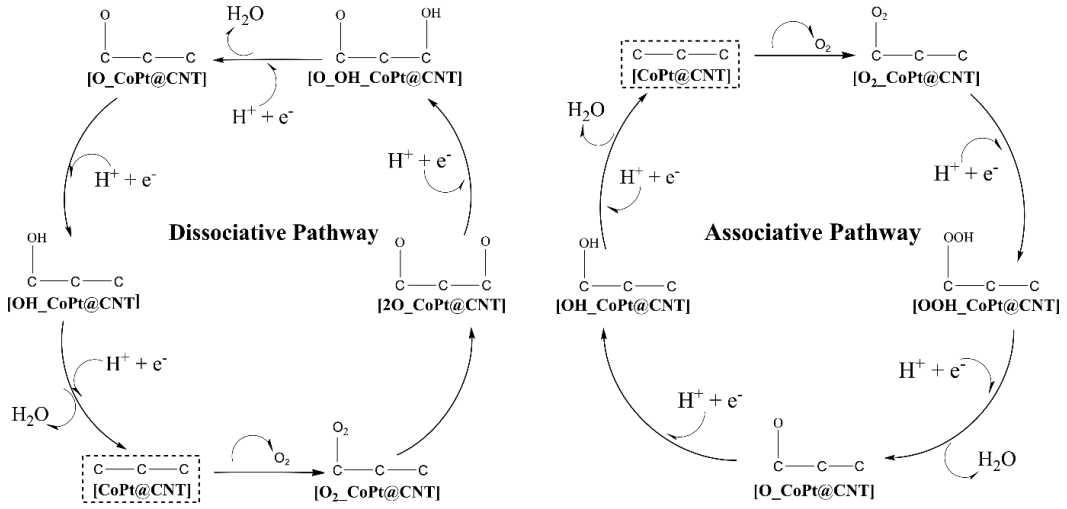


Figure 4.4: *Schematics of 4e⁻ transfer mechanism of ORR on the surface of the CoPt@CNT system. (The material enclosed within the dotted rectangle represents the CoPt@CNT where the ORR process occurs).*

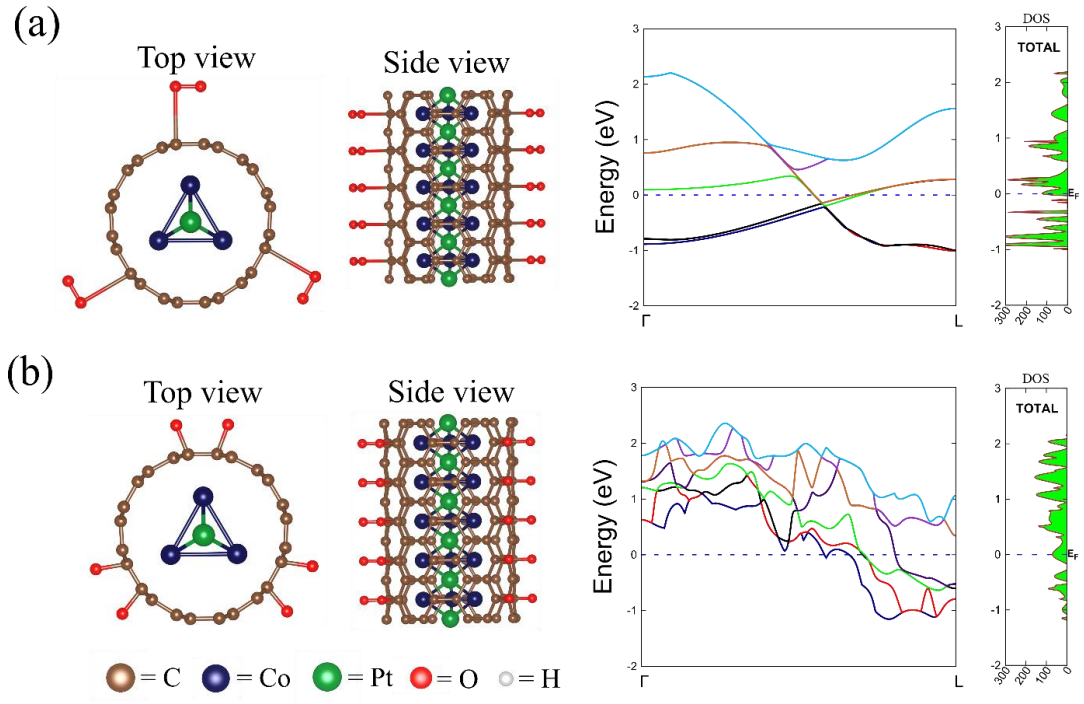


Figure 4.5: *Top view and side view, electronic band structure, and total DOS of the equilibrium structure of (a) O_2_CoPt@CNT and (b) 2O_CoPt@CNT reaction intermediates.*

Step 2: In this step, the O_2 molecule attached to the carbon atom dissociates into two activated oxygen atoms ($O_2^* \rightarrow 2O^*$). Here, "activated oxygen atoms" refers to the

adsorbed oxygen atom species in a reactive state. These adsorbed oxygen atoms form intermediate species and participate in subsequent steps of the ORR. The dissociation of the adsorbed O_2 molecule produces two O atoms, where each O atom retains a doublet ground state (two unpaired electrons). This unpaired electron configuration is critical for ORR kinetics, as it drives O_2 activation and subsequent steps of the $4e^-$ pathway on the surface of the CoPt@CNT material. Then one activated oxygen atom gets attached to another carbon atom on the surface of CoPt@CNT material which results in the formation of 2O_CoPt@CNT reaction intermediate. The equilibrium structure of 2O_CoPt@CNT is represented in Figure 4.5b, where the two activated oxygen atoms were attached to two different carbon atoms of the CoPt@CNT material. After the O_2 bond dissociation, the reaction intermediate 2O_CoPt@CNT is formed from the O_2_CoPt@CNT intermediate with an adsorption energy (ΔE) of approximately -0.10 eV and a Gibbs free energy (ΔG) of about 0.16 eV. The equilibrium structure of 2O_CoPt@CNT reaction intermediate has a lattice constant c = 2.46 Å. The average bond distance between carbon and oxygen atoms was 1.53 Å obtained by the DFT-D3 method. Figure 4.5b depicts the electronic band structures and total DOS of 2O_CoPt@CNT reaction intermediate which has been computed using a ***Γ-L*** direction. In the total DOS, there is high electron density around the $\mathbf{E_F}$ due to mass electron transfer which results in charge redistribution between the CoPt@CNT material and adsorbed O_2 molecule.

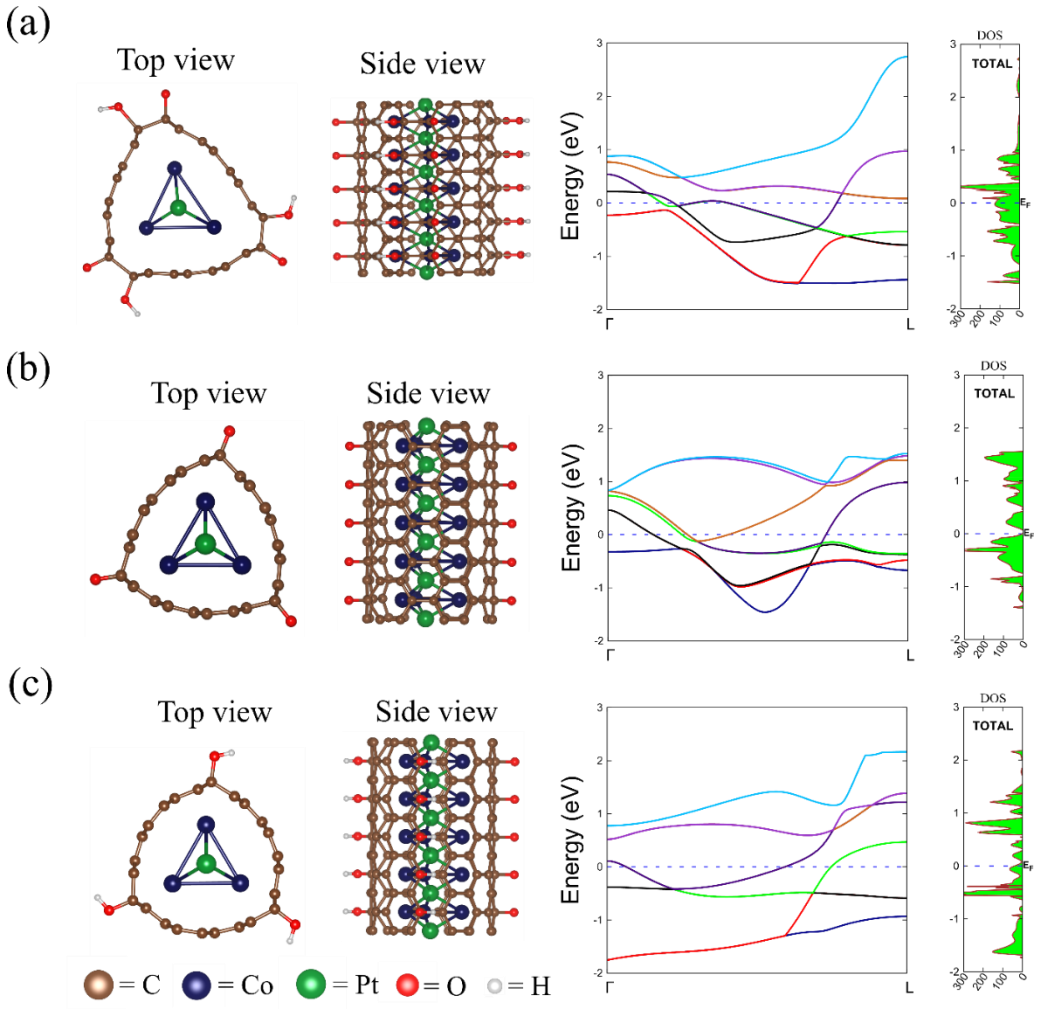


Figure 4.6: Top view and side view, band structure, and total DOS of the equilibrium structure of (a) O_OH_CoPt@CNT, (b) O_CoPt@CNT, and (c) OH_CoPt@CNT.

Step 3: In this step under acidic conditions, the combination of one activated oxygen atom from 2O_CoPt@CNT with a proton (H^+) and an electron (e^-) forms O_OH_CoPt@CNT reaction intermediate. The solution is the source of H^+. This reaction step was completed with an adsorption energy (ΔE) change of -1.64 eV and a corresponding Gibbs free energy (ΔG) change of -1.15 eV. The equilibrium structure of the O_OH_CoPt@CNT reaction intermediate is depicted in Figure 4.6a. The DFT-D3 method has been applied to study the electronic properties of the O_OH_CoPt@CNT reaction intermediate. In the O_OH_CoPt@CNT reaction intermediate, one activated oxygen atom and hydroxyl group (OH^-) are bonded with two different carbon atoms of the CoPt@CNT material. The lattice parameter i.e., lattice constants of O_OH_CoPt@CNT was found to be c = 2.52 Å. The equilibrium C–O and O–H bond lengths were 1.75 Å and 1.23 Å. The electronic properties i.e., band

structures and total DOS of O_OH_CoPt@CNT intermediate have been computed by using ***Γ-L*** path which is shown in Figure 4.6a.

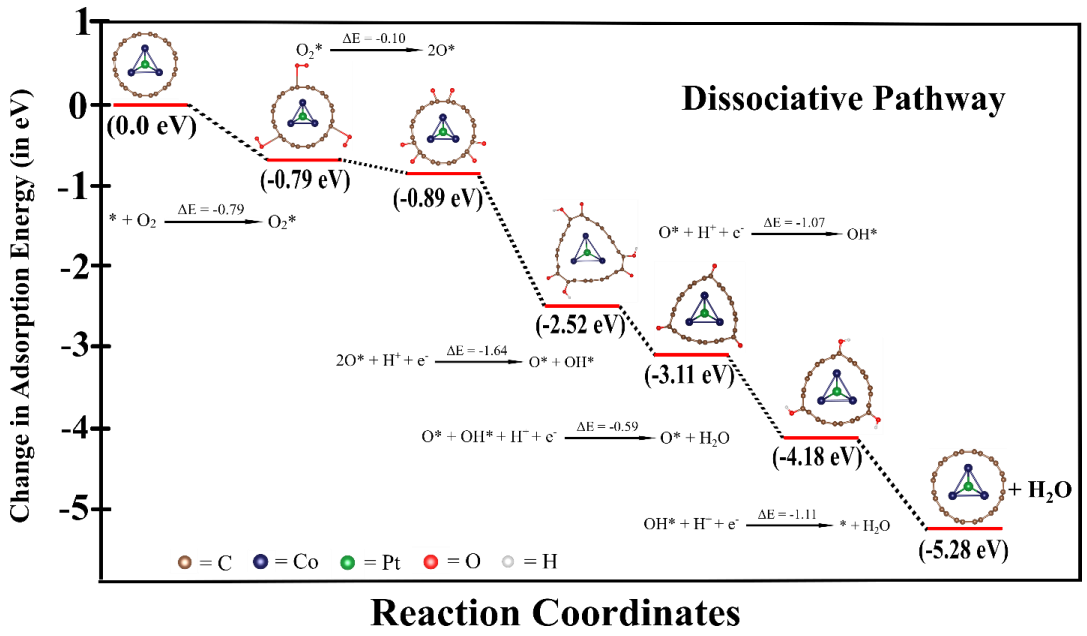


Figure 4.7: *Change in adsorption energy profile for various reaction intermediates involved during the dissociative mechanism of the ORR on the surface of the CoPt@CNT.*

Step 4: In the next step of the ORR mechanism, the hydroxyl group (OH^-) of the O_OH_CoPt@CNT reaction intermediate then combines with one proton and one electron to form a water molecule. The removal of one water molecule from the O_OH_CoPt@CNT intermediate after protonation leads to the formation of a new reaction intermediate namely O_CoPt@CNT. The completion of this reaction step involved with the cost of electronic energy (ΔE) -0.59 eV and free energy (ΔG) of -1.03 eV obtained by the DFT-D method. The negative values of ΔE and ΔG indicate that this reaction step is both energetically and thermodynamically favorable. The equilibrium structure of the O_CoPt@CNT reaction intermediate is illustrated in Figure 4.6b, with one activated oxygen atom attached to the carbon atom of CoPt@CNT material. The equilibrium lattice constant was found to be c = 2.49 Å. We found that the equilibrium C–O bond distance was 1.36 Å. Here, ***Γ-L*** k-path has been used to compute the electronic band structures and total DOS of O_CoPt@CNT reaction intermediate as shown in Figure 4.6b.

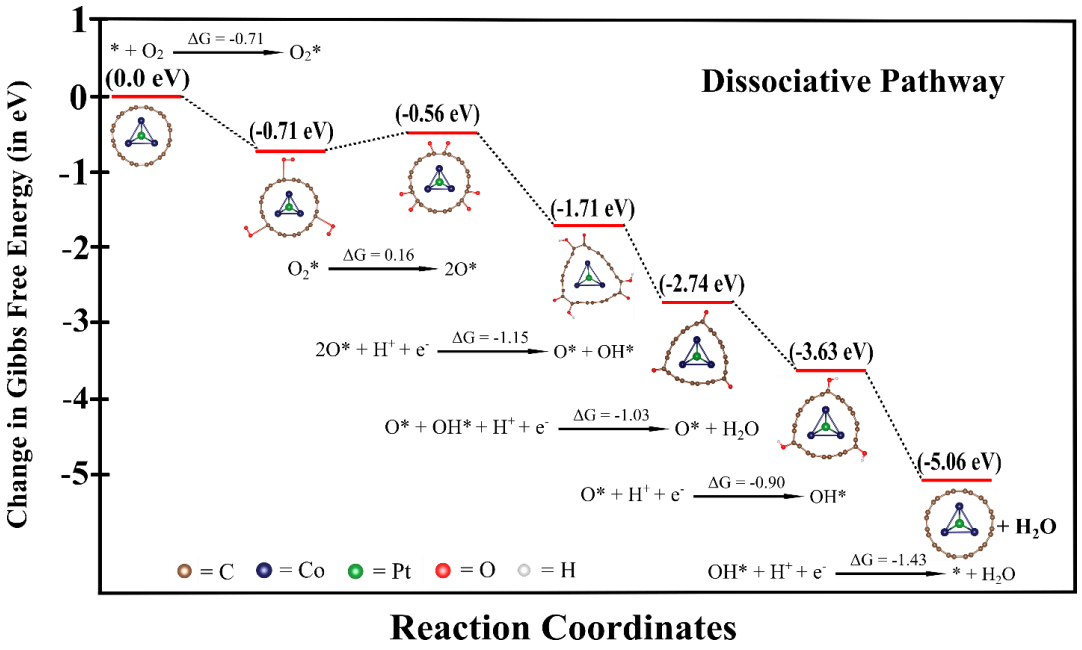


Figure 4.8: Gibbs free energy profile for the dissociative pathway of the ORR on the surface of the CoPt@CNT.

Step 5: The equilibrium structure of the OH_CoPt@CNT reaction intermediate is represented in Figure 4.6c. The formation of the OH_CoPt@CNT reaction intermediate takes place when another activated oxygen atom attached to the carbon atom of the O_CoPt@CNT intermediate reacts with one electron and one proton. So, in the equilibrium structure of OH_CoPt@CNT intermediate, only OH adsorbate is attached to the carbon atom. The formation of the OH_CoPt@CNT reaction intermediate from the O_CoPt@CNT intermediate involves the change of electronic energy (ΔE) change of -1.07 eV and free energy (ΔG) change of -0.90 eV. We found that the equilibrium lattice constant of OH_CoPt@CNT reaction intermediate was c = 2.50 Å. The optimized C–O and O–H bond lengths were 1.44 Å and 0.96 Å. The DFT-D3 method has been utilized to compute the electronic properties of OH_CoPt@CNT intermediate. Both the electronic band structures and total DOS calculations of OH_CoPt@CNT reaction intermediate are illustrated in Figure 4.6c, which is computed using ***Γ-L*** direction. The addition of one more electron and proton to the OH_CoPt@CNT reaction intermediate leads to the removal of the second water (H_2O) molecule with an adsorption energy cost of about -1.11 eV. This reaction step was completed with a Gibbs free energy (ΔG) change of approximately -1.43 eV. The negative value of change in adsorption energy and Gibbs free energy signifies that this reaction step is thermodynamically and energetically favorable. Hence, the ORR mechanism on the

surface of the CoPt@CNT system occurs via successive steps in a complete cycle where four electrons and four protons are simultaneously utilized to reduce O_2 to two water molecules. The lattice constant c and average bond distance of the reaction intermediates of the dissociative pathway are reported in Table 4.2. The change in adsorption energy and Gibbs free energy of all reaction intermediates involved in the dissociative pathway of ORR are listed in Table 4.3. The change in adsorption energy profile and Gibbs free energy profile of the dissociative path are shown in Figures 4.7 and 4.8. In the free energy profile, all the reaction steps are downhill, and the negative value of change of both the adsorption energy and Gibbs free energy of each reaction intermediate demonstrates that the active site present on the surface of the CoPt@CNT material is energetically and thermodynamically favorable for ORR reaction efficiently.

Table 4.2: *Lattice constant c and average bond distance of different reaction intermediates of the dissociative pathway.*

ORR intermediates	**Lattice constant (c) (Å)**	**Average bond distance (Å)**		
		C–O	**O–O**	**O–H**
O_2_CoPt@CNT	c=2.46	1.59	1.52	-
2O_CoPt@CNT	c=2.46	1.53	-	-
O_OH_CoPt@CNT	c=2.52	1.75	-	1.23
O_CoPt@CNT	c=2.49	1.36	-	-
OH_CoPt@CNT	c=2.50	1.44	-	0.96

Table 4.3: *Change in adsorption energy (ΔE) and change in Gibbs free energy (ΔG) of various reaction intermediates of the dissociative mechanism of the ORR.*

O_2 reduction reaction steps	**Change in adsorption energy ΔE (eV)**	**Change in Gibbs free energy ΔG (eV)**
[CoPt@CNT] → [O_2_CoPt@CNT]	-0.79	-0.71
[O_2_CoPt@CNT] → [2O_CoPt@CNT]	-0.89	-0.56
[2O_CoPt@CNT] → [O_OH_CoPt@CNT]	-2.52	-1.71
[O_OH_CoPt@CNT] → [O_CoPt@CNT]	-3.11	-2.74
[O_CoPt@CNT] → [OH_CoPt@CNT]	-4.18	-3.63
[OH_CoPt@CNT] → [CoPt@CNT]	-5.28	-5.06

4.6 Associative Reaction Mechanism

Here, we have also explored the associative mechanism of O_2 reduction reaction on the surface of the CoPt@CNT material by studying various reaction intermediate geometries. In the associative mechanism, the first reaction step involves the O_2 adsorption on the surface of the CoPt@CNT. Figure 4.4 shows the schematic diagram of the associative $4e^-$ transfer mechanism of ORR on the surface of the CoPt@CNT system. In the next step, the adsorbed O_2 (in the O_2_CoPT@CNT reaction intermediate) reacts with one proton and one electron to form the OOH_CoPt@CNT reaction intermediate. The equilibrium structure of the OOH_CoPt@CNT reaction intermediate has one hydrogen atom attached to the O_2 molecule on the surface of the CoPt@CNT material as displayed in Figure 4.9a. The electronic band structure and total DOS of the OOH_CoPt@CNT reaction intermediate are depicted in Figures 4.9b and c, which have been computed using a ***Γ-L*** direction. We found that the equilibrium lattice constant of the OOH_CoPt@CNT reaction intermediate was c = 2.50 Å. Additionally, the optimized O–H and O–O bond lengths were found to be 0.97 Å and 1.51 Å, obtained by the DFT-D3 method.

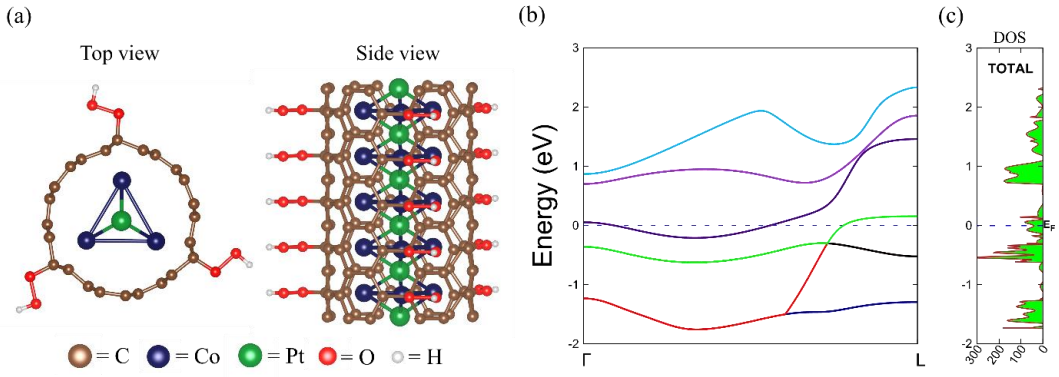


Figure 4.9: *(a) Top and side views, (b) electronic band structures, and (c) total DOS of equilibrium OOH_CoPt@CNT reaction intermediate computed by the DFT-D3 method.*

The formation of the OOH_CoPt@CNT reaction intermediate from the O_2_CoPt@CNT intermediate involves a change of free energy -0.25 eV and the change of electronic energy (ΔE) approximately -0.65 eV. The energy cost required for this reaction step to occur is negative, which implies that the formation of the OOH_CoPt@CNT reaction intermediate is spontaneous and thermodynamically favorable. In the further step, one more electron and proton react with the OOH_CoPt@CNT reaction intermediate to form water molecule. This reaction step

leads to the formation of O_CoPt@CNT reaction intermediate with the cost of free energy (ΔG) -1.87 eV (the value of ΔE is about -1.60 eV) obtained by the DFT-D3 method. Again, the addition of one electron and one proton to the O_CoPt@CNT results in the formation of OH_CoPt@CNT reaction intermediate with an energy cost (ΔG) -0.90 eV and the value ΔE is about -1.70 eV. In the last step, a second water molecule is formed after the combination of one more electron and proton to the OH_CoPt@CNT reaction intermediate with the value of ΔE = -0.47 eV. This last reaction step occurred with a cost of energy (ΔG) about -1.43 eV. Table 4.4 lists all the reaction intermediates of the associative pathway with their change in adsorption energy (ΔE) and change in Gibbs free energy (ΔG). Figures 4.10 and 4.11 depict the change in both adsorption energy profile and Gibbs free energy profile for various reaction intermediates involved in the associative pathway of ORR. In the free energy profile, all the reaction steps are downhill, which confirms the thermodynamic favorability and excellent catalytic activity of the CoPt@CNT material for catalyzing ORR through the $4e^-$ reduction pathway. Hence, a total of four electrons and four protons are used to reduce O_2 to two water molecules on the surface of the CoPt@CNT material. Therefore, we mainly focused on both the dissociative and associative reaction mechanisms, as it appears to be the most likely reduction pathway, the associative reaction mechanism as obtained in the present investigation. The atomic configurations of the associative ORR intermediates along the reaction path are explained here.

We have studied ORR via the formation of H_2O_2 pathway ($2e^-$ transfer mechanism) on the surface of CoPt@CNT material to compare with the $4e^-$ transfer mechanism. H_2O_2 (Hydrogen peroxide) or O intermediate is formed after protonation of the OOH intermediate via the addition of one electron and a proton. The change in Gibbs free energy (ΔG) for the formation of H_2O_2 from the OOH intermediate was -1.51 eV. Whereas the formation of O intermediate from the OOH reaction intermediate was -1.87 eV. Comparing the values of ΔG in both cases, the $4e^-$ pathway will suppress the H_2O_2 pathway as the formation of the O intermediate is spontaneous and thermodynamically favorable. So, the ORR mechanism will follow a $4e^-$ path selectivity on the surface of the CoPt@CNT material.

Table 4.4: *Values of change in adsorption energy (ΔE) and change in Gibbs free energy (ΔG) of various reaction intermediates involved in the associative pathway of the ORR on the surface of the CoPt@CNT material.*

ORR steps	Change in adsorption energy ΔE (eV)	Change in Gibbs free energy ΔG (eV)
[CoPt@CNT] → [O_2_CoPt@CNT]	-0.79	-0.71
[O_2_CoPt@CNT] → [OOH_CoPt@CNT]	-1.44	-0.97
[OOH_CoPt@CNT] → [O_CoPt@CNT]	-3.04	-2.84
[O_CoPt@CNT] → [OH_CoPt@CNT]	-4.74	-3.74
[OH_CoPt@CNT] → [CoPt@CNT]	-5.22	-5.17

In the present study, we have investigated the ORR mechanism on the surface of the CoPt@CNT material. The ORR mechanism followed both associative and dissociative pathways through a $4e^-$ reduction mechanism on the surface of the CoPt@CNT material. We have calculated both the values of ΔE and ΔG of each reaction intermediate involved in the ORR mechanism. The dissociative pathway that involves O–O bond dissociation has been examined in the present study. The values of ΔE and ΔG for the step involving O_2 dissociation were found to be -0.10 eV and 0.16 eV, obtained by the DFT-D method. The values of ΔE and ΔG in the O_2 dissociation step is very weak, which suggests that O_2 may easily break into atomic O on the surface of CoPt@CNT if we apply an energy (ΔG) +0.16 eV indicating a slight uphill. The associative pathway involves the protonation of the O_2 molecule via the addition of an electron ($e^–$) and proton (H^+), which forms an OOH intermediate. After the O_2 adsorption, the formation of the OOH intermediate occurred with a cost of free energy (ΔG) -0.25 eV which is downhill indicating thermodynamically more favorable than previous one. The values of both ΔE and ΔG for the formation of the OOH intermediate are significantly lower than the O_2 dissociation energy. This indicates that the CoPt@CNT favors OOH formation rather than the O_2 dissociation pathway during the ORR process. So, the associative pathway is more favorable than the dissociative pathway on the surface of CoPt@CNT material.

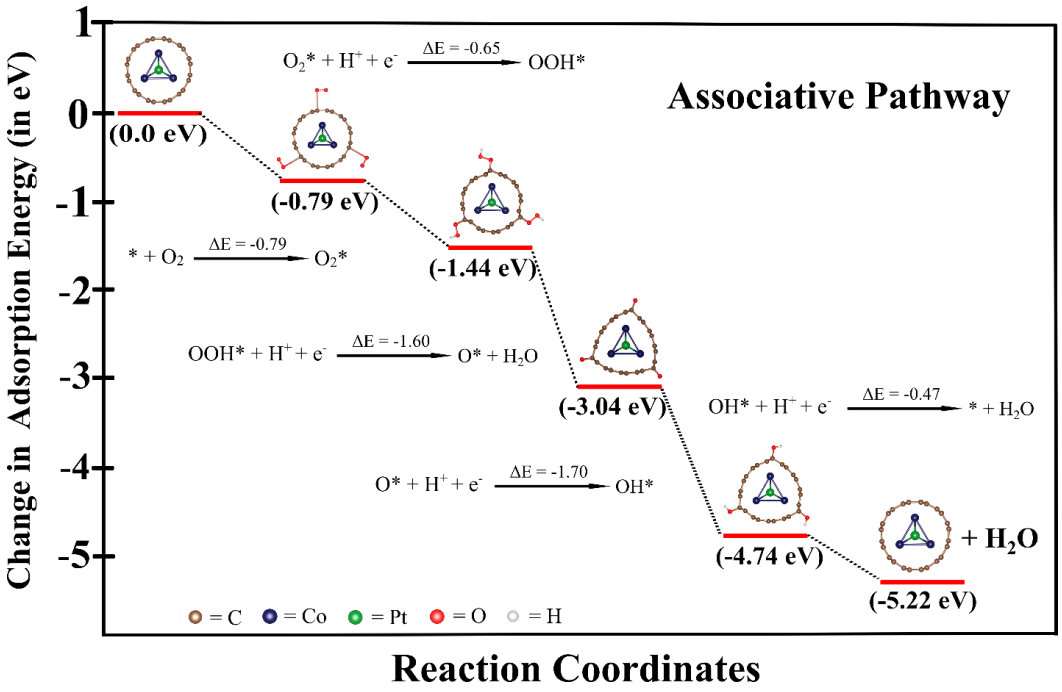


Figure 4.10: *Change in adsorption energy profiles for the reaction intermediates of the associative pathway of the ORR on the surface of the CoPt@CNT material.*

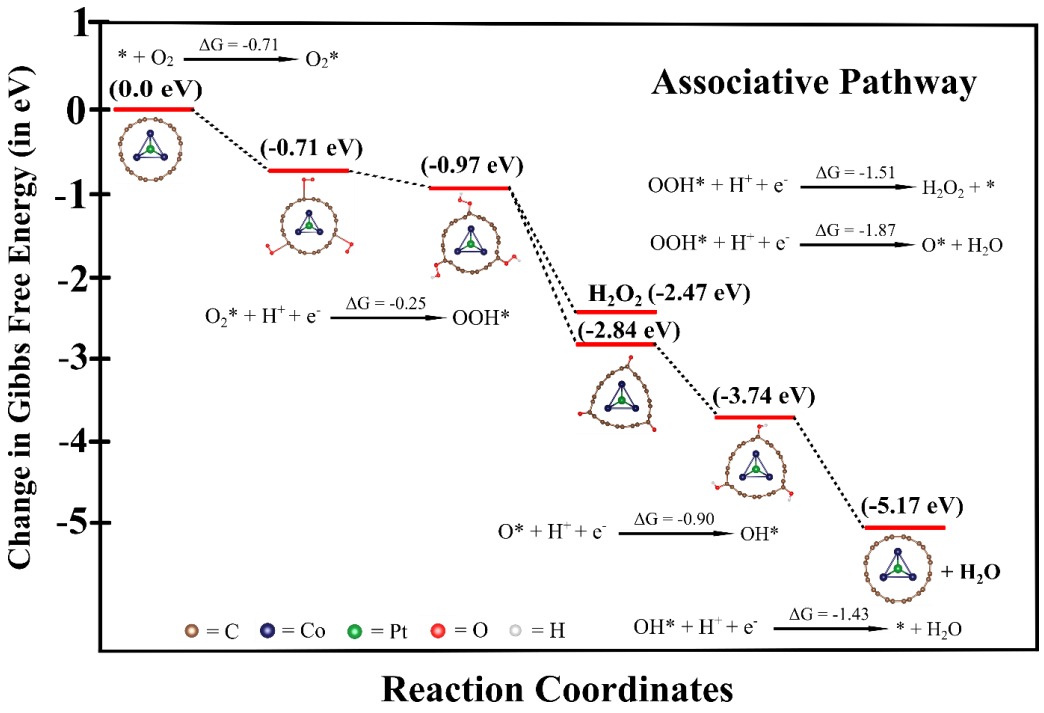


Figure 4.11: *Gibbs free energy profile for the associative pathway of the ORR on the surface of the CoPt@CNT.*

To investigate the ORR activity of CoPt@CNT, we have compared our results with the recent theoretical finding for Co@SWCNT reported by Singh and Pakhira employing the same B3LYP-D3 DFT method.[43] Earlier, Niu et al. demonstrated the

excellent ORR electrocatalytic activity of CoNi@NCNT material through theoretical studies. The enhanced catalytic performance of CoNi@NCNT was attributed to the synergistic effects between the NCNT and the encapsulated CoNi nanoparticles at the apical domain.[30] Similarly, encapsulated nanoparticle (Co or CoPt) inside the CNT significantly enhanced the electrocatalytic activity of the CNT surface for O_2 adsorption due to synergistic charge transfer at the nanoparticle-CNT interface. The O_2 adsorption energy on CoPt@CNT was -0.79 eV, whereas Singh and Pakhira reported O_2 adsorption energy of +0.15 eV for Co@SWCNT material. The significantly stronger O_2 adsorption on CoPt@CNT suggests that it enhances O_2 activation compared to Co@SWCNT. The O_2 adsorption is energetically more favorable on the surface of CoPt@CNT, which is crucial during the initial step of ORR. Like Co@SWCNT, CoPt@CNT material demonstrates $4e^-$ ORR selectivity over $2e^-$ H_2O_2 pathway. However, the ORR mechanism favors the associative path (reaction path involving $O_2^* \rightarrow OOH^*$) on the surface of CoPt@CNT, whereas Co@SWCNT favors an O_2 dissociation path ($O_2^* \rightarrow 2O^*$). Overall, the ORR catalytic activity of CoPt@CNT is comparable to the Co@SWCNT material.

Overpotential is the additional potential required to overcome the energy barrier of a reaction system in ORR. Lower overpotential indicates better catalytic activity and more efficient use of the catalyst material.[31,51] The reaction step with the maximum free energy change is the potential-determination step (PDS) in the ORR.[13] In the ORR process, overpotential is determined using the following equation,

$$\eta^{ORR} = \frac{\Delta G_{max}}{e^-} + 1.23\ V \tag{4.4}$$

Here, the O_2 dissociation reaction step ($O_2^* \rightarrow 2O^*$) is the rate-determining step in the ORR mechanism as depicted in Figure 4.8. The computed barrier height was found to be 0.16 eV. The ORR overpotential was found to be 1.39 V. It has been observed from both experimental and theoretical points of view that the ORR overpotential on real conventional Pt/C could be 0.69∼1.68 V.[31] The overpotential of CoPt@CNT material falls within this range. Liu et al. theoretically found that the bulk Pt (111) surface has exhibited an ORR overpotential of about 1.04 V.[21] Shui et al. found that in acidic PEM fuel cells, nitrogen doped graphene/multi-walled CNT composite as cathode catalyst has shown an ORR overpotential of 0.43 V.[41] Our studied material CoPt@CNT has a higher overpotential than the best-known Pt catalyst. However, it is

comparable to other best performing electrocatalyst, which have relatively moderate overpotentials. Though CoPt@CNT could not outperform the pure Pt catalyst, it can be used as a cathodic electrode in the fuel cells for ORR where the concentration of the Pt in the system studied here.

4.7 Summary

In summary, we computationally studied both the structural and electronic properties of equilibrium CNT by employing the DFT-D3 method. Then, we computationally encapsulated the Co-Pt nanoparticles within the optimized CNT to obtain CoPt@CNT material. The equilibrium structure of the CoPt@CNT material has been obtained by utilizing the same DFT-D3 method. We performed electronic properties calculation of the CoPt@CNT system at its equilibrium structure. The electronic band structures and total DOS of CoPt@CNT have been computed using the k vector ***Γ-L*** pathway. We found that the CoPt@CNT material has zero band gap ($E_g = 0$) and there is a presence of a large electronic DOS around the $\mathbf{E_F}$ in the total DOS which proves that it is metallic in nature. We further studied the ORR mechanism on the surface of the CoPt@CNT material based on the CHE models. In this study, we explored both the associative and dissociative mechanisms to realize the catalytic activity of CoPt@CNT material towards ORR. In particular, the CHE model-based computations demonstrated that the subject material is a promising ORR electrocatalyst candidate with an outstanding catalytic activity/performance and a high $4e^-$ reduction pathway selectivity. We have calculated the change of adsorption energy and Gibbs free energy of all the reaction intermediates involved in the ORR mechanism. Our study found that the formation of the O_2_CoPt@CNT reaction intermediate occurred after the adsorption of the O_2 molecule on the surface of the CoPt@CNT material with the values of ΔE and ΔG about -0.79 and -0.71 eV, respectively. All of the reaction steps in the change in electronic energy profile and Gibbs free energy profile of both associative and dissociative mechanisms of ORR are downhill. Negative values of change in both the adsorption energies and Gibbs free energy of various reaction intermediates show that no external energy input is needed. From our energy calculation, we found that the occurrence of each step in the ORR mechanism is spontaneous and thermodynamically feasible. The active sites present on the surface of the CoPt@CNT material are thermodynamically and energetically favorable for the O_2 reduction reaction. In summary, the studied material CoPt@CNT can be used as an excellent electrocatalyst for the ORR in fuel

cells. The present research work provides an insight into the evolution of CoPt@CNT electrocatalyst towards ORR and a deep understanding of the nature of active sites. We hope that our study will help to explore new efficient electrocatalysts for green energy conversion devices such as fuel cells and MABs. Our findings highlight the potential of the subject materials as viable alternatives to Pt-based electrodes, demonstrating their suitability as excellent components for fuel cells.

4.8 References

[1] J. Bi, X. Zhai, J. Chi, X. Wu, S. Chen, X. Wang, L. Wang, Ultrafine $CoPt_3$ nanoparticles encapsulated in nitrogen-doped carbon nanospheres for efficient water electrolysis, Electrochem. Sci. Adv. 2 (2022) e2100082.

[2] Z. Cai, M. Kamiko, I. Yamada, S. Yagi, $PtCo_3$ Nanoparticle-Encapsulated Carbon Nanotubes as Active Catalysts for Methanol Fuel Cell Anodes, ACS Appl. Nano Mater. 4 (2021) 1445–1454.

[3] X. Chen, R. Hu, F. Bai, DFT Study of the Oxygen Reduction Reaction Activity on Fe−N_4-Patched Carbon Nanotubes: The Influence of the Diameter and Length, Materials 10 (2017) 549.

[4] M. del Cueto, P. Ocón, J.M.L. Poyato, Comparative Study of Oxygen Reduction Reaction Mechanism on Nitrogen-, Phosphorus-, and Boron-Doped Graphene Surfaces for Fuel Cell Applications, J. Phys. Chem. C 119 (2015) 2004–2009.

[5] D. Deng, L. Yu, X. Chen, G. Wang, L. Jin, X. Pan, J. Deng, G. Sun, X. Bao, Iron encapsulated within pod-like carbon nanotubes for oxygen reduction reaction, Angew. Chemie Int. Ed. 52 (2013) 371–375.

[6] R. Dovesi, A. Erba, R. Orlando, C.M. Zicovich-Wilson, B. Civalleri, L. Maschio, M. Rérat, S. Casassa, J. Baima, S. Salustro, others, Quantum-mechanical condensed matter simulations with CRYSTAL, Wiley Interdiscip. Rev. Comput. Mol. Sci. 8 (2018) e1360.

[7] A. Erba, J. Baima, I. Bush, R. Orlando, R. Dovesi, Large-scale condensed matter DFT simulations: performance and capabilities of the CRYSTAL code, J. Chem. Theory Comput. 13 (2017) 5019–5027.

[8] K. Gong, F. Du, Z. Xia, M. Durstock, L. Dai, Nitrogen-doped carbon nanotube

arrays with high electrocatalytic activity for oxygen reduction, Science 323 (2009) 760–764.

[9] S. Grimme, Accurate description of van der Waals complexes by density functional theory including empirical corrections, J. Comput. Chem. 25 (2004) 1463–1473.

[10] S. Grimme, Semiempirical GGA-type density functional constructed with a long-range dispersion correction, J. Comput. Chem. 27 (2006) 1787–1799.

[11] S. Grimme, J. Antony, S. Ehrlich, H. Krieg, A consistent and accurate ab initio parametrization of density functional dispersion correction (DFT-D) for the 94 elements H-Pu, J. Chem. Phys. 132 (2010) 154104.

[12] G.E. Halkos, E.-C. Gkampoura, Reviewing usage, potentials, and limitations of renewable energy sources, Energies 13 (2020) 2906.

[13] R. Hu, Y. Li, Q. Zeng, J. Shang, Role of active sites in N-coordinated Fe-Co dual-metal doped graphene for oxygen reduction and evolution reactions: A theoretical insight, Appl. Surf. Sci. 525 (2020) 146588.

[14] X. Jin, J. Yan, X. Liu, Q. Zhang, Y. Huang, Y. Wang, C. Wang, Y. Wu, Spatial Confinement of Pt Nanoparticles in Carbon Nanotubes for Efficient and Selective H_2 Evolution from Methanol., Adv. Sci. 11 (2024) e2306893.

[15] K. Kumar, P. Gairola, M. Lions, N. Ranjbar-Sahraie, M. Mermoux, L. Dubau, A. Zitolo, F. Jaouen, F. Maillard, Physical and Chemical Considerations for Improving Catalytic Activity and Stability of Non-Precious-Metal Oxygen Reduction Reaction Catalysts, ACS Catal. 8 (2018) 11264–11276.

[16] Y. Leng, K. Jin, T. Wang, H. Sun, Facile Preparation of Cobalt Nanoparticles Encapsulated Nitrogen-Doped Carbon Sponge for Efficient Oxygen Reduction Reaction., Polymers 15 (2023) 521.

[17] J.-R. Li, M.-X. Liu, X. Liu, X.-H. Yu, Q.-Z. Li, Q. Sun, T. Sun, S. Cao, C.-C. Hou, The Recent Progress of Oxygen Reduction Electrocatalysts Used at Fuel Cell Level, Small Methods 8 (2023) 2301249.

[18] T. Li, G. Luo, K. Liu, X. Li, D. Sun, L. Xu, Y. Li, Y. Tang, Encapsulation of Ni_3Fe Nanoparticles in N-Doped Carbon Nanotube–Grafted Carbon Nanofibers

as High-Efficiency Hydrogen Evolution Electrocatalysts, Adv. Funct. Mater. 28 (2018) 1805828.

[19] S. Liang, C. Liang, High-Density Cobalt Nanoparticles Encapsulated with Nitrogen-Doped Carbon Nanoshells as a Bifunctional Catalyst for Rechargeable Zinc-Air Battery, Materials 12 (2019) 243.

[20] Q. Liao, H. Kuroki, T. Tamaki, M. Arao, M. Matsumoto, H. Imai, T. Yamaguchi, Three-Dimensionally Connected Platinum–Cobalt Nanoparticles as Support-Free Electrocatalysts for Oxygen Reduction, ACS Appl. Nano Mater. 8 (2025) 3323–3332.

[21] J. Liu, M. Jiao, L. Lu, H.M. Barkholtz, Y. Li, Y. Wang, L. Jiang, Z. Wu, D. Liu, L. Zhuang, C. Ma, J. Zeng, B. Zhang, D. Su, P. Song, W. Xing, W. Xu, Y. Wang, Z. Jiang, G. Sun, High performance platinum single atom electrocatalyst for oxygen reduction reaction, Nat. Commun. 8 (2017) 15938.

[22] Y. Liu, H. Jiang, Y. Zhu, X. Yang, C. Li, Transition metals (Fe, Co and Ni) encapsulated in nitrogen-doped carbon nanotubes as bi-functional catalysts for oxygen electrode reactions, J. Mater. Chem. A 4 (2016) 1694–1701.

[23] L.E.B. Lucchetti, P. A. S. Autreto, J.M. de Almeida, M.C. Santos, S. Siahrostami, Unravelling catalytic activity trends in ceria surfaces toward the oxygen reduction and water oxidation reactions, React. Chem. Eng. 8 (2023) 1285–1293.

[24] G.M. Milligan, Z.-F. Yao, D.L.M. Cordova, B. Tong, M.Q. Arguilla, Single Quasi-1D Chains of Sb_2Se_3 Encapsulated within Carbon Nanotubes, Chem. Mater. 36 (2024) 730–741.

[25] K. Momma, F. Izumi, VESTA3 for three-dimensional visualization of crystal, volumetric and morphology data, J. Appl. Crystallogr. 44 (2011) 1272–1276.

[26] H.J. Monkhorst, J.D. Pack, Special points for Brillouin-zone integrations, Phys. Rev. B 13 (1976) 5188.

[27] Y. Nie, X. Xu, X. Wang, M. Liu, T. Gao, B. Liu, L. Li, X. Meng, P. Gu, J. Zou, CoNi Alloys Encapsulated in N-Doped Carbon Nanotubes for Stabilizing Oxygen Electrocatalysis in Zinc–Air Battery, Nanomaterials 13 (2023) 1788.

[28] L. Niu, G. Liu, Y. Li, J. An, B. Zhao, J. Yang, D. Qu, X. Wang, L. An, Z. Sun, CoNi alloy nanoparticles encapsulated in N-doped graphite carbon nanotubes as an efficient electrocatalyst for oxygen reduction reaction in an alkaline medium, ACS Sustain. Chem. Eng. 9 (2021) 8207–8213.

[29] W. Niu, S. Pakhira, G. Cheng, F. Zhao, N. Yao, J.L. Mendoza-Cortes, B.E. Koel, Reaction-driven restructuring of defective $PtSe_2$ into ultrastable catalyst for the oxygen reduction reaction, Nat. Mater. 23 (2024) 1704–1711.

[30] W. Niu, S. Pakhira, K. Marcus, Z. Li, J.L. Mendoza-Cortes, Y. Yang, Apically dominant mechanism for improving catalytic activities of N-doped carbon nanotube arrays in rechargeable zinc-air battery, Adv. Energy Mater. 8 (2018) 1800480.

[31] J.K. Nørskov, J. Rossmeisl, A. Logadottir, L. Lindqvist, J.R. Kitchin, T. Bligaard, H. Jónsson, Origin of the Overpotential for Oxygen Reduction at a Fuel-Cell Cathode, J. Phys. Chem. B 108 (2004) 17886–17892.

[32] J.C. Ortiz-Herrera, H. Cruz-Martinez, O. Solorza-Feria, D.I. Medina, Recent progress in carbon nanotubes support materials for Pt-based cathode catalysts in PEM fuel cells, Int. J. Hydrogen Energy 47 (2022) 30213–30224.

[33] S. Pakhira, Rotational dynamics of the organic bridging linkers in metal-organic frameworks and their substituent effects on the rotational energy barrier, RSC Adv. 9 (2019) 38137–38147.

[34] S. Pakhira, D. Mandal, B. Mondal, A.K. Das, Theoretical study of spectroscopy, interaction, and dissociation of linear and T-shaped isomers of RgClF (Rg = He, Ne, and Ar) van der Waals complexes, Struct. Chem. 23 (2012) 681–692.

[35] S. Pakhira, K. Sen, C. Sahu, A.K. Das, Performance of dispersion-corrected double hybrid density functional theory: A computational study of OCS-hydrocarbon van der Waals complexes, J. Chem. Phys. 138 (2013) 164319.

[36] K. Parveen, S. Pakhira, Designing organic bridging linkers of metal–organic frameworks for enhanced carbon dioxide adsorption, New J. Chem. 48 (2024) 13700–13714.

[37] M.F. Peintinger, D.V. Oliveira, T. Bredow, Consistent Gaussian basis sets of

triple-zeta valence with polarization quality for solid-state calculations, J. Comput. Chem. 34 (2013) 451–459.

[38] M. Shao, Q. Chang, J.-P. Dodelet, R. Chenitz, Recent advances in electrocatalysts for oxygen reduction reaction, Chem. Rev. 116 (2016) 3594–3657.

[39] E.F. Sheka, L.A. Chernozatonskii, Bond Length Effect on Odd-Electron Behavior in Single-Walled Carbon Nanotubes, J. Phys. Chem. C 111 (2007) 10771–10779.

[40] P. Shen, Electrochemical Oxygen Reduction Fundamental and Applications, Springer, 2021.

[41] J. Shui, M. Wang, F. Du, L. Dai, N-doped carbon nanomaterials are durable catalysts for oxygen reduction reaction in acidic fuel cells, Sci. Adv. 1 (2015) e1400129.

[42] A. Singh, S. Pakhira, Unraveling the Electrocatalytic Activity of Platinum Doped Zirconium Disulfide toward the Oxygen Reduction Reaction, Energy & Fuels 37 (2023) 567–579.

[43] A. Singh, S. Pakhira, Revealing the Mechanism and Activity of O_2 Reduction Reaction of Co Nanocluster Encapsulated by Carbon Nanotube, Energy & Fuels 38 (2024) 11837–11851.

[44] A.B. Stambouli, Fuel cells: The expectations for an environmental-friendly and sustainable source of energy, Renew. Sustain. Energy Rev. 15 (2011) 4507–4520.

[45] G.-L. Tian, M.-Q. Zhao, D. Yu, X.-Y. Kong, J.-Q. Huang, Q. Zhang, F. Wei, Nitrogen-doped graphene/carbon nanotube hybrids: in situ formation on bifunctional catalysts and their superior electrocatalytic activity for oxygen evolution/reduction reaction, Small 10 (2014) 2251–2259.

[46] H. Ulbricht, G. Moos, T. Hertel, Physisorption of molecular oxygen on single-wall carbon nanotube bundles and graphite, Phys. Rev. B 66 (2002) 75404.

[47] S.N. Upadhyay, S. Pakhira, Mechanism of electrochemical oxygen reduction reaction at two-dimensional Pt-doped $MoSe_2$ material: an efficient

electrocatalyst, J. Mater. Chem. C 9 (2021) 11331–11342.

[48] S.N. Upadhyay, S. Pakhira, Nanostructured Pt-doped 2D $MoSe_2$: an efficient bifunctional electrocatalyst for both hydrogen evolution and oxygen reduction reactions, Phys. Chem. Chem. Phys. 24 (2022) 22823–22844.

[49] H. Wang, Q. Dong, L. Lei, S. Ji, P. Kannan, P. Subramanian, A.P. Yadav, Co Nanoparticle-Encapsulated Nitrogen-Doped Carbon Nanotubes as an Efficient and Robust Catalyst for Electro-Oxidation of Hydrazine, Nanomaterials 11 (2021) 2857.

[50] Z.-L. Wang, D. Xu, J.-J. Xu, X.-B. Zhang, Oxygen electrocatalysts in metal-air batteries: from aqueous to nonaqueous electrolytes, Chem. Soc. Rev. 43 (2014) 7746–7786.

[51] Z. Wu, G. Yang, Q. Zhang, Z. Liu, F. Peng, Deciphering the high overpotential of the oxygen reduction reaction via comprehensively elucidating the open circuit potential, Energy Environ. Sci. 17 (2024) 3338–3346.

[52] J. Xiao, J. Wang, Z. Xue, T. Zhang, J. Wang, Q. Li, The study of oxygen reduction reaction on Ge-doped MoS_2 monolayer based on first principle, Int. J. Energy Res. 45 (2021) 13748–13759.

[53] L. Yadav, S. Pakhira, Exploring and Elucidating the CO_2 Reduction Mechanisms on the Surface of Two-Dimensional Nitrogen-Vacancy (VN) Hexagonal Boron Nitride, Energy & Fuels 38 (2024) 18800–18813.

[54] D. Zhang, R. Ding, Y. Tang, L. Ma, Y. He, Stable Co/N-Doped Carbon Nanotubes as Catalysts for Oxygen Reduction, ACS Appl. Nano Mater. 5 (2022) 10026–10035.

[55] J. Zhang, W. Suo, Y. Han, Y. Cao, Y. Xu, M. Wang, Z. Liang, Y. Wang, H. Zheng, R. Cao, Co nanoparticles encapsulated in N-doped carbon nanotube materials derived from new metal–organic frameworks for oxygen electrocatalysis, J. Mater. Chem. A 13 (2025) 669–679.

[56] H. Zhao, Y. Chen, H. Zuo, L. Li, L. Li, F. Ai, Z. Tang, T. Xing, Y. Zhang, L. Tao, Z. Tian, H. Yang, X. Geng, B. An, Enhanced activity and durability of Pt nanoclusters catalyst by using nitrogen-doped carbon layer coated carbon

nanotubes as anchors and nanowires for ORR, Catal. Today 438 (2024) 114811.

[57] Y. Zhao, D. Liu, Y. Tian, Y. Zhai, C. Tian, S. Li, T. Xing, Z. Li, P. Dai, Fe_3N Nanoparticle-Encapsulated N-Doped Carbon Nanotubes on Biomass-Derived Carbon Cloth as Self-Standing Electrocatalyst for Oxygen Reduction Reaction, Nanomaterials 13 (2023) 2439.

[58] G. Zhong, S. Li, S. Xu, W. Liao, X. Fu, F. Peng, Nickel Nanoparticles Encapsulated in Nitrogen-Doped Carbon Nanotubes as Excellent Bifunctional Oxygen Electrode for Fuel Cell and Metal-Air Battery, ACS Sustain. Chem. Eng. 6 (2018) 15108–15118.

Chapter 5

An Investigation of Electrocatalytic Activity of the FeCe Nanoparticle Encapsulated Carbon Nanotube towards Oxygen Reduction Reaction

In this chapter, the Fe-Ce nanoparticles encapsulated within carbon nanotubes (FeCe@CNT) for the oxygen reduction reaction (ORR) have been investigated. The structural and electronic properties, i.e., electronic band structure and total density of states (DOS) of the FeCe@CNT material have been studied by employing first-principles based DFT-D3 method. Our present study found that the FeCe@CNT material has conducting properties due to its zero electronic band gap ($E_g = 0$). The electronic bands cross the Fermi energy level (E_F) with a large electron density of states around the E_F in total DOS, confirming its conducting nature of the subject material. This study explored all the reaction steps involved in the ORR mechanism on the surface of the FeCe@CNT system. The O_2 adsorption on the surface of the FeCe@CNT system occurred with an adsorption energy (ΔE) of -1.67 eV. This study found that the ORR mechanism on the surface of FeCe@CNT material proceeds through the four-electron ($4e^-$) transfer mechanism. The associative pathway of the ORR along with various reaction intermediates were explored with their adsorption energy. Our energy calculation demonstrates that the active sites on the FeCe@CNT material are thermodynamically favorable for catalyzing ORR. Our study found that the FeCe@CNT material is a potential candidate that can be used in the fuel cell as cathodic electrode material. The valuable insights revealed on (strong) FeCe nanoparticle interaction with the CNT advance the interfacial design of novel electrocatalysts towards ORR.

5.1 Introduction

In recent decades, various electrocatalysts for ORR have been explored by researchers which are carbon-based materials such as carbon nanotubes (CNTs) and nitrogen-doped carbon nanotubes (NCNTs) due to their unique property. Chen et al. found that NCNTs exhibited high ORR activity comparable to platinum-based catalysts.[1] The encapsulation of nanocluster within CNTs has received significant attention from researchers.[2–5] Recently, Niu et al. explored that the CoNi@NCNT/NF material showed excellent electrocatalytic activity for ORR and HER.[6] It has been experimentally found that the Ni_3Fe nanoalloy encapsulated within CNT/NCNT demonstrated excellent electrocatalytic activity for HER.[7] It is the synergic effect between the encapsulated metal nanoparticle and the CNT/NCNT that makes these materials a good cathodic material for ORR by improving the electronic properties. The interaction between the CNT and nanoparticle reduces the activation energy barrier and increases the stability during the chemical reaction.[8] It has been observed that high ORR activity and stability are achieved because of transition metal centers (e.g., Cu, Fe, and Co) in the metal nanoparticle encapsulated in CNT.[9] Yang et al. explored that iron/iron carbide (Fe/Fe_3C)-encapsulated in CNTs showed good bifunctional electrocatalytic activity for ORR and OER.[10] Recently, Zhan et al. synthesized Fe_3N nanoparticle encapsulated NCNT on the surface of a flexible carbon cloth, e.g., Fe_3N@NCNT/CC, and they found that it showed satisfactory ORR performance.[11] Recently, Singh and Pakhira theoretically studied the Co nanoparticle-encapsulated single-walled carbon nanotube (Co@SWCNT) and found that it has excellent catalytic activity for ORR.[12] Similarly, in one of our recent previous work, we have explored the CoPt@CNT material that have shown excellent catalytic activity for ORR mechanism.[13] This experimental and theoretical research inspired us to explore and study new non-noble based electrocatalysts for ORR, namely FeCe@CNT material. We have computationally designed Pt-free, FeCe@CNT material and investigated its electronic properties and electrocatalytic activities towards ORR.

In the present study, we have investigated the subject material FeCe@CNT as a potential candidate for catalyzing O_2 reduction reaction. At the beginning, we studied the equilibrium structure and electronic properties of a pristine carbon nanotube (CNT). We found that the pristine CNT is metallic in nature as there is a large electron density around the $\mathbf{E}_F$. Then, we computationally encapsulated Fe-Ce nanoparticles within the

equilibrium structure of the pristine CNT to make our studied material FeCe@CNT. The motivation for incorporating cerium (Ce) with iron (Fe) in our current work is due to Ce's unique electronic and redox properties. Some studies reported that the cerium-based catalysts have high ORR/OER performance due to the redox activity and oxygen vacancy formation.[14,15] The synergistic effect is achieved when the Ce atom is incorporated with the Fe in the carbon nanotubes (CNTs), where the Ce generally enhances the electronic environment of the Fe atoms towards subject reaction, i.e., ORR. The combination of Fe and Ce nanoparticles increases the electronic structure of the outer carbon wall in the FeCe@CNT material for efficient O_2 adsorption. Various studies have emphasized the significance of the synergistic interaction between encapsulated nanoparticles and CNTs, providing a valuable concept for developing well-stabilized electrocatalysts.[16] Experimentally, it has been found that the Ce doping in N-doped carbon frameworks demonstrates excellent ORR activity and durability.[17] Bi et al. found that the synergistic effect of Co and Pt with the carbon support enhances the electrocatalytic activity of $CoPt_3$@NC for HER and OER.[18] Recently, Singh and Pakhira theoretically explored the ORR mechanism on the surface of the Co@SWCNT material.[12] Theoretically and experimentally, Niu et al. designed and studied the catalytic activity of CNTs and NCNTs encapsulated by CoNi nanocluster which enhances the ORR activity of the CoNi@NCNT material.[6] These theoretical and experimental works have motivated us to explore the FeCe@CNT material for ORR. We hope that future experimental work could focus on synthesizing well-defined FeCe@CNT and other CNT-based materials for fuel cell applications towards ORR.

We thoroughly analyzed the equilibrium geometry and studied the electronic properties, i.e., electronic band structure, electronic band gap (E_g) and total electronic density of states (TDOS) of the FeCe@CNT material. In the TDOS, a large electron DOS around the $\mathbf{E_F}$ confirms the conducting nature of the FeCe@CNT material which is essential for an electrocatalyst towards ORR. We found that the FeCe@CNT's catalytic activity emerges due to the synergic effect between carbon nanotube and Fe-Ce nanoparticle. After confirming the conducting nature of the FeCe@CNT material, we started to explore both the associative and dissociative ORR mechanisms to investigate its electrocatalytic activity. We studied each reaction intermediate of the ORR mechanism by calculating their adsorption energy (E_{ads}). In this study, we have not discussed the

dissociative mechanism because the energy required during the O_2 dissociation step ($O_2^* \rightarrow 2O^*$) was highly positive which is unfavorable for the initiation of ORR process. The positive value of adsorption energy in the case of the O_2 dissociation step signifies that an input of external energy is needed for this step to occur which is thermodynamically and energetically unfavorable for the ORR. Hence, this study focused on the associative mechanism and calculation of the relative adsorption energy of all the reaction intermediates involved in the ORR mechanism. Our adsorption energy (ΔE) calculations show that the formation of the reaction intermediates at successive steps is spontaneous and energetically feasible during the ORR process. Our study demonstrated that the subject material FeCe@CNT is an excellent ORR electrocatalyst. Our studied FeCe@CNT material can be a potential electrode material in fuel cells for efficiently reducing oxygen molecule to water.

5.2 Computational Details

The equilibrium crystal structure, electronic properties, band structure, and TDOS have been computed using the first principle-based hybrid periodic density functional theory (DFT).[19–21] All DFT calculations have been done using the CRYSTAL 17 suite code.[22–24] The B3LYP-D3 method has been employed in the current study to obtain the equilibrium structures and to explore the reaction mechanisms.[20,21] Grimme's weak 3rd order dispersion corrections (-D3) are used to account for long-range van der Waals interactions.[25,26] Here, Gaussian-type of basis sets were used in the *ab initio*-based CRYSTAL17 suite code to describe the atomic orbitals. Here, spin polarized calculations have been performed to find the equilibrium structure and analyze the electronic properties of the studied material. The basis sets used for Fe and C atoms were of triple-ζ valence with polarization quality Fe_pob_TZVP_2012 and C_pob_TZVP_2012. The effective core potential Ce_ECP_Meyer_2009 was used for the Ce atom. In our present calculation, the Monkhorst-Pack method was employed to integrate the Brillouin zone.[27] A 4*4*8 Monkhorst-Pack k-point grid was used for the structural optimization of the subject material. The "ATOMSPIN" and "SPINLOCK" keywords are used to define the electron occupancy either spin up or spin down in the *ab initio* CRYSTAL 17 program.[28,29] A visualization software VESTA was used to visualize the equilibrium structure of various reaction intermediates.[30] The atomic orbital of Fe, C, and Ce atoms were used to compute the TDOS of the FeCe@CNT material during the present calculation.

5.3 Theoretical Calculation and Equation

In the present study, we have studied the electrocatalytic activity of the FeCe@CNT material by exploring the ORR mechanism on its surface. Each reaction intermediate step has been thoroughly studied by calculating the adsorption energy of every adsorbate which is given by,

$$E_{ads} = E_{adsorbate/FeCe@CNT} - E_{FeCe@CNT} - E_{adsorbate} \quad (1)$$

where $E_{adsorbate/FeCe@CNT}$ represents the total energy of the FeCe@CNT system with the adsorbate, and $E_{FeCe@CNT}$ and $E_{adsorbate}$ are the energies of the FeCe@CNT system and adsorbate entity, respectively. A chemical reaction is said to be exothermic if the adsorption energy is negative because no external energy input is required for the reaction step to occur. A negative adsorption energy is energetically favorable during the subject reaction because energy is released, which can be used to drive the other reaction steps. In the present study, the thermodynamic analysis of the ORR pathway on FeCe@CNT material is entirely based on the adsorption energy (ΔE) rather than fully corrected Gibbs free energies (ΔG). The reported overpotential in this work is estimated using ΔE as an approximation to ΔG within the computational hydrogen electrode (CHE) framework. Zero-point energy and entropic corrections were not included in the present calculations.

5.4 Results and Discussions

A 3D periodic unit cell was employed to model the FeCe@CNT structure. The FeCe@CNT model consists of a Fe_3Ce nanocluster (Fe:Ce = 3:1) encapsulated within a (6,6) armchair single-walled carbon nanotube (tube diameter ≈ 9.35 Å, a = b = 21.65 Å, c = 2.49 Å). The initial geometry positions a central Ce atom at the CNT axis (0,0,0) surrounded by three symmetry-equivalent Fe atoms in a tetrahedral-like configuration (maximum Fe-Fe distance ≈ 5.24 Å) at z = -0.5, ensuring complete encapsulation with lateral separation greater than 15 Å between periodic images. The electronic properties of the equilibrium FeCe@CNT material have been studied employing the B3LYP-D3 (i.e., DFT-D3) method. We have considered a unit cell of the van der Waals (vdW) crystal to present both the CNT and FeCe@CNT materials in the present investigation, so that the computations and analysis can be easily performed by imposing the symmetry in the CRYSTAL17 suite code.[31–34] The equilibrium structure of the FeCe@CNT material is depicted in Figure 5.1a and it has a hexagonal $\boldsymbol{P\bar{6}}$ space group

symmetry. The equilibrium lattice parameter of the vdW crystal structure of the subject material i.e., the lattice constants and bond angles of FeCe@CNT material were found to be a = b = 21.65 Å, c = 2.49 Å, and α = β = 90°, γ = 120° respectively. The electronic band structures calculations and total density of states (TDOS) of the FeCe@CNT material are depicted in Figure 5.1b which was computed by employing a highly symmetric ***Γ-K-M-L-A-H-L-Γ*** *k*-vector direction. Our study has found that the FeCe@CNT material is metallic in nature as some electronic energy bands overlap with each other and cross the $\mathbf{E_F}$ as shown in Figure 5.1b. The metallic nature of FeCe@CNT material is clear from its TDOS calculations shown in Figure 5.1b due to the presence of a significant electron density of states at the $\mathbf{E_F}$. The synergic effect between the Fe-Ce nanoparticle and carbon nanotube (CNT) makes the FeCe@CNT material an excellent catalytic material because mass electron and charge transfer becomes easy during the chemical reaction. The electron density from the ***d***-subshell of Fe and Ce atoms contribute to the TDOS of the FeCe@CNT material, which makes it a conducting material as shown in Figure 5.1c. Further, after confirming the conducting nature of FeCe@CNT, the ORR mechanism on the surface of the FeCe@CNT material has been explored based on the computational hydrogen electrode (CHE) model.

Previous studies have experimentally synthesized Co@SWCNT and investigated its catalytic applications, including the hydrogen evolution reaction (HER) and lithium–sulfur batteries, using both experimental and theoretical approaches.[35,36] Similarly, cobalt-encapsulated nitrogen-doped carbon nanotubes have been experimentally synthesized, and their applications towards the ORR and OER have been reported.[37–39] Experimentally, Fe/N-doped carbon nanotubes (Fe/N-CNTs) have been synthesized using one-pot grinding-calcination of iron salts with CNTs and nitrogen precursors. Fe/N-CNTs demonstrated an excellent ORR performance in microbial fuel cells and alkaline media.[40] Wang et al. experimentally synthesized Ce-doped Fe-N-C/Fe_3C nanosheets by ZIF-assisted molten salt pyrolysis method, and they found that it exhibited enhanced bifunctional ORR/OER performance due to synergistic Fe-Nx and Ce-N active sites.[41] Our current study is purely based on theoretical study, whereas precise FeCe@CNT remains unexplored experimentally. The encapsulation of FeCo alloy nanoparticles inside CNTs is achieved by the CVD method and explored for catalysis.[42] These experimental studies (bimetallic encapsulation via CVD/pyrolysis method) indicate that FeCe@CNT material is synthetically plausible, though there are

no direct reports. However, controlling bimetal dispersion to prevent aggregation, achieving uniform encapsulation for stability under ORR conditions, and scaling beyond laboratory synthesis are the main challenges during the synthesis process. Future experimental synthesis and ORR performance validation of FeCe@CNT are anticipated, guided by established bimetallic CNT encapsulation precedents. This study provides detailed mechanistic insights into the ORR mechanism via the DFT-D3 method. Our work is inherently theoretical and lacks direct experimental comparison, and it suggests to the experimentalists to synthesize the system and study the ORR activity.

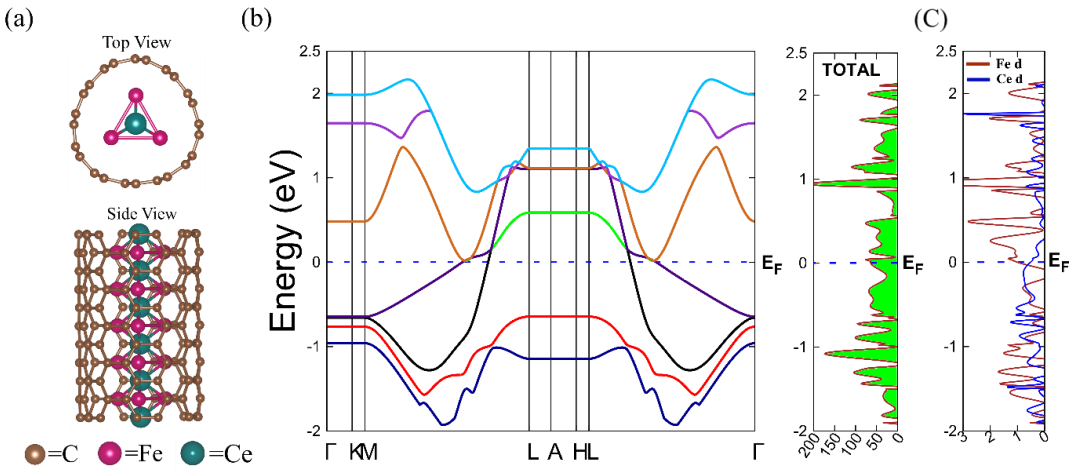


Figure 5.1: *(a) Top and side views of the equilibrium structure of the FeCe@CNT, (b) electronic band structure and the total DOS of the FeCe@CNT material, and (C) PDOS depicting the contribution from the d subshell electron density of Fe and Ce atoms.*

In this study, Mulliken charge analysis of the FeCe@CNT system was performed to understand the nature and extent of charge transfer within the material. From the Mulliken charge analysis, we found that the main charge transfer occurs from the Ce to the Fe atoms, with each Fe gaining the electronic charges about 0.3-0.4 |e| and Ce losing the charges roughly one electron in total. Also, a part of this charge is further delocalized from the Fe atoms to the adjacent carbon atoms in the FeCe@CNT material. This charge redistribution shows that the encapsulated Fe-Ce cluster acts as an electronic promoter that increases the nearby CNT carbon surface with electrons. Hence, the carbon sites on the CNT surface act as the primary active centers for O_2 adsorption during the ORR. The overall ORR process on the Fe@CNT surface is efficiently promoted by the charge transfer between the encapsulated Fe-Ce cluster and the surrounding carbon network.

ORR Mechanism

The ORR mechanism has been investigated on the surface of the FeCe@CNT material based on the computational hydrogen electrode (CHE) model. Figure 5.2 depicts the schematic representation of the $4e^-$ transfer mechanism of associative ORR on FeCe@CNT surface.

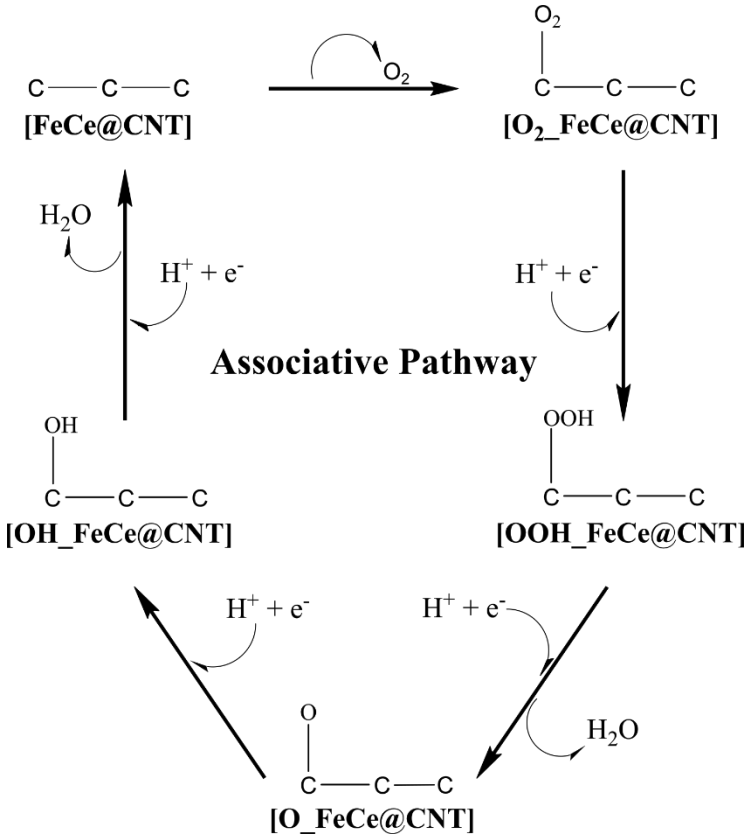


Figure 5.2: *Schematic of the associative four-electron transfer pathway on the FeCe@CNT surface.*

Step 1. O_2 adsorption: The very first step of ORR mechanism is the O_2 molecule adsorption on the surface of the FeCe@CNT material as shown in Figure 5.2. The O_2 molecule gets attached to the carbon (C) atom on the surface of the FeCe@CNT material which leads to the generation of O_2_FeCe@CNT reaction intermediate. We analyzed the equilibrium structure of O_2_FeCe@CNT reaction intermediate and studied its electronic properties by using the DFT-D3 method. We found that the equilibrium structure of the O_2_FeCe@CNT reaction intermediate has hexagonal $P\bar{6}$ space group symmetry depicted in Figure 5.3a. The equilibrium lattice parameters of the O_2_FeCe@CNT reaction intermediate were a = b = 21.59 Å, c = 2.51 Å, and α = β = 90˚, γ =120˚, respectively, obtained by the DFT-D3 method. The equilibrium C−C and C−O bond distances were 1.44 Å and 2.87 Å, respectively, computed at the same level

of theory. The electronic band structure and TDOS of the O_2_FeCe@CNT reaction intermediate were calculated by using a highly symmetric ***Γ-K-M-L-A-H-L-Γ*** path and it is depicted in Figure 5.3b. In the TDOS, a small electron density exists near the $\mathbf{E_F}$. Also, a few bands cross and overlap above the $\mathbf{E_F}$ which shows the excellent conductivity of the O_2_FeCe@CNT reaction intermediate for electron and charge transfer during the ORR. Our DFT study reveals that the electronic band gap of the O_2_FeCe@CNT intermediate is zero, resulting in it being purely conducting in nature. The O_2 adsorption on the surface of the FeCe@CNT material occurred with a cost of energy -1.67 eV. The negative value of adsorption energy in the O_2 adsorption step signifies that the formation of O_2_FeCe@CNT from the FeCe@CNT intermediate is spontaneous. In this step, no external input of energy is needed for the occurrence of this step, and it is energetically feasible.

Liu et al. found that the nickel-iron nanoparticle encapsulated in carbon nanotubes (NiFe@CNTs) demonstrated excellent ORR activity.[43] Recently, we have proposed the CoPt@CNT as an excellent electrocatalytic material for ORR using the DFT method. The excellent catalytic activity of CoPt@CNT is due to the synergetic effects between the CoPt nanoparticle and carbon nanotube (CNT).[13] Similarly, in the FeCe@CNT material, the synergetic effect promotes better electron transfer and high stability during the ORR process, and the costly element Pt has been removed from here. In some studies, remarkable ORR performance has been shown by encapsulating the first-row transition metal nanoparticles (Fe, Co, Ni) in nitrogen-doped CNTs (NCNTs).[44] The electrons are transferred from the encapsulated metal core to the N-doped carbon wall, which tunes the local electronic structure of the carbon surface that facilitates easy ORR activity. In the FeCe@CNT, the intimate contact between the FeCe nanoparticle and the CNT surface induces electronic interactions that optimize the adsorption energy for ORR intermediates. A theoretical study on Fe encapsulated single-walled carbon nanotube (Fe@SWCNT) conducted by Deng et al. proposed that the O_2 adsorption energy on the pristine Fe@SWCNT was +0.03 eV.[45] Ulbricht et al. experimentally found that the adsorption energy of the O_2 molecule on SWCNT was +0.80 eV.[46] Recently, Singh and Pakhira proposed that the O_2 adsorption energy on Co@SWCNT material was +0.15 eV.[12] In our recent study, we have found out that the O_2 adsorption on CoPt@CNT takes place with an adsorption energy of -0.79 eV.[13] In this study, the O_2 adsorption energy on the FeCe@CNT material obtained was -1.67

eV, which is negative. The lower value of O_2 adsorption energy for FeCe@CNT (-1.67 eV) signifies easy and stable adsorption of O_2 on the CNT surface. The O_2 adsorption on the FeCe@CNT surface is exothermic and energetically favorable during the initial stage of the ORR mechanism. These results confirm that our subject material FeCe@CNT is a novel material that can be used in the fuel cell for efficiently catalyzing the ORR process.

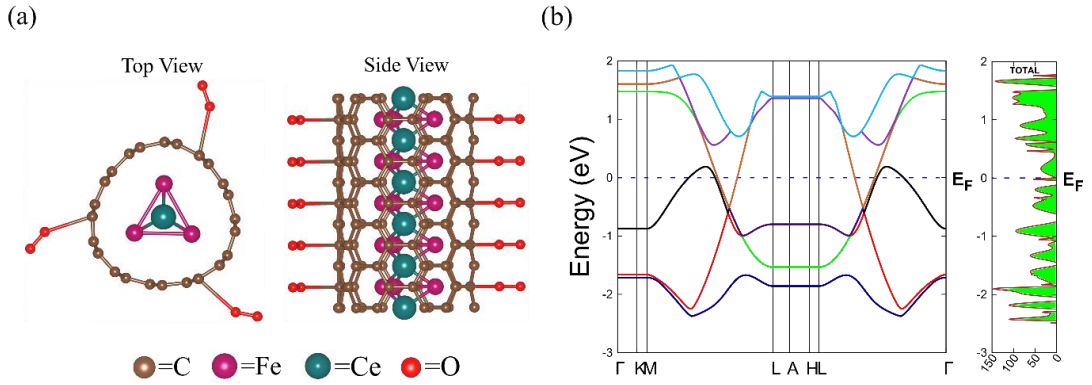


Figure 5.3: *(a) Top and side views of the equilibrium structure of O_2_FeCe@CNT, and (b) the electronic band structure and the total DOS of the O_2_ FeCe@CNT reaction intermediate.*

Table 5.1: *The equilibrium lattice parameter and symmetry of all the reaction intermediates involved in the associative mechanism of ORR.*

System	Lattice parameters (in Å)	Lattice angles (in degrees)	Space group symmetry	Average bond lengths (in Å)		
				C−C	C−O	O−H
FeCe@CNT	a=b=21.65, c=2.49	α=β=90, γ=120	$P\bar{6}$	1.43	-	-
O_2_FeCe@CNT	a=b=21.59, c= 2.51	α=β=90, γ=120	$P\bar{6}$	1.44	2.87	-
OOH_FeCe@CNT	a=b=21.85, c=2.50	α=β=90, γ=120	$P\bar{6}$	1.61	1.46	0.97
O_FeCe@CNT	a=b=22.84, c=2.48	α=β=90, γ=120	$P\bar{6}$	1.48	1.35	-
OH_FeCe@CNT	a=b=18.78, c=2.54	α=β=90, γ=120	$P\bar{6}$	1.79	1.44	0.96

Chen et al. employed a (6,6)-CNT model with Fe-N_4 active sites in supercells of 24-48 C atoms. A single ORR intermediate (*O/*OH) per cell resulted in ~6-9 Å periodic spacing between sites. They found that the calculated adsorption energies matched graphene benchmarks despite CNT curvature, without applying lateral interaction corrections.[47] Kuzmin et al. modeled M-N_4-doped (6,6)-SWCNT (M = Cu, Ag, Zn)

in ~24 C atom cells, with ORR intermediate (OOH*/OH*) adsorbed on adjacent C/N sites at <6 Å.[48] Their study revealed that full ORR free-energy profiles were obtained without larger supercells, suggesting minimal lateral interactions at these low spacings. These studies confirm ORR intermediates adsorb at close distances (6-9 Å periodic, <6 Å local) without significant interference, as evidenced by validated adsorption energies and full mechanistic profiles. The FeCe@(6,6)-CNT (9.35 Å diameter) follows this established methodology for studying the ORR mechanism. Our (6,6)-CNT model encapsulating Fe-Ce nanocluster, with a diameter of 9.35 Å, aligns with Niu et al. (2018), who showed that smaller CNT diameters produce tighter circumferential spacing of active sites (~7-9 Å) due to enhanced curvature.[6] Thus, the chosen unit cell size and active site density ensure reliable DFT-D predictions of ORR thermodynamics and kinetics of the subject FeCe@CNT material, consistent with literature precedents and curvature effects.

Step 2. Formation of the OOH intermediate: Figure 5.4a shows the optimized structure of the OOH_FeCe@CNT reaction intermediate. The OOH_FeCe@CNT reaction intermediate forms when an electron (e^-) and proton (H^+) react with the attached O_2 molecule on the surface of O_2_FeCe@CNT intermediate. This reaction step occurred with an adsorption energy of -0.10 eV. Here, the negative adsorption energy signifies that this reaction step is energetically feasible. The equilibrium structure of OOH_FeCe@CNT intermediate exhibits $\boldsymbol{P\bar{6}}$ space group symmetry. It was determined that the lattice parameter of the equilibrium OOH_FeCe@CNT intermediate measures a = b = 21.85 Å, c = 2.50 Å, and α = β = 90˚, γ = 120˚, respectively, computed by the same DFT-D3 method. The equilibrium C−C and C−O bond lengths were found to be 1.61 Å and 1.46 Å obtained by the same level of theory. Additionally, the equilibrium O−H bond length was calculated to be 0.97 Å. Our present study on the electronic properties of the OOH_FeCe@CNT reaction intermediate reveals that it has zero band gap. The electronic band structure and TDOS of the OOH_FeCe@CNT intermediate are represented in Figure 5.4b. A highly symmetric ***Γ-K-M-L-A-H-L-Γ*** path was utilized to plot the electronic band structures of the OOH_FeCe@CNT reaction intermediate. In the band structure calculations, we can see some bands overlapping with each other and a small electron density is present near the $\mathbf{E_F}$ in the TDOS which signifies the conducting nature of the OOH_FeCe@CNT reaction intermediate as depicted in Figure 5.4b. The equilibrium lattice parameter, lattice constant and space

group symmetry of all the reaction intermediates of ORR mechanism are listed in Table 5.1.

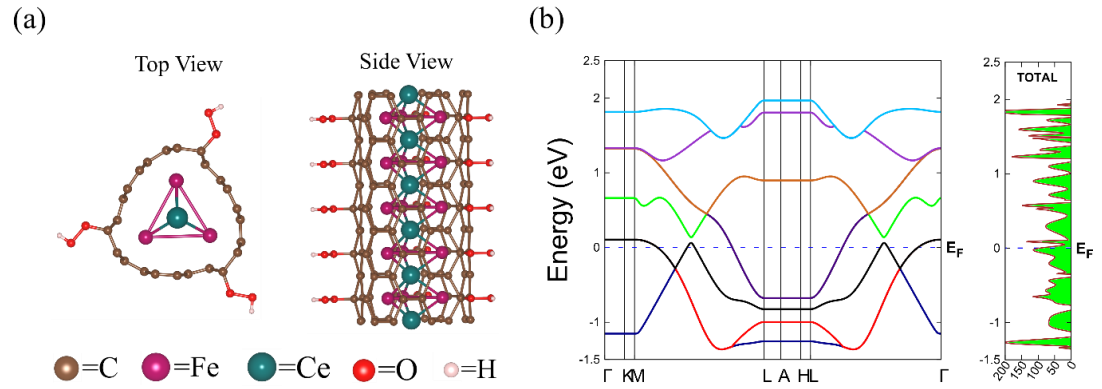


Figure 5.4: *(a) Equilibrium structure (top and side views) of OOH_FeCe@CNT, and (b) the electronic band structure and the total DOS of the OOH_FeCe@CNT reaction intermediate.*

Step 3. Removal of the first H_2O molecule: In the next step, one more electron and proton simultaneously react with the OOH_FeCe@CNT reaction intermediate to generate the first water molecule and a new reaction intermediate O_FeCe@CNT is formed. The reaction intermediate O_FeCe@CNT formed from OOH_FeCe@CNT intermediate with an adsorption energy of about -2.59 eV. The negative value of adsorption energy in this step signifies that it is thermodynamically and energetically favorable for ORR. No additional energy is required during this step to occur as it is an exothermic reaction. The O_FeCe@CNT reaction intermediate has only one activated oxygen atom attached to the surface of the FeCe@CNT material as depicted in Figure 5.5a. This study has found that the equilibrium structure of the O_FeCe@CNT reaction intermediate has a hexagonal $\boldsymbol{P\bar{6}}$ symmetry. The equilibrium lattice parameters of the O_FeCe@CNT material were found to be a = b = 22.84 Å, c = 2.48 Å, and α = β = 90˚, γ = 120,˚ respectively, computed by the DFT-D level of theory. The equilibrium C−C and C−O bond distances were 1.48 Å and 1.35 Å. The electronic band structure and TDOS of O_FeCe@CNT reaction intermediate is displayed in Figure 5.5b which have been computed using the high symmetric ***Γ-K-M-L-A-H-L-Γ*** direction. A small electron density near the $\mathbf{E_F}$ in the TDOS confirms the semiconducting nature of the O_FeCe@CNT intermediate which favors the reaction process for easy transfer of electron and charge.

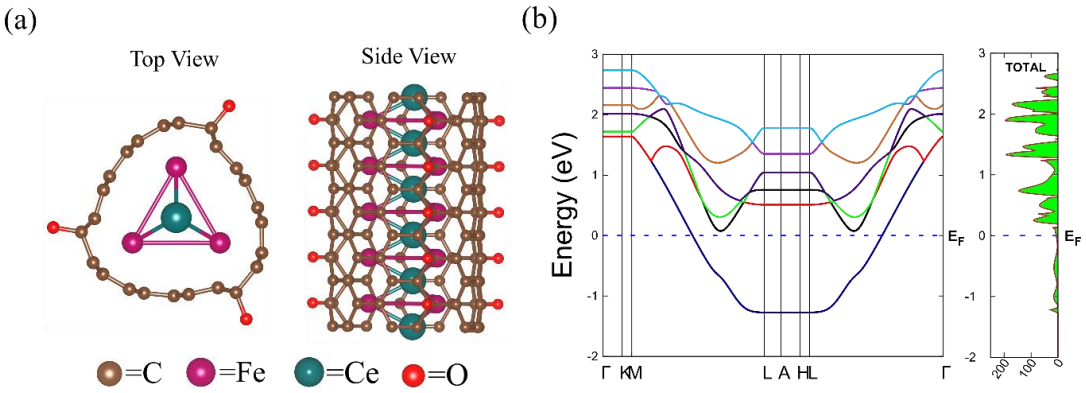


Figure 5.5: (a) Top view and side view of the equilibrium structure of O_FeCe@CNT, and (b) the band structure and the total DOS of the O_FeCe@CNT intermediate.

Step 4. Formation of OH reaction intermediate: The next step of the associative mechanism involves the formation of a new reaction intermediate OH_FeCe@CNT due to the combination of one more proton and electron with O_FeCe@CNT intermediate. This reaction step occurred with an energy cost of ΔE = -0.98 eV as tabulated in Table 5.2. The equilibrium structure of OH_FeCe@CNT intermediate is depicted in Figure 5.6a. The optimized lattice parameters of OH_FeCe@CNT material are a = b = 18.78 Å, c = 2.54 Å and α = β = 90˚, γ = 120˚, respectively. In the OH_FeCe@CNT reaction intermediate, the average values of C−C and C−O bond distances are 1.79 Å and 1.44 Å whereas, the optimized O−H bond length is 0.96 Å. The electronic band structure of the OH_FeCe@CNT reaction intermediate has been computed using a high symmetric ***Γ-K-M-L-A-H-L-Γ*** path followed by the original k-path of the CNT to compare the results. Both the electronic band structure and TDOS calculations of the OH_FeCe@CNT intermediate are depicted in Figure 5.6b.

Table 5.2: Relative adsorption energy of various intermediates during the associative pathway of ORR on the surface of the FeCe@CNT material.

ORR steps	Adsorption energy ΔE (in eV)	Relative adsorption energy (in eV)
[FeCe@CNT] → [O_2_FeCe@CNT]	-1.67	-1.67
[O_2_FeCe@CNT] → [OOH_FeCe@CNT]	-0.10	-1.78
[OOH_FeCe@CNT] → [O_FeCe@CNT]	-2.59	-4.37
[O_FeCe@CNT] → [OH_FeCe@CNT]	-0.98	-5.35
[OH_FeCe@CNT] → [FeCe@CNT]	-0.46	-5.81

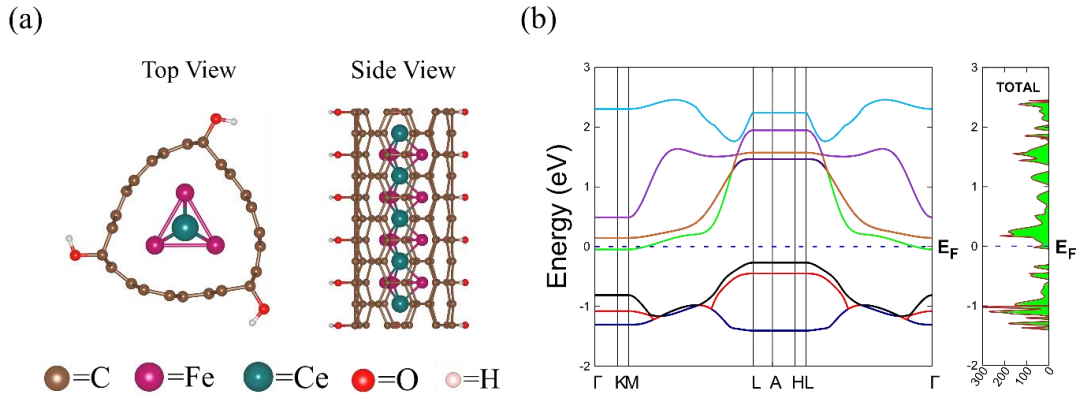


Figure 5.6: *(a) Equilibrium structure depicting the top and side views of OH_FeCe@CNT, and (b) the electronic band structure and total DOS of the OH_FeCe@CNT intermediate.*

Step 5. Second H_2O molecule formation: In the last step of ORR mechanism, one more electron and proton react simultaneously with the OH_FeCe@CNT intermediate to produce a second water (H_2O) molecule with an energy cost of ΔE = -0.46 eV. The adsorption energy profile for all the reaction intermediates of the associative pathway occurred on the surface of the FeCe@CNT material is represented in Figure 5.7. The adsorption energy (ΔE) and relative adsorption energy of all the reaction intermediates of ORR is listed in Table 5.2. In the adsorption energy profile, all the reaction intermediates steps are negative and downhill which proves the excellent energetics and thermodynamic favorability of the FeCe@CNT material for O_2 reduction reaction. The ORR mechanism will follow a $4e^-$ path selectivity via associative pathway on the surface of the FeCe@CNT material. The ORR overpotential ($\eta = \frac{\Delta G_{max}}{e^-} + 1.23\ V$) was found to be 1.13 eV; as the value of ΔE ~ ΔG = -0.46 eV in the last step to form the H_2O.

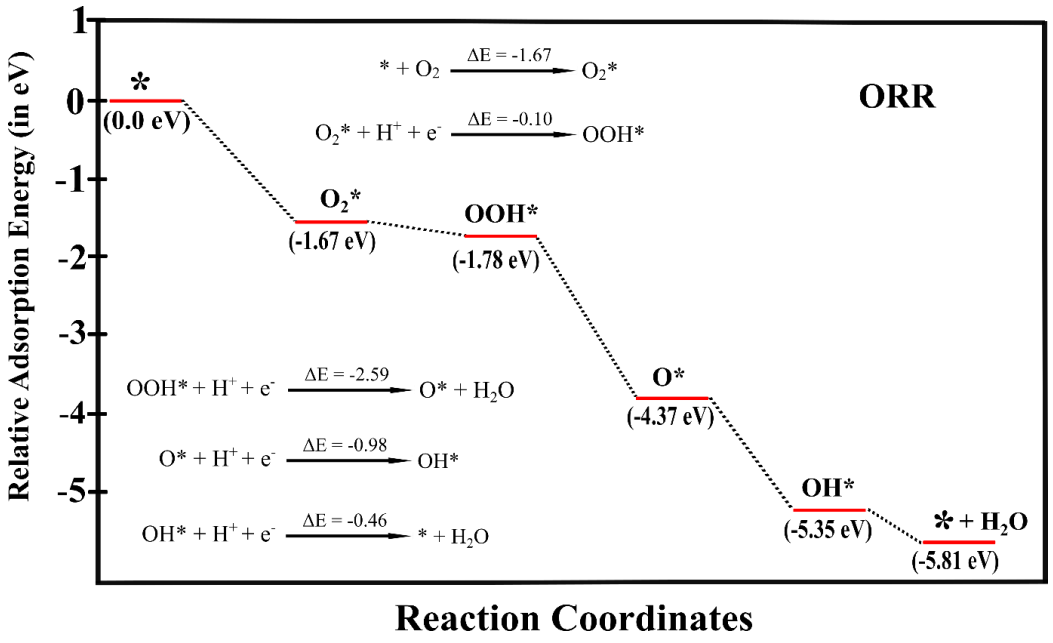


Figure 5.7: *Adsorption energy profile of various reaction intermediates of the associative mechanism of ORR on the surface of the FeCe@CNT material.*

Liu et al. proposed that the Pt (111) surface has exhibited the ORR activity with an overpotential about 1.04 V.[49] In our recent study, we found that the cobalt-platinum encapsulated carbon nanotube (CoPt@CNT) exhibited an ORR overpotential of about 1.07 V.[13] It has been found that the ORR overpotential on real conventional Pt/C could be 0.69~1.68 V.[50] Nitrogen-doped graphene/multi-walled CNT composite as a cathode catalyst has shown an ORR overpotential of 0.43 V.[51] FeCe@CNT exhibits a slightly higher overpotential (1.13 eV) compared to the pristine Pt and Pt-based electrocatalysts. However, the ORR activity is comparable to the other reported electrocatalysts, which have relatively moderate overpotentials. FeCe@CNT could not perform better than the pure Pt catalyst with low overpotential. However, it can be used as an alternative cathodic material in the fuel cells for efficiently catalyzing the ORR process with the reduced cost. Niu et al. experimentally showed that the CoNi@NCNT material exhibited excellent electrocatalytic activity for ORR and OER. The high catalytic performance of CoNi@NCNT is due to the synergistic effects between the NCNT and the encapsulated CoNi nanoparticles.[6] Singh and Pakhira found that the stability and electrocatalytic activity of the CNT surface were enhanced by encapsulating the Co nanocluster inside the SWCNT.[12] Similarly, the FeCe@CNT material has shown enhanced stability and ORR activity is achieved due to nanocluster

encapsulation by the CNT wall, which is reasonable accord with the other reported studies.

5.5 Spin Density Calculation

In this work, electron spin density calculations have been performed for all the reaction intermediates of the ORR involved in the associative mechanism. Spin density is the difference in the distribution of spin-up (α) and spin-down (β) electrons in a material. The location of unpaired electrons can be found through spin density calculation and their contribution to the overall magnetic behavior can be estimated. The transfer of electrons and charge can be better understood by learning the electron spin density calculations with analysis.[31,52–55] The DFT-D3 method has been used to compute the electron spin density computations of the ORR intermediates with the pristine FeCe@CNT material in the present study. The Fe atom encapsulated at the center of the CNT is the primary source of spin density due to its unpaired ***3d*** electrons, which strongly interact with the surrounding Ce atoms and the π-system of CNT. The Ce atoms with their partially filled ***4f*** and ***5d*** orbitals hybridize with the Fe ***3d*** orbital and help to spread the spin density more effectively across the surface of the subject material. When an O_2 molecule get adsorbed on the outer surface of the CNT, it is not directly bonded to the encapsulated Fe atom. Still, the spin density plots in Figure 5.8 clearly show that the electron density from Fe through Ce and the CNT spreads toward the O_2, which weakens its O−O bond and activates it for the subsequent proton-electron transfer steps of the ORR. The contribution of Fe and Ce underscores their cooperative role in enhancing the catalytic efficiency of the FeCe@CNT material. Figure 5.8a-e depicts the spin density plots of each reaction intermediates involved in the ORR mechanism. In the spin density plots, the sky-blue region represents spin-up (α) density, whereas the spin-down (β) density is represented by yellow color. The spin density plots indicate a transfer of unpaired electrons during the ORR process.

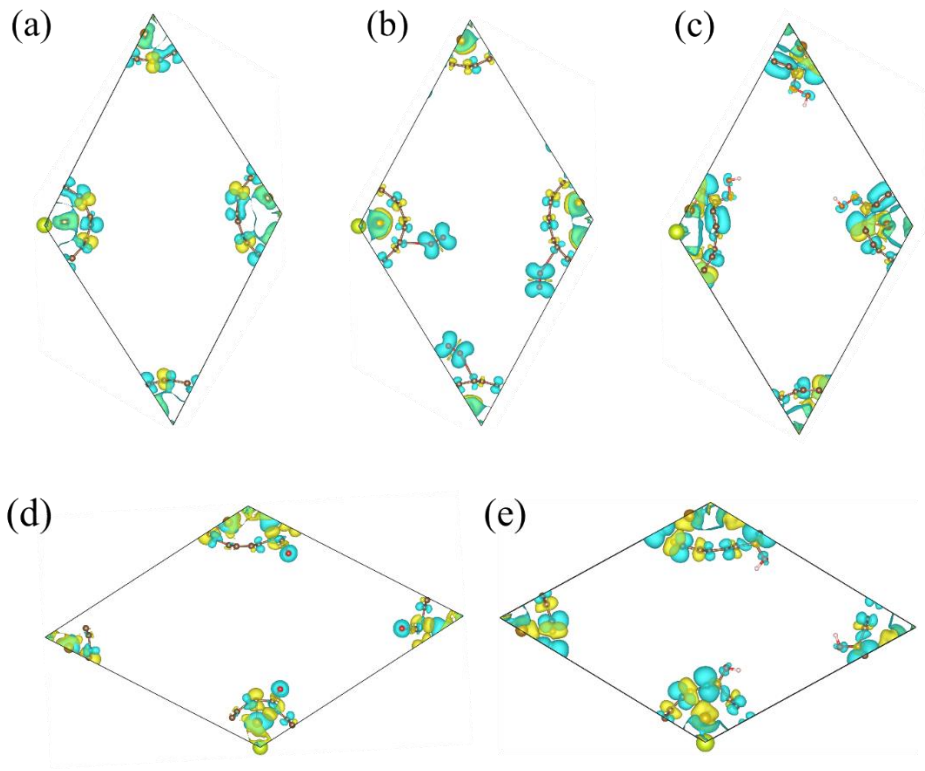


Figure 5.8: *Spin density plot of all the reaction intermediates of the ORR mechanism: (a) pure FeCe@CNT, (b) O_2_FeCe@CNT, (c) OOH_FeCe@CNT, (d) O_FeCe@CNT and (e) OH_FeCe@CNT. The sky-blue color represents positive α spin-up electron density, and the yellow color represents negative β spin-down electron density.*

5.6 Summary

In the present study, the structural and electronic properties of the pristine FeCe@CNT material have been studied by employing the periodic hybrid DFT-D3 method, considering a vdW crystal model system. Our results reveal that the equilibrium structure of the FeCe@CNT material acquires a stable hexagonal $\boldsymbol{P\bar{6}}$ space group symmetry, and its TDOS confirms a metallic nature, arising primarily from the strong contribution of Fe and Ce *d*-orbitals near the Fermi level. This metallic character is crucial for efficient electron transfer, making FeCe@CNT an attractive material for electrocatalytic applications. We have further explored the ORR pathway on the surface of the FeCe@CNT material by evaluating the adsorption energies (ΔE) of key intermediates. The present investigation has found that the adsorption of an O_2 molecule on the surface of the FeCe@CNT occurs with an energy cost of -1.67 eV, signifying a spontaneous and energetically favorable activation of O_2 molecules. We found that the dissociative pathway is thermodynamically unfavorable due to its highly positive adsorption energy, indicating that the reaction predominantly proceeds through the

associative mechanism. The formation of the OOH intermediate in associative mechanism is energetically favorable and spontaneous because the energy cost for this step to occur is -0.10 eV. We have explored all the reaction steps of the associative pathway on the FeCe@CNT surface. Our energy calculation, including the adsorption energy and the relative adsorption energy of different reaction intermediates, proves that the active sites on the surface of the FeCe@CNT material are energetically and thermodynamically favorable for ORR. Overall, our findings establish the FeCe@CNT material as a highly promising non-noble-metal catalyst with excellent activity toward the ORR. The cooperative interaction between the Fe and Ce atoms with the CNT enables efficient O_2 activation and ensures favorable stabilization of all the reaction intermediate. This interaction enhances the catalytic performance while reducing reliance on expensive noble metals such as Pt. Notably, the present study provides fundamental insights into the structural and electronic properties of FeCe@CNT and underscores its potential as a cost-effective, stable, and sustainable electrocatalyst. The insights gained from this work can guide the rational design of next-generation carbon-supported transition-metal catalysts for clean and green energy conversion technologies, particularly in fuel cells and metal-air batteries. We hope that our current study can be useful in finding more stable, low cost and efficient electrocatalysts for ORR which can drive the research towards finding clean and green energy-converting devices.

5.7 References

[1] Z. Chen, D. Higgins, H. Tao, R.S. Hsu, Z. Chen, Highly Active Nitrogen-Doped Carbon Nanotubes for Oxygen Reduction Reaction in Fuel Cell Applications, J. Phys. Chem. C 113 (2009) 21008–21013.

[2] L.M. Ericson, H. Fan, H. Peng, V.A. Davis, W. Zhou, J. Sulpizio, Y. Wang, R. Booker, J. Vavro, C. Guthy, A.N.G. Parra-Vasquez, M.J. Kim, S. Ramesh, R.K. Saini, C. Kittrell, G. Lavin, H. Schmidt, W.W. Adams, W.E. Billups, M. Pasquali, W.-F. Hwang, R.H. Hauge, J.E. Fischer, R.E. Smalley, Macroscopic, neat, single-walled carbon nanotube fibers., Science 305 (2004) 1447–1450.

[3] A.B. Dalton, S. Collins, E. Muñoz, J.M. Razal, V.H. Ebron, J.P. Ferraris, J.N. Coleman, B.G. Kim, R.H. Baughman, Super-tough carbon-nanotube fibres., Nature 423 (2003) 703.

[4] Q. Zhang, J.-Q. Huang, W.-Z. Qian, Y.-Y. Zhang, F. Wei, The road for nanomaterials industry: a review of carbon nanotube production, post-treatment, and bulk applications for composites and energy storage., Small 9 (2013) 1237–1265.

[5] J. Le Xie, C.X. Guo, C.M. Li, Construction of one-dimensional nanostructures on graphene for efficient energy conversion and storage, Energy Environ. Sci. 7 (2014) 2559–2579.

[6] W. Niu, S. Pakhira, K. Marcus, Z. Li, J.L. Mendoza-Cortes, Y. Yang, Apically dominant mechanism for improving catalytic activities of N-doped carbon nanotube arrays in rechargeable zinc-air battery, Adv. Energy Mater. 8 (2018) 1800480.

[7] T. Li, G. Luo, K. Liu, X. Li, D. Sun, L. Xu, Y. Li, Y. Tang, Encapsulation of Ni_3Fe Nanoparticles in N-Doped Carbon Nanotube Grafted Carbon Nanofibers as High-Efficiency Hydrogen Evolution Electrocatalysts, Adv. Funct. Mater. (2018) 1805828.

[8] H. Tabassum, A. Mahmood, B. Zhu, Z. Liang, R. Zhong, S. Guo, R. Zou, Recent advances in confining metal-based nanoparticles into carbon nanotubes for electrochemical energy conversion and storage devices, Energy Environ. Sci. 12 (2019) 2924–2956.

[9] Y. Yao, H. Chen, C. Lian, F. Wei, D. Zhang, G. Wu, B. Chen, S. Wang, Fe, Co, Ni nanocrystals encapsulated in nitrogen-doped carbon nanotubes as Fenton-like catalysts for organic pollutant removal., J. Hazard. Mater. 314 (2016) 129–139.

[10] W. Yang, X. Liu, X. Yue, J. Jia, S. Guo, Bamboo-like Carbon Nanotube/Fe_3C Nanoparticle Hybrids and Their Highly Efficient Catalysis for Oxygen Reduction, J. Am. Chem. Soc. 137 (2015) 1436–1439.

[11] Y. Zhao, D. Liu, Y. Tian, Y. Zhai, C. Tian, S. Li, T. Xing, Z. Li, P. Dai, Fe_3N Nanoparticle-Encapsulated N-Doped Carbon Nanotubes on Biomass-Derived Carbon Cloth as Self-Standing Electrocatalyst for Oxygen Reduction Reaction, Nanomaterials 13 (2023) 2439.

[12] A. Singh, S. Pakhira, Revealing the Mechanism and Activity of O_2 Reduction Reaction of Co Nanocluster Encapsulated by Carbon Nanotube, Energy & Fuels 38 (2024) 11837–11851.

[13] D. Halba, A. Ojha, S. Pakhira, Cobalt–Platinum Nanoparticle Encapsulated within Carbon Nanotube for Superior O_2 Reduction Reaction, ACS Appl. Energy Mater. 8 (2025) 7948–7962.

[14] H. Zhang, Y. Wang, D. Song, L. Wang, Y. Zhang, Y. Wang, Cerium-based electrocatalysts for oxygen evolution/reduction reactions: progress and perspectives, Nanomaterials 13 (2023) 1921.

[15] T. Masuda, H. Fukumitsu, K. Fugane, H. Togasaki, D. Matsumura, K. Tamura, Y. Nishihata, H. Yoshikawa, K. Kobayashi, T. Mori, K. Uosaki, Role of Cerium Oxide in the Enhancement of Activity for the Oxygen Reduction Reaction at Pt–CeO_x Nanocomposite Electrocatalyst - An in Situ Electrochemical X-ray Absorption Fine Structure Study, J. Phys. Chem. C 116 (2012) 10098–10102.

[16] Z. Wang, S. Xiao, Z. Zhu, X. Long, X. Zheng, X. Lu, S. Yang, Cobalt-embedded nitrogen doped carbon nanotubes: a bifunctional catalyst for oxygen electrode reactions in a wide pH range, ACS Appl. Mater. Interfaces 7 (2015) 4048–4055.

[17] L. Kashinath, K. Byrappa, Ceria boosting on in situ nitrogen-doped graphene oxide for efficient bifunctional ORR/OER activity, Front. Chem. 10 (2022) 889579.

[18] J. Bi, X. Zhai, J. Chi, X. Wu, S. Chen, X. Wang, L. Wang, Ultrafine $CoPt_3$ nanoparticles encapsulated in nitrogen-doped carbon nanospheres for efficient water electrolysis, Electrochem. Sci. Adv. 2 (2022) e2100082.

[19] V. Kumar, S. Pakhira, Mechanistic Understanding of Efficient Electrocatalytic Hydrogen Evolution Reaction on 2D Monolayer WSSe Janus Transition Metal Dichalcogenide, Mol. Syst. Des. Eng. 8 (2023) 1060–1074.

[20] A.D. Becke, Density-functional thermochemistry. I. The effect of the exchange-only gradient correction, J. Chem. Phys. 96 (1992) 2155–2160.

[21] A. Singh, S. Pakhira, Unraveling the Electrocatalytic Activity of Platinum Doped Zirconium Disulfide toward the Oxygen Reduction Reaction, Energy & Fuels 37

(2023) 567–579.

[22] R. Dovesi, F. Pascal, B. Civalleri, K. Doll, N. M. Harrison, I. Bush, P. D'Archo, Y. Noel, M. Rerat, P. Carbonniere, M. Causa, S. Salustro, V. Lacivita, B. Kirtman, A. M. Ferrari, F. S. Gentile, J. Baima, M. Ferrero, R. Demichelis and M. D. L. Pierre, The CRYSTAL Code, 1976–2020 and beyond, a Long Story, J. Chem. Phys. 152 (2020) 204111.

[23] G.-C. Wang, L. Jiang, X.-Y. Pang, J. Nakamura, Cluster and Periodic DFT Calculations: The Adsorption of Atomic Nitrogen on M(111) (M = Cu, Ag, Au) Surfaces, J. Phys. Chem. B 109 (2005) 17943–17950.

[24] V. Kumar, D. Halba, S.N. Upadhyay, S. Pakhira, Electrocatalytic Performance of 2D Monolayer WSeTe Janus Transition Metal Dichalcogenide for Highly Efficient H_2 Evolution Reaction, Langmuir 40 (2024) 14872–14887.

[25] S. Pakhira, S.N. Upadhyay, Efficient electrocatalytic H_2 evolution mediated by 2D Janus MoSSe transition metal dichalcogenide, Sustain. Energy Fuels 6 (2022) 1733–1752.

[26] S. Pakhira, J.L. Mendoza-Cortes, Quantum nature in the interaction of molecular hydrogen with porous materials: implications for practical hydrogen storage, J. Phys. Chem. C 124 (2020) 6454–6460.

[27] H.J. Monkhorst, J.D. Pack, Special points for Brillouin-zone integrations, Phys. Rev. B 13 (1976) 5188.

[28] S. Salustro, A.M. Ferrari, R. Orlando, R. Dovesi, Comparison between cluster and supercell approaches: the case of defects in diamond, Theor. Chem. Acc. 136 (2017) 1–13.

[29] S. Pakhira, K.P. Lucht, J.L. Mendoza-Cortes, Iron intercalation in covalent-organic frameworks: A promising approach for semiconductors, J. Phys. Chem. C 121 (2017) 21160–21170.

[30] K. Momma, F. Izumi, VESTA 3 for three-dimensional visualization of crystal, volumetric and morphology data, J. Appl. Crystallogr. 44 (2011) 1272–1276.

[31] W. Niu, S. Pakhira, G. Cheng, F. Zhao, N. Yao, J.L. Mendoza-Cortes, B.E. Koel, Reaction-driven restructuring of defective $PtSe_2$ into ultrastable catalyst for the

oxygen reduction reaction, Nat. Mater. 23 (2024) 1704–1711.

[32] K. Liang, S. Pakhira, Z. Yang, A. Nijamudheen, L. Ju, M. Wang, C.I. Aguirre-Velez, G.E. Sterbinsky, Y. Du, Z. Feng, J.L. Mendoza-Cortes, Y. Yang, S-Doped MoP Nanoporous Layer Toward High-Efficiency Hydrogen Evolution in pH-Universal Electrolyte, ACS Catal. 9 (2019) 651–659.

[33] S.N. Upadhyay, D. Halba, L. Yadav, S. Pakhira, Illuminating the Role of Mo Defective 2D Monolayer $MoTe_2$ toward Highly Efficient Electrocatalytic O_2 Reduction Reaction, Langmuir 39 (2023) 17700–17712.

[34] Y. Lei, S. Pakhira, K. Fujisawa, X. Wang, O.O. Iyiola, N. Perea López, A. Laura Elías, L. Pulickal Rajukumar, C. Zhou, B. Kabius, N. Alem, M. Endo, R. Lv, J.L. Mendoza-Cortes, M. Terrones, Low-temperature Synthesis of Heterostructures of Transition Metal Dichalcogenide Alloys ($WxMo_{1-x}S_2$) and Graphene with Superior Catalytic Performance for Hydrogen Evolution, ACS Nano 11 (2017) 5103–5112.

[35] K.A. Samawi, E.A.-A. Salman, H.A. Hasan, H.M.A. Mahmoud, S.M. Mohealdeen, G. Abdulkareem-Alsultan, E. Abdulmalek, M.F. Nassar, Single-atom cobalt encapsulated in carbon nanotubes as an effective catalyst for enhancing sulfur conversion in lithium-sulfur batteries, Mol. Syst. Des. Eng. 9 (2024) 464–476.

[36] Y. Xiao, W. Wang, Q. Wu, High active and easily prepared cobalt encapsulated in carbon nanotubes for hydrogen evolution reaction, Int. J. Hydrogen Energy 45 (2020) 3948–3958.

[37] Y. Liu, H. Jiang, Y. Zhu, X. Yang, C. Li, Transition metals (Fe, Co, and Ni) encapsulated in nitrogen-doped carbon nanotubes as bi-functional catalysts for oxygen electrode reactions, J. Mater. Chem. A 4 (2016) 1694–1701.

[38] S. Kumar, R. Kumar, N. Goyal, A. Vazhayil, A. Yadav, N. Thomas, B. Sahoo, N-doped carbon nanotubes nucleated through cobalt nanoparticles as bifunctional catalysts for zinc-air batteries, ACS Appl. Nano Mater. 7 (2024) 7865–7882.

[39] S. Liang, C. Liang, High-Density Cobalt Nanoparticles Encapsulated with

Nitrogen-Doped Carbon Nanoshells as a Bifunctional Catalyst for Rechargeable Zinc-Air Battery, Materials 12 (2019) 243.

[40] D. Zhang, R. Ding, C. Zhang, Y. Tang, T. Yuan, Q. Dong, L. Bi, S. Shi, Y. He, Efficient Synthesis of Fe/N-Doped Carbon Nanotube as Highly Active Catalysts for Oxygen Reduction Reaction in Alkaline Media, Langmuir 38 (2022) 9310–9320.

[41] L. Wang, X. Liu, K. Su, W. Liu, F. Niu, X. Li, H. Yue, H. Dong, S. Yang, Y. Yin, Ce-Doped Fe–N–C/Fe_3C Nanosheets as an Efficient Oxygen Electrocatalyst under Alkaline and Acidic Media, ACS Appl. Nano Mater. 7 (2024) 22855–22864.

[42] J. Zhang, J.-O. Müller, W. Zheng, D. Wang, D. Su, R. Schlögl, Individual Fe−Co Alloy Nanoparticles on Carbon Nanotubes: Structural and Catalytic Properties, Nano Lett. 8 (2008) 2738–2743.

[43] Q. Liu, F. Wang, E. Hu, R. Hong, T. Li, X. Yuan, X.-B. Cheng, N. Cai, R. Xiao, H. Zhang, Nickel-iron nanoparticles encapsulated in carbon nanotubes prepared from waste plastics for low-temperature solid oxide fuel cells, IScience 25 (2022) 104855.

[44] W. Wan, S. Wei, J. Li, C.A. Triana, Y. Zhou, Transition metal electrocatalysts encapsulated into N-doped carbon nanotubes on reduced graphene oxide nanosheets: efficient water splitting through synergistic effects, J. Mater. Chem. A 7 (2019) 15145–15155.

[45] D. Deng, L. Yu, X. Chen, G. Wang, L. Jin, X. Pan, J. Deng, G. Sun, X. Bao, Iron encapsulated within pod-like carbon nanotubes for oxygen reduction reaction, Angew. Chemie Int. Ed. 52 (2013) 371–375.

[46] H. Ulbricht, G. Moos, T. Hertel, Physisorption of molecular oxygen on single-wall carbon nanotube bundles and graphite, Phys. Rev. B 66 (2002) 75404.

[47] X. Chen, R. Hu, F. Bai, DFT Study of the Oxygen Reduction Reaction Activity on Fe−N_4-Patched Carbon Nanotubes: The Influence of the Diameter and Length, Materials 10 (2017) 549.

[48] A. V Kuzmin, B.A. Shainyan, Theoretical Density Functional Theory Study of

Electrocatalytic Activity of MN_4-Doped (M = Cu, Ag, and Zn) Single-Walled Carbon Nanotubes in Oxygen Reduction Reactions, ACS Omega 6 (2021) 374–387.

[49] J. Liu, M. Jiao, L. Lu, H.M. Barkholtz, Y. Li, Y. Wang, L. Jiang, Z. Wu, D. Liu, L. Zhuang, C. Ma, J. Zeng, B. Zhang, D. Su, P. Song, W. Xing, W. Xu, Y. Wang, Z. Jiang, G. Sun, High performance platinum single atom electrocatalyst for oxygen reduction reaction, Nat. Commun. 8 (2017) 15938.

[50] J.K. Nørskov, J. Rossmeisl, A. Logadottir, L. Lindqvist, J.R. Kitchin, T. Bligaard, H. Jónsson, Origin of the Overpotential for Oxygen Reduction at a Fuel-Cell Cathode, J. Phys. Chem. B 108 (2004) 17886–17892.

[51] J. Shui, M. Wang, F. Du, L. Dai, N-doped carbon nanomaterials are durable catalysts for oxygen reduction reaction in acidic fuel cells, Sci. Adv. 1 (2015) e1400129.

[52] G. Bruno, G. Macetti, L. Lo Presti, C. Gatti, Spin Density Topology, Molecules 25 (2020) 3537.

[53] S.N. Upadhyay, V. Kumar, N. Sharma, S. Pakhira, Enhanced Catalytic Performance of Vanadium-Doped MoS_2 as a Multifunctional Electrocatalyst toward ORR, OER, and HER Applications, ACS Appl. Energy Mater. 8 (2025) 8937–8949.

[54] A. Singh, S. Pakhira, Exploring the Active Site and Catalytic Activity of N-Coordinated Ni_2 Dual-Atom Catalysts for Oxygen Reduction Reaction, ACS Appl. Energy Mater. 8 (2025) 1544–1560.

[55] L. Yadav, S. Pakhira, Exploring and Elucidating the CO_2 Reduction Mechanisms on the Surface of Two-Dimensional Nitrogen-Vacancy (VN) Hexagonal Boron Nitride, Energy & Fuels 38 (2024) 18800–18813.

Chapter 6

Illuminating the role of Mo Defective 2D Monolayer $MoTe_2$ toward Highly Efficient Electrocatalytic O_2 Reduction Reaction

The fuel cell is one of the solutions to current energy problems as it comes under green and renewable energy technology. The primary limitation of a fuel cell lies in the relatively slow rate of O_2 reduction reactions (ORR) that take place on the cathode, and this is an all-important reaction. An efficient electrocatalyst provides the advancement of green energy-based fuel cell technology, and it can speed up the ORR process. The present chapter provides the study of non-noble metal-based electrocatalyst for ORR. We have computationally designed a 3 × 3 supercell model of metal defective (Mo-defective) $MoTe_2$ transition metal dichalcogenide (TMD) material to study its electrocatalytic activity toward ORR. This work provides a comprehensive analysis of all reaction intermediates that play a role in ORR on the surfaces of metal-deficient $MoTe_2$. The first-principles-based dispersion-corrected density functional theory (in short DFT-D) method was implemented to analyze the reaction-free energies (ΔG) for each ORR reaction step. The present study indicates that the ORR on the surface of metal-defective $MoTe_2$ follows the $4e^-$ transfer mechanism. This study suggests that the 2D Mo-defective $MoTe_2$ TMD has the potential to be an effective ORR electrocatalyst in fuel cells.

6.1 Introduction

Proton exchange membrane fuel cells (PEMFs) and zinc-air batteries (ZABs) are among the next-generation green energy alternatives that offer sustainable options in contrast to traditional sources of energy.[1] A fuel cell cannot give a hundred percent energy converting efficiency due to the energy losses at the cathode or ORR side. On the cathode, breaking the double bond of oxygen is very difficult, as the bond energy is

extremely high (498 kJ/mol). The reaction rate of ORR of the cathode is at least six times less than that of the anode for hydrogen oxidation reactions. The assistance of an efficient catalyst is required to accelerate the ORR kinetics.[7] For the effective completion of ORR, it should be functional below the equilibrium potential of 1.23 V, and the electrocatalyst should adhere to a $4e^-$ transfer mechanism.[8] The amount of free energy for each of the four stages of the charges transfer process should correspond to the equilibrium potential (1.23 V) for a $4e^-$ pathway for the reduction of oxygen to H_2O.[8,9] Noble metal-based electrolyte catalysts (Pt and Pd) have been widely acknowledged as effective electrocatalysts for the purpose of effective ORR until now. However, their extensive use in fuel cells for the purpose of ORR is proving to be difficult due to their small quantity and high cost.[10] Therefore, it is an exciting area of research to develop some noble metal-free catalyst which is cheap, earth-abundant, and environmentally friendly.[3]

Researchers have shown interest in two-dimensional transition metal dichalcogenides (2D TMDs) because of their unique qualities, which are quite different from their bulk structures.[3,11,12] Recent studies show that these 2D TMDs have various applications in modern science and technology, in which they can be promising electrocatalysts for the potential oxygen reduction reaction.[12] On the other hand, the pure two-dimensional TMDs themselves do not provide a strong argument for their catalytic potential; however, we can fine-tune the catalytic potential of these TMDs through edge engineering, defect engineering, strain engineering, heteroatom doping, other composite materials, and phase transitions. We can predict that the defective engineering of these 2D TMDs can enhance their catalytic activity by providing more reactive sites on the basal planes.[3,11–14] A theoretical study showed that a single Pt atom doped into the pure 2D monolayer $MoSe_2$ material with the doping percentage of 25% per 2 × 2 unit cell improves its electrocatalytic properties by making it conductive (lowering the band gap of the $MoSe_2$ TMD from 2.1 to 0 eV) in order to facilitate the $4e^-$ transfer mechanism of ORR.[3] The adsorption of the oxygen molecule was reported to be improved by the heteroatom doping (such as P, N, and O) in the pristine MoS_2, and the electrocatalytic activity of ORR was also discovered to be increased.[15–18]

This study looked at two different types of $MoTe_2$ materials; 2D monolayers of pristine $MoTe_2$ and 3 × 3 supercell of Mo-defective $MoTe_2$. We examined the relaxed

structures and assessed the electronic properties, including the energy band gap and density of states, for both materials. Based on electronic property calculations, the pure 2D monolayer $MoTe_2$ exhibits an electronic energy band gap (noted by E_g) approximately ~1.69 eV. There is an absence of electronic density at the Fermi level (E_F) in the total density of states (DOS) calculations; hence, it cannot transfer the electrons easily, and in turn, it cannot be used as an effective candidate for ORR. In the context of metal-air batteries and fuel cells, the ORR plays a pivotal role. This reaction involves the reduction of oxygen molecules to form oxygen-containing species or water. Efficient ORR catalysts typically have active sites that can strongly adsorb oxygen molecules on the surface of the catalyst, facilitating their subsequent reduction. However, the surface of pristine 2D monolayer $MoTe_2$ TMD lacks sufficient active sites with the required adsorption capability for oxygen molecules. It lacks the intrinsic ability to effectively facilitate the oxygen reduction process, which involves breaking the oxygen–oxygen (O–O) bond and subsequent reduction steps.

A computational study performed by Sun and co-workers suggests that the pristine 2D monolayer $MoTe_2$ is not suitable for ORR as an electrocatalyst.[19] In their research, it was observed that the active sites of 2H-$MoTe_2$ are primarily concentrated at the edges of the layer. However, the dominant sites, which are the highly exposed basal-plane Te sites, prove to be inert in supporting the two-electron ($2e^-$) ORR, ultimately leading to low catalytic efficiency. In particular, it has been hypothesized that the monolayer of 1T′–$MoTe_2$ is semimetallic which is more suitable for electrocatalyst applications than semiconductor 2H–$MoTe_2$. Consequently, 1T′–$MoTe_2$ has potential electrocatalytic activity for the $2e^-$ ORR as it has basal plane activity.

Another study performed by Gao and co-workers revealed that the pristine 2D monolayer $MoTe_2$ is not a promising catalyst for ORR because of the lack of active sites on its surface. They doped it with dual transition metal atoms to study the electrocatalytic activity, and they found that the doping of dual transition metal atoms in the original and pure 2D $MoTe_2$ enhances the electrocatalytic activity by changing its electronic properties.[20]

Creating one Mo-vacancy in the 3 × 3 supercell of pristine 2D monolayer $MoTe_2$ results in reduction of its energy bandgap (E_g) from 1.69 to 0.53 eV obtained by the DFT-D method. During some important electrochemical reactions such as ORR, HER, OER, etc., electrical conductivity of the electrocatalyst plays a crucial role compared to the other general chemical reactions. Since the pure 2D monolayer $MoTe_2$ TMD has a wide

electronic bandgap (E_g), it cannot have better electrocatalytic activity toward ORR and the rate of electron transfer is hindered by the large band gap. Mo-defective 2D monolayer $MoTe_2$ TMD material shows a low electronic band gap, which is about 0.53 eV computed by the DFT-D method in the present investigation, and it may show better electrocatalytic activity toward the ORR. Considering the obtained theoretical results of the Mo-defective 2D monolayer $MoTe_2$, we further extended our computational study to perform all the reactions involved in the ORR mechanism. For each reaction step, we calculated reaction free energy, total DOS, and change in energy band structure. The 2D monolayer Mo-defective $MoTe_2$ TMD used in the current investigation of the ORR mechanism demonstrates outstanding electrocatalytic activity toward ORR.

6.2 Methods and Computational Details

The quantum mechanical hybrid periodic DFT approach have been implemented in CRYSTAL17 program to calculate the optimized geometry, single-point energy and electronic properties.[21,22] In the present investigation, all the calculations have been performed by employing the well-known B3LYP DFT method that describe the exchange and correlation effect.[21,23,24] Here, to incorporate all long-range weak van der Waals (vdW) interactions, Grimme's third order (-D3) semiempirical dispersion corrected parameters were employed in the present investigation.[13,25–27] CRYSTAL17 uses a more efficient Gaussian-type atomic basis set for DFT-D hybrid periodic calculations compared to a plane wave.[25,26,28,29] In the present study, we have used Mo_SC_HAYWSC-311(d31)G_cora_1997[30] basis set for Mo atoms, and for Te, O, and H atoms, triple-ζ valence with polarization quality (TZVP)[31,32] Gaussian basis sets were used and these Gaussian basis sets were implemented in CRYSTAL17. Self-consistent field (SCF) calculations were executed with a convergence criterion of 10^{-7} atomic units (a.u.) on both the total energy and electronic computations. We aligned the X and Y directions parallel to each other with the Z-direction perpendicular to the plane of the Mo–Te monolayer and utilized a supercell for our calculations. The height of the unit cell was intentionally set to 500 Å, which means that there was no periodicity along the Z direction, as prescribed by the 2D slab model in the CRYSTAL17 code. In this context, approximately 500 Å of vacuum region was incorporated into the calculations for the 2D slab structure of the TMD.[23,24] The reciprocal space was sampled with a 20

× 20 × 1 k-points Monkhorst–Pack[33] grid for the geometry optimization used for the electronic structure computations of both the 2D monolayer Mo-defective $MoTe_2$ as well as the pure $MoTe_2$ TMD materials. Once the equilibrium structures of both systems were established, the same DFT-D method was employed to ascertain the electronic properties, encompassing the band structure, electronic band gap (E_g), Fermi energy (E_F) position, and total DOS. For the band structure plotting, the k-vector path chosen followed the high symmetric k-direction, which is noted by ***Γ–M–M−Γ***, within the first Brillouin Zone, taking into account the hexagonal original symmetry of the TMDs like 2D monolayer graphene. The total DOS was calculated by utilizing the atomic orbitals of both Mo and Te. In this study, electrostatic potentials were taken into account, meaning that the energy calculations for both the band structures and the total DOS were performed relative to the vacuum (i.e., with respect to the vacuum). The DFT-D (i.e., B3LYP-D3) method proved to be highly effective, as it not only provided accurate geometric information for the 2D structure but also minimized the influence of spin contaminations on density and energy in the present computations.[34,35] All geometric structures and orbitals were visualized by the VESTA package.[36]

6.3 Material Preparation

To acquire the relaxed geometry of the pristine 2D $MoTe_2$ single layer TMD, the first-principles-based periodic dispersion-corrected hybrid density functional theory, or DFT-D calculation method, was employed. Following the acquisition of the equilibrium geometry, the unit cell of the pure 2D monolayer $MoTe_2$ was enlarged to create a 3 × 3 supercell. Subsequently, one Mo atom was removed from the supercell of the 2D single layer $MoTe_2$ TMD to generate the 2D monolayer Mo-defective $MoTe_2$ material. After creating one Mo defect, the defect concentration of the metal atom was calculated to be 11.11%, and the overall defect concentration of the 2D monolayer Mo defective material was calculated to be 3.70%. A theoretical investigation has been carried out to attain the relaxed geometrical structure and electronic properties, including electronic band structure and total electronic DOS, for both the 2D monolayer $MoTe_2$ and the Mo-defective $MoTe_2$ materials. The same DFT-D method was used for both materials. It was observed that the equilibrium geometry of the pristine 2D single layer $MoTe_2$ exhibits "$P\bar{6}m_2$" space group symmetry, whereas the optimized geometry of the Mo-defective 2D single layer $MoTe_2$ features "P1" symmetry. We have calculated the formation energy of Mo-defective $MoTe_2$ and the formation energy is

about 4.24 eV. The calculated energy value for the formation of single Mo defect in the 2D monolayer $MoTe_2$ is almost similar to the Mo vacancy formation energy in 2D monolayer MoS_2 (4.3 eV).[37] The concentration of the metal (Mo) defect is around 11.11% in the present calculations. Figure 6.1a depicts the relaxed structure of pristine 2D monolayer $MoTe_2$, and Figure 6.1b depicts the Mo-defective 2D monolayer of $MoTe_2$ TMD where the metal (Mo) vacancy is highlighted by the blue dotted circle. The rounded arrow and the minus sign indicate that the Mo atom has been removed from the original structure, which is shown in Figure 6.1a.

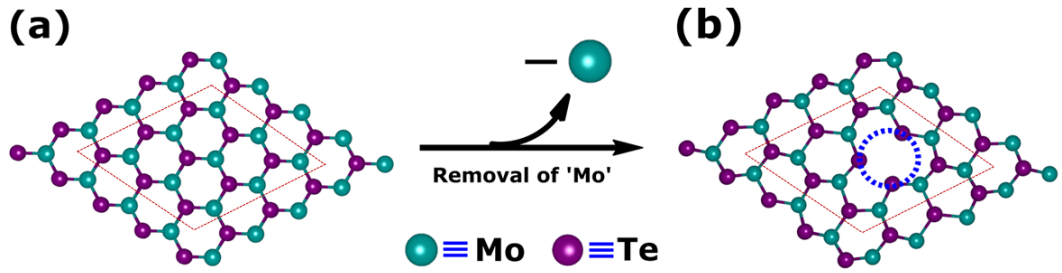


Figure 6.1: *Representation of top view of 3 × 3 × 1 pure 2D single layer slab of the $MoTe_2$ (left side) and Mo-defective 2D monolayer slab of $MoTe_2$ (right side). The red dotted lines show the 3 × 3 supercell of both structures.*

6.4 Theoretical Calculations and Equations

All the ORR steps were explored with respect to the computational hydrogen electrode (CHE) model. The quantification of interactions between the ORR intermediates, and Mo-defective 2D monolayer $MoTe_2$ was done by the adsorption energy calculations using the following equation,

$$E_{ads} = E_{total} - (E_{sub} + E_{int}) \tag{6.1}$$

where E_{total} is the total energy of the Mo-defective 2D monolayer $MoTe_2$ + ORR intermediate, E_{sub} is the energy of the Mo-defective 2D monolayer $MoTe_2$, and E_{int} is the energy of ORR intermediates.

The Nørskov group recommends using the CHE model for calculating the free energies (G) of chemical species in electrochemical reactions through DFT calculations. To initiate this calculation, the reference potential is established at the equilibrium potential of a reversible hydrogen electrode (RHE). Under these conditions, with an electrode potential (U) set at 0 V and a standard H_2 pressure of 1 bar, protons and electrons exist

in equilibrium with molecular hydrogen (H_2). As a result, the chemical potential of a proton–electron pair can be determined using the following equation:

$$\mu(H^+) + \mu(e^-) = (H^+ + e^-) = \mu(0.5H_2) = 0.5\mu(H_2) \quad (6.2)$$

When an electrode potential U is applied, the chemical potential of the electron decreases by eU, and this relationship can be expressed as

$$\mu(H^+ + e^-) = 0.5\mu(H_2) - eU \quad (6.3)$$

Thus, it is possible to assess the proton–electron pair's chemical potential. Then, it is possible to determine each intermediate's free energy in a reaction by

$$G = E_{ZPE} + E_{DFT} + \int C_P dT - TS \quad (6.4)$$

where the zero-point vibrational energy, ground state energy, and entropy, as determined by the DFT technique, are denoted by E_{ZPE}, E_{DFT}, and S, respectively. The temperature (T) of the reaction intermediate is 298.15 K, and the change of Gibbs free energy (ΔG_{ads}) of the adsorbates was determined at the condition pH = 0 by using the equation below:

$$\Delta G_{ads} = \Delta E_{ads} + \Delta E_{ZPE} - T\Delta S - neU \quad (6.5)$$

where ΔG_{ads} stands for adsorption-free energy, ΔE_{ZPE} stands for zero-point vibrational energy (ZPE), and ΔS stands for the change of entropy.

6.5 Results and Discussion

Our current study commenced with the design and optimization of the structure of a one-unit cell of the pristine 2D single layer $MoTe_2$ transition metal dichalcogenide (TMD) material. This material has periodicity only along the x- and y-axes, and there is an absence of periodicity along the z-direction. The equilibrium structure of the pure 2D $MoTe_2$ TMD has been determined, yielding the optimized lattice parameters a = b = 3.40 Å and interfacial angles α = β = 90.0º and γ = 120.0º. The space-group symmetry of the equilibrium structure is $P\bar{6}m_2$. The average bond length of the Mo–Te bond in equilibrium structure of the 2D monolayer $MoTe_2$ material is approximately 2.66 Å. Table 6.1 compiles the lattice parameters and interfacial angles with average optimized bond lengths, all of which align with previously reported findings.[38,39] In Figure 6.2a, the equilibrium geometry of the 2D single layer $MoTe_2$ is depicted from both the top view and the side view.

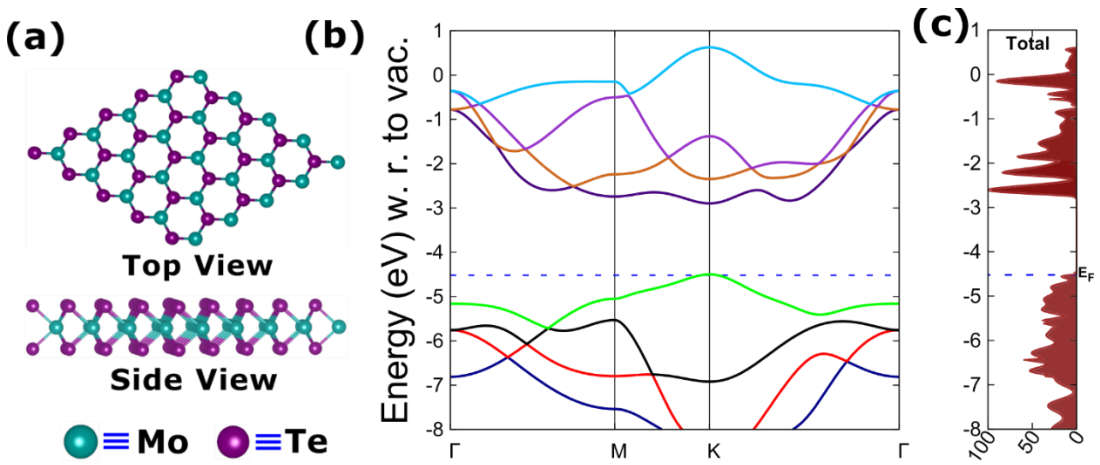


Figure 6.2: *Graphical representation of top view and side view, (b) energy band structures, and (c) total DOS of the pristine 2D monolayer $MoTe_2$ TMD material.*

After achieving the equilibrium structure of the 2D $MoTe_2$ TMD, electronic property calculations, including band structure, electronic band gap (E_g), position of Fermi energy level (E_F) in the electronic properties calculations, and total DOS, were conducted at relaxed geometry of the 2D $MoTe_2$ monolayer. A total of 8 electronic energy bands have been plotted around the E_F, and the results of this study show that the value of the energy band gap of 2D monolayer $MoTe_2$ TMD is approximately 1.69 eV (direct energy band gap) at the K-point according to band structure calculations as shown in Figure 6.2b. The same result was obtained by the total DOS calculations; i.e., there is an absence of electronic density around the E_F. The Fermi energy (E_F) was determined to be at −4.49 eV, and the E_F has been drawn by a dotted blue color line shown in both the electronic band structure and the DOS calculations. Figure 6.2b,c displays the band structure and total DOS of the 2D $MoTe_2$ TMD, respectively. Our present findings are well harmonized with the earlier reports.[40]

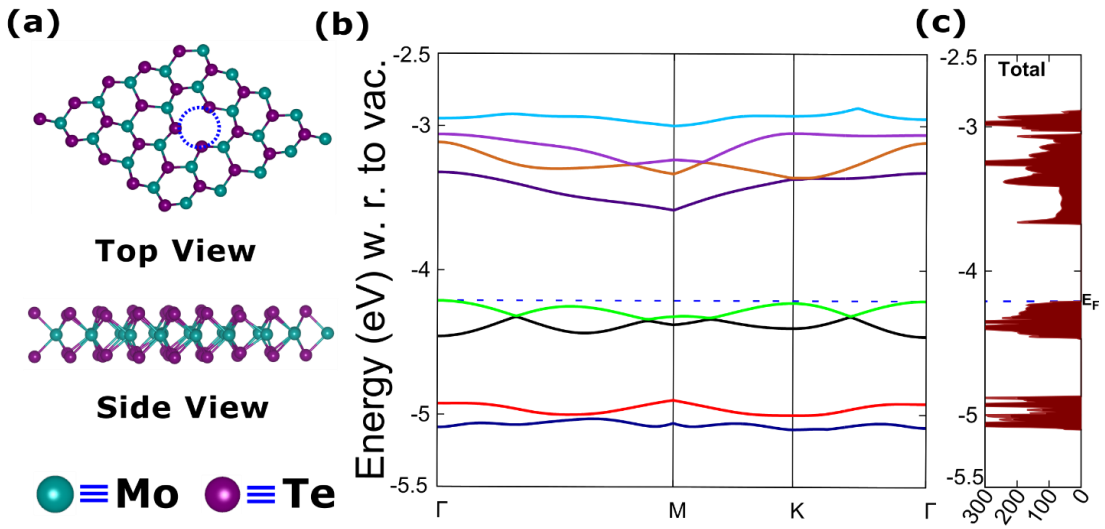


Figure 6.3: *(a) Graphical representation of top view and side view, (b) energy band structure, and (c) total DOS of the Mo-defective 2D monolayer $MoTe_2$ TMD.*

The Mo-defective site is indicated by a blue dotted circle in Figure 6.3a, which also displays the top and side views of the relaxed geometry of Mo-defective 2D single layer $MoTe_2$. After the geometry optimization, it was found that the interfacial angles were $\alpha = \beta = 90.0^{o}$, and $\gamma = 118.92^{o}$, while the equilibrium lattice constants were a = 10.08 Å and b = 10.40 Å. The optimized lattice constants were obtained to be almost an equal value of three times that of the 2D monolayer $MoTe_2$. The electronic properties were calculated at the relaxed structure of the Mo-defective 2D monolayer $MoTe_2$ TMD, including the electronic band structures, location of the Fermi level (in both the band structures as well as DOS) and electronic band gap (E_g) with the total DOS calculations. A total of 8 bands were plotted just around the corner of the E_F, and the band gap was calculated to be 0.53 eV (indirect band gap), which decreased to approximately 1.13 eV in comparison to the pure 2D monolayer $MoTe_2$ (1.69 eV). The total DOS calculation showed a similar result as that obtained from the band structure calculations. The E_F of the Mo-defective 2D monolayer $MoTe_2$ is at 4.21 eV. There is no significant shifting in the E_F level. The band gap decreased as a result of the conduction bands shifting toward the E_F level. The electronic band structures with the total DOS computations of the Mo-defective 2D single layer $MoTe_2$ TMD are shown in Figure 6.3b,c, respectively and the E_F of the material, around which eight electronic bands with the DOS have been plotted, is shown by the blue color dotted line. The computed average equilibrium Mo–Te bond length is 2.72 Å, which is 0.06 Å longer than the equilibrium Mo–Te bond length (2.66 Å) in the case of the pure 2D single layer

$MoTe_2$ TMD. The reduction in the band gap of Mo-defective 2D monolayer $MoTe_2$ makes it more effective to transfer the electrons during the ORR process, which was difficult in the case of pure 2D single layer $MoTe_2$ TMD. All the discussions related to equilibrium geometry, lattice constants interfacial angles, space group symmetry, average bond length, and electronic band gap of both the pristine $MoTe_2$ and Mo-defective $MoTe_2$ TMD have been listed in Table 6.1.

Table 6.1: *Equilibrium lattice constants, average bond length, electronic band gaps, interfacial angles, and space group symmetry of 2D monolayer $MoTe_2$ and defective 2D monolayer $MoTe_2$.*

System	Lattice constant (a, b, c in Å)	Angle (α, β, γ in degree)	Space group symmetry	Average bond length (distance in Å)	Electronic band gap (E_g in eV)	Reference
2D Monolayer $MoTe_2$	$a = b = 3.40$	α = β = 90.0 γ = 120.0	$P\bar{6}m2$	Mo – Te 2.66	1.64 (Direct)	This work
2D Monolayer $MoTe_2$ (Previously reported)	a = b = 3.54	α = β =90.0 γ = 120.0	$P\bar{6}m2$	Mo - Te 2.71	1.72 (Direct)	[38–40]
2D Monolayer Mo-Defective $MoTe_2$	a = 10.08 b = 10.40	α = β = 90.0 γ = 118.92	*P1*	Mo - Te 2.72	0.53	This work

After studying the equilibrium structures, geometries with the electronic properties of both the pure 2D $MoTe_2$ and Mo-defective 2D monolayer $MoTe_2$ TMDs, we observed a drastic reduction in energy band gap and then we were keen to study and explore the electrocatalytic activity of the computationally designed Mo-defective 2D monolayer $MoTe_2$ for effective ORR as a cathode material. The primary objective of the study was to determine whether this electrode material could be a potential fuel cell electrode material. In this study, we have examined both the dissociative as well as the associative mechanisms after adsorption of O_2 molecules on the surface of Mo defective 2D monolayer $MoTe_2$ TMD. We have calculated the change in free energy during protonation reaction for both mechanisms (noted by dissociative and associative mechanisms) of the subject reaction. The calculated change of free energy (ΔG) for the formation of O*_OH* intermediate is −1.11 eV obtained by the DFT-D method. The negative value suggests that this step is spontaneous and thermodynamically favorable.

For the formation of OOH* reaction intermediate, the free energy change is calculated to be +0.58 eV. This positive value suggests that this step is not spontaneous and extra external energy is required for the formation of this step. According to our current findings, the O_2 reduction reaction occurred on the surface of Mo-defective 2D single layer $MoTe_2$ TMD material, supporting the dissociative reaction mechanism over the associative mechanism, because all reaction free energies are negative, which indicates thermodynamically favorable, and all potential energy curve steps in the dissociative mechanism are downhill.

In continuation to our study, we first adsorb molecular oxygen onto the surface of Mo defective 2D monolayer $MoTe_2$ material, followed by successively loading hydrogen atoms over the molecular and atomic oxygen to create different reaction intermediates and then optimizing the structures that were created in steps (i) and (ii). Equation 6.3 was used to determine the stable ORR intermediates, which are those having a negative adsorption energy. The complete steps involved in the whole mechanism of ORR have been discussed from step 1 to step 5, followed by the calculation of reaction free energy, changes in lattice constants, and the electronic properties of the various reaction intermediates.

Step 1: Adsorption of O_2

Molecular O_2 adsorption, the very first step of the ORR process is quite critical for the whole reaction process. We have assessed the adsorption energy of the O_2 molecules on the exteriors of both the 2D monolayer pristine $MoTe_2$ and the Mo-defective $MoTe_2$ TMDs. The energy associated with the adsorption of O_2 plays a pivotal role in the ORR by determining the strength of the interaction between the adsorption of O_2 and the electrolyte. This, in turn, has a significant impact on the reaction rate. Achieving an appropriate adsorption energy is crucial for optimizing the efficiency of the ORR process in various electrochemical systems and catalysts. The O_2 adsorption energy on the surface of pure 2D $MoTe_2$ TMD is about +0.38 eV computed by the DFT-D method, which suggests the endothermic and nonspontaneous nature of the ORR.

Now, the O_2 adsorption was carried out at two different sites (above the Mo-defective site and next to the ring site near the Mo-defect) on the surface of Mo-defective 2D monolayer $MoTe_2$ TMD to investigate the more energetically favorable site for O_2 adsorption. We calculated the adsorption energies of molecular O_2 at the two different

sites. It was found that the site where O_2 was adsorbed, as shown in Figure 6.4a, had a more favorable energetics with an adsorption energy of −1.02 eV. The conventional Sabatier principle suggests that the interaction energy between reactants and catalysts should fall within the range of −0.5 to −2 eV. Therefore, an adsorption energy of −1.02 eV for O_2 in the context of the oxygen reduction reaction aligns appropriately within this range, falling between −0.5 and −2 eV.[41,42]

We have performed the charge analysis of the 2D monolayer Mo defective $MoTe_2$ by performing Mulliken charge population analysis using the "PPAN" keyword implemented in the CRYSTAL17 suite code. Mulliken charge analysis for Mo-defective 2D monolayer $MoTe_2$ revealed a substantial charge transfer from the Te atoms located at the defective site to the inner Mo atoms. This results in a net charge of −0.213 for Mo and 0.213 |e| for Te, respectively. The activation of the O_2 molecule can be initiated by the positively charged Te sites, which provide an empty p-orbital. This activation step in turn triggers the ORR process. Te^+ can form chemical bonds or interactions with O_2 molecules through electrostatic forces. O_2 is a neutral molecule, but it contains two oxygen atoms with partial negative charges due to the electronegativity difference between oxygen and other elements. Te^+, being positively charged, can attract partially negatively charged oxygen atoms in O_2 through electrostatic interactions. The equilibrium bond length of O_2 was increased from 1.22 Å (in the case of free gas O_2) to 1.35 Å. When the oxygen molecule approaches the surface of the Mo-defective 2D monolayer $MoTe_2$, the adsorption energy becomes more negative, indicating stronger adsorption. However, simultaneously, the bond length of O–O elongates. The elongation in the bond length of O–O implies that the oxygen atoms are moving farther apart from each other. The degree of elongation in this context is approximately 0.13 Å, and this aligns well with previous reports.[5,41,42] In this step, the value of change in Gibbs free energy (which is noted by ΔG) is approximately −0.57 eV. Additionally, the optimized bond distances of the Mo–Te and Te–O bonds at equilibrium condition are approximately 2.71 and 2.22 Å, respectively, as calculated by the same DFT-D method. The average bond length of Mo–Te at the equilibrium position has been increased from 2.63 to 2.71 Å by an amount of 0.08 Å. Figure 4a–c displays the equilibrium geometry, band structure, and total DOS calculations for the O_2 adsorbed on the Mo-defective 2D monolayer $MoTe_2$. From the band structure calculations, it is found that the band gap energy has now been reduced

to 0 eV after the adsorption of molecular oxygen as one energy band is crossing the E_F because of that, a large electronic DOS is found around the E_F shown in the Figure 6.4c. The E_F in this step is found at −4.81 eV. The E_F has been shifted down from the earlier step by an amount of energy −0.32 eV and hence, the blue color band from the conduction band crosses the E_F which makes the material conducting in nature. The catalyst has transitioned to a metallic state, signified by a band gap reduction to 0 eV. This alteration permits the efficient transfer of electrons from the electrode to the adsorbed species. All pertinent information regarding the optimized lattice parameters (which are also known as lattice constants), band gap, space group symmetry, and average bond distances of the O_2* adsorbed on the Mo-defective 2D monolayer $MoTe_2$ at the equilibrium condition are detailed in Table 6.2.

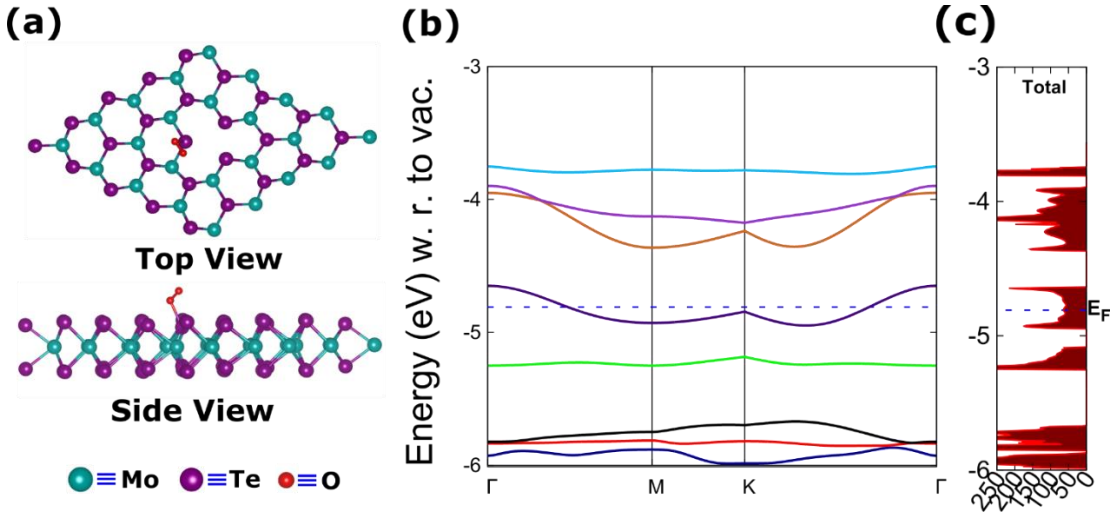


Figure 6.4: *(a) Graphical representation of top view and side view, (b) energy band structures, and (c) total DOS of the O_2 adsorbed 2D monolayer Mo-defective $MoTe_2$ TMD material.*

Step 2: Dissociation of O_2* into 2O*

The next step of the ORR is the dissociation of O_2 molecule into two activated oxygen atoms (2O*) on the surface of Mo-defective $MoTe_2$ TMD which we have discussed in the previous step that the two oxygen atoms were moving far from each other. This is known as the dissociation of O_2. The DFT-D computed change of the Gibbs free energy in the present reaction step results in a value of approximately −0.78 eV. This step is feasible and thermodynamically favorable as relative Gibbs free energy change is negative. The dissociated oxygen atom was adsorbed on the next Te-site located at the defective region. Figure 6.5a–c show the equilibrium geometry, band structure, and total DOS calculations of the 2O* adsorbed Mo-defective 2D monolayer $MoTe_2$. The

two Te–O bonds (at two separate Te sites close to the defect on the catalytic surface) were determined to have equilibrium bond lengths of 1.90 and 1.91 Å, respectively. The average equilibrium bond length of the Mo–Te bond, which has increased by 0.25 Å as a result of the O_2* adsorption phase, was discovered to be 2.96 Å. The dissociation of the O_2* molecule into 2O* leads to open an electronic band gap of 0.66 eV displayed in Figure 6.5b. The band form conduction band region, which has crossed the E_F, has now been shifted upward and all the conduction bands are shifted above the E_F, and all four bands from valence bands region are shrinked and shifted toward the E_F. However, there is no electronic density of states at the Fermi energy level of −5.92 eV as represented in Figure 6.5c. The total DOS calculation shows similar results depicted in Figure 6.5c. Table 6.2 summarizes all of the discussion regarding the equilibrium bond lengths, band gap, and space group symmetry with lattice parameters of the 2O* adsorbed Mo-defective 2D monolayer $MoTe_2$.

Table 6.2: *Equilibrium structural constraints, lattice parameters, and electronic band gap (E_g) of the different reaction intermediates of ORR occurring on the surface of Mo-Defective $MoTe_2$ TMD material.*

Intermediates	**Equilibrium lattice constants**	**Interfacial angles**	**Space group symmetry**	**Electronic band gap (E_g)**	**Equilibrium average bond lengths**		
					Mo-Te	**Te-O**	**Te-OH**
O_2*	*a* = 10.48 *b* = 10.48	α = β = 90.0 γ = 122.21	*P1*	0.00	2.71	2.22	-
2O*	*a* = 10.18 *b* = 10.27	α = β = 90.0 γ = 118.42	*P1*	0.66	2.96	1.91	-
OH_O*	*a* = 10.41 *b* = 10.27	α = β = 90.0 γ = 119.35	*P1*	0.61	2.71	1.91	2.06
O*	*a* = 10.05 *b* = 10.43	α = β = 90.0 γ = 118.88	*P1*	0.39	2.71	1.89	-
OH*	*a* = 10.30 *b* = 10.52	α = β = 90.0 γ = 118.98	*P1*	0.40	2.71	-	2.04

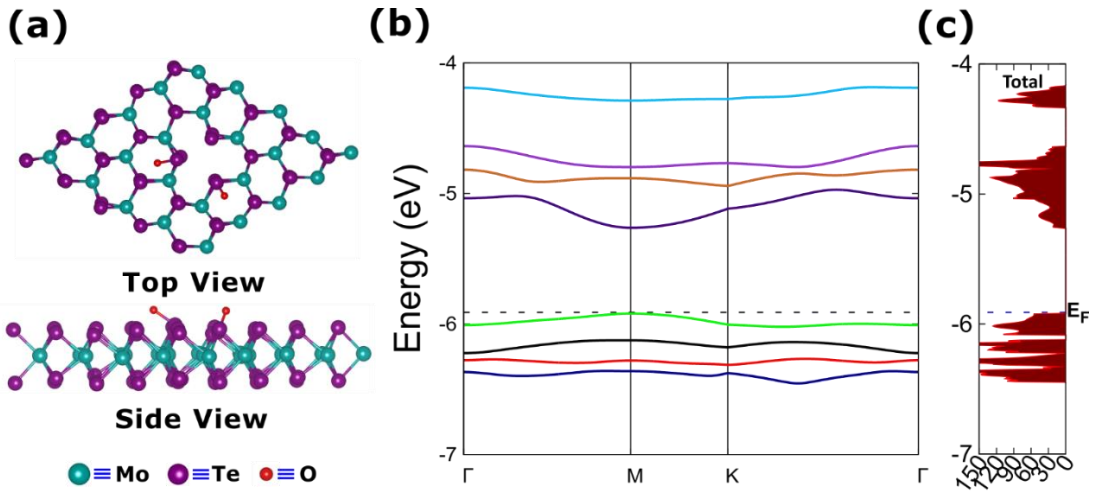


Figure 6.5: (a) Graphical representation of equilibrium geometry, (b) energy band structures, and (c) total DOS of the 2O adsorbed Mo-defective 2D monolayer $MoTe_2$ material.*

Step 3: Formation of OH*_O* (Protonation of 2O*)

The initial protonation step, or the third step, involved absorbing a proton with an alteration in Gibbs free energy (ΔG), which is approximately −1.11 eV, as shown in Table 6.3. One activated oxygen atom on the surface of the Mo-defective 2D single layer $MoTe_2$ TMD is coupled with one proton from the anode side in this phase, which is the first protonation stage of the O_2 reduction reaction process. Figure 6.6a shows the equilibrium geometry for this step. The equilibrium bond length of Mo–Te in this reaction step was decreased to its earlier value (in the case of the O_2 adsorption step) 2.71 Å from 2.96 Å (computed in the second step of ORR) by an amount of 0.25 Å. The band gap was calculated to be 0.61 eV and the E_F is at −5.13 eV for this reaction step based on the band structure and DOS calculation (shown in the blue dotted line Figure 6.6b,c). Figure 6.6c, which presents outcomes comparable to those from the band structure calculations, is where the DOS calculation is illustrated. The computed energy band gap for this step was 0.61 eV, which is 0.05 eV less energy than the calculated energy band gap for the previous step (0.66 eV). The equilibrium bond length for Te–O is approximately 1.91 Å, and for Te–OH, 2.06 Å approximately. While the second Te–O bond length increased following protonation by an amount 0.16 Å, we did not notice any change in the first Te–O bond length. Table 6.2 contains all of the information related to the equilibrium bond lengths, space group symmetry, and electronic band gap with the equilibrium lattice parameters of the OH*_O* adsorbed Mo-defective 2D monolayer $MoTe_2$.

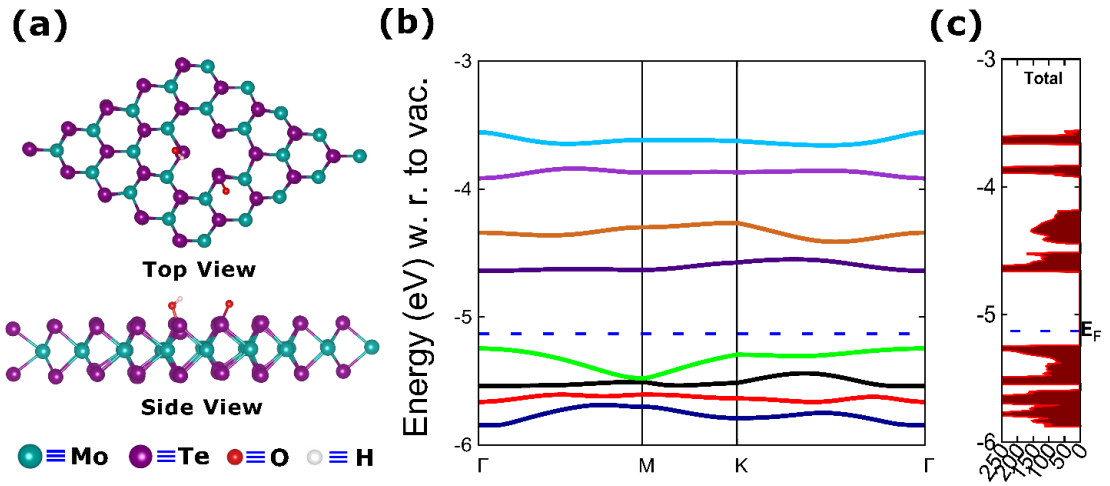


Figure 6.6: *(a) Graphical representation of equilibrium geometry, (b) electronic band structures, and (c) total DOS of the OH*_O* adsorbed Mo-defective 2D monolayer $MoTe_2$ material.*

Step 4: Removal of H_2O (O* adsorption)

This step was executed through the removal of a water (H_2O) molecule from the outer surface of Mo-defective $MoTe_2$. In this reaction step, one electron and one proton were combined and introduced to another OH* while H_2O was simultaneously removing from the catalyst's surface. At this point, only one adsorbed and activated O is here on the surface of the Mo-defective 2D monolayer $MoTe_2$ catalyst. This reaction step took place at the cost of the −1.06 eV Gibbs free energy change (ΔG) reported in Table 6.3. The negative value of ΔG in the current reaction step indicates that this step is viable and thermodynamically conducive. The optimized bond length of the Mo–Te bond remained unchanged at the equilibrium, but the Te–O bond length was reduced by 0.02 Å during this specific reaction step. The band structure and total DOS calculations were conducted using the optimized geometry of the O*-adsorbed Mo-defective 2D monolayer $MoTe_2$, and the results are illustrated in Figure 6.7b,c. The value of Eg (band gap) in this step has been estimated to be 0.39 eV, which is a reduction of 0.22 eV from the previous ORR step (OH*-O* adsorbed Mo-defective 2D monolayer $MoTe_2$) where the band gap was 0.61 eV. The position of the E_F at this step has been identified at −4.99 eV, as indicated by the blue dotted line in both the band structure and total DOS calculations, as illustrated in Figure 6.7b,c. All the pertinent data concerning optimized lattice parameters, band gap, and symmetry with various equilibrium bond distances of O*-adsorbed Mo-defective 2D monolayer $MoTe_2$ is presented in Table 6.2.

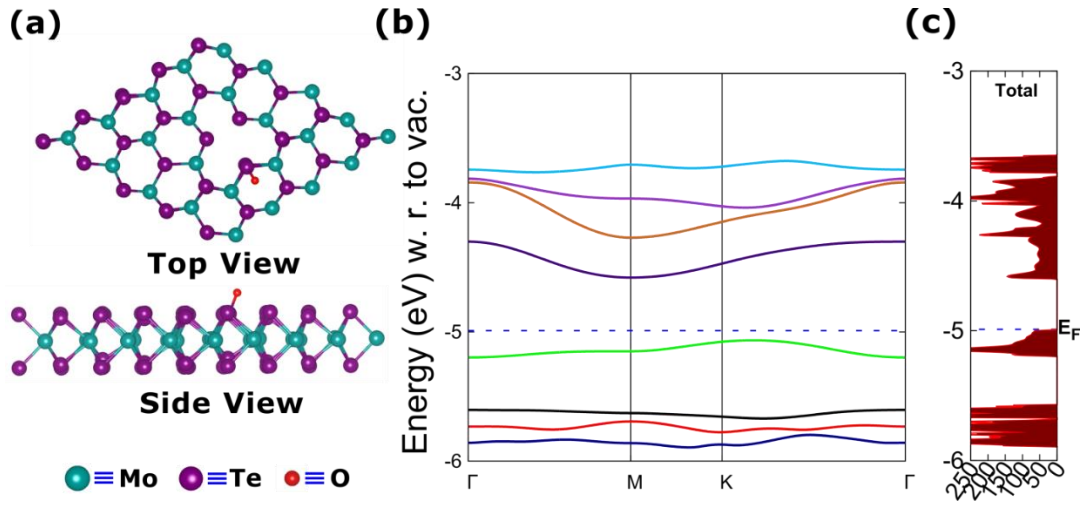


Figure 6.7: *(a) Graphical representation of equilibrium geometry of top view and side view, (b) energy band structure, and (c) total DOS of the O* adsorbed Mo-defective 2D monolayer $MoTe_2$ material.*

Step 5: Adsorption of OH*

Once again, the protonation reaction of activated oxygen (O*) took place through the addition of H* ($H^+ + e^-$). The creation and adsorption of OH* on the surface of the Mo-defective 2D monolayer $MoTe_2$ occurred with s associated Gibbs free energy change (ΔG) of −0.85 eV in this specific reaction step. The negative value of ΔG (as presented in Table 6.3) for this reaction step signifies that the reaction is both achievable and thermodynamically beneficial. The steadiness geometry of the OH*-adsorbed Mo-defective 2D monolayer $MoTe_2$ is shown in Figure 6.8a. Subsequent to the geometry optimization and free energy calculations of the OH*-adsorbed Mo-defective 2D monolayer $MoTe_2$, band structure and total DOS calculations were carried out. These calculations were conducted to investigate the effects of protonation. The band gap energy in this step was found to be 0.40 eV and the band structures of the OH* adsorbed Mo-defective 2D monolayer $MoTe_2$ is depicted in Figure 6.8b. The band structure calculations reveal a slight increase in the band gap, amounting to only 0.01 eV, compared to the previous step, where the band gap was calculated to be 0.39 eV. The total DOS calculation is displayed in Figure 6.8c, and the band gap (Eg ~ 0.40 eV) obtained from the DOS calculations is in good agreement with the band structure calculations. The equilibrium bond length of Mo–Te bond did not change as it was 2.71 Å. The Te–OH bond length was found to be 2.04 Å in this reaction step. All pertinent information, including equilibrium lattice parameters, band gap, symmetry, and

equilibrium bond distances of OH*-adsorbed Mo-defective 2D monolayer $MoTe_2$, is presented in Table 6.2.

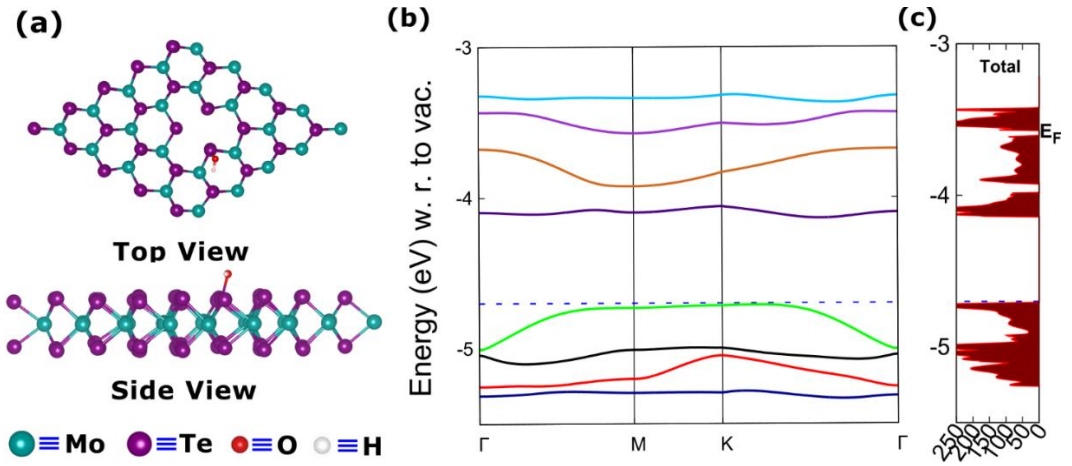


Figure 6.8: *(a) Equilibrium geometry of top view and side view, (b) energy band structure, and (c) total DOS of OH* adsorbed Mo-defective 2D monolayer $MoTe_2$ material.*

Step 6: Removal of the Second H_2O

The final step in this ORR mechanism involves the removal of the second H_2O molecule from the surface of the Mo-defective $MoTe_2$ TMD electrocatalyst. In this step, OH* is again protonated by adding electrons and protons from the anode, and the value of ΔG in this stage is −0.55 eV, as shown in Table 6.3. The negative change in Gibbs free energy for this particular reaction step signifies that the reaction is not only feasible but also thermodynamically stable, rendering this reaction step thermodynamically favorable.

At the condition of standard hydrogen electrode (SHE) when pH = 0, the defective site of the 2D monolayer $MoTe_2$ is active for the ORR. The chalcogen atoms are energetically more favorable for adsorbing various reaction intermediates in the ORR compared to the metal atoms present in 2D TMDs.[3,43] We examined all of the steps within the ORR mechanism by calculating the relative free energy of each individual step under the conditions of U = 0 and pH = 0. To study the role of pH during electrocatalysis comprehensively, it is essential to consider the solvation effects and how they interact with electrochemical reactions. Avoiding solvation effects simplifies the computational model and allows for a more direct examination of the intrinsic catalytic properties, such as bond breaking and formation energies, without the additional complexity of solvent interactions. To manage computational costs, we opted

to exclude solvent phase calculations in our current study. Instead, we conducted all of our calculations at pH = 0. The changes in free energy for each reaction step have been computed and are provided in Table 6.3. Figure 6.9 illustrates the graph of reaction free energy, often referred to as potential energy surfaces, incorporating the changes in the free energy (ΔG) for each step. All of the listed relative Gibbs free energies during the different reaction steps (Figure 6.9, Table 6.3) are negative, indicating that all reaction intermediates have a positive thermodynamic profile.

Table 6.3: *Free energy change (ΔG in eV) and the relative free energy (expressed in eV) for all the intermediates during the ORR carried out on the surface of Mo-Defective $MoTe_2$ TMD material are listed here.*

ORR steps	ΔG (eV)	Relative free energy (eV)
* + O_2 → O_2*	-0.57	-0.57
O_2* → 2O*	-0.78	-1.35
2O* → OH*_O*	-1.11	-2.46
OH*_O* → O* + H_2O	-1.06	-3.52
O* → OH*	-0.85	-4.37
OH* → * + H_2O	-0.55	-4.92

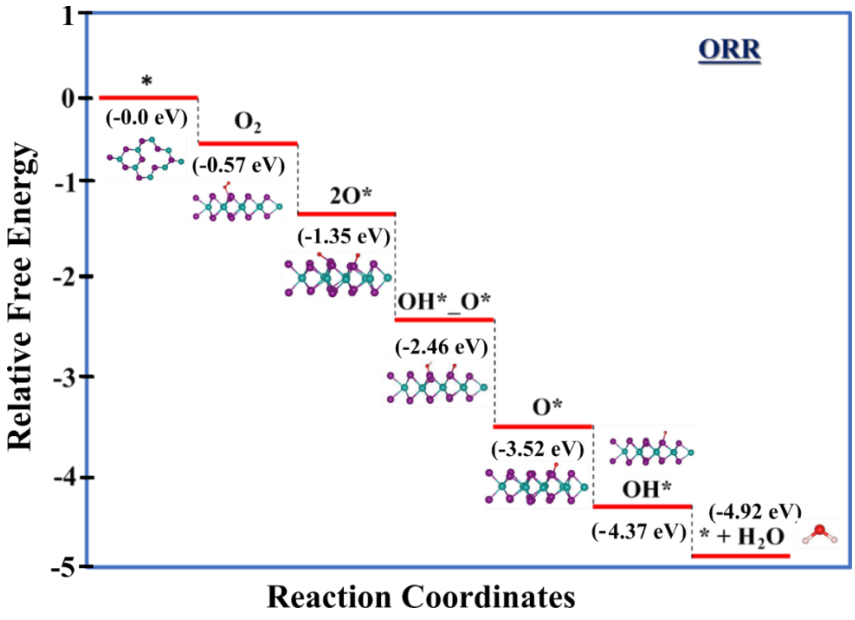


Figure 6.9: *Calculated profiles of relative free energy for the 4e⁻ transfer mechanism of the ORR on the surface of Mo-defective 2D monolayer $MoTe_2$ material.*

Figure 6.9 illustrates the relative Gibbs free energy graph of the O_2 reduction reaction pathway occurring on the surface of a Mo-defective two-dimensional monolayer of $MoTe_2$ TMD. This diagram serves as a comprehensive overview of the entire ORR mechanism, which reveals that all of the individual reaction stages of the O_2 reduction on the surface of Mo-defective $MoTe_2$ exhibit negative values for changes in free energy, indicating that all of these steps are exothermic. So, the downhill step in the free energy diagram for every single ORR intermediate step indicates that the whole ORR process takes place naturally, hence in turn, thermodynamically favorable. Through computational analysis, it was determined that the ORR catalyzed by defective $MoTe_2$ commences with the adsorption of O_2 and progresses through a $4e^-$ dissociative pathway. In this pathway, the O═O bond is fully split after the second electron transfer. The change of free energy for the removal of H_2O from the surface of Mo-defective $MoTe_2$ was calculated to be −0.55 eV. The obtained value of ΔG for the removal of the H_2O molecule from the catalytic surface suggests that this process will occur readily and spontaneously. After the removal of the second H_2O from the surface, the catalytic surface of Mo-defective 2D monolayer $MoTe_2$ becomes free for the next reaction cycle. Hence, the Mo-defective 2D monolayer $MoTe_2$ shows enhanced catalytic activity toward the ORR. The ORR mechanism follows the four-electron pathway and is completed through the following process: $O_2 \rightarrow O2^* \rightarrow O_O^* \rightarrow O^* + H_2O \rightarrow OH^* \rightarrow H_2O$. Table 6.2 presents the optimized structural properties, lattice parameters, and electronic band gaps (E_g) at the equilibrium position of all of the intermediates involved in the subject reaction on the surface of Mo-defective $MoTe_2$ TMD.

In this study, we have utilized the hybrid periodic density functional theory method with the dispersion-corrections (DFT-D) technique to ascertain the equilibrium structure and energy throughout the O_2 reduction rection progression on the surface of a Mo-defective 2D monolayer of $MoTe_2$. This solid surface reaction occurs on the surface of the Mo-defective 2D monolayer of $MoTe_2$ TMD material. In the field of catalysis, the investigation of solvent effects holds great significance. Additionally, it is both captivating and relevant to comprehend the chemical reaction mechanisms in solvent phase for a variety of electrochemical reactions. Nonetheless, accurately representing the appropriate model system of a solvent is a complex endeavor in theoretical and computational electrocatalysis, and modeling the various stages of a reaction can be computationally expansive.[54,55] In DFT calculations, it is common to

simplify the system by ignoring the solvent phase and instead approximating it as a vacuum or gas phase. This simplification is often used because including the solvent explicitly in calculations can significantly increase the computational complexity. We have integrated the relative free energy changes for reactions in which the solvation effects are negligible. The influence of solvent is neglected while performing calculations in the gas phase. However, solvation effects can be significant, especially for reactions involving charged species or highly polar molecules. To account for this, relative free energy changes are often incorporated to correct for the neglect of solvation effects. These corrections aim to approximate what would happen in a solvent.

Avoiding solvation effects simplifies the computational model and allows for a more direct examination of the intrinsic catalytic properties, such as bond breaking and formation energies, without the additional complexity of solvent interactions. In our current study, we omitted solvent phase calculations due to computational cost considerations.

Theoretical Overpotential

The ORR overpotential in acidic media can be determined from the minimum Gibbs free energy of ORR steps.[44]

$$\eta^{ORR} = 1.23 - \frac{min\ (\Delta G\ of\ ORR\ steps)}{e} \tag{6.6}$$

To achieve optimal catalytic performance, all the free energies of the ORR steps should be equal to or exceed 4.92 eV/4, which is equivalent to 1.23 eV. This corresponds to all reaction free energies becoming zero at a balance potential of 1.23 V. In this study, we found that the final step, which is producing a second H_2O, could be the potential deciding factor for ORR. We calculated the overpotential value using equation (6.6). The calculated value of the overpotential was found to be 0.68 V. A low overpotential suggests that ORR can be produced at lower energy inputs, which is an important factor in the effectiveness of electrochemical equipment like fuel cells or batteries.

6.6 Spin Density Calculations

The electron spin densities of the Mo-defective 2D monolayer $MoTe_2$ TMD as well as all of the reaction steps implied in the subject reaction have been computed in the present investigation. The variance of spin densities, which calculates the difference of

α and β electrons, has been plotted in Figure 6.10a–f. The α state is referred to as "spin up", and the β state is referred to as "spin down". Spin density calculations are one of the methods to predict the presence of unpaired electrons (or the electron cloud region or locus) in the system of interest. The total electron density is the sum of the α and β spins of the electrons involved in the systems, and the difference between the "spin up" and "spin down" electrons densities develop in nonzero spin polarization and localized electron density. The role of electron density clouds in electrocatalysts during the ORR is to facilitate the transfer of electrons and participate in the reaction mechanism. In the ORR, the electron density clouds in the electrocatalyst help to facilitate the transfer of electrons from the electrode surface to the oxygen molecules. The electron density clouds also provide a favorable environment for the adsorption and desorption of oxygen species during the ORR. Oxygen molecules can interact with the electrocatalyst surface, and their adsorption involves the redistribution of electron density in both the oxygen molecule and the electrocatalyst. In Figure 6.10a, cyan and yellow bubbles are electron density clouds in the defective region of the Mo defective $MoTe_2$ TMD. This indicates that the defective areas are more active for the ORR. The difference in charge density quantifies the redistribution of electron charge due to the interaction between an atom and vacancy. Yellow and cyan colors represent charge depletion and accumulation, respectively, in Figure 6.10. At the defect site, there is electrostatic interaction, and some weak van der Waals interactions are present. At the defect site of the 2D monolayer Mo-defective $MoTe_2$ TMD, the van der Waals interactions between neighboring atoms should still be present because these forces depend on the distance and relative orientation of atoms. However, the presence of a vacancy can affect the local electronic and structural properties of the TMD, and these effects may indirectly influence the strength and nature of van der Waals interactions at the vacancy site. The difference in charge density indicates that the positive charge is predominantly concentrated in the center of the O atoms parallel to the O–O bond, whereas the negative charge is predominantly concentrated on the O atoms, resulting in repulsive interactions. Generally, the accumulated negative charge on the O atoms plays a role in dissociating O_2.

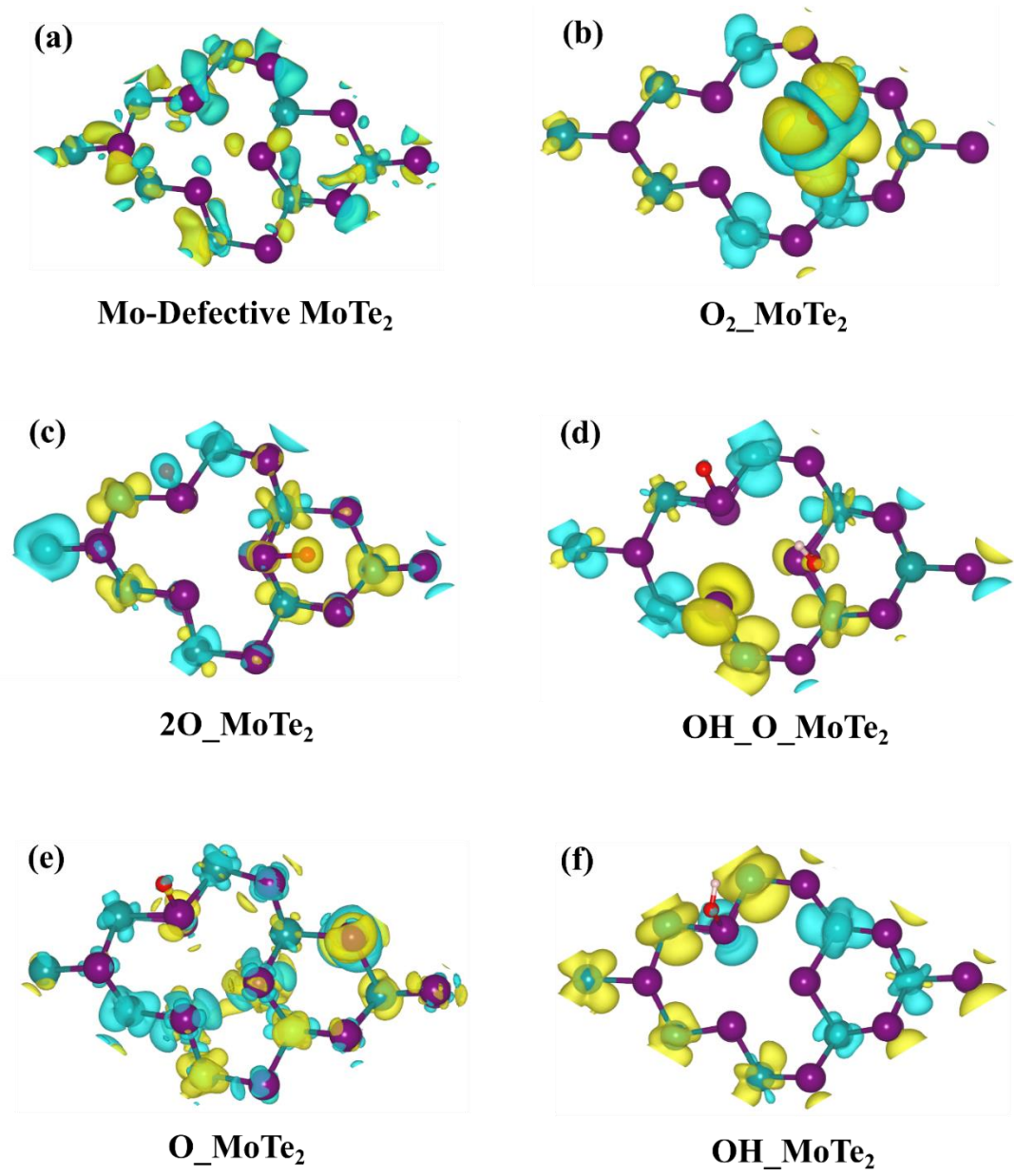


Figure 6.10: *Spin density calculations of (a) Mo-defective 2D monolayer of $MoTe_2$, (b) O_2* adsorbed on the Mo-defective 2D monolayer $MoTe_2$ material, (c) 2O* adsorbed Mo-defective 2D monolayer $MoTe_2$ material, (d) OH*_O* adsorbed Mo- defective 2D monolayer $MoTe_2$ material, (e) O* adsorbed Mo-defective 2D monolayer $MoTe_2$ material and (f) OH* adsorbed Mo-defective 2D monolayer $MoTe_2$ material.*

6.7 Summary

In summary, geometry optimization and electronic property calculations for pristine 2D $MoTe_2$ were conducted utilizing the DFT-D (density functional theory with dispersion corrections) method, which is incorporated into the CRYSTAL17. The direct band of the $MoTe_2$ 2D Monolayer TMD was found to be 1.64 eV. No electronic density was observed in the vicinity of Fermi energy levels. Therefore, this material cannot be used

as electrode material to perform ORR application effectively. 2D monolayer $MoTe_2$ with a Mo vacancy defect reduces the band gap by 1.11 eV. The band gap in the case of the Mo-defective 2D monolayer $MoTe_2$ was observed to be 0.53 eV. Low value of electronic band gap favors easy electron transfer from the valence band to conduction band. After completing the calculations for the equilibrium geometry, band structure, and DOS of the Mo-defective 2D monolayer $MoTe_2$, we proceeded with a comprehensive investigation of the reaction pathways associated with the O_2 reduction process. To gain a deeper understanding of the thermodynamics of the reaction, we examined the relative Gibbs free energy of an individual reaction step during the ORR process. For each reaction step, the Gibbs free energy (ΔG) changes are negative. This indicates that the ORR has an exothermic nature. All reaction steps are, therefore, thermodynamically favorable. DFT-D calculation predicts $4e^-$ reduction pathway selectivity for Mo defective 2D monolayer $MoTe_2$. The calculated change in free energy demonstrates that all of the reaction steps are not only feasible but also occur spontaneously and are thermodynamically favorable. Specifically, calculations using the CHE model revealed that the Mo-defective 2D monolayer $MoTe_2$ serves as a highly promising Pt-free electrocatalyst for the ORR in future fuel cell applications. It exhibits exceptional catalytic activity. It is important to emphasize that while the potential applications of defective 2D $MoTe_2$ for ORR are promising, there are still challenges to overcome such as scalability, stability, and long-term performance of ORR catalysts. Nevertheless, ongoing research and development efforts in this field have the potential to pave the way for more efficient and sustainable technologies for energy conversion and storage in the near future. It is anticipated that the theoretical and computational results of our studies will motivate experimental, computational and theoretical work toward the development of more two-dimensional Pt-free ORR catalysts.

6.8 References

[1] M. Winter, R.J. Brodd, What are batteries, fuel cells, and supercapacitors?, Chem. Rev. 104 (2004) 4245–4270.

[2] M.K. Debe, Electrocatalyst approaches and challenges for automotive fuel cells, Nature 486 (2012) 43–51.

[3] S.N. Upadhyay, S. Pakhira, Mechanism of electrochemical oxygen reduction reaction at two-dimensional Pt-doped $MoSe_2$ material: an efficient

electrocatalyst, J. Mater. Chem. C 9 (2021) 11331–11342.

[4] J. Hui, S. Pakhira, R. Bhargava, Z.J. Barton, X. Zhou, A.J. Chinderle, J.L. Mendoza-Cortes, J. Rodríguez-López, Modulating Electrocatalysis on Graphene Heterostructures: Physically Impermeable Yet Electronically Transparent Electrodes, ACS Nano 12 (2018) 2980–2990.

[5] Y. Wang, Y. Li, T. Heine, PtTe Monolayer: Two-Dimensional Electrocatalyst with High Basal Plane Activity toward Oxygen Reduction Reaction, J. Am. Chem. Soc. 140 (2018) 12732–12735.

[6] V.S. and P.N.R. N. M. MarkovicÂ, T. J. Schmidt, Oxygen Reduction Reaction on Pt and Pt Bimetallic Surfaces: A Selective Review, Fuel Cells 1 (2001) 105–116.

[7] D. Malko, T. Lopes, E. Symianakis, A.R. Kucernak, The intriguing poison tolerance of non-precious metal oxygen reduction reaction (ORR) catalysts, J. Mater. Chem. A 4 (2016) 142–152.

[8] R. Ma, G. Lin, Y. Zhou, Q. Liu, T. Zhang, G. Shan, M. Yang, J. Wang, A review of oxygen reduction mechanisms for metal-free carbon-based electrocatalysts, Npj Comput. Mater. 5 (2019) 78.

[9] H.W. Kim, V.J. Bukas, H. Park, S. Park, K.M. Diederichsen, J. Lim, Y.H. Cho, J. Kim, W. Kim, T.H. Han, J. Voss, A.C. Luntz, B.D. McCloskey, Mechanisms of two-electron and four-electron electrochemical oxygen reduction reactions at nitrogen-doped reduced graphene oxide, ACS Catal. 10 (2020) 852–863.

[10] V. Tripkovic, T. Vegge, Potential- and Rate-Determining Step for Oxygen Reduction on Pt(111), J. Phys. Chem. C 121 (2017) 26785–26793.

[11] J. Ekka, S.N. Upadhyay, F.J. Keil, S. Pakhira, Unveiling the role of 2D monolayer Mn-doped MoS_2 material: toward an efficient electrocatalyst for H_2 evolution reaction , Phys. Chem. Chem. Phys. 24 (2022) 265–280.

[12] S.N. Upadhyay, J. Akash, K. Satrughna, S. Pakhira, Recent advancements of two-dimensional transition metal dichalcogenides and their applications in electrocatalysis and energy storage, Emergent Mater. 4 (2021) 951–970.

[13] Y. Lei, S. Pakhira, K. Fujisawa, X. Wang, O.O. Iyiola, N. Perea López, A. Laura

Elías, L. Pulickal Rajukumar, C. Zhou, B. Kabius, N. Alem, M. Endo, R. Lv, J.L. Mendoza-Cortes, M. Terrones, Low-temperature Synthesis of Heterostructures of Transition Metal Dichalcogenide Alloys ($W_xMo_{1-x}S_2$) and Graphene with Superior Catalytic Performance for Hydrogen Evolution, ACS Nano 11 (2017) 5103–5112.

[14] S.J. Rowley-Neale, J.M. Fearn, D.A.C. Brownson, G.C. Smith, X. Ji, C.E. Banks, 2D molybdenum disulphide (2D-MoS_2) modified electrodes explored towards the oxygen reduction reaction, Nanoscale 8 (2016) 14767–14777.

[15] H. Huang, X. Feng, C. Du, W. Song, High-quality phosphorus-doped MoS_2 ultrathin nanosheets with amenable ORR catalytic activity, Chem. Commun. 51 (2015) 7903–7906.

[16] Y. Singh, S. Back, Y. Jung, Activating Transition Metal Dichalcogenides by Substitutional Nitrogen-Doping for Potential ORR Electrocatalysts, ChemElectroChem 5 (2018) 4029–4035.

[17] S. Jayabal, G. Saranya, J. Wu, Y Liu, D Geng, X Meng, Understanding the High-Electrocatalytic Performance of Two-Dimensional MoS_2 Nanosheets and Their Composite Materials, J. Mater. Chem. A 5 (2017) 24540–24563.

[18] H. Huang, X. Feng, C. Du, S. Wu, W. Song, Incorporated oxygen in MoS_2 ultrathin nanosheets for efficient ORR catalysis, J. Mater. Chem. A 3 (2015) 16050–16056.

[19] X. Sun, X. Zhu, Y. Wang, Y. Li, 1T′-$MoTe_2$ monolayer: A promising two-dimensional catalyst for the electrochemical production of hydrogen peroxide, Chinese J. Catal. 43 (2022) 1520–1526.

[20] C. Gao, D. Rao, H. Yang, S. Yang, J. Ye, S. Yang, C. Zhang, X. Zhou, T. Jing, X.H. Yan, Dual transition-metal atoms doping: an effective route to promote the ORR and OER activity on $MoTe_2$, New J. Chem. 45 (2021) 5589–5595.

[21] R. Dovesi, F. Pascale, B. Civalleri, K. Doll, N.M. Harrison, I. Bush, P. D'Arco, Y. Noël, M. Rérat, P. Carbonnière, M. Causà, S. Salustro, V. Lacivita, B. Kirtman, A.M. Ferrari, F.S. Gentile, J. Baima, M. Ferrero, R. Demichelis, M. De La Pierre, The CRYSTAL code, 1976-2020 and beyond, a long story, J. Chem.

Phys. 152 (2020) 204111.

[22] G.C. Wang, L. Jiang, X.Y. Pang, J. Nakamura, Cluster and periodic DFT calculations: The adsorption of atomic nitrogen on M(111) (M = Cu, Ag, Au) surfaces, J. Phys. Chem. B 109 (2005) 17943–17950.

[23] A.D. Becke, A new mixing of Hartree-Fock and local density-functional theories, J. Chem. Phys. 98 (1993) 1372–1377.

[24] C. Sahu, S. Pakhira, K. Sen, A.K. Das, A computational study of detoxification of lewisite warfare agents by british anti-lewisite: Catalytic effects of water and ammonia on reaction mechanism and kinetics, J. Phys. Chem. A 117 (2013) 3496–3506.

[25] S. Pakhira, J.L. Mendoza-Cortes, Tuning the Dirac Cone of Bilayer and Bulk Structure Graphene by Intercalating First Row Transition Metals Using First-Principles Calculations, J. Phys. Chem. C 122 (2018) 4768–4782.

[26] S. Pakhira, Rotational dynamics of the organic bridging linkers in metal-organic frameworks and their substituent effects on the rotational energy barrier, RSC Adv. 9 (2019) 38137–38147.

[27] S. Pakhira, K.P. Lucht, J.L. Mendoza-Cortes, Iron intercalation in covalent-organic frameworks: A promising approach for semiconductors, J. Phys. Chem. C 121 (2017) 21160–21170.

[28] K. Liang, S. Pakhira, Z. Yang, A. Nijamudheen, L. Ju, M. Wang, G.E. Sterbinsky, Y. Du, Z. Feng, J.L. Mendoza-cortes, Y. Yang, S-Doped MoP Nanoporous Layer Towards High- Efficiency Hydrogen Evolution in pH-Universal Electrolyte, ACS Catal. 9 (2019) 651–659.

[29] S. Pakhira, J.L. Mendoza-Cortes, Intercalation of first row transition metals inside covalent-organic frameworks (COFs): A strategy to fine tune the electronic properties of porous crystalline materials, Phys. Chem. Chem. Phys. 21 (2019) 8785–8796.

[30] F. Corà, A. Patel, N.M. Harrison, C. Roettic, C. Richard, A. Catlowa, Anab initio Hartree–Fock study of α-MoO_3, J. Mater. Chem. 7 (1997) 959–967.

[31] J. Laun, D. Vilela Oliveira, T. Bredow, Consistent gaussian basis sets of double-

and triple-zeta valence with polarization quality of the fifth period for solid-state calculations, J. Comput. Chem. 39 (2018) 1285–1290.

[32] D. Vilela Oliveira, J. Laun, M.F. Peintinger, T. Bredow, BSSE-correction scheme for consistent gaussian basis sets of double- and triple-zeta valence with polarization quality for solid-state calculations, J. Comput. Chem. 40 (2019) 2364–2376.

[33] H.J. Monkhorst, J.D. Pack, Special points for Brillonin-zone integrations, Phys. Rev. B 13 (1976) 5188.

[34] S. Pakhira, R.I. Singh, O. Olatunji-Ojo, M. Frenklach, W.A. Lester, Quantum Monte Carlo Study of the Reactions of CH with Acrolein: Major and Minor Channels, J. Phys. Chem. A 120 (2016) 3602–3612.

[35] R. Puttaswamy, R. Nagaraj, P. Kulkarni, H.K. Beere, S.N. Upadhyay, R.G. Balakrishna, N. Sanna Kotrappanavar, S. Pakhira, D. Ghosh, Constructing a High-Performance Aqueous Rechargeable Zinc-Ion Battery Cathode with Self-Assembled Mat-like Packing of Intertwined Ag(I) Pre-Inserted $V_3O_7{\cdot}H_2O$ Microbelts with Reduced Graphene Oxide Core, ACS Sustain. Chem. Eng. 9 (2021) 3985–3995.

[36] K. Momma, F. Izumi, VESTA 3 for three-dimensional visualization of crystal, volumetric and morphology data, J. Appl. Crystallogr. 44 (2011) 1272–1276.

[37] J.Y. Noh, H. Kim, Y.S. Kim, Stability and electronic structures of native defects in single-layer MoS_2, Phys. Rev. B 89 (2014) 205417.

[38] H.H. Huang, X. Fan, D.J. Singh, H. Chen, Q. Jiang, W.T. Zheng, Controlling phase transition for single-layer MTe_2 (M = Mo and W): Modulation of the potential barrier under strain, Phys. Chem. Chem. Phys. 18 (2016) 4086–4094.

[39] W.G. Dawson, D.W. Bullett, Electronic structure and crystallography of $MoTe_2$ and WTe_2, J. Phys. C Solid State Phys. 20 (1987) 6159–6174.

[40] J. Yang, T. Lü, Y.W. Myint, J. Pei, D. Macdonald, J.C. Zheng, Y. Lu, Robust Excitons and Trions in Monolayer $MoTe_2$, ACS Nano 9 (2015) 6603–6609.

[41] Y. Ji, H. Dong, C. Liu, Y. Li, The progress of metal-free catalysts for the oxygen reduction reaction based on theoretical simulations, J. Mater. Chem. A 6 (2018)

13489–13508.

[42] X. Liu, Y.F. Song, X. Wen, Y. Bai, J. Liu, P. Ren, W. Guo, T. Wang, W. Chen, Q. Peng, Y. Yang, Y.W. Li, Oxygen adsorption-induced morphological evolution of Hägg iron carbide at high oxygen chemical potentials, J. Phys. Chem. C 125 (2021) 3055–3065.

[43] G. Chen, J. Liu, Q. Li, P. Guan, X. Yu, L. Xing, J. Zhang, R. Che, A direct H_2O_2 production based on hollow porous carbon sphere-sulfur nanocrystal composites by confinement effect as oxygen reduction electrocatalysts, Nano Res. 12 (2019) 2614–2622.

[44] S. Das, S. Bhattacharjee, S. Mondal, S. Dutta, N. Bothra, S. Pati, S. Bhattacharyya, Bimetallic Zero-Valent Alloy with Measured High-Valent Surface States to Reinforce the Bifunctional Activity in Rechargeable Zinc-Air Batteries, ACS Sustain. Chem. Eng. 9 (2021) 14868–14880.

Chapter 7

Conclusions and Future Perspectives

This chapter summarizes the main findings of the Thesis. It highlights the key conclusions drawn from our research on novel materials. It also covers future directions and new research ideas for perovskite oxides, CNTs, and 2D TMDs.

7.1 Major Conclusion

In conclusion, this Thesis explores novel material for electrocatalysis, electrocatalysis design, mainly investigating the ORR mechanism on the surface of perovskite oxide, CNTs and 2D TMDs. The present work have studied the structural and electronic properties of these novel materials, and their electrocatalytic activity for ORR mechanism have been explored.

In the first part of the Thesis, we have computationally designed a 2D monolayer $LaNiO_3$ and studied the equilibrium structure, electronic properties, band structure and total density of states (DOS) using the PBE-D3 method. The electronic band gap of 2D monolayer $LaNiO_3$ was found to be 0.25 eV. We have explored the ORR mechanism on the surface of the 2D monolayer $LaNiO_3$ by studying each reaction intermediate employing the computational hydrogen electrode (CHE) model. Both dissociative and associative pathways have been studied by computing Gibbs free energy and relative Gibbs free energy of various reaction intermediates of the ORR mechanism. Our study found that the rate-determining step is the desorption of OH, which generates the second water molecule and regenerates the active surface of the 2D monolayer $LaNiO_3$ for subsequent O_2 adsorption. The associated overpotential was determined to be 1.08 V. To sum up, our results demonstrate that 2D monolayer $LaNiO_3$ displays excellent electrocatalytic performance, positioning it as a potential candidate for fuel cells demanding efficient ORR catalysts. We hope our present findings guide development of efficient, non-noble ORR electrocatalysts for fuel cell applications.

In the second part of the Thesis, we employed the DFT-D3 method to investigate the structural and electronic properties of the cobalt-platinum nanoparticle encapsulated within carbon nanotube (CoPt@CNT). Our investigation of the electronic properties confirms that CoPt@CNT is a conducting material ($E_g = 0$) due to the synergistic effect between the CoPt nanoparticle and CNT. The change in Gibbs free energy (ΔG) and adsorption energy (ΔE) of each reaction intermediate have been calculated to analyze the electrocatalytic activity of CoPt@CNT towards ORR. We found that the occurrence of each step of ORR mechanism are energetically and thermodynamically favorable on the surface of CoPt@CNT. Our calculations reveal that the O_2 dissociation is the rate-determining step in the ORR mechanism, exhibiting a computed barrier height of 0.16 eV. The corresponding ORR overpotential was found to be 1.39 V. This study provides key insights into the evolution of the CoPt@CNT electrocatalyst during the oxygen reduction reaction (ORR) while offering a deeper understanding of its active sites. This work contributes to the development of efficient, cost-effective ORR catalysts, driving key advancements in fuel cell technology.

In the third part of the Thesis, we computationally encapsulated FeCe nanoparticle within CNT (FeCe@CNT) and studied the structural and electronic properties, band gap and total DOS employing DFT-D3 method. Our study found that FeCe@CNT has metallic nature due to the presence of large electron density of states (DOS) around the Fermi level (E_F). We further studied ORR mechanism on the surface of FeCe@CNT by computing the adsorption energy (ΔE) of key reaction intermediates. The O_2 adsorption energy on FeCe@CNT surfaces was found to be -1.67 eV, indicating spontaneous and energetically favorable O_2 activation. It was found that the ORR mechanism follows 4e-transfer pathway and predominantly proceeds through the associative mechanism. The theoretical ORR overpotential was found to be 1.13 V. Our energy calculations for ORR intermediates confirm that the active sites on the FeCe@CNT surface are energetically favorable for the ORR process. Our study establish the FeCe@CNT material as a highly promising non-noble-metal catalyst with excellent activity towards the ORR. This study aims to guide the discovery of stable, low-cost, efficient ORR electrocatalysts, advancing clean energy-conversion technologies.

In the fourth part of the Thesis, we have computationally designed a 3×3 supercell model of Mo-defective 2D $MoTe_2$ TMD and conducted geometry optimization and electronic properties calculation utilizing the DFT-D method. Our band structure

calculation found that the Mo defective $MoTe_2$ is a low band gap (Eg = 0.53 eV) semiconductor. We have examined the ORR mechanism on the surface of Mo defective 2D monolayer $MoTe_2$. We found that the change in Gibbs free energy of each reaction step are negative, which indicates that ORR has an exothermic nature. The calculated overpotential was found to be 0.68 V. This low overpotential indicates that the ORR can proceed with minimal energy input, a critical factor for maximizing the efficiency of electrochemical devices such as fuel cells and batteries. Our calculations using the CHE model indicate that the Mo defective $MoTe_2$ TMD is a highly promising, Pt-free electrocatalyst for the ORR and could be attractive for fuel-cell applications. We anticipate that our theoretical and computational findings will inspire further experimental and theoretical efforts to develop additional 2D Pt-free ORR electrocatalysts.

In this thesis, taken together, the four studies reveal a consistent relationship between electronic structure and ORR activity. A finite electronic density at or near the Fermi level (E_F) is a prerequisite. Pristine 2D $MoTe_2$, with a 1.64 eV direct band gap and no states at E_F, is unsuitable for ORR, whereas introducing a Mo vacancy narrows the gap to 0.53 eV and makes every step of the $4e^-$ pathway downhill in free energy profile. The metallic systems (2D $LaNiO_3$, CoPt@CNT, FeCe@CNT) all have a large density of states (DOS) at E_F, but they differ in how strongly they activate O_2. In FeCe@CNT, where Fe and Ce d-states dominate near E_F, O_2 adsorbs most strongly ($\Delta E = -1.67$ eV), compared with −0.79 eV for CoPt@CNT. Metallic character thus ensures efficient electron transfer but does not by itself determine activation strength, which also depends on the d-state character at the active sites and on the geometry, as seen in the cleaving of $LaNiO_3$ into a high-surface-area monolayer and the confinement of nanoparticles within CNTs. Because these conclusions rest on thermodynamic (CHE) analysis at different levels of theory, they should be read as qualitative trends.

7.2 Future Perspectives

The present thesis has advanced our understanding and design of perovskite oxides, CNTs, and 2D TMDs for the oxygen reduction reaction (ORR). Future work should broaden this effort to a wider range of perovskite oxide compositions, 2D TMD phases, and CNT architectures to discover candidates with superior ORR performance. Exploring less-studied compositions and structural motifs could uncover electronic and surface features that improve electrocatalytic activity.

- Future work on perovskite oxides for the ORR should focus on enhancing intrinsic activity and long-term durability through precise lattice engineering, defect control, and tailored surface modifications. Future studies should include high-throughput computational screening and machine-learning-driven design to identify optimal cation substitutions, such as A-site deficiency or B-site doping, aimed at tuning the electronic structure and regulating oxygen vacancy concentration in perovskite oxides. They should also cover the development of advanced hybrid architectures that integrate perovskites with conductive carbon frameworks or other synergistic supports to mitigate conductivity limitations and optimize mass/charge transport.
- Future work should include encapsulating a broader range of nanoparticles inside CNTs and N-doped CNTs (NCNTs), then systematically studying their structural and electronic properties and their electrocatalytic performance for ORR, HER and OER. Future research should focus on diversifying non-precious metal decoration and implementing advanced multi-heteroatom doping strategies within the CNT or NCNT architecture to synergistically refine electronic properties and maximize catalytic performance.
- Future research should explore a diverse range of 2D transition metal dichalcogenides (2D TMDs) to assess their bifunctional electrocatalytic potential for the oxygen reduction reaction (ORR) and hydrogen evolution reaction (HER). This includes systematic tuning of TMD electronic and structural properties through doping, defect engineering, and hybridization with nanomaterials like graphene or perovskites to improve activity, stability, and selectivity. Additionally, investigating 2D heterostructures and alloys via controlled layering of distinct TMDs or heteroatom doping can induce synergistic effects that enhance overall performance, ultimately enabling the design of high-performance TMD-based electrocatalysts for sustainable energy applications.
- Future work will target non-precious metal catalysts for ORR with activity comparable to or better than Pt/Pd benchmarks, while also ensuring improved long-term stability, scalability, and cost-effectiveness for practical fuel cell applications.

In summary, the Thesis future scope includes exploring diverse compositions of novel materials (e.g., perovskite oxides, CNTs and 2D TMDs), optimizing their structural and electronic properties for electrocatalysis, investigating heterostructures and alloys, and developing non-noble metal catalysts with comparable or superior ORR activity to noble metal benchmarks.

Supporting Information

Cobalt-Platinum Nanoparticle Encapsulated within Carbon Nanotube for Superior O_2 Reduction Reaction

Dikeshwar Halba[1], Anshuman Ojha[1] and Srimanta Pakhira[1,2*]

[1] Theoretical Condensed Matter Physics and Advanced Computational Materials Science Laboratory, Department of Physics, Indian Institute of Technology Indore (IIT Indore), Simrol, Khandwa Road, Indore, Madhya Pradesh, 453552, India.

[2] Theoretical Condensed Matter Physics and Advanced Computational Materials Science Laboratory, Centre for Advanced Electronics (CAE), Indian Institute of Technology Indore, Simrol, Khandwa Road, Indore, Madhya Pradesh, 453552, India.

*Corresponding author: spakhira@iiti.ac.in (or) spakhirafsu@gmail.com

Contents	**Page**
Title	187
List of Contents	187
1. Optimized Structures (.cif format)	188
1.1 Equilibrium CNT (.cif format)	188
1.2 Equilibrium CoPt@CNT (.cif format)	189
2. Equilibrium Structures (.cif format) for ORR intermediates	191
2.1. Equilibrium O2_CoPt@CNT (.cif format)	191
2.2. Equilibrium 2O_CoPt@CNT (.cif format)	193
2.3. Equilibrium O_OH_CoPt@CNT (.cif format)	194
2.4. Equilibrium O_CoPt@CNT (.cif format)	196
2.5. Equilibrium OH_CoPt@CNT (.cif format)	198
2.6. Equilibrium OOH_CoPt@CNT (.cif format)	200
3. Dispersion-Corrected DFT Investigation of ORR Mechanism on CoPt@CNT	201

1. Optimized Structures (.cif format)

The crystallographic information file (CIF) format for the equilibrium structure of carbon nanotube (CNT) and CoPt@CNT material, along with the various reaction intermediates involved in the associative and dissociative mechanisms of oxygen reduction reaction (ORR) are provided below:

1.1 Equilibrium CNT (.cif format)

_chemical_name_common	'CNT'
_cell_length_a	24.324499
_cell_length_b	24.324499
_cell_length_c	2.444800
_cell_angle_alpha	90.000000
_cell_angle_beta	90.000000
_cell_angle_gamma	120.000000
_cell_volume	1252.742362
_space_group_name_H-M_alt	' P 6 '
_space_group_IT_number	168

loop_

_space_group_symop_operation_xyz

'x, y, z'

'-y, x-y, z'

'-x+y, -x, z'

'-x, -y, z'

'y, -x+y, z'

'x-y, x, z'

loop_

_atom_site_label

_atom_site_occupancy

_atom_site_fract_x

_atom_site_fract_y

_atom_site_fract_z

_atom_site_adp_type

_atom_site_U_iso_or_equiv

_atom_site_type_symbol

C001	1.0	0.186380	0.107490	0.141850
C007	1.0	0.180640	0.132210	0.641050
C013	1.0	0.131670	0.179830	0.140830
C019	1.0	0.152310	0.168740	0.642030

1.2 Equilibrium CoPt@CNT (.cif format)

_chemical_name_common	' CoPt_CNT '
_cell_length_a	20.793501
_cell_length_b	20.793501
_cell_length_c	2.477100
_cell_angle_alpha	90.000000
_cell_angle_beta	90.000000
_cell_angle_gamma	120.000000
_cell_volume	927.533029
_space_group_name_H-M_alt	' P -6 '

```
_space_group_IT_number                  174

loop_
_space_group_symop_operation_xyz
   'x, y, z'
   '-y, x-y, z'
   '-x+y, -x, z'
   'x, y, -z'
   '-y, x-y, -z'
   '-x+y, -x, -z'


loop_
   _atom_site_label
   _atom_site_occupancy
   _atom_site_fract_x
   _atom_site_fract_y
   _atom_site_fract_z
   _atom_site_adp_type
   _atom_site_U_iso_or_equiv
   _atom_site_type_symbol
   C001         1.0    0.220950      0.147090      0.500000
   C004         1.0    0.192060      0.197720      0.500000
   CO007        1.0    0.110000      0.091850      0.500000
   C010         1.0   -0.225680     -0.151820      0.500000
```

C013	1.0	-0.197160	-0.200830	0.500000
C016	1.0	0.223780	0.114300	-0.000000
C019	1.0	0.167930	0.212830	-0.000000
C022	1.0	-0.228920	-0.119680	0.000000
C025	1.0	-0.173230	-0.215650	0.000000
PT028	1.0	0.000000	0.000000	0.000000

2. Equilibrium Structures (.cif format) for ORR intermediates

2.1 Equilibrium O_2_CoPt@CNT (.cif format)

_chemical_name_common	' O_2_CoPt@CNT '
_cell_length_a	21.743099
_cell_length_b	21.743099
_cell_length_c	2.464800
_cell_angle_alpha	90.000000
_cell_angle_beta	90.000000
_cell_angle_gamma	120.000000
_cell_volume	1009.148760
_space_group_name_H-M_alt	' P -6 '
_space_group_IT_number	174

loop_

_space_group_symop_oper
ation_xyz 'x, y, z'

'-y, x-y, z'

'-x+y, -x, z'

'x, y, -z'

'-y, x-y, -z'

'-x+y, -x, -z'

loop_

_atom_site_label

_atom_site_occupancy

_atom_site_fract_x

_atom_site_fract_y

_atom_site_fract_z

_atom_site_adp_type

_atom_site_U_iso_or_equiv

_atom_site_type_symbol

O1	1.0	0.285360	0.211810	-0.500000
C2	1.0	0.209020	0.143190	-0.500000
C3	1.0	0.180230	0.189870	-0.500000
Co4	1.0	0.092350	0.078840	-0.500000
C5	1.0	-0.215240	-0.148910	-0.500000
C6	1.0	-0.186670	-0.194820	-0.500000
O7	1.0	0.255130	0.261490	-0.500000
C8	1.0	0.215030	0.113650	0.000000
C9	1.0	0.158180	0.205690	0.000000
C10	1.0	-0.219120	-0.118440	0.000000
C11	1.0	-0.163130	-0.208470	0.000000
PT12	1.0	0.000000	0.000000	0.000000

2.2 Equilibrium 2O_CoPt@CNT (.cif format)

```
_chemical_name_common                  ' 2O_CoPt@CNT '
_cell_length_a                         21.743099
_cell_length_b                         21.743099
_cell_length_c                         2.464800
_cell_angle_alpha                      90.000000
_cell_angle_beta                       90.000000
_cell_angle_gamma                      120.000000
_cell_volume                           1009.148760
_space_group_name_H-M_alt              ' P -6 '
_space_group_IT_number                 174

loop_
_space_group_symop_oper
  ation_xyz 'x, y, z'
  '-y, x-y, z'
  '-x+y, -x, z'
  'x, y, -z'
  '-y, x-y, -z'
  '-x+y, -x, -z'

loop_
  _atom_site_label
  _atom_site_occupancy
```

_atom_site_fract_x

_atom_site_fract_y

_atom_site_fract_z

_atom_site_adp_type

_atom_site_U_iso_or_equiv

_atom_site_type_symbol

O1	1.0	0.350017	0.269566	-0.500000
C2	1.0	0.209020	0.143190	-0.500000
C3	1.0	0.180230	0.189870	-0.500000
Co4	1.0	0.092350	0.078840	-0.500000
C5	1.0	-0.215240	-0.148910	-0.500000
C6	1.0	-0.186670	-0.194820	-0.500000
O7	1.0	0.325080	0.311900	-0.500000
C8	1.0	0.215030	0.113650	0.000000
C9	1.0	0.158180	0.205690	0.000000
C10	1.0	-0.219120	-0.118440	0.000000
C11	1.0	-0.163130	-0.208470	0.000000
PT12	1.0	0.000000	0.000000	0.000000

2.3 Equilibrium O_OH_CoPt@CNT (.cif format)

_chemical_name_common	' O_OH_CoPt@CNT '
_cell_length_a	12.7528
_cell_length_b	12.7528
_cell_length_c	2.5249
_cell_angle_alpha	90.000000
_cell_angle_beta	90.000000

_cell_angle_gamma 120.000000

_cell_volume 225.6151

_space_group_name_H-M_alt ' P -6 '

_space_group_IT_number 174

loop_

_space_group_symop_oper
ation_xyz 'x, y, z'

'-y, x-y, z'

'-x+y, -x, z'

'x, y, -z'

'-y, x-y, -z'

'-x+y, -x, -z'

loop_

_atom_site_label

_atom_site_occupancy

_atom_site_fract_x

_atom_site_fract_y

_atom_site_fract_z

_atom_site_adp_type

_atom_site_U_iso_or_equiv

_atom_site_type_symbol

C1 1.0 0.41341 0.23132 -0.50000

C4	1.0	0.39520	0.34900	-0.50000
Co7	1.0	0.17110	0.16025	-0.50000
C10	1.0	-0.33833	-0.18192	-0.50000
C13	1.0	-0.29349	-0.26086	-0.50000
O16	1.0	0.49914	0.45756	-0.50000
O19	1.0	-0.46274	0.27789	-0.50000
H35	1.0	-0.43353	0.21952	-0.50000
C22	1.0	0.36029	0.15787	-0.00000
C25	1.0	0.32403	0.34083	-0.00000
C28	1.0	-0.34939	-0.12979	0.00000
C31	1.0	-0.26432	-0.29774	0.00000
PT34	1.0	0.00000	0.00000	0.00000

2.4 Equilibrium O_CoPt@CNT (.cif format)

_chemical_name_common	' O_CoPt_CNT '
_cell_length_a	12.344000
_cell_length_b	12.344000
_cell_length_c	2.486800
_cell_angle_alpha	90.000000
_cell_angle_beta	90.000000
_cell_angle_gamma	120.000000
_cell_volume	328.158229
_space_group_name_H-M_alt	' P -6 '
_space_group_IT_number	174

```
loop_
_space_group_symop_oper
  ation_xyz 'x, y, z'
  '-y, x-y, z'
  '-x+y, -x, z'
  'x, y, -z'
  '-y, x-y, -z'
  '-x+y, -x, -z'


loop_
  _atom_site_label
  _atom_site_occupancy
  _atom_site_fract_x
  _atom_site_fract_y
  _atom_site_fract_z
  _atom_site_adp_type
  _atom_site_U_iso_or_equiv
  _atom_site_type_symbol
  C001      1.0   0.355400   0.282000   -0.500000
  C004      1.0   0.356350   0.407750   -0.500000
  CO007     1.0   0.144430   0.201720   -0.500000
  C010      1.0  -0.345850  -0.252870   -0.500000
  C013      1.0  -0.275990  -0.314300   -0.500000
  O016      1.0   0.472210  -0.488530   -0.500000
  C019      1.0   0.356500   0.225960   -0.000000
```

C022	1.0	0.283530	0.400550	-0.000000
C025	1.0	-0.374960	-0.213640	0.000000
C028	1.0	-0.233860	-0.336180	0.000000
PT031	1.0	0.000000	0.000000	0.000000

2.5 Equilibrium OH_CoPt@CNT (.cif format)

```
_chemical_name_common                  ' OH_CoPt@CNT '
_cell_length_a                         25.148899
_cell_length_b                         25.148899
_cell_length_c                         2.495200
_cell_angle_alpha                      90.000000
_cell_angle_beta                       90.000000
_cell_angle_gamma                      120.000000
_cell_volume                           1366.702332
_space_group_name_H-M_alt              ' P -6 '
_space_group_IT_number                 174

loop_
_space_group_symop_oper
  ation_xyz 'x, y, z'
  '-y, x-y, z'
  '-x+y, -x, z'
  'x, y, -z'
  '-y, x-y, -z'
  '-x+y, -x, -z'
```

```
loop_
  _atom_site_label
  _atom_site_occupancy
  _atom_site_fract_x
  _atom_site_fract_y
  _atom_site_fract_z
  _atom_site_adp_type
  _atom_site_U_iso_or_equiv
  _atom_site_type_symbol
  C1     1.0   0.182260   0.118570   -0.500000
  C2     1.0   0.175550   0.175070   -0.500000
  Co3    1.0   0.090040   0.083333   -0.500000
  C4     1.0   -0.183240  -0.120160  -0.500000
  C5     1.0   -0.162350  -0.162600  -0.500000
  O6     1.0   0.227850   0.230900   -0.500000
  C7     1.0   0.185750   0.092400   0.000000
  C8     1.0   0.138850   0.168880   0.000000
  C9     1.0   -0.183720  -0.092280  0.000000
  C10    1.0   -0.143930  -0.176310  0.000000
  PT11   1.0   0.000000   0.000000   0.000000
  H12    1.0   0.264329   0.227642   -0.500000
```

2.6 Equilibrium OOH_CoPt@CNT (.cif format)

```
_chemical_name_common      ' OOH_CoPt@CNT '

_cell_length_a                         21.743099
_cell_length_b                         21.743099
_cell_length_c                         2.464800
_cell_angle_alpha                      90.000000
_cell_angle_beta                       90.000000
_cell_angle_gamma                      120.000000
_cell_volume                           1009.148760
_space_group_name_H-M_alt              ' P -6 '
_space_group_IT_number                 174

loop_
_space_group_symop_oper
  ation_xyz 'x, y, z'
  '-y, x-y, z'
  '-x+y, -x, z'
  'x, y, -z'
  '-y, x-y, -z'
  '-x+y, -x, -z'

loop_
  _atom_site_label
  _atom_site_occupancy
  _atom_site_fract_x
```

_atom_site_fract_y

_atom_site_fract_z

_atom_site_adp_type

_atom_site_U_iso_or_equiv

_atom_site_type_symbol

O1	1.0	0.32950	0.28741	-0.50000
C4	1.0	0.20902	0.14319	-0.50000
C7	1.0	0.18023	0.18987	-0.50000
Co10	1.0	0.09235	0.07884	-0.50000
C13	1.0	-0.21524	-0.14891	-0.50000
C16	1.0	-0.18667	-0.19482	-0.50000
O19	1.0	0.30000	0.33305	-0.50000
H35	1.0	0.34222	0.37936	-0.50000
C22	1.0	0.21503	0.11365	-0.00000
C25	1.0	0.15818	0.20569	-0.00000
C28	1.0	-0.21912	-0.11844	0.00000
C31	1.0	-0.16313	-0.20847	0.00000
PT34	1.0	0.00000	0.00000	0.00000

3. Dispersion-Corrected DFT Investigation of ORR Mechanism on CoPt@CNT

We considered the van der Waals (vdW) crystal structure of CNT bundles to encapsulate CoPt nanoparticles within pure CNT. We have used a high symmetric hexagonal-shaped 3D unit cell with the CNTs (considering a vdW crystal) situated at the corners/vertices of the unit cell where we dedicatedly considered 3D vdW crystal structure of the system. This was considered to make easier for high level computation and suitability of the CRYSTAL17 suite code where we can impose the symmetry of the vdW crystal to perform the faster calculations with reasonable time. A periodic arrangement of three-dimensional structure is formed by the CNTs positioned at the

vertices of the high symmetric hexagonal-shaped 3D vdW unit cell. The parameters *a* and *b* define the distance between two adjacent CNTs (inter-tube spacing from the center of the tube) in the unit cell. The perpendicular lattice constant to that of the tube is physically meaningful because it defines the equilibrium spacing between adjacent CNTs. The lattice parameter c represents periodicity along the CNT tube axis (i.e., z-axis). We have not used any vacuum space along the c direction and there is a periodicity which makes it as a long CNTs or CoPt@CNT. There is a vdW interaction between adjacent CNTs at the periodic boundaries, which is critical for their structural stability and physical properties. We have employed the DFT-D3 calculation, which incorporates this vdW interaction.

The DFT-D3 method has been employed to study the structural and electronic properties of CNT, CoPt@CNT, and reaction intermediates of ORR. After geometry optimization, we found that the equilibrium structure of pristine CNT has a hexagonal ***P6*** space group symmetry. Thelattice parameters of pure CNT obtained are a = b = 24.32 Å, c = 2.44 Å, α = β = 90˚, and γ = 120˚, respectively, which agrees well with the previous reports. The equilibrium structure of the CoPt@CNT system acquired a hexagonal ***P6̄*** space group symmetry. The equilibrium lattice parameter i.e., lattice constants and bond angles of the CoPt@CNT were found to be a = b = 20.79 Å, c = 2.48 Å, α = β = 90˚, and γ = 120˚, respectively. A highly symmetric k-vector ***Γ-K-M-L-A-H-L-Γ*** direction has been implemented to compute the electronic band structures and total DOS of the CNT and CoPt@CNT material as shown in Figures S1a and S1b.

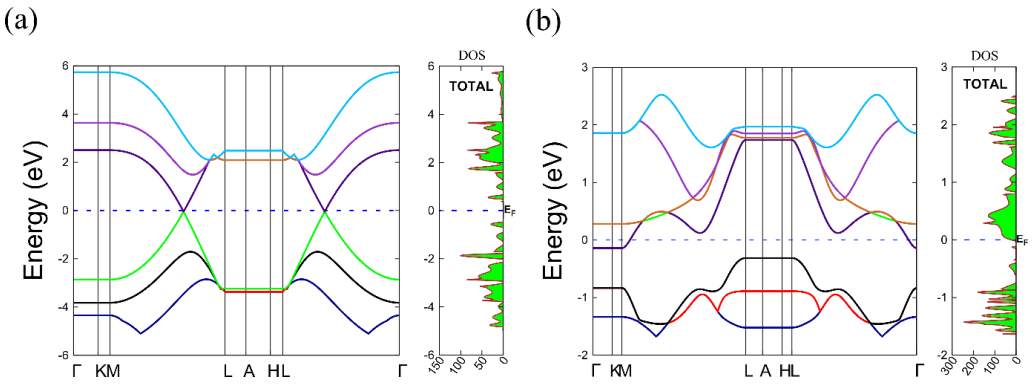


Figure S1: *Electronic band structure and total DOS of the equilibrium (a) CNT, and (b) CoPt@CNT material.*

Table S1: *Equilibrium lattice constants, lattice angles, and symmetry of all reaction intermediates of ORR.*

ORR intermediates	Lattice constants (Å)	Lattice angles	Space group symmetry
O2_CoPt@CNT	a=b=21.74, c=2.46	α=β=90˚, γ=120˚	$P\bar{6}$
2O_CoPt@CNT	a=b=21.74, c=2.46	α=β=90˚, γ=120˚	$P\bar{6}$
O_OH_CoPt@CNT	a=b=12.75, c=2.52	α=β=90˚, γ=120˚	$P\bar{6}$
O_CoPt@CNT	a=b=12.34, c=2.49	α=β=90˚, γ=120˚	$P\bar{6}$
OH_CoPt@CNT	a=b=25.15, c=2.50	α=β=90˚, γ=120˚	$P\bar{6}$
OOH_CoPt@CNT	a=b=24.15 , c=2.50	α=β=90˚,γ=120˚	$P\bar{6}$

We have studied the structural and electronic properties of ORR intermediates using the same DFT-D3 method. Equilibrium lattice parameters, lattice constants, lattice angles, and symmetry of various reaction intermediates of ORR are depicted in Table S1.

The electronic band structures and total DOS plot of all reaction intermediates of the ORR mechanism are illustrated in Figure S2, which has been computed using a highly symmetric ***Γ-K-M-L-A-H-L-Γ*** k-path**.** All equilibrium structures have zero band gap, and there is a presence of small electron density in the total DOS. This confirms excellent catalytic activity and charge transfer during the whole ORR reaction steps. Our energy calculations demonstrated excellent catalytic activity of the CoPt@CNT material towards ORR.

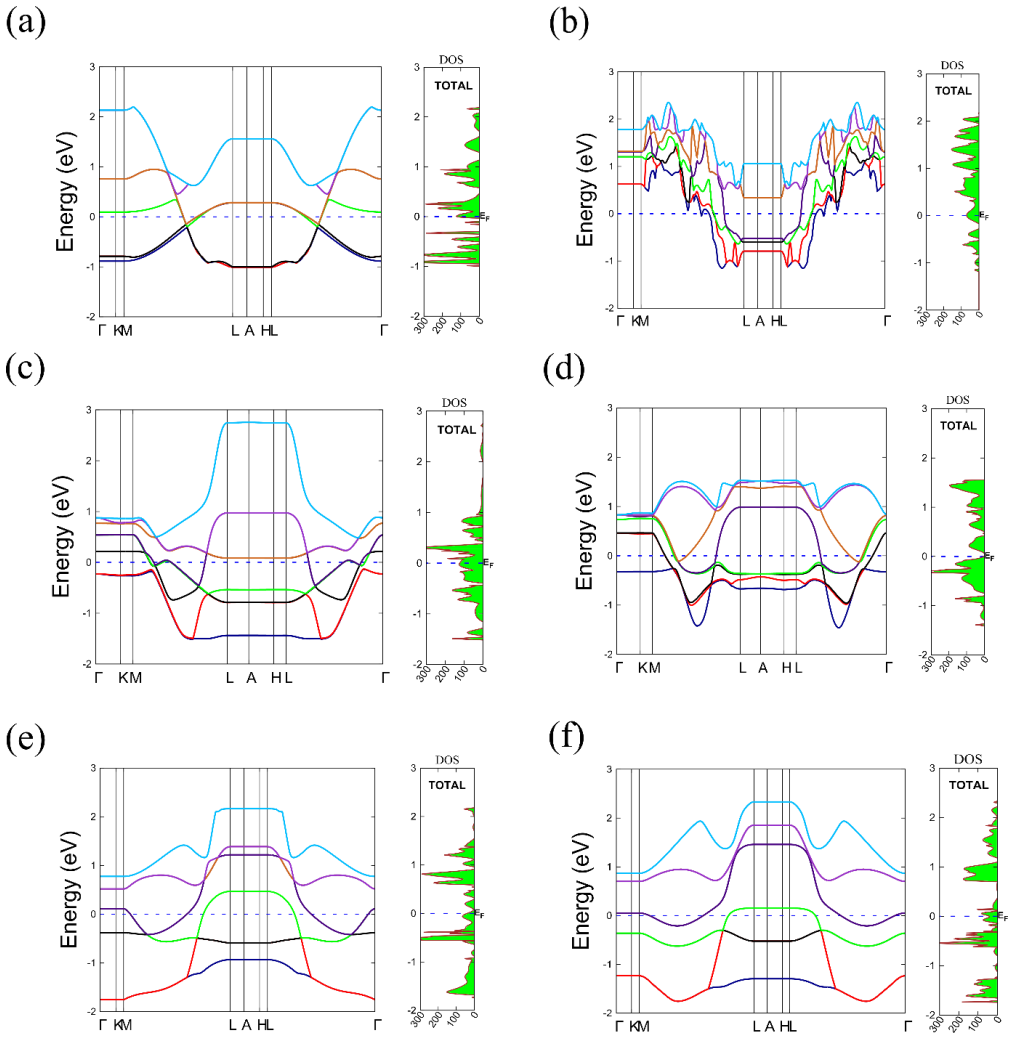


Figure S2: *Electronic band structure and total DOS of equilibrium (a) O_2_CoPt@CNT and (b) 2O_CoPt@CNT, (c) O_OH_CoPt@CNT, (d) O_CoPt@CNT, (e) OH_CoPt@CNT, and (f) OOH_CoPt@CNT obtained by DFT-D3 method.*

Spin Density Calculations and Plot

We have performed the electronic spin density calculation of the CoPt@CNT material and the various reaction intermediates of the ORR mechanism. Spin densities are used to get information about the distribution of unpaired electrons available for chemical reactions in the studied intermediates. The electron spin density plots of reaction intermediates of ORR were computed using the same DFT-D3 method, as depicted in Figure S3. The isosurface with sky blue color corresponds to positive spin (α-spin) densities, whereas the yellow color corresponds to negative spin (β-spin) densities.

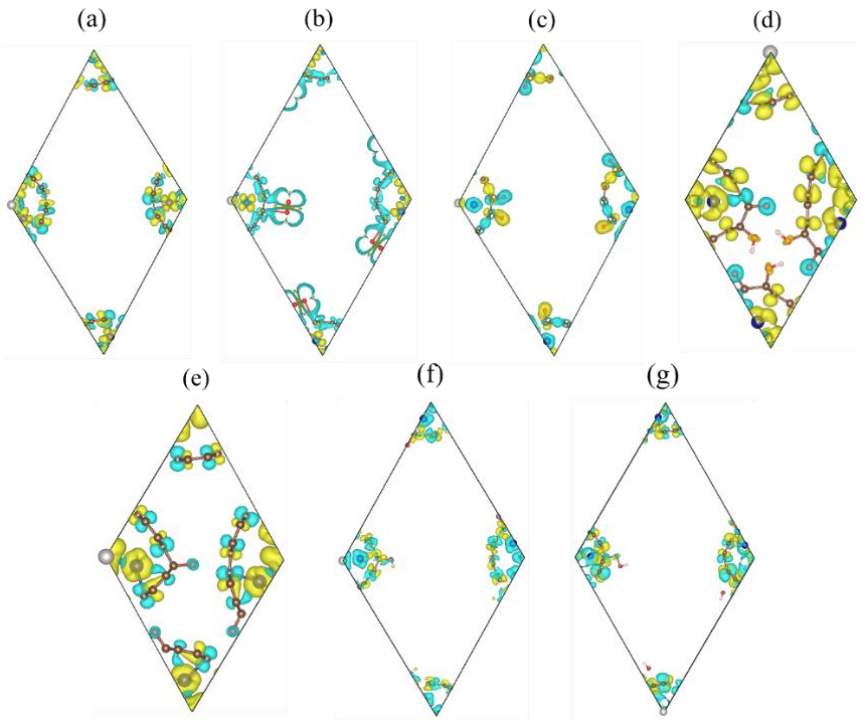


Figure S3: *Electron spin density of (a) pure CoPt@CNT, (b) O_2_CoPt@CNT, (c) 2O_CoPt@CNT, (d) O_OH_CoPt@CNT, (e) O_CoPt@CNT, (f) OH_CoPt@CNT, and (g) OOH_CoPt@CNT reaction intermediates. The sky-blue color shape represents the positive values (α-spin up), and the yellow color shape shows the negative values (β-spin down).*

Here, we have modeled a van der Waals (vdW) crystal structure of CoPt@CNT bundles to study the ORR mechanism. The adjacent nanotubes in this configuration interact via van der Waals forces, due to which the lattice constants are unequal. The lattice constants a and b represent the inter-tube spacing in the highly symmetric hexagonal-shaped 3D vdW unit cell. In our vdW 3D system, variable cell relaxation is appropriate to determine equilibrium spacing. In this case, the CNTs will interact due to vdW interaction as we have simulated a 3D crystal structure of the subject material using the DFT-D3 method. We acknowledge that while simulating a 1D system, lattice constants a and b should be significantly large to prevent interactions between the periodic images.

Table S2: *Relative adsorption energy and relative Gibbs free energy of various reaction intermediates of the dissociative mechanism of ORR. Here, we have defined that the relative adsorption energy and relative Gibbs free energy of ORR intermediates are the difference of the change of the electronic energy (E) and Gibbs free energy (G) between two consecutive reaction steps/intermediates obtained by the present computations and accordingly reported in Tables S2 and S3.*

O_2 reduction reaction steps	**Relative adsorption energy ΔE (eV)**	**Relative Gibbs free energy ΔG (eV)**
[CoPt@CNT] → [O_2_CoPt@CNT]	-0.79	-0.71
[O_2_CoPt@CNT] → [2O_CoPt@CNT]	-0.10	0.16
[2O_CoPt@CNT] → [O_OH_CoPt@CNT]	-1.64	-1.15
[O_OH_CoPt@CNT] → [O_CoPt@CNT]	-0.59	-1.03
[O_CoPt@CNT] → [OH_CoPt@CNT]	-1.07	-0.90
[OH_CoPt@CNT] → [CoPt@CNT]	-1.11	-1.43

Table S3: *Relative adsorption energy and relative Gibbs free energy of various reaction intermediates of the associative mechanism of ORR.*

ORR steps	**Relative adsorption energy ΔE (eV)**	**Relative Gibbs free energy ΔG (eV)**
[CoPt@CNT] → [O2_CoPt@CNT]	-0.79	-0.71
[O2_CoPt@CNT] → [OOH_CoPt@CNT]	-0.65	-0.25
[OOH_CoPt@CNT] → [O_CoPt@CNT]	-1.60	-1.87
[O_CoPt@CNT] → [OH_CoPt@CNT]	-1.70	-0.90
[OH_CoPt@CNT] → [CoPt@CNT]	-0.47	-1.43